IN-39-CR

443

P-218

A Progress Report

July 1, 1993 to December 31, 1993

NASA-UVA LIGHT AEROSPACE ALLOY AND STRUCTURES TECHNOLOGY PROGRAM (LA^2ST)

NASA-LaRC Grant NAG-1-745

Submitted to:

National Aeronautics and Space Administration
Langley Research Center
Hampton, Virginia 23681-0001

Attention:

Mr. Richard J. Siebels, Grants Officer
MS 126

For Review by:

Mr. Dennis L. Dicus, Grant Monitor
Metallic Materials Branch, MS 188A

Submitted by:

Richard P. Gangloff
Professor

Report No. UVA/528266/MSE94/114
March 15, 1994

DEPARTMENT OF MATERIALS SCIENCE AND ENGINEERING

SCHOOL OF
ENGINEERING
& APPLIED SCIENCE

University of Virginia
Thornton Hall
Charlottesville, VA 22903

UNIVERSITY OF VIRGINIA
School of Engineering and Applied Science

The University of Virginia's School of Engineering and Applied Science has an undergraduate enrollment of approximately 1,500 students with a graduate enrollment of approximately 600. There are 160 faculty members, a majority of whom conduct research in addition to teaching.

Research is a vital part of the educational program and interests parallel academic specialties. These range from the classical engineering disciplines of Chemical, Civil, Electrical, and Mechanical and Aerospace to newer, more specialized fields of Applied Mechanics, Biomedical Engineering, Systems Engineering, Materials Science, Nuclear Engineering and Engineering Physics, Applied Mathematics and Computer Science. Within these disciplines there are well equipped laboratories for conducting highly specialized research. All departments offer the doctorate; Biomedical and Materials Science grant only graduate degrees. In addition, courses in the humanities are offered within the School.

The University of Virginia (which includes approximately 2,000 faculty and a total of full-time student enrollment of about 17,000), also offers professional degrees under the schools of Architecture, Law, Medicine, Nursing, Commerce, Business Administration, and Education. In addition, the College of Arts and Sciences houses departments of Mathematics, Physics, Chemistry and others relevant to the engineering research program. The School of Engineering and Applied Science is an integral part of this University community which provides opportunities for interdisciplinary work in pursuit of the basic goals of education, research, and public service.

NASA-UVA LIGHT AEROSPACE ALLOY AND STRUCTURES TECHNOLOGY PROGRAM

LA^2ST

Program Director:

Richard P. Gangloff

Co-principal Investigators:

John R. Scully
Edgar A. Starke, Jr.
Glenn E. Stoner
Earl A. Thornton
Franklin E. Wawner, Jr.
John A. Wert

NASA-LaRC Grant Monitor:

Dennis L. Dicus

Report No. UVA/528266/MSE94/114
March 15, 1994

Copy No._____

TABLE OF CONTENTS

TABLE OF CONTENTS (continued)

NASA-UVA LIGHT AEROSPACE ALLOY AND STRUCTURES TECHNOLOGY PROGRAM

EXECUTIVE SUMMARY

The NASA-UVa Light Aerospace Alloy and Structures Technology (LA^2ST) Program was initiated in 1986, and continues a high level of activity, with projects being conducted by graduate students and faculty advisors in the Departments of Materials Science and Engineering, and Mechanical and Aerospace Engineering at the University of Virginia. This work is funded by the NASA-Langley Research Center under Grant NAG-1-745. Here, we report on progress achieved between July 1 and December 31, 1993.

The objective of the LA^2ST Program is to conduct interdisciplinary graduate student research on the performance of next generation, light weight aerospace alloys, composites and thermal gradient structures in collaboration with NASA-Langley researchers. Specific technical objectives are presented for each research project. We generally aim to produce relevant data and basic understanding of material mechanical response, environmental/corrosion behavior, and microstructure; new monolithic and composite alloys; advanced processing methods; new solid and fluid mechanics analyses; measurement and modeling advances; and critically, a pool of educated graduate students for aerospace technologies.

The accomplishments presented in this report are as follows.

- oo Four research areas are actively investigated, including: (1) Mechanical and Environmental Degradation Mechanisms in Advanced Light Metals and Composites, (2) Aerospace Materials Science, (3) Mechanics of Materials and Composites for Light Aerospace Structures, and (4) Thermal Gradient Structures.

- oo Thirteen research projects are being conducted by 8 PhD and 4 MS level graduate students, 7 faculty members, and 1 Research Associate from two departments in the School of Engineering and Applied Science at UVa. Each project is planned and executed in conjunction with a specific branch and technical monitor at NASA-LaRC.

- oo Two undergraduates were recruited to conduct research at NASA-LaRC during the Summer of 1994. No undergraduates are currently participating in LA^{2}ST research at UVa.

- oo Accomplishments between July and December of 1993 include 3 journal or proceedings publications, 1 NASA progress report, 4 presentations at national technical meetings, and 1 thesis. One student graduated during this reporting period with the Masters of Science Degree. The LA^{2}ST totals since 1986 are 71 publications (38 archival journal or book publications), 14 PhD dissertations or MS theses, 81 external technical presentations, 16 NASA progress reports, and 2 NASA Contractor Reports. Since 1986, 27 graduate students, including 25 citizens of the United States, have been involved with LA^{2}ST research; 15 have received the MS or PhD degree. Four post-doctoral research associates have participated in LA^{2}ST research.

- oo ***Research on mechanisms of localized corrosion and environmental fracture in Al-Cu-Li-Mg-Ag alloy X2095 and compositional variations*** has successfully developed a test technique to encompass simultaneous control of fracture mechanics and electrochemical parameters. This technique should provide for the rapid quantification of the EAC susceptibility of various Al-Li-Cu alloys as a function of stress intensity, aqueous environment and applied potential. (Project 4)

- oo ***Research on hydrogen interactions with Al-Li-Cu alloy 2090 and model alloys*** identified the presence of several hydrogen trapping states in aluminum alloy 2090, and demonstrated that the significance of these states to the total amount of trapped hydrogen present depends on the aging condition of the material. (Project 5)

- oo ***Research on metastable pitting of aluminum alloys*** established the electrochemical criteria that govern the stabilization of pits on aluminum in chloride solutions. Evaluation of pitting inhibitors, in the context of these criteria, illuminated those factors that are affected by inhibitors. This work is enabled by a NASA Graduate Student Researchers Program Fellowship (Under-Represented Minority Focus). (Project 6)

- *Research on the cryogenic fracture of Al-Cu-Li-In alloys* investigated the variation in through-thickness grain structure and the influence of this microstructure on the dominant fracture mode in 2090-T81 plate. (Project 2)

- *Research on the fracture toughness of Weldalite™* shows that extreme variability in replicate fracture toughness values is in large part explained by modest differences in aged specimen hardness, coupled with a strong yield strength dependence of K_{JIC}, particularly for the alloy with low Cu and Li. For a given aging condition, the fracture toughnesses of both 4.6Li-1.5Cu and 4.0Li-1.0Cu are essentially constant with decreasing test temperature from 25 to -185°C, in spite of substantially higher yield strengths at cryogenic temperatures. (Project 3)

- *Research on the elevated temperature fracture toughness of advanced I/M aluminum alloys* demonstrates that the critical plastic strain controlled micromechanical model reasonably predicts the temperature independence of the initiation toughness of I/M 2519, modified with Mg and Ag. Increased tensile ductility at elevated temperatures is countered by temperature-dependent decreases in elastic modulus, yield strength and work hardening capacity. Two metallurgical fracture mechanisms were identified: void initiation at primary undissolved Θ, and premature void coalescence by a strain localization or "void sheeting" process between primary Θ nucleated voids. Void sheets may involve Al-Cu-Mn dispersoids. (Project 1)

- *Research on the precipitation hardening and microstructural stability of Al-Si-Ge-Cu alloys* shows that the relationship between the cube of the average radii of SiGe diamond structure precipitates is roughly linear, as predicted by coarsening theory (Lifshitz and Wagner). However, a better fit is observed with a linear relationship between the fifth power of the average radii and aging time. The estimated precipitate-matrix interfacial energy of 500 to 800 mJ/m^2 is in the expected range. An increase of the yield strength of the ternary alloy by a factor of about 1.5 is expected if the composition of the alloy is chosen to cancel the atomic size misfit. (Project 9)

oo ***Research on the response of Ti-1100/SCS-6 composites to thermal exposure*** in air (800°C, 100 hours, longitudinal samples) indicates that composite strength loss is the result of matrix embrittlement, and not fiber degradation. Models are being developed to describe the composite strength loss due to matrix embrittlement, interfacial degradation, and the presence of low-strength-producing, secondary flaws on the fibers that form during fabrication and subsequent thermal exposure. (Project 7)

oo ***Research on superplastic forming of Weldalite™*** has determined that grain rotation due to grain boundary sliding appears to be the primary mechanism of microstructural evolution in all alloys and orientations investigated. All the mechanisms investigated, except for intragranular slip, were operative in the continuous recrystallization process. The influence of each mechanism depended on initial microstructure: grain size, grain morphology, and orientation of high-angle boundaries. Processing to obtain an initial microstructure that facilitates grain boundary sliding should lead to enhanced superplastic properties. The presence of some high-angle boundaries oriented out of the rolling plane could promote continuous recrystallization.

(Project 8)

oo ***Research to evaluate wide-panel aluminum alloy extrusions*** has been initiated. Panels of Reynolds Metals Weldalite™ alloys 2195 and X2096 will be processed in Russia in the first quarter of 1994. Preliminary work at UVa implemented the popLA software package for texture analysis by the orientation distribution function, and for prediction of in-plane yield strength aniostropy. (Project 8)

oo ***Research to incorporate environmental effects into fracture mechanics fatigue life prediction codes such as NASA FLAGRO*** is progressing in two directions.

++ Methods to increase crack tip strain rate do not promote environmental cracking in the S-L 7075-T651/aqueous NaCl system. Rising load testing, ripple loading, and trapezoidal/hold-time fatigue do not enhance da/dt relative to the quasi-static load case. The linear superposition model is inadequate in modeling corrosion fatigue crack growth. Fatigue is strongly chloride environment-enhanced, but loading frequency and hold-time-independent for this system over a wide range of stress intensities. (Program 10a)

++ For α/β Ti-6Al-4V in moist air and aqueous NaCl, fatigue crack growth rate is environment-enhanced, and increases with increasing R at constant applied ΔK, but is constant with increasing effective ΔK from compliance; mean stress intensity does not influence intrinsic damage. This alloy exhibits multi-sloped power law relationships between da/dN and ΔK; transition behavior is unique to aggressive environments and is not caused by crack closure. (Project 10b)

oo ***Research on thermoviscoplastic behavior*** of high temperature alloy plates demonstrates material and geometric nonlinearities. Tests of Hastelloy-X plates heated by quartz lamps provide temperature, displacement, and strain data for validation of finite element analysis. Material tests provide Bodner-Partom constitutive model data for Hastelloy-X and aluminum alloy 8009. Future research includes tests of stiffened titanium alloy panels. (Project 11)

INTRODUCTION

Background

In 1986 the Metallic Materials Branch in the Materials Division of the NASA-Langley Research Center initiated sponsorship of graduate student engineering and scientific research in the Department of Materials Science and Engineering at the University of Virginia[1]. This work emphasized the mechanical and corrosion behavior of light aerospace alloys, particularly Al-Li-Cu based compositions, in aggressive aerospace environments[2-4].

In the Fall of 1988, the scope of this program increased to incorporate research at UVa on the development and processing of advanced aerospace materials[5]. Additional funding was provided by the Metallic Materials and Mechanics of Materials Branches at NASA-LaRC. In early 1989 the program was further enhanced to include interdisciplinary work on solid mechanics and thermal structures, with funding from several Divisions within the Structures Directorate at NASA-LaRC[6]. The Departments of Civil Engineering (Applied Mechanics Program) and of Mechanical and Aerospace Engineering at UVa participated in this expanded program. With this growth, the NASA-UVa Light Aerospace Alloy and Structures Technology Program (or LA^{2}ST Program) was formed within the School of Engineering and Applied Science at UVa.

Since 1989, the LA^{2}ST program has operated with full participation from about 10 faculty and 15 graduate students, as outlined in the last eight progress reports[7-15] and five grant renewal proposals[16-20]. Some contraction in the scope of the LA^{2}ST Program occurred in 1993, with the elimination of two programs in solid mechanics and thermal structures[19]. One of these programs was restored in 1994[20]. Four 2-day Grant Review Meetings were held in June or July of 1990, 1991, and 1993 at the Langley Research Center, with over 25 faculty and graduate students from UVa participating[15]. Since 1990, undergraduate engineering students have been involved in research projects at both NASA-LaRC and UVa.

In October of 1991, Dean E.A. Starke proposed a substantial enhancement to the base LA^{2}ST Program[21,22]. The objective of this

supplement is to involve UVa faculty with engineering scientists from aluminum alloy producers and airframe manufacturers in a broad research program to develop aluminum alloys and composites for elevated temperature High Speed Civil Transport applications. This research began in January of 1992 and the results are separately reported.

Problem and Needs

Future aerospace structures require high performance light alloys and metal matrix composites with associated processing and fabrication techniques; new structural design methods and concepts with experimental evaluations; component reliability/durability/damage tolerance prediction procedures; and a pool of masters and doctoral level engineers and scientists. Work on advanced materials and structures must be interdisciplinary and integrated. The thermal and chemical effects of aerospace environments on light metals and composites are particularly important to material performance. Nationally, academic efforts in these areas are limited. The NASA-UVa LA^{2}ST Program addresses these needs.

LA^{2}ST Program

As detailed in the original proposal[6] and affirmed in the most recent renewal[20], faculty from the Departments of Materials Science and Engineering, Mechanical and Aerospace Engineering, and Civil Engineering and Applied Mechanics at UVa are participating in the LA^{2}ST research and education program focused on high performance, light weight, aerospace alloys and structures. We aim to develop long term and interdisciplinary collaborations between graduate students, UVa faculty, and NASA-Langley researchers.

Our research efforts are producing basic understanding of materials performance, new monolithic and composite alloys, advanced processing methods, solid and fluid mechanics analyses, and measurement advances. A major product of the LA^{2}ST program is graduate students with interdisciplinary education and research experience in materials science, mechanics and mathematics. These advances should enable various NASA technologies.

The scope of the LA^{2}ST Program is broad. Four research areas are being investigated, including:

- oo Mechanical and Environmental Degradation Mechanisms in Advanced Light Metals and Composites,
- oo Aerospace Materials Science,
- oo Mechanics of Materials and Composites for Light Aerospace Structures,
- oo Thermal Gradient Structures.

Thirteen research projects are currently ongoing within these four areas and are reported here. These projects currently involve seven faculty, one research associate and twelve graduate students. Over one-half the graduate students are currently at the doctoral level (8 of 12), all are citizens of the United States, one is supported by the NASA Minority Grant Program, and three are cosponsored by the University of Virginia Academic Enhancement Program or private industry. In each case the research provides the basis for the thesis or dissertation requirement of graduate studies at the University of Virginia. Each project is developed in conjunction with a specific LaRC researcher. Research is conducted at either UVa or LaRC, and under the guidance of UVa faculty and NASA staff. Participating students and faculty are closely identified with a NASA-LaRC branch.

Organization of Progress Report

This progress report first provides LA^{2}ST Program administrative information including statistics on the productivity of faculty and graduate student participants, a history of current and graduated students, refereed or archival publications, and a list of ongoing projects with NASA and UVa advisors.

Eleven sections summarize the technical accomplishments of each research project, emphasizing the period from July 1 to December 31, 1993. Each program section contains a brief narrative of objective, background and problem statement, recent progress, conclusions and immediate milestones.

Appendices I through III document grant-sponsored publications, conference participation and citations of all LA^2ST Progress Reports.

References

1. R.P. Gangloff, G.E. Stoner and M.R. Louthan, Jr., "Environment Assisted Degradation Mechanisms in Al-Li Alloys", University of Virginia, Proposal No. MS-NASA/LaRC-3545-87, October, 1986.

2. R.P. Gangloff, G.E. Stoner and R.E. Swanson, "Environment Assisted Degradation Mechanisms in Al-Li Alloys", University of Virginia, Report No. UVA/528266/MS88/101, January, 1988.

3. R.P. Gangloff, G.E. Stoner and R.E. Swanson, "Environment Assisted Degradation Mechanisms in Advanced Light Metals", University of Virginia, Report No. UVA/528266/MS88/102, June, 1988.

4. R.P. Gangloff, G.E. Stoner and R.E. Swanson, "Environment Assisted Degradation Mechanisms in Advanced Light Metals", University of Virginia, Report No. UVA/528266/MS89/103, January, 1989.

5. T.H. Courtney, R.P. Gangloff, G.E. Stoner and H.G.F. Wilsdorf, "The NASA-UVa Light Alloy Technology Program", University of Virginia, Proposal No. MS NASA/LaRC-3937-88, March, 1988.

6. R.P. Gangloff, "NASA-UVa Light Aerospace Alloy and Structures Technology Program", University of Virginia, Proposal No. MS NASA/LaRC-4278-89, January, 1989.

7. R.P. Gangloff, "NASA-UVa Light Aerospace Alloy and Structures Technology Program", University of Virginia, Report No. UVA/528266/MS90/104, August, 1989.

8. R.P. Gangloff, "NASA-UVa Light Aerospace Alloy and Structures Technology Program", University of Virginia, Report No. UVA/528266/MS90/105, December, 1989.

9. R.P. Gangloff, "NASA-UVa Light Aerospace Alloy and Structures Technology Program", UVa Report No. UVA/528266/MS90/106, June, 1990.

10. R.P. Gangloff, "NASA-UVa Light Aerospace Alloy and Structures Technology Program", UVa Report No. UVA/528266/MS91/107, January, 1991.

11. R.P. Gangloff, "NASA-UVa Light Aerospace Alloy and Structures Technology Program", UVa Report No. UVA/528266/MS91/108, July, 1991.

12. R.P. Gangloff, "NASA-UVa Light Aerospace Alloy and Structures Technology Program", UVa Report No. UVA/528266/MS92/109, January, 1992.

13. R.P. Gangloff, "NASA-UVa Light Aerospace Alloy and Structures Technology Program", UVa Report No. UVA/528266/MS93/111, July, 1992.

14. R.P. Gangloff, "NASA-UVa Light Aerospace Alloy and Structures Technology Program", UVa Report No. UVA/528266/MSE93/112, March, 1993.

15. R.P. Gangloff, "NASA-UVa Light Aerospace Alloy and Structures Technology Program", UVa Report No. UVA/528266/MSE93/113, July, 1993.

16. R.P. Gangloff, "NASA-UVa Light Aerospace Alloy and Structures Technology Program", University of Virginia, Proposal No. MS-NASA/LaRC-4512-90, November, 1989.

17. R.P. Gangloff, "NASA-UVa Light Aerospace Alloy and Structures Technology Program", University of Virginia, Proposal No. MS-NASA/LaRC-4841-91, September, 1990.

18. R.P. Gangloff, "NASA-UVa Light Aerospace Alloy and Structures Technology Program", University of Virginia, Proposal No. MS-NASA/LaRC-5219-92, October, 1991.

19. R.P. Gangloff, "NASA-UVa Light Aerospace Alloy and Structures Technology Program", University of Virginia, Proposal No. MSE-NASA/LaRC-5691-93, November, 1992.

20. R.P. Gangloff, "NASA-UVa Light Aerospace Alloy and Structures Technology Program", Proposal No. MSE-NASA/LaRC-6074-94, University of Virginia, Charlottesville, VA, November, 1993.

21. R.P. Gangloff, E.A. Starke, Jr., J.M. Howe and F.E. Wawner, "NASA-UVa Light Aerospace Alloy and Structures Technology Program: Supplement on Aluminum Based Materials for High Speed Aircraft", University of Virginia, Proposal No. MS NASA/LaRC-5215-92, October, 1991.

22. R.P. Gangloff, E.A. Starke, Jr., J.M. Howe and F.E. Wawner, "NASA-UVa Light Aerospace Alloy and Structures Technology Program: Supplement on Aluminum Based Materials for High Speed Aircraft", University of Virginia, Proposal No. MSE NASA/LaRC-5691-93, November, 1992.

SUMMARY STATISTICS

Table I documents the numbers of students and faculty who participated in the LA^{2}ST Program, both during this reporting period and since the program inception in 1986. Academic and research accomplishments are indicated by the degrees awarded, publications and presentations. Specific graduate students and research associates who participated in the LA^{2}ST Program are named in Tables II and III, respectively.

TABLE I: LA^{2}ST Program Statistics

	Current 7/1/93 to 12/31/93	Cumulative 1986 to 12/31/93
PhD Students--UVa:	7	17
--NASA-LaRC:	1	1
MS Students--UVa:	3	7
--NASA:	1	1
--VPI:	0	1
Undergraduates--UVa:	0	9
--NASA-LaRC:	0	11
Faculty--UVa:	7	11
--VPI:	0	1
Research Associates--UVa:	1	4
PhD Awarded:	0	10
MS Awarded:	1	5

TABLE I: LA²ST Program Statistics (continued)

	Current 7/1/93 to 12/31/93	Cumulative 1986 to 12/31/93
Employers--NASA:	0	2
--Federal:	0	3
--University:	0	1
--Industry:	0	4
--Next degree:	1	3
Publications:	3	71
Presentations:	4	81
Dissertations/Theses:	1	14
NASA Reports:	1	16

TABLE II

GRADUATE STUDENT PARTICIPATION IN THE NASA-UVa LA^{2}ST PROGRAM

December, 1993

POS #	GRADUATE STUDENT EMPLOYER	ENTERED PROGRAM	DEGREE COMPLETED	LANGLEY RESIDENCY	RESEARCH TOPIC	UVa/NASA-LaRC ADVISORS
1.	R. S. Piascik NASA-Langley	6/86	Ph.D. 10/89		Damage Localization Mechanisms in Corrosion Fatigue of Aluminum-Lithium Alloys	R. P. Gangloff D. L. Dicus
2.	J. P. Moran NIST	9/88	Ph.D. 12/89		An Investigation of the Localized Corrosion and Stress Corrosion Cracking Behavior of Alloy 2090	G. E. Stoner W. B. Lisagor
3.	R. G. Buchheit Sandia National Laboratories	6/87	Ph.D. 12/90		Measurements and Mechanisms of Localized Aqueous Corrosion in Aluminum-Lithium Alloys	G. E. Stoner D. L. Dicus
4.	D. B. Gundel Ph.D.-UVa	9/88	M.S. 12/90		Investigation of the Reaction Kinetics Between SiC Fibers and Titanium Matrix Composites	F. E. Wawner W. B. Brewer
5.	F. Rivet (VPI)	9/88	M.S. 12/90		Deformation and Fracture of Aluminum-Lithium Alloys: The Effect of Dissolved Hydrogen	R. E. Swanson (VPI) D. L. Dicus
6.	C. Copper Ph.D.-UVa	4/89	M.S. 12/90		Design of Cryogenic Tanks for Space Vehicles	W. D. Pilkey J. K. Haviland D. R. Rummler M.J. Shuart
7.	J. A. Wagner NASA-Langley	6/87	Ph.D.	PhD Research @ LaRC	Temperature Effects on the Deformation and Fracture of Al-Li-Cu-In Alloys	R. P. Gangloff W. B. Lisagor J. C. Newman
8.	W. C. Porr, Jr. David Taylor Naval Ship R&DC	1/88	Ph.D. 6/92		Elevated Temperature Facture of an Advanced Powder Metallurgy Aluminum Alloy	R. P. Gangloff C. E. Harris

TABLE II (continued)

GRADUATE STUDENT PARTICIPATION IN THE NASA-UVa LA^{2}ST PROGRAM

(continued)

POS #	GRADUATE STUDENT EMPLOYER	ENTERED PROGRAM	DEGREE COMPLETED	LANGLEY RESIDENCY	RESEARCH TOPIC	UVa/NASA-LaRC ADVISORS
9.	J. B. Parse Consultant	9/88	Ph.D. 6/92		Quantitative Characterization of the Spatial Distribution of Particles in Materials	J. A. Wert D. R. Tenney
10.	D. C. Slavik Knolls Atomic Power Laboratory	9/89	Ph.D. 6/93		Environment Enhanced Fatigue of Advanced Aluminum Alloys and Composites	R. P. Gangloff D. L. Dicus
11.	C. L. Lach NASA-Langley	9/89	M.S.	MS Research @LaRC	Effect of Temperature on the Fracture Toughness of Weldalite™ 049	R. P. Gangloff W. B. Lisagor
12.	R. J. Kilmer General Motors	11/89	Ph.D. 9/93		Effect of Zn Additions on the Environmental Stability of Alloy 8090	G. E. Stoner W. B. Lisagor
13.	M. F. Coyle	12/89	Ph.D.		Visoplastic Response of High Temperature Structures	E. A. Thornton J. H. Starnes, Jr.
14.	C. J. Lissenden University of Kentucky; Engineering Mechanics	9/90	Ph.D. 6/93		Inelastic Response of Metal Matrix Composites Under Biaxial Loading	C. T. Herakovich M. J. Pindera W. S. Johnson
15.	C. Cooper AMP Incorporated	1/91	Ph.D. 6/93		Shell Structures Analytical Modeling	W. D. Pilkey J. K. Haviland M. Shuart J. Stroud

TABLE II (continued)

GRADUATE STUDENT PARTICIPATION IN THE NASA-UVa LA^{2}ST PROGRAM

(continued)

16.	Douglas Wall	4/91	Ph.D.		Measurements and Mechanisms of Localized Corrosion in Al-Li-Cu Alloys	G. E. Stoner D. L. Dicus
17.	S. W. Smith	4/91	Ph.D.		Hydrogen Interactions with Al-Li Alloys	J. R. Scully W. B. Lisagor
18.	D. B. Gundel	4/91	Ph.D.		Effect of Thermal Exposure on the Mechanical Properties of Titanium/SiC Composites	F. E. Wawner W. B. Brewer
19.	K. McCarthy	5/91	M.S. 6/93 (Nonthesis)		Shell Structures Analytical Modeling	W. D. Pilkey M. J. Shuart J. Stroud
20.	M. Lyttle	12/91	M.S.		Superplasticity in Al-Li-Cu Alloys	J. A. Wert T. T. Bales
21.	T. Johnson NASA-LaRC	12/91	Ph.D. 6/93	(NASA Minority Grantee)	Shell Structures Analytical Modeling	W. D. Pilkey M. J. Shuart J. Stroud
22.	S. T. Pride	12/91	Ph.D.	(NASA Minority Grantee)	Metastable Pitting of Al Alloys	J. R. Scully D. L. Dicus
23.	M. A. Rowley	1/92	M.S.	(UVa AEP Sponsored)	Viscoplasticity of Metals	E. A. Thornton J. H. Starnes, Jr.
24.	M. J. Haynes	9/92	M.S.		Elevated Temperature Fracture of Advanced IM Al Alloys	R. P. Gangloff TBD
25.	M. Mason	9/92	M.S.		Environmental Effects in Fatigue Life Prediction	R. P. Gangloff R. S. Piascik

TABLE II (continued)
GRADUATE STUDENT PARTICIPATION IN THE NASA-UVa LA^{2}ST PROGRAM
(continued)

26.	M. Lyttle	1/94	Ph.D.	Wide-Panel Aluminum Alloy Extrusions	J.A. Wert W.B. Lisagor
27.	H.J. Koenigsmann	6/93	Ph.D.	Precipitation Hardening and Microstructural Stability in Al-Si-Ge-Cu	E.A. Starke, Jr. W.B. Lisagor

TABLE III

Post-Doctoral Research Associate Participation

in NASA-UVA LA^2ST Program

Pos #	Research Assoc.	Tenure	Research	Supervisor
1.	Yang Leng	3/89 to 12/91	Elevated Temperature Deformation and Fracture of PM AL Alloys and Composites	R. P. Gangloff
2.	Farshad Mizadeh	7/89 to 12/91	Deformation of Metal Matrix Composites	C. T. Herakovich and Marek-Jerzy Pindera
3.	A.K.Mukhopadhyay	6/91 to 6/92	Aluminum Alloy Development	E. A. Starke, Jr.
4.	Sang-Shik Kim	12/91 to 2/94	Environmental Fatigue Life Prediction	R. P. Gangloff

GRANT PUBLICATIONS: (REFEREED JOURNALS, ARCHIVAL PROCEEDINGS AND NASA CONTRACTOR REPORTS)

The following papers are based on research conducted under LA^{2}ST Program support, and are published in the referred or archival literature.

38. J.B. Parse and J.A. Wert, "Effects of Deformation Processing on the Oxide Particle Distribution in PM Al Alloy Sheet", Metallurgical Transactions A, in review (1993).

37. R.S. Piascik and R.P. Gangloff, "Environmental Fatigue of an Al-Li-Cu Alloy: Part III - Modeling of Crack Tip Hydrogen Damage", Metallurgical Transactions A, in review (1993).

36. R.G. Buchheit, G.E. Stoner and G.J. Shiflet, "Corrosion Properties of a Rapidly Solidified $Al_{90}Fe_5Gd_5$ Alloy", J. Electrochem. Soc., in review (1993).

35. M.T. Lyttle and J.A. Wert, "Modeling of Continuous Recrystallization in Aluminum Alloys," Journal of Materials Science, in press, 1994.

34. E.A. Thornton and J.D. Kolenski, "Viscoplastic Response of Structures with Intense Local Heating", Journal of Aerospace Engineering, in press (1993).

33. R.P. Gangloff, R.S. Piascik, D.L. Dicus and J.C. Newman, "Fatigue Crack Propagation in Aerospace Aluminum Alloys", Journal of Aircraft, in press (1993).

32. D. Gundel, P. Taylor and F. Wawner, "The Fabrication of Thin Oxide Coatings on Ceramic Fibers by a Sol-Gel Technique", Journal of Materials Science, in press (1993).

31. W.C. Porr, Jr. and R.P. Gangloff, "Elevated Temperature Fracture of RS/PM Alloy 8009: Part I-Fracture Mechanics Behavior", Metall. Trans. A, in press (1993).

30. R.G. Buchheit, J.P. Moran and G.E. Stoner, "The Electrochemical Behavior of the T_1 (Al_2CuLi) Intermetallic Compound and Its Role in Localized Corrosion of Al-3Cu-2Li Alloys", Corrosion, in press (1993).

29. E.A. Thornton, M.F. Coyle, and R.N. McLeod, "Experimental Study of Plate Buckling Induced by Spatial Temperature Gradients," Journal of Thermal Stresses, in press (1993).

PAGE 14 INTENTIONALLY BLANK

28. E.A. Thornton, "Thermal Buckling of Plates and Shells," Applied Mechanics Reviews, Vol. 46, No. 10, pp. 485-506 (1993).

27. R.P. Gangloff and Sang Shik Kim, "Environment Enhanced Fatigue Crack Propagation in Metals: Inputs to Fracture Mechanics Life Prediction", NASA CR-191538, NASA-Langley Research Center, Hampton, VA (1993).

26. R.S. Piascik and R.P. Gangloff, "Environmental Fatigue of an Al-Li-Cu Alloy: Part II - Microscopic Hydrogen Cracking Processes", Metall. Trans. A, Vol. 24A, pp. 2751-2762 (1993).

25. D.C. Slavik, J.A. Wert and R.P. Gangloff, "Determining Fracture Facet Crystallography Using Electron Back Scatter Patterns and Quantitative Tilt Fractography", Journal of Materials Research, Vol. 8, pp. 2482-2491 (1993).

24. D.C. Slavik, C.P. Blankenship, Jr., E.A. Starke, Jr. and R.P. Gangloff, "Intrinsic Fatigue Crack Growth Rates for Al-Li-Cu-Mg Alloys in Vacuum", Metall. Trans. A, Vol. 24A, pp. 1807-1817 (1993).

23. D. Gundel and F. Wawner, "The Influence of Defects on the Response of Titanium/SiC Fiber Composites to Thermal Exposure", Composites Engineering, Vol. 4, No. 1, pp. 47-65 (1993).

22. J.B. Parse and J.A. Wert, "A Geometrical Description of Particle Distributions in Materials", Modeling and Simulation in Materials Science and Engineering, Vol. 1, pp. 275-296 (1993).

21. D.C. Slavik and R.P. Gangloff, "Microscopic Processes of Environmental Fatigue Crack Propagation in Al-Li-Cu Alloy 2090", in Fatigue '93, Vol. II, J.-P. Bailon and J.I. Dickson, eds., EMAS, West Midlands, UK, pp. 757-765 (1993).

20. C.J. Lissenden, M-J. Pindera and C.T. Herakovich, "Response of SiC/Ti Tubes Under Biaxial Loading in the Presence of Damage," Damage Mechanics in Composites, D.H. Allen and D.C. Lagoudas, Eds., ASME-AMD-Vol. 150, pp. 73-90 (1992).

19. J.A. Wagner and R.P. Gangloff, "Fracture Toughness of Al-Li-Cu-In Alloys", Scripta Metallurgica et Materialia, Vol. 26, pp. 1779-1784 (1992).

18. R.G. Buchheit, Jr., J.P. Moran, F.D. Wall, and G.E. Stoner, "Rapid Anodic Dissolution Based SCC of 2090 (Al-Li-Cu) by Isolated Pit Solutions," Parkins Symposium on Fundamental Aspects of Stress Corrosion Cracking, S.M. Bruemmer, E.I. Meletis, R.H. Jones, W.W. Gerberich, F.P. Ford and R.W. Staehle, eds., TMS-AIME, Warrendale, PA, p. 141 (1992).

17. J.P. Moran, R.G. Buchheit, Jr., and G.E. Stoner, "Mechanisms of SCC of Alloy 2090 (Al-Li-Cu) - A Comparison of Interpretations from Static and Slow Strain Rate Techniques", Parkins Symposium on Fundamental Aspects of Stress Corrosion Cracking, S.M. Bruemmer, E.I. Meletis, R.H. Jones, W.W. Gerberich, F.P. Ford and R.W. Staehle, eds., TMS-AIME, Warrendale, PA, p. 159 (1992).

16. R.J. Kilmer, T.J. Witters and G.E. Stoner, "Effect of Zn Additions on the Precipitation Events and Implications to Stress Corrosion Cracking Behavior in Al-Li-Cu-Mg-Zn Alloys", Proceedings of the Sixth International Al-Li Conference, M. Peters and P.J. Winkler, eds., DGM Informationsgesellschaft, Verlag, pp. 755-760 (1992).

15. C.T. Herakovich and J.S. Hidde, "Response of Metal Matrix Composites with Imperfect Bonding", Ultramicroscopy, Vol. 40, pp. 215-228 (1992).

14. R.G. Buchheit, Jr., F.D. Wall, G.E. Stoner and J.P. Moran, "Stress Corrosion Cracking of Al-Li-Cu-Zr Alloy 2090 in Aqueous Cl^- and Mixed Cl^-/CO_3^{-2} Environments", CORROSION/91, Paper No. 99, NACE, Houston, TX (1991).

13. R.P. Gangloff, D.C. Slavik, R.S. Piascik and R.H. Van Stone, "Direct Current Electrical Potential Measurement of the Growth of Small Fatigue Cracks", in Small Crack Test Methods, ASTM STP 1149, J.M. Larsen and J.E. Allison, eds., ASTM, Philadelphia, PA, pp. 116-168 (1992).

12. R.J. Kilmer and G.E. Stoner, "The Effect of Trace Additions of Zn on the Precipitation Behavior of Alloy 8090 During Artificial Aging", Proceedings, Light Weight Alloys for Aerospace Applications II, E.W. Lee, ed., TMS-AIME, Warrendale, PA, pp. 3-15, 1991.

11. W.C. Porr, Jr., Anthony Reynolds, Yang Leng and R.P. Gangloff, "Elevated Temperature Cracking of RSP Aluminum Alloy 8009: Characterization of the Environmental Effect", Scripta Metallurgica et Materialia, Vol. 25, pp. 2627-2632 (1991).

10. J. Aboudi, J.S. Hidde and C.T. Herakovich, "Thermo-mechanical Response Predictions for Metal Matrix Composites", in Mechanics of Composites at Elevated and Cryogenic Temperatures, S.N. Singhal, W.F. Jones and C.T. Herakovich, eds., ASME AMD, Vol. 118, pp. 1-18 (1991).

9. R.S. Piascik and R.P. Gangloff, "Environmental Fatigue of an Al-Li-Cu Alloy: Part I - Intrinsic Crack Propagation Kinetics in Hydrogenous Environments", Metallurgical Transactions A, Vol. 22A, pp. 2415-2428 (1991).

8. W.C. Porr, Jr., Y. Leng, and R.P. Gangloff, "Elevated Temperature Fracture Toughness of P/M Al-Fe-V-Si", in Low Density, High Temperature Powder Metallurgy Alloys, W.E. Frazier, M.J. Koczak, and P.W. Lee, eds., TMS-AIME, Warrendale, PA, pp. 129-155 (1991).

7. Yang Leng, William C. Porr, Jr. and Richard P. Gangloff, "Time Dependent Crack Growth in P/M Al-Fe-V-Si at Elevated Temperatures", Scripta Metallurgica et Materialia, Vol. 25, pp. 895-900 (1991).

6. R.J. Kilmer and G.E. Stoner, "Effect of Zn Additions on Precipitation During Aging of Alloy 8090", Scripta Metallurgica et Materialia, Vol. 25, pp. 243-248 (1991).

5. D.B. Gundel and F.E. Wawner, "Interfacial Reaction Kinetics of Coated SiC Fibers", Scripta Metallurgica et Materialia, Vol. 25, pp. 437-441 (1991).

4. R.G. Buchheit, Jr., J.P. Moran and G.E. Stoner, "Localized Corrosion Behavior of Alloy 2090-The Role of Microstructural Heterogeneity", Corrosion, Vol. 46, pp. 610-617 (1990).

3. Y. Leng, W.C. Porr, Jr. and R.P. Gangloff, "Tensile Deformation of 2618 and Al-Fe-Si-V Aluminum Alloys at Elevated Temperatures", Scripta Metallurgica et Materialia, Vol. 24, pp. 2163-2168 (1990).

2. R.P. Gangloff, "Corrosion Fatigue Crack Propagation in Metals", in Environment Induced Cracking of Metals, R.P. Gangloff and M.B. Ives, eds., NACE, Houston, TX, pp. 55-109 (1990).

1. R.S. Piascik and R.P. Gangloff, "Aqueous Environment Effects on Intrinsic Corrosion Fatigue Crack Propagation in an Al-Li-Cu Alloy", in Environment Induced Cracking of Metals, R.P. Gangloff and M.B. Ives, eds., NACE, Houston, TX, pp. 233-239 (1990).

COMPLETED PROJECTS: (1986 to present reporting period)

1. DAMAGE LOCALIZATION MECHANISMS IN CORROSION FATIGUE OF ALUMINUM-LITHIUM ALLOYS
   Faculty Investigator: R.P. Gangloff
   Graduate Student: Robert S. Piascik
   Degree: PhD
   UVa Department: Materials Science and Engineering (MS&E)
   NASA-LaRC Contact: D. L. Dicus (Metallic Materials)
   Start Date: June, 1986
   Completion Date: November, 1989
   Employment: NASA-Langley Research Center

2. AN INVESTIGATION OF THE LOCALIZED CORROSION AND STRESS CORROSION CRACKING BEHAVIOR OF ALLOY 2090 (Al-Li-Cu)
   Faculty Investigator: Glenn E. Stoner
   Graduate Student: James P. Moran
   Degree: PhD
   UVa Department: MS&E
   NASA-LaRC Contact: W.B. Lisagor (Metallic Materials)
   Start Date: September, 1988
   Completion Date: December, 1989
   Co-Sponsor: ALCOA
   Employment: ALCOA Laboratories

3. MECHANISMS OF LOCALIZED CORROSION IN AL-LI-CU ALLOY 2090
   Faculty Investigator: G.E. Stoner
   Graduate Student: R.G. Buchheit
   Degree: PhD
   UVa Department: MS&E
   NASA-LaRC Contact: D.L. Dicus (Metallic Materials)
   Start Date: June, 1987
   Completion Date: December, 1990
   Cosponsor: Alcoa
   Employment: Sandia National Laboratories

4. DEFORMATION AND FRACTURE OF ALUMINUM-LITHIUM ALLOYS: THE EFFECT OF DISSOLVED HYDROGEN
   Faculty Investigator: R.E. Swanson (VPI)
   Graduate Student: Frederic C. Rivet
   Degree: MS
   VPI Department: Materials Engineering
   NASA-LaRC Contact: D.L. Dicus (Metallic Materials)
   Start Date: September, 1988
   Completion Date: December, 1990
   Employment: Not determined

5. INVESTIGATION OF THE REACTION KINETICS BETWEEN SiC FIBERS AND SELECTIVELY ALLOYED TITANIUM MATRIX COMPOSITES AND DETERMINATION OF THEIR MECHANICAL PROPERTIES

Faculty Investigator: F.E. Wawner
Graduate Student: Douglas B. Gundel
Degree: MS
UVa Department: MS&E
NASA-LaRC Contact: D.L. Dicus and W.B. Brewer (Metallic Materials)
Start Date: January, 1989
Completion Date: December, 1990
Employment: Graduate School, University of Virginia; PhD candidate on LA^{2}ST Program; Department of Materials Science

6. DESIGN OF CRYOGENIC TANKS FOR SPACE VEHICLES

Faculty Investigators: W.D. Pilkey and J.K. Haviland
Graduate Student: Charles Copper
Degree: MS
UVa Department: Mechanical and Aerospace Engineering (MAE)
NASA-LaRC Contact: D.R. Rummler (Structural Mechanics Division), R.C. Davis and M.J. Shuart (Aircraft Structures)
Start Date: April, 1989
Completion Date: December, 1990
Employment: Graduate School, University of Virginia; PhD candidate on NASA-Headquarters sponsored program; Department of Mechanical and Aerospace Engineering

7. ELEVATED TEMPERATURE FRACTURE OF AN ADVANCED RAPIDLY SOLIDIFIED, POWDER METALLURGY ALUMINUM ALLOY

Faculty Investigator: R.P. Gangloff
Graduate Student: William C. Porr, Jr.
Degree: PhD
UVa Department: MS&E
NASA-LaRC Contact: C.E. Harris (Mechanics of Materials)
Start Date: January, 1988
Completion Date: June, 1992
Employment: David Taylor Naval Ship R&D Center

8. QUANTITATIVE CHARACTERIZATION OF THE SPATIAL DISTRIBUTION OF PARTICLES IN MATERIALS: APPLICATION TO MATERIALS PROCESSING
   Faculty Investigator: John A. Wert
   Graduate Student: Joseph Parse
   Degree: PhD
   UVa Department: MS&E
   NASA-LaRC Contact: D.R. Tenney (Materials Division)
   Start Date: September, 1988
   Completion Date: June, 1992
   Employment: Private Consultant

9. ENVIRONMENTAL FATIGUE CRACK GROWTH AND CRACKING MECHANISMS IN Al-Li-Cu Alloy 2090
   Faculty Investigator: R.P. Gangloff
   Graduate Student: Donald C. Slavik
   Degree: PhD
   UVa Department: MS&E
   NASA-LaRC Contact: D.L. Dicus (Metallic Materials)
   Start Date: September, 1989
   Completion Date: June, 1993
   Employment: Knolls Atomic Power Laboratory

10. INELASTIC DEFORMATION OF METAL MATRIX COMPOSITES UNDER BIAXIAL LOADING
   Faculty Investigators: Carl T. Herakovich and Marek-Jerzy Pindera
   Graduate Student: Mr. Clifford J. Lissenden
   Degree: PhD
   UVa Department: Civil Engineering and the Applied Mechanics Program
   NASA-LaRC Contact: W.S. Johnson (Mechanics of Materials)
   Start Date: September, 1990
   Completion Date: June, 1993
   Employment: University of Kentucky, Department of Engineering Mechanics

11. EFFECT OF TEMPERATURE ON THE RESPONSE OF METALLIC SHELL STRUCTURES
   Faculty Investigators: W.D. Pilkey and J.K. Haviland
   Graduate Student: Karen McCarthy
   Degree: MS (non-thesis)
   Graduate Student: Theodore Johnson (NASA Minority Grantee)
   Degree: PhD
   Employment: NASA-LaRC

Graduate Student: Charles Copper
Degree: PhD
Employment: AMP Incorporated
UVa Department: MAE
NASA-LaRC Contact: Drs. M.J. Shuart and Jeffrey Stroud (Aircraft Structures)
Start Date: April, 1991
Completion Date: May, 1993

12. EFFECTS OF Zn ADDITIONS ON THE PRECIPITATION AND STRESS CORROSION CRACKING BEHAVIOR OF ALLOY 8090
Faculty Investigator: Glenn E. Stoner
Graduate Student: Raymond J. Kilmer
Degree: PhD
Department: MS&E
NASA-LaRC Contact: W.B. Lisagor (Metallic Materials)
Start Date: September, 1989
Completion Date: September, 1993
Cosponsor: Alcoa
Employment: General Motors

13. PROCESSING AND SUPERPLASTIC PROPERTIES OF WELDALITE™ SHEET
Faculty Investigator: John A. Wert
Graduate Student: Mark Lyttle
Degree: MS
Department: MS&E
NASA-LaRC Contact: T.T. Bales (Metallic Materials)
Start Date: September, 1991
Anticipated Completion Date: December, 1993

ADMINISTRATIVE PROGRESS

Faculty Participation

Professor E.A. Starke incorporated a research project into the LA^{2}ST program during this reporting period. Professor Herakovich will resume participation in the 1994 program.

Brochure

The brochure prepared in March of 1991 was employed to advertise the LA^{2}ST program during this reporting period. Copies were nationally distributed to stimulate graduate and undergraduate recruitment.

Graduate Student Recruitment

The LA^{2}ST Program has encountered no problems in recruiting the best graduate students entering the participating Departments at UVa, and in sufficient numbers to achieve our education and research objectives. Professor Wert recruited Mr. Mark Lyttle into the PhD program under LA^{2}ST sponsorship. Mr. Lyttle received the MS degree in Materials Science and Engineering at UVa in the Winter of 1993. Professor Gangloff recruited Mr. Zuhair Gasem into the PhD program under partial LA^{2}ST support. Mr. Gasem received the MS degree in Materials Science and Engineering from the University of Connecticut in the Fall of 1993.

Undergraduate Research Participation

In April of 1990, the LA^{2}ST Program was increased in scope to include undergraduate engineering students[3]. Four students worked at NASA-LaRC during the Summer of 1990, none were recruited for the 1991 program, and seven were successfully recruited to work at NASA-LaRC during the Summer of 1992. Each student was, at the time, a rising senior in an engineering or science major closely related to aerospace materials and mechanics. Represented universities have included Harvard, Georgia Institute of Technology, Virginia Polytechnic Institute, Duke, the University of Missouri, California Polytechnical Institute, and North Carolina State University.

Professor Glenn E. Stoner assumed responsibility for the 1993 Summer Undergraduate Program. No qualified applicants were identified for 1993 Summer employment at NASA-LaRC. During this reporting period, he

successfully recruited two undergraduates in Materials Science and Engineering at Duke and North Carolina State University to work at NASA-LaRC during the Summer of 1994.

Complementary Programs at UVa

The School of Engineering and Applied Science at UVa has targeted light materials and thermal structures research for aerospace applications as an important area for broad growth. The LA^{2}ST Program is an element of this thrust. Several additional programs are of benefit to LA^{2}ST work.

In 1988, the Board of Visitors at UVa awarded SEAS an Academic Enhancement Program Grant in the area of Light Thermal Structures. University funds have been used to seed the establishment of a world-class center of excellence which incorporates several SEAS Departments. This program is lead by Professor Thornton and directly benefits NASA.

The Light Metals Center has existed within the Department of Materials Science and Engineering at UVa for the past ten years under the leadership of Dean Starke. A Virginia Center for Innovative Technology Development Center in Electrochemical Science and Engineering was established in 1988 with Professor G.E. Stoner as Director. Professors Pilkey, Thornton and Gangloff recently completed NASA-Headquarters sponsored research to examine "Advanced Concepts for Metallic Cryo-thermal Space Structures"[4,5].

References

1. R.P. Gangloff, E.A. Starke, Jr., J.M. Howe and F.E. Wawner, "NASA-UVa Light Aerospace Alloy and Structures Technology Program: Supplement on Aluminum Based Materials for High Speed Aircraft", University of Virginia, Proposal No. MS NASA/LaRC-5215-92, October, 1991.

2. R.P. Gangloff, "NASA-UVa Light Aerospace Alloy and Structures Technology Program", University of Virginia, Proposal No. MSE-NASA/LaRC-5691-93, November, 1992.

3. R.P. Gangloff, "NASA-UVa Light Aerospace Alloy and Structures Technology Program: A Supplementary Proposal", University of Virginia, Proposal No. MS NASA/LaRC-4677-90, April, 1990.

4. W.P. Pilkey, "Advanced Concepts for Metallic Cryo-thermal Space Structures", University of Virginia Proposal No. MAE-NASA/HQ-4462-90, August, 1989.

5. W.P. Pilkey, "Advanced Concepts for Metallic Cryo-thermal Space Structures", University of Virginia Report No. UVA/528345/MAE91/101, February, 1991.

CURRENT PROJECTS

MECHANICAL AND ENVIRONMENTAL DEGRADATION MECHANISMS IN ADVANCED LIGHT METALS AND COMPOSITES

1. ELEVATED TEMPERATURE DAMAGE TOLERANCE OF ADVANCED INGOT METALLURGY WROUGHT ALUMINUM ALLOYS
   Faculty Investigator: R.P. Gangloff
   Graduate Student: Michael J. Haynes
   UVa Department: MS&E
   NASA-LaRC Contact: To be determined (Metallic Materials)
   Start Date: September, 1992
   Completion Date: September, 1994
   Project #1

2. CRYOGENIC TEMPERATURE EFFECTS ON THE DEFORMATION AND FRACTURE OF Al-Li-Cu and Al-Li-Cu-In ALLOYS
   Faculty Investigator: R.P. Gangloff
   Graduate Student: John A. Wagner; PhD candidate and NASA-LaRC employee
   UVa Department: MS&E
   NASA-LaRC Contacts: W.B. Lisagor (Metallic Materials) and J.C. Newman (Mechanics of Materials)
   Start Date: June, 1987
   Anticipated Completion Date: December, 1994
   Project #2

3. THE EFFECT OF CRYOGENIC TEMPERATURE ON THE FRACTURE TOUGHNESS OF WELDALITE™ X2095
   Faculty Investigator: R.P. Gangloff
   Graduate Student: Cynthia L. Lach; MS candidate and NASA-LaRC employee
   UVa Department: MS&E
   NASA-LaRC Contacts: W.B. Lisagor (Metallic Materials)
   Start Date: August, 1990
   Anticipated Completion Date: December, 1994
   Project #3

4. MECHANISMS OF LOCALIZED CORROSION IN 2090 AND X2095
   Faculty Investigator: G.E. Stoner
   Graduate Student: Douglas Wall; PhD candidate
   UVa Department: MS&E
   NASA-LaRC Contact: M.S. Domack (Metallic Materials)
   Start Date: April, 1991
   Completion Date: May, 1994
   Cosponsor: Reynolds Metals Company (A. Cho)
   Project #4

5. HYDROGEN INTERACTIONS IN ALUMINUM-LITHIUM ALLOY 2090 AND SELECTED MODEL ALLOYS

Faculty Investigator: John R. Scully
Graduate Student: Stephen W. Smith; PhD Candidate
Department: MS&E
NASA-LaRC Contact: W.B. Lisagor and D.L. Dicus (Metallic Materials)
Start Date: April, 1991
Anticipated Completion Date: December, 1994
Cosponsor: Virginia CIT
Project #5

6. METASTABLE PITTING OF Al ALLOYS IN HALIDE SOLUTIONS

Faculty Investigators: John R. Scully and J.L. Hudson
Graduate Student: Sheldon T. Pride: PhD Candidate
Department: Chemical Engineering
NASA-LaRC Contact: D.L. Dicus (Metallic Materials)
Start Date: September, 1991
Anticipated Completion Date: To be determined
Cosponsor: NASA Graduate Student Researchers Program; Under Represented Minority Emphasis
Project #6

AEROSPACE MATERIALS SCIENCE

7. THE EFFECT OF THERMAL EXPOSURE ON THE MECHANICAL PROPERTIES OF Ti-1100/SCS-6 COMPOSITES

Faculty Investigator: F.E. Wawner
Graduate Student: Douglas B. Gundel; PhD candidate
UVa Department: MS&E
NASA-LaRC Contact: D.L. Dicus and W.B. Brewer (Metallic Materials)
Start Date: April, 1991
Anticipated Completion Date: May, 1994
Project #7

8. PROCESSING AND SUPERPLASTIC PROPERTIES OF WELDALITE™ SHEET

Faculty Investigator: John A. Wert
Graduate Student: Mark Lyttle; MS Candidate
UVa Department: MS&E
NASA-LaRC Contact: T.T. Bales (Metallic Materials)
Start Date: September, 1991
Anticipated Completion Date: September, 1993
Project #8

9. EVALUATION OF WIDE-PANEL ALUMINUM ALLOY EXTRUSIONS
   Faculty Investigator: John A. Wert
   Graduate Student: Mark T. Lyttle, Ph.D. Candidate
   UVa Department: Materials Science and Engineering
   NASA-LaRC Contact: T. Bales
   Start Date: September, 1993
   Completion Date: August, 1996
   Project #8

10. PRECIPITATION HARDENING AND MICROSTRUCTURAL STABILITY IN Al-Si-Ge AND Al-Si-Ge-Cu ALLOYS
   Faculty Investigator: E.A. Starke, Jr.
   Graduate Student: H.J. Koenigsmann, Ph.D. Candidate
   UVa Department: Materials Science and Engineering
   NASA-LaRC Contact: W.B. Lisagor
   Start Date: September, 1993
   Completion Date: To be determined
   Project #9.

MECHANICS OF MATERIALS FOR LIGHT AEROSPACE STRUCTURES

11. ENVIRONMENTAL EFFECTS IN FATIGUE LIFE PREDICTION: MODELING CRACK PROPAGATION IN LIGHT AEROSPACE ALLOYS
   Faculty Investigator: R.P. Gangloff
   Graduate Students: Mark Mason; MS Candidate
   Zuhair Gasem; PhD Candidate
   Edward Richey III; MS Candidate (Mechanical and Aerospace Engineering)
   Post Doctoral Research Associate: Dr. Sang-Shik Kim
   UVa Department: MS&E
   NASA-LaRC Contact: R.S. Piascik (Mechanics of Materials)
   Start Date: January, 1992
   Anticipated Completion Date: December, 1994 (Mason)
   December, 1994 (Richey)
   December, 1996 (Gasem)
   Project #10

THERMAL GRADIENT STRUCTURES

12. EXPERIMENTAL STUDY OF THE NONLINEAR VISCOPLASTIC RESPONSE OF HIGH TEMPERATURE STRUCTURES

Faculty Investigator: Earl A. Thornton
Graduate Student: Marshall F. Coyle; PhD candidate
UVa Department: Mechanical and Aerospace Engineering
NASA-LaRC Contact: James H. Starnes, Jr. (Aircraft Structures)
Start Date: January, 1990
Anticipated Completion Date: To be determined
Cosponsor: UVa Academic Enhancement Program
Project #11

RESEARCH PROGRESS AND PLANS (July 1 to December 31, 1993)

Research progress, recorded during the period from July 1, 1993 to December 31, 1993, is summarized for each project in the following sections. The standard format includes the background, program objective, recent progress, conclusions, and immediate next milestones.

Project #1 Elevated Temperature Damage Tolerance of Advanced Ingot Metallurgy Wrought Aluminum Alloys

Michael J. Haynes and Richard P. Gangloff

Background and Problem Statement

A significant effort is currently aimed at developing advanced aluminum alloys for elevated temperature aerospace applications, particularly for airframes such as the high speed civil transport[1,2]. Since existing precipitation hardened aluminum alloys (e.g., 2024, 7075/7475 and 2090/8090) may not be sufficient to meet microstructural stability combined with strength/toughness requirements, new compositions of both wrought ingot metallurgy (I/M) and rapidly solidified powder metallurgy (RS/PM) alloys are under development. As promising compositions are determined, it is necessary to characterize the critical effects of loading rate and temperature on fracture toughness and creep-fatigue damage tolerance, and to establish metallurgical fracture mechanisms and predictive micromechanical models for such properties.

Objective

The objective of this MS research project is to characterize the flaw damage tolerance, particularly the tensile fracture toughness, of emerging ingot metallurgy wrought aluminum alloy sheet as a function of temperature and loading rate. Metallurgical aspects of the time-temperature dependent fracture will be identified, and the fracture process will be micromechanically modeled.

Technical Approach

Three ingot metallurgy wrought aluminum alloys (I/M 2650, I/M 2519+Mg, and I/M 2519+Mg+Ag) were chosen for this study, with compositions as given in the 1993 LA^{2}ST renewal proposal[3]. The majority of work has focused on I/M 2519 with Ag and Mg additions (Alcoa Heat S689248: Al-5.75Cu-0.52Mg-0.30Mn-0.49Ag-0.16Zr-0.09V; wt%).

The approach to this research was outlined in past renewal proposals[2,3]. In summary, our approach focuses on:

(1) Characterizing microstructures of as-received (I/M) Al-Cu-Mg-X alloys through optical, scanning electron, and transmission electron microscopy.

(2) Implementing J-Integral fracture mechanics methods and DCPD crack length measurements to measure crack initiation and propagation resistance at ambient, cryogenic and elevated temperatures.

(3) Defining initiation and growth fracture toughness as a function of temperature and actuator displacement rate.

(4) Establishing microstructural fracture paths and mechanisms through SEM fractography, crack tip profiles, and transmission electron microscopy.

(5) Performing uniaxial compression tests to determine yield strength, strain hardening exponent and strain rate sensitivity.

(6) Employing smooth and notched bar tensile tests to estimate intrinsic fracture strains.

(7) Evaluating the predictive capabilities of micromechanical models in explaining the temperature dependence of ductile fracture initiation toughness, K_{JICi}.

Progress During the Reporting Period

Microstructural Characterization

The 1993 LA^{2}ST proposal summarizes the precipitates observed in the three alloys studied[3]. Optical microscopy of AA2519 + (Mg,Ag) identified 1 to 10 μm diameter second phase particles. Energy dispersive x-ray analysis

identified most of these particles as undissolved Θ constituent, but some of the smaller constituents were identified as Mn and Fe-bearing. Larger constituent particles contained cracks oriented normal to the rolling direction, presumably induced during hot rolling. Transmission electron microscopy identified two populations of dispersoids; Al-Cu-Mn dispersoids (≈0.2 μm in diameter) and Al-Cu-Zr dispersoids. Skrotzki, Shiflet, and Starke report that this alloy is recrystallized (at least, for material solution heat treated for 1 hr at 520°C) based on a recrystallization texture and a lack of subgrain structure in TEM observations[4].

Fracture Toughness Characterization

Fracture toughness data for AA2650 and Mg modified AA2519 are presented elsewhere for 3.2 mm thick compact tension specimens[3,5]. J-Δa curves, at a constant actuator displacement rate of 0.27 μm/sec, were produced at temperatures of 25, 75, 100, 125, 150, and 175°C for Mg plus Ag modified AA2519. At 150°C, J-Δa data were determined for crosshead displacement rates yielding 4 to 5 mm of crack growth in times ranging from 30 seconds to 7 days. Plane strain ductile fracture initiation toughness (K_{JICi}) was determined from J_i, the J-integral value corresponding to the first detectable rise in direct current potential drop, by $K_{JICi} = (J_iE/(1-\upsilon^2))$. At a measured crack extension of 4 mm, a K value was similarly calculated from J to rank the crack growth resistance of 2519 + (Mg,Ag) as a function of temperature. This latter parameter reflects crack growth resistance under fully plane stress deformation.

Crack initiation and growth toughness of the alloy is summarized as a function of temperature in Figure 1a and as a function of actuator displacement rate in Figure 1b. Initiation toughness is independent of temperature for a displacement rate producing 4 to 5 mm of crack growth in 3 hours, while crack growth resistance rises to a peak level of 113 MPa√m at 75°C and decreases monotonically as temperature is increased to 175°C. As the actuator displacement rate is reduced at 150°C, both K_{JICi} and crack growth resistance drastically decrease.

Microscopic Fracture Processes

For a constant displacement rate of 0.27 μm/sec, microvoid coalescence is the operating fracture mechanism in 2519 + (Mg,Ag) at all temperatures. A montage of SEM fractographs offers several insights (see Figure 2) into the ambient temperature fracture process. The larger dimples (≈5 to 25 μm in diameter) are associated with void initiation and growth from primarily undissolved Θ particles with some contribution from manganese and iron bearing constituents. Large constituents observed in dimples possessed microscopically flat fracture facets, consistent with the cracked particles found in the as-received material. In some cases transverse cracking or complete shattering of the constituents are observed, and one may conclude that primary void initiation is mainly from particle fracture and not from matrix-particle decohesion.

A second feature of interest is "void sheeting" separating clusters of larger dimples, as marked by "vs" on the montage (Figure 2). Void sheets consist of smaller dimples (≈0.25 to 5 μm in diameter) that arise due to the presence of smaller second phase particles in strain localized regions between primary voids[6,7]. Based on high magnification SEM tilt fractography and TEM observations, Al-Cu-Mn dispersoids are tentatively identified as associated with and perhaps responsible for void sheets propagation. As temperature increases, the dimples associated with void sheets increase in size.

Metallographic profile sections of the crack tip at ambient temperature (Figure 3a) and 150°C (Figure 3b) corroborate both the presence of void sheets and crack initiation due to Θ particle fracture. Crack growth was interrupted at a K level of approximately 85 MPa√m for both samples, and void sheeting behavior is markedly different for the two temperatures. Void sheeting is less prevalent at 150°C as indicated by shorter "canal" regions between primary voids and also by areas ahead of the crack tip with a high amount of local damage; areas that are not yet linked to the crack tip by the void sheet mechanism. We speculate that resistance to void sheeting at higher temperatures is attributable to a higher strain rate sensitivity which

stabilizes the accelerated, localized deformation between primary voids[8].

Uniaxial Tensile and Compressive Flow Properties

Table 1 presents the results of uniaxial compression and tension testing of Ag plus Mg modified AA2519. The average of compressive and tensile yield strength decreases from 504 MPa at 25°C to 404 MPa at 175°C, while tensile reduction in area increases by approximately 59 percent.

Compression samples (5.18 mm in height) were tested at an actuator displacement rate of 0.33 μm/sec. The Ramberg-Osgood (R-O) constitutive equation was fit to the experimental compression flow curves, and can be expressed as[9]:

$$\frac{\epsilon}{\epsilon_o} = \frac{\sigma}{\sigma_o} + \alpha\left(\frac{\sigma}{\sigma_o}\right)^n$$

where σ_o is a reference stress, ϵ_o is a reference strain given by σ_o/E, E is elastic modulus, α is a constant (assumed to equal 1), and n is the Ramberg-Osgood strain hardening exponent. Table 1 lists σ_o and n values that reflect the decreasing yield strength and decreasing work hardening capacity of the alloy as temperature is increased. From 1.0% to 5.0% true strain, the R-O strain hardening exponent and its standard error were determined according to ASTM standard E646-78 from linear regression analysis of plastic strain and true stress data logarithmically plotted. R-O strain hardening exponents plus pertinent statistics are listed in Table 2. Figure 4 shows the R-O curve fits for experiments at 25, 75, 100, 125, and 150°C (A satisfactory regression was not possible at 175°C). The equation accurately fits the data above strains of 1%, but overestimates the experimental data from yielding to 1% strain (experimental data for $\epsilon < 0.01$ were omitted for clarity).

Micromechanical Modeling

The temperature dependence of the lane strain, ductile crack growth initiation toughness, K_{JICi}, was predicted with a critical plastic strain-controlled model[10,11]. For fracture initiation, the model requires that crack tip plastic strain exceeds a critical level (ϵ_f^*) over a characteristic microstructural

distance (l^*). ϵ_f^*, a material property, represents the intrinsic fracture resistance in the crack tip process zone. That is, this parameter is the strain level required to produce the degree of damage corresponding to K_{JICi} and for the level of constraint characteristic of the plane strain crack tip. By employing this criteria; McMeeking's finite element analysis of the strain field ahead of a plane-strain crack tip[12]; and the relationships between CTOD, J-Integral, and K; an expression for K_{JICi} can be derived as[10]:

$$K_{JICi} = \sqrt{\frac{\sigma_{ys} E l^*}{(1-\nu^2) d_n} \left(\frac{\bar{\epsilon}_f^*}{C1} \right)^{\frac{1}{C2}}}$$

d_n, C1 and C2 are constants determined from curve fits to FEM analyses of Shih[13] and McMeeking[12], respectively. σ_{ys} values were taken as the average of tensile and compressive yield strengths, and ϵ_f^* values were approximated from reduction in area of tensile specimens by:

$$\bar{\epsilon}_f^* = (1/\gamma)(-\ln(1-\%RA))$$

where $\gamma = 7$ was chosen to account for crack tip stress field triaxiality[10].

The critical distance is generally treated as a curve fitting parameter in ductile fracture modeling, and is often found to equal between 1 and 5 times the spacing of primary void nucleating particles. Rigorously, one should define l^* by a statistical analysis of the distribution of void nucleating particles in a unit volume of alloy, coupled with the "strength" of such void nucleation sites and the strain gradient ahead of the crack tip. Following Ritchie's work on cleavage fracture of steels, l^* would then represent the distance ahead of the crack tip necessary for the optimal balance between sufficient weak link sites and sufficient plastic strain for void nucleation. At this stage in the analysis, we select a critical distance of 30 μm based on the approximate spacing of the larger voids in Figure 2 and the spacing of undissolved Θ particles from metallographic sections. No fundamental or absolute significance is attached to this critical distance, however, the value is of the correct order of magnitude and should be temperature independent,

allowing for a prediction of the temperature dependence of K_{JICi}.

Temperature-dependent inputs to the model are included in Table 3, along with predicted and measured values of K_{JICi}. Predicted values accurately estimate measured K_{JICi}, with a maximum difference of 2.1 MPa√m between predicted and measured initiation toughnesses. Figure 5 displays the accuracy of the model. Separate linear regression analyses of the measurements and of the model predictions each confirm a constant K_{JICi} with increasing temperature up to 175°C. (The error bar represents the maximum variation in measured K_{JICi} from three experiments at 25°C, and is plotted about the mean or single-measured toughness at each elevated temperature.)

The result in Figure 5 is notable. First, all parameters in the micromechanical model were independently selected and are reasonable based on current understanding. Both l^* and ε_f^* are complex parameters that can be debated, however, best estimates accurately predict room temperature toughness. These same values accurately modeled the temperature-(in)dependence of K_{JICi}. It is likely that errors in critical distance and local fracture resistance are constant with increasing temperature; hence the ability to predict the temperature dependence of K_{JICi} strongly supports the framework of the critical strain micromechanical model. Physically, this model explains how tensile ductility increases substantially with increasing temperature, while plane strain fracture toughness is temperature independent. For alloy development, micromechanical modeling shows that the aim should be to improve tensile ductility, while accounting for the effects of yield strength, work hardening exponent and modulus on K_{JICi}. Tensile ductility is governed by the growth to coalescence of microvoids, a process that is sensitive to microstructure (eg., undissolved particles, constituents and dispersoids) as well as work hardening and strain rate hardening.

Conclusions

1. Fracture initiation toughness is high for AA2519 + (Mg,Ag) with a substantial volume fraction of undissolved Θ, and is invariant with

increasing temperature to 175°C.

2. The critical plastic strain controlled model accurately predicts a constant fracture initiation toughness with increasing temperature, where elastic modulus and yield strength decrease and tensile reduction in area increases as temperature rises.

3. SEM fractography and optical metallography crack profiles show that microvoid damage accumulates primarily at undissolved and processing-cracked Θ particles; Void coalescence occurs prior to primary void impingement by a void sheeting mechanism involving smaller second phase particles.

4. Shape and size distributions of the particles involved in void sheeting correlate reasonably well to the observed size and shape of Al-Cu-Mn dispersoids observed by TEM microscopy.

5. Tensile fracture occurs by microvoid processes at all temperatures and short-term loading rates. Fractographic and crack profile observations suggest that void sheeting is less prevalent at higher temperatures, possibly due to an increased strain rate sensitivity stabilizing deformation between primary voids.

Proposed Research for Next Reporting Period

Work in the first half of 1994 will concentrate on further understanding the inherent elevated temperature fracture processes. Specifically, we propose to:

- Fracture circumferentially notched tensile bars over the full temperature range to better estimate the intrinsic fracture strain, $\dot{\varepsilon}_f^*$, of 2519 + (Mg,Ag) in a triaxial stress field at the crack tip.
- Interrupt notched tensile tests before fracture to confirm observed microscopic fracture mechanisms, and to study the effect of either triaxiality or temperature on void sheeting.
- Perform "strain rate change" tests to determine the strain rate

sensitivity of flow stress for 2519 + (Mg,Ag) at 25°C and 150°C. Strain rate sensitivity values, determined over the proper strain rate regime, will reflect resistance to localized deformation between primary voids during ductile fracture; that is, the- resistance to the void sheeting mechanism. The problem in this regard is to estimate the strain rate regime relevant to deformation between two growing microvoids.

- Examine, on a polished surface, slip morphology and the degree of slip localization for samples strained between 1% and 10% at 25°C and 150°C.

Additional fracture toughness and flaw damage tolerance data will be generated to further evaluate the candidacy of 2519 + (Mg,Ag) for the HSCT application. Experiments will include:

- Replicate J-Δa curve experiments at appropriate temperatures between 25°C and 150°C, and new experiments at several cryogenic temperatures to extend the temperature range of characterization and micromechanical modeling.
- Evaluation of the effect of thermal exposure for 1000 hours at 135°C on fracture toughness at 25°C and 150°C. Differences in fracture mechanisms compared to the unexposed alloy will be explored. An elevated temperature test may further degrade toughness of the exposed specimen.
- Fracture toughness characterization of 2519 + (Mg,Ag), of modified composition (Alcoa C416: Al-5.4Cu-0.5Mg-0.3Mn-0.5Ag-0.13Zr; wt%) to reduce the amount of primary Θ phase, if the material is provided to UVa.

References

1. R.P. Gangloff, E.A. Starke, Jr., J.M. Howe and F.E. Wawner, Jr., "Aluminum Based Materials for High Speed Aircraft", University of Virginia, Proposal No. MS-NASA/LaRC-5215-92, October (1991)

2. R.P. Gangloff, "NASA-UVa Light Aerospace Alloy and Structures Technology Program", Proposal No. MSE-NASA/LaRC-5691-93, University of Virginia (1992).

3. R.P. Gangloff, "NASA-UVa Light Aerospace Alloy and Structures Technology Program", Proposal No. MSE-NASA/LaRC-6074-94, University of Virginia, Charlottesville, VA, November (1993).

4. B. Skrotzki, G.J. Shiflet, and E.A. Starke, Jr., "University of Virginia HSR Aluminum Based Materials Grant Review", Hampton, VA, January (1994).

5. R.P. Gangloff, "NASA-UVa Light Aerospace Alloy and Structures Technology Program", University of Virginia Report No. UVA/528266/MS94/113, July (1993).

6. T.B. Cox and J.R. Low, Jr., Metall. Trans. A, Vol 5A (1974) pp. 1457-1470.

7. R.H. Van Stone, T.B. Cox, J.R. Low, and J.A. Psioda., Int. Metals Rev., Vol 30 (1985) pp. 157-179.

8. P.F. Thomason, Ductile Fracture of Metals, Pergamon Press, Oxford, UK, (1990) pp. 105-111.

9. J. Chakrabarty, Theory of Plasticity, McGraw Hill Book Co., New York, (1987)

10. B.P. Somerday, "Elevated Temperature Fracture Toughness of a SiC Particulate Reinforced 2009 Aluminum Composite", Masters Thesis, University of Virginia (1993) pp. 111-119.

11. R.O. Ritchie, W.L. Server, and R.A. Wullaert, Metall. Trans. A, Vol 10A (1979) pp. 1557-1570.

12 R.M. McMeeking, J. Mech. Phys. Solids, Vol 25 (1977) pp. 357-381.

13 C.F. Shih, J. Mech. Phys. Solids, Vol 29 (1981) pp. 305-326.

Table 1 - Uniaxial Compressive and Tensile Flow Properties of AA2519+Mg+Ag

Temperature (°C)	E (GPa)	σ_{ys}^{c} (MPa)	σ_{ys}^{t} (MPa)	σ_{uts}^{t} (MPa)	RA (%)	σ_o (MPa)	n
25	72.4	493	515	566	35	524	22
75	68.4	485	505	536	34	510	28
100	67.6	469	489	510	46	497	33
125	66.3	440	479	487	45	474	44
150	64.9	434	451	453	48	450	61
175	63.7	388	420	422	54	---	--

Table 2 - Ramberg-Osgood Strain Hardening Exponent Statistics

Temperature °C	n	r^2	σ	95% Confidence Interval	# of data points in regression
25	22.0	0.989	0.93	± 2.1	12
75	28.3	0.991	0.81	± 1.8	13
100	32.5	0.993	0.80	± 1.7	14
125	44.1	0.861	5.61	± 12.5	12
150	60.7	0.941	5.40	± 12.5	10

Table 3 - Critical Plastic Strain-Controlled Model Predictions for AA2519+Mg+Ag

$\sigma_o/E=0.003$; $C1=0.1256$; $C2=1.228$; $\gamma=7$; $l^*=30\ \mu m$; $\upsilon=0.3$

Temperature (°C)	d(n)	E (GPa)	σ_{ys}^{avg} (MPa)	$\bar{\varepsilon}_f^*$ (%)	K_{JIC} Measured (MPa$\sqrt{m}$)	K_{JIC} Predicted (MPa$\sqrt{m}$)
25	0.65	72.4	504	6.2	30.9	32.2
75	0.68	68.4	495	5.9	32.0	29.9
100	0.70	67.6	475	8.8	31.8	33.8
125	0.71	66.3	459	8.4	31.5	31.9
150	0.73	64.9	443	9.3	31.7	31.9
175	0.75	63.7	404	11.1	30.9	32.0

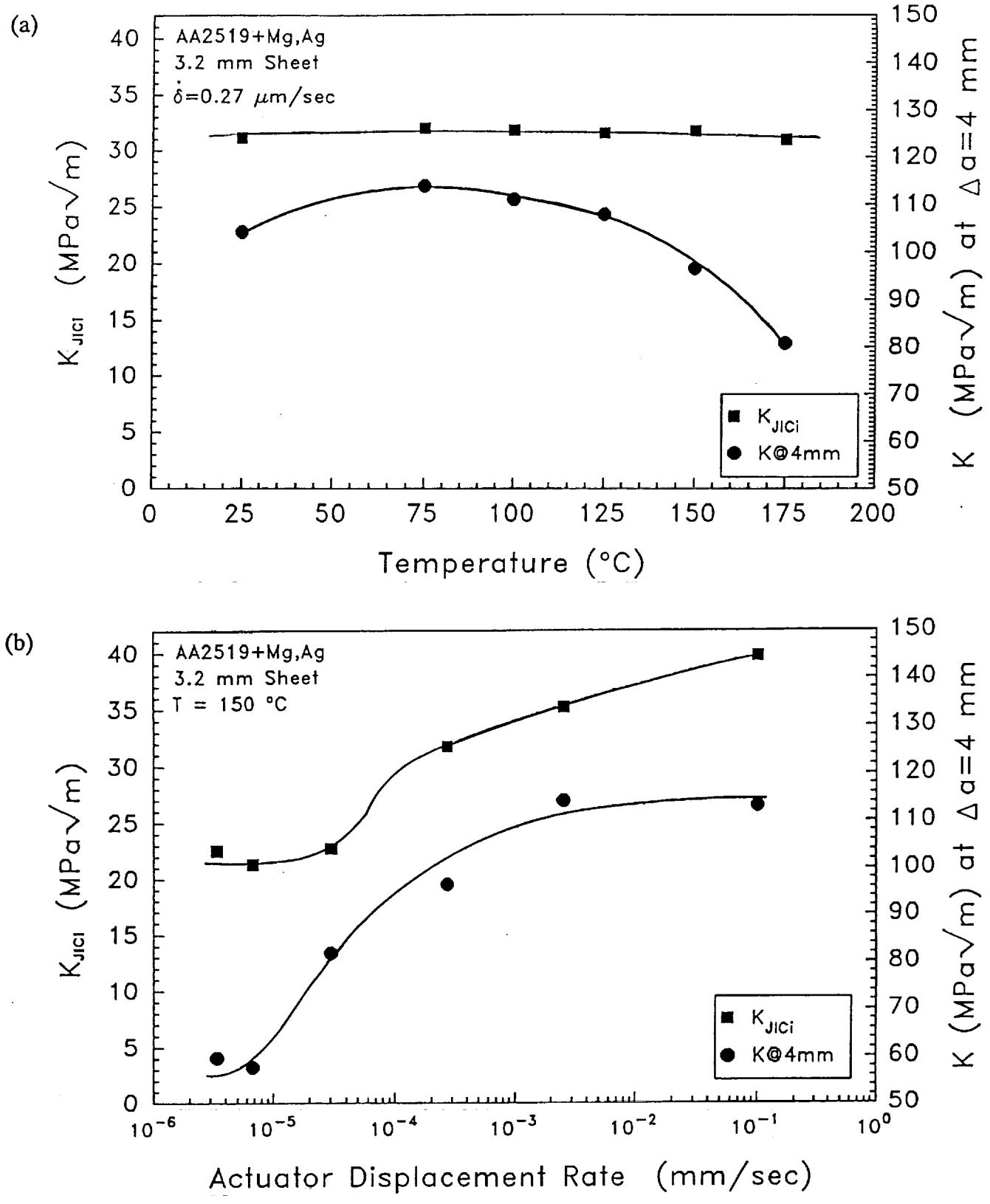

Figure 1 Initiation fracture toughness, K_{JICi}, and plane stress crack growth toughness, $K_{@4mm}$, of AA2519-T87 (+ Mg and Ag) as a function of: (a) temperature at a single actuator displacement rate of 0.27 μm/sec, and (b) actuator displacement rate at a single temperature of 150 °C.

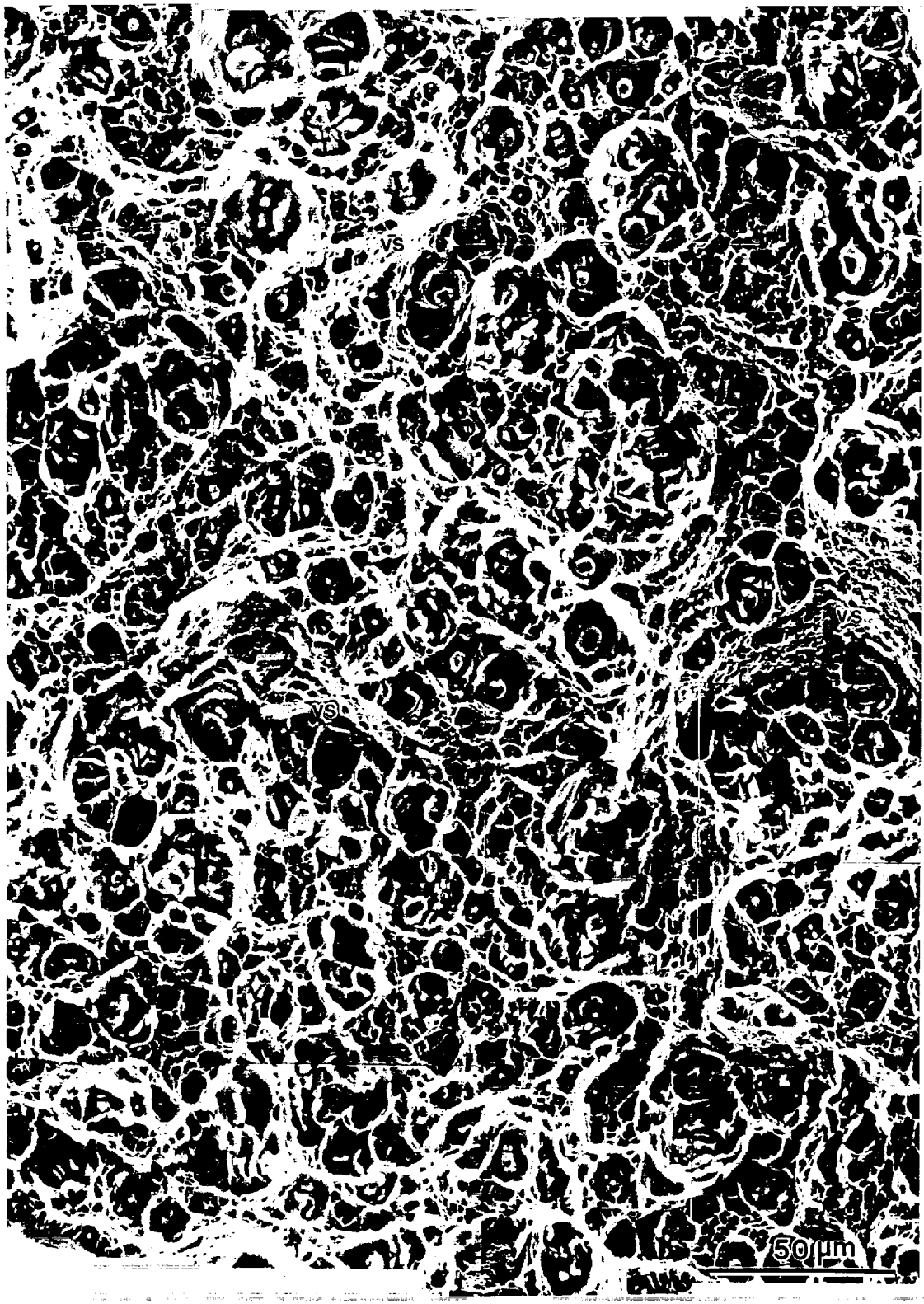

Figure 2 Montage of SEM fractographs displaying the ambient temperature plane strain fracture surface of AA2519-T87 (+ Mg and Ag); void sheet areas are marked by "vs".

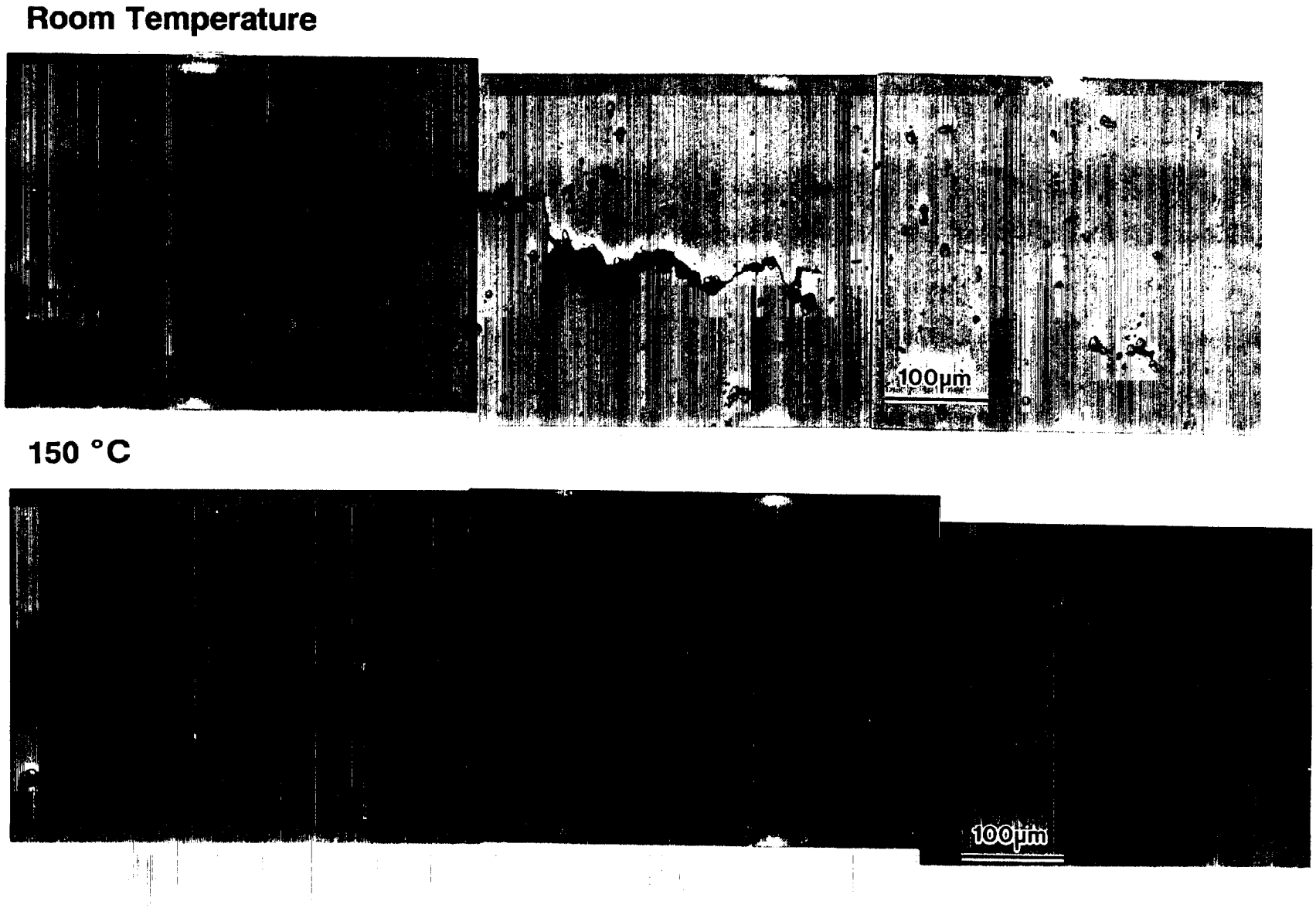

Figure 3 Metallographic profile sections of an AA2519-T87 (+ Mg and Ag) crack tip in C(T) specimens tested at a constant displacement rate of 0.27 μm/sec for: (a) 25°C, and (b) 150°C. Both profiles were polished to the midplane and crack growth was interrupted at K≈85 MPa√m.

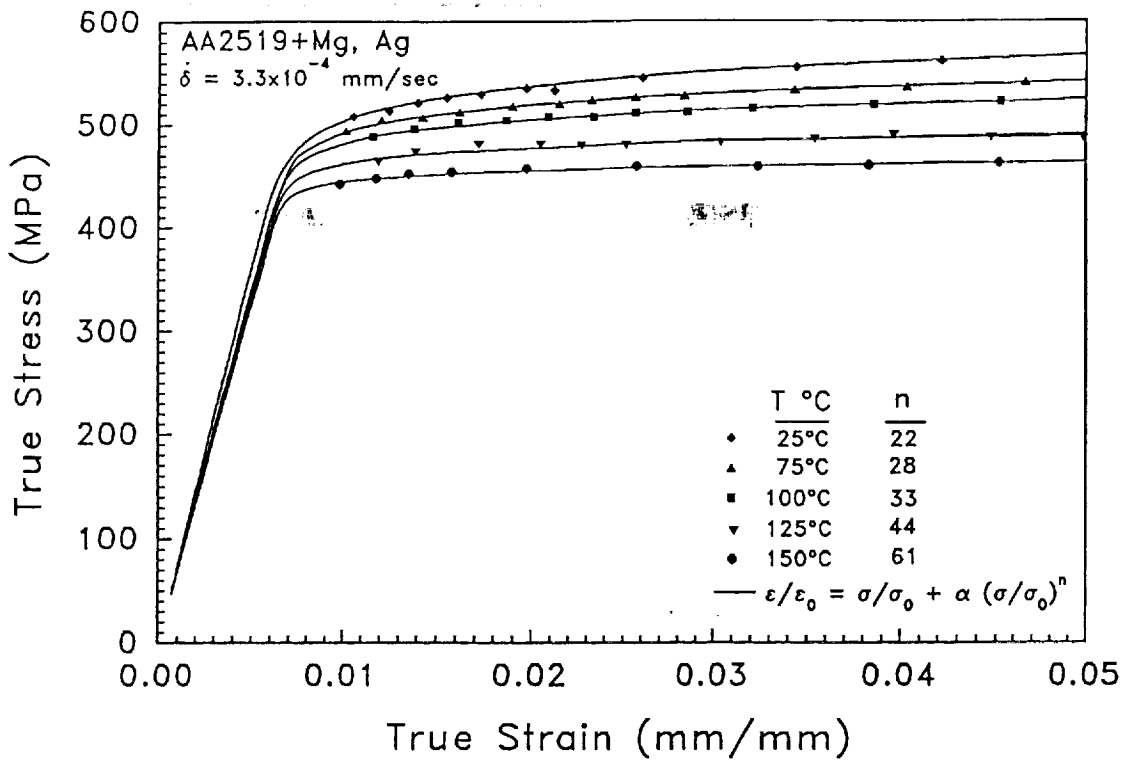

Figure 4 Uniaxial compression true stress-true strain "flow" curves for AA2519-T87 (+ Mg and Ag) as a function of temperature. Experimental data are compared to curve fits of the Ramberg-Osgood constitutive relationship.

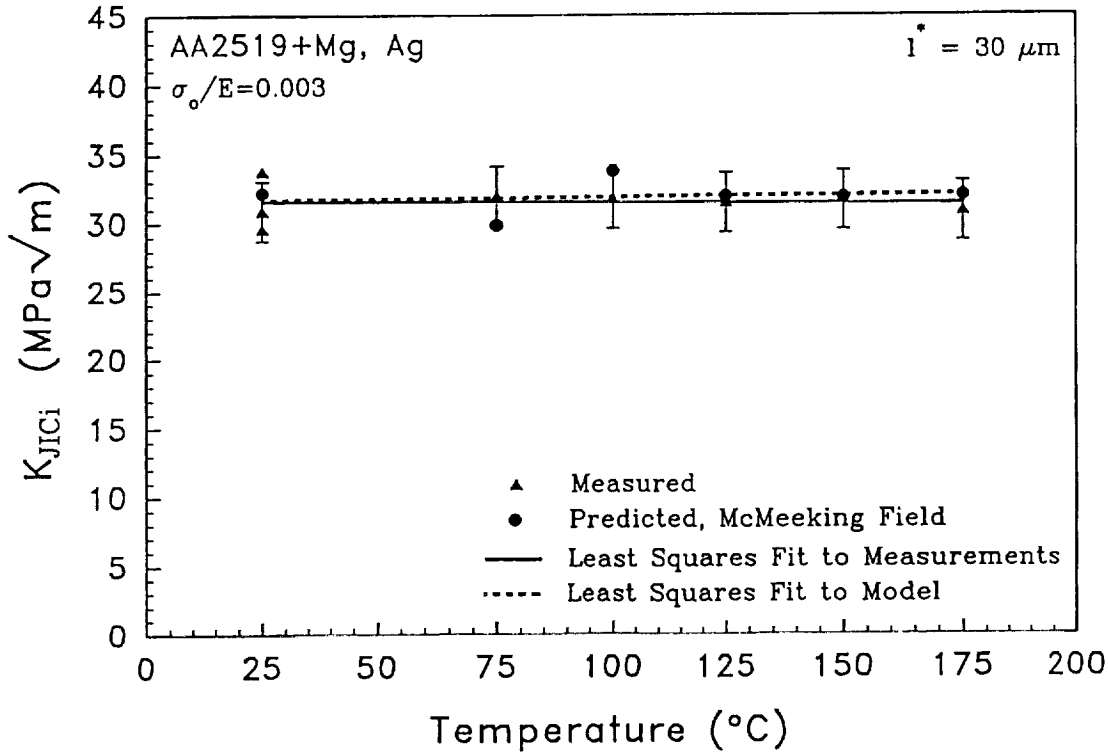

Figure 5 Predictions of initiation toughness ,K_{JICi}, versus temperature of AA2519-T87 (+ Mg and Ag); calculated from the critical plastic strain-controlled model and compared to experimentally measured values.

Project #2 Cryogenic Temperature Effects on the Deformation and Fracture of Al-Li-Cu and Al-Li-Cu-In Alloys

John A. Wagner and R.P. Gangloff

Objective

The objective of this PhD research is to characterize and optimize the crack initiation and growth fracture toughnesses of Al-Li-Cu-Zr and Al-Li-Cu-Zr-In alloys for cryogenic propellant tank applications. The aim of the program is to understand microscopic fracture mechanisms as influenced by temperature, stress state and microstructure.

Approach

The approach to this objective was outlined in the proposal for the 1993 LA^{2}ST Program[1]. In summary our approach focuses on several areas including: (1) produce experimental direct chill cast Al-Li-Cu-Zr alloys with and without indium additions, (2) characterize both experimental Al-Li-Cu-Zr alloys and commercially available 2090-T81 plate, (3) implement J-integral fracture mechanics methods to measure crack initiation and fracture resistance for primarily plane stress and plane strain conditions at ambient and cryogenic temperatures, (4) establish the effect of stress state, temperature and microstructure on fracture toughness, (5) analyze fracture surfaces and correlate fracture features with grain structure, and (6) develop and apply advanced mechanical test and metallographic techniques to investigate the deformation and fracture processes that are relevant to crack initiation and growth toughnesses.

Recent Research Focus

As documented in the last progress report[2], research conducted during the last two reporting periods has primarily focused on the mechanisms and evolution of fracture events in 2090-T81 plate at 25 and -185°C.

Recent Results

Alloy Microstructure

The material studied during this reporting period was 19.1 mm thick unrecrystallized 2090-T81 plate, commercially available from Alcoa. The nominal composition of the alloy was Al-2.30Li-2.85Cu-0.10Zr-0.07Fe wt.%. The near peak aged condition, T81, was achieved by aging stretched material at 163°C for 24 hours. The microstructure was primarily unrecrystallized and with an intense {110}<112> deformation texture at the midplane[3]. Metallographic sections of the grain structure were prepared using standard hand polishing techniques through a 0.05 μm colloidal silica polish, and then were given one of three final treatments: etched by swabbing with Graf-Sargent solution for approximately 45 seconds; electropolished in a mixture of 33 volume percent nitric acid in methanol; or electroetched in boric acid modified Barker's reagent. Electropolished specimens were examined in a scanning electron microscope (SEM) in the backscattered electron (Bse-) mode.

Examination of the structure using Bse- imaging techniques showed a large variation in grain/subgrain size through the thickness of the plate, Figure 1, and has been previously observed for 2090-T81 plate[4,5]. There appears to be three distinct types of grains/subgrains present in the structure: (1) pancake shaped grains elongated in the rolling direction with a thickness of approximately 40 to 100 μm, (2) elongated subgrains approximately 10 to 20 μm in thickness (bottom of inset Figure 1), and (3) a more equiaxed subgrain structure approximately 5.0 μm in size (top of inset Figure 1). Complete assessment of the grain/subgrain boundary misorientation is forthcoming. The large variation in grain/subgrain size could be a result of constituent/dispersoid particles causing inhomogeneous strain distribution during the processing from ingot to plate[6]. In areas of the plate which received more strain, it is speculated that rearrangement of the substructure to a more equiaxed structure with higher misorientation would occur and precipitation along these boundaries may be enhanced.

Short Transverse Tensile Properties

Subsize tensile specimens, with the tensile axis in the short transverse, ST, direction were tested to estimate the boundary strength of 2090-T81 at ambient and cryogenic temperatures. With the thickness of the pancake grains on the order of 40 to 100 μm, numerous boundaries oriented perpendicular to the loading axis lie along the 6.3 mm gage section of the subsize specimens and it was postulated that fracture would occur along one of these boundaries. In addition since the structure of the 2090 was unrecrystallized with a strong deformation texture, the ST properties are expected to be low[7].

Because the gage section of the ST tensile specimens was of reduced length and continuous radius, specimens did not conform to standard size and exhibited constrained behavior. The level of triaxial constraint was estimated using the ratio of the mean stress to the effective stress and the equation[8]:

$$\left(\frac{\sigma_m}{\bar{\sigma}}\right) = \frac{1}{3} + \ln\left(\frac{r}{2R} + 1\right)$$

where σ_m is mean or hydrostatic stress, $\bar{\sigma}$ is effective stress, 2r is the notch root net section ligament (ie., diameter, d) and R is the notch tip radius. In a uniaxial tension test, $\sigma_m/\bar{\sigma} = 0.33$ compared to $\sigma_m/\bar{\sigma} = 0.50$ for the ST subsize tension specimens. Table I presents the results of ST tensile tests at 25 and -185°C. Failure strength was calculated by dividing the maximum load by the original cross-sectional area. Longitudinal failure strengths for subsize specimens of the same geometry as the ST specimens are also presented for comparison. There is a slight increase in the failure strength of ST specimens at -185°C suggesting that the boundaries may strengthen somewhat at cryogenic temperatures.

Fracture Toughness Results

Fracture toughness behavior was determined using elastic-plastic fracture toughness experiments which conformed to ASTM Standard E813-

89[9] and employed the single specimen unloading compliance technique. Compact tension specimens, either 1.6 mm thick or 12.0 mm thick, the latter with 1.2 mm deep sidegrooves, were machined from the midplane of the plate in the LT orientation. Fatigue precracking was preformed at a stress ratio (R) of 0.1 at ambient temperature. Ambient and cryogenic fracture toughness tests were conducted in an environmentally controlled chamber in-line with a servohydraulic load frame. The environment for ambient tests was laboratory air at approximately 25°C. Cryogenic tests were conducted in gaseous nitrogen at -185°C ± 2°C. Temperature was monitored by a thermocouple attached to the specimen grips. Prior to testing at -185°C, specimens were held at temperature a minimum of 0.5 hours. Further details of the test procedures have been reported previously[3].

Table II presents the results of J-integral fracture toughness testing conducted at 25 and -185°C for 12.0 and 1.6 mm thick specimens in the LT orientation. Figure 2 presents typical J-Δa plots for 12.0 and 1.6 mm thick specimens at the two test temperatures. It was assumed that since $25(J_{Ic}/\sigma_{ys})$~0.6 mm, 1.6 mm specimens were of sufficient thickness to provide valid J_{Ic} results typical of plane strain constraint. J_{Ic} values were determined from the intersection of the power law regression line of the data with the 0.2 mm offset from the blunting line according to ASTM Standard E813-89[9]. (The blunting line equals $2\sigma_{ys}\Delta a$.) Because J_{Ic} from this procedure does not appear to accurately estimate the crack initiation toughness for all conditions examined in 2090-T81, an alternate definition of the J level at initiation was employed by using a 0.1 mm offset. A curve was fitted through the J-Δa data, and the intersection of the 0.1 mm offset and the data curve was defined as J_i. By using a 0.1 mm offset instead of the standard 0.2 mm offset, and by not forcing the data to conform to a power law fit, the effect of the slope of the R-curve after initiation has been reduced and may give a more meaningful J initiation value. K_i values were calculated from measured J_i using the relationship $K_i=(J_iE/(1-\nu^2))^{1/2}$ where E is Young's modulus and v is Poisson's ratio. Tearing modulus, T_R, was used to assess resistance to stable crack growth after crack initiation and was determined from the relationship

$T_R=(E/\sigma_o)dJ/d\Delta a$, where σ_o is the flow stress equal to $(\sigma_{ys}+\sigma_{uts})/2$ and $dJ/d\Delta a$ is the slope of the J-Δa curve in the region of stable crack growth[10]. Values of $dJ/d\Delta a$ were determined from a least squares linear regression analysis of J-Δa from Δa of 0.2 to 1.5 mm.

Effect of Stress State on Toughness

T = 25°C: With reference to Table II and Figure 2, at ambient temperature 1.6 mm thick specimens exhibit slightly higher initiation toughness, J_i, compared to 12.0 mm thick specimens with sidegrooves. Although the initiation toughness, J_i, of 12.0 and 1.6 mm specimens were similar, the overall R-curve behavior was significantly different at ambient temperature. The more steeply rising R-curve which is reflected in a higher tearing modulus, T_R, for the 1.6 mm thick specimen can be attributed to thin sheet plane stress fracture during stable crack growth. However, the average T_R of 2.9 for 1.6 mm thick specimens is still significantly below the T_R of 11.8 for current cryotank material 2219-T87 with a specimen thickness of 3.8 mm[11].

Figure 3 presents full thickness cross sections of 12.0 and 1.6 mm thick specimens tested at 25 and -185°C. Table III summarizes the dominant fracture modes for each of these four cases. The primary macroscopic fracture mode for the 12.0 mm thick specimen at 25°C is transgranular shear (TGS), with a shear crack crossing numerous grains before arresting at a delamination, Figure 3A. When a TGS crack propagated across a large grain in which subgrain boundaries were not heavily decorated, the fracture morphology was relatively featureless. In comparison, in regions where the substructure was more equiaxed and heavily decorated fracture was more tortuous and intersubgranular (ISG) in nature.

The macroscopic fracture mode in 1.6 mm thick specimens at 25°C was relatively flat, with no delaminations in the central region, which transitions to shear fracture at the specimen surface, Figure 3B. Fracture in the central region which is probably well described by plane strain initiation toughness, is again transgranular in nature but appears to be more ductile than the TGS fracture observed for thicker specimens, Figure 4. However, the initiation

toughness values, J_i, of the two specimen thicknesses are not comparable because of the delamination induced fracture mode transition to the shear fracture process in the 12.0 mm thick specimens.

-185°C: At -185°C, the most significant difference in the toughness behavior between 12.0 and 1.6 mm thick specimens was apparent when comparing the initiation toughness, J_i, Table II and Figure 2. J_i increased from an average of 13 kJ/m^2 for 12.0 mm thick specimens to 27 kJ/m^2 for 1.6 mm thick specimens. In contrast if J_{Ic} is used as a measure of the initiation toughness, values for 12.0 and 1.6 mm thick specimens are almost identical, approximately 16.5 kJ/m^2, because of the forced fit of the data with a power law curve. This can lead to a misleading interpretation about the apparent similarity of initiation toughness of the two different thickness specimens. Examination of the initial portion of R-curves strongly suggest that the initiation toughness of the 1.6 mm thick specimen is significantly higher than that of the 12.0 mm thick specimen. This result is unexpected and not understood from either a continuum fracture mechanics or a microscopic fracture mechanism perpsective. If plane strain is claimed for fracture of each thickness at 25°C, then it should be similarly operative at -185°C. More extensive delamination in the thicker specimen should only increase J_i compared to the thin specimen case. The microscopic fracture modes for these two cases are similar; there is no physical reason for the very high K_{Ji} values for the thin specimen at the cryogenic temperature, Table II. The data in Figure 2 continue to be compromised by problems in resolving the early stage of crack growth by the unloading compliance method.

In comparison the T_R (least squares linear regression analysis of J-Δa from Δa of 0.2 to 1.5 mm) is similar for the two different thicknesses. The average T_R for 12.0 mm thick specimens is 2.8 compared to 3.1 for 1.6 mm thick specimens. Macroscopically, fracture in specimens of both thicknesses was characterized by delaminations with associated regions of TGS fracture, Figures 3C and 3D. This observation suggests that the similarity in T_R may be related to the similarity in the macroscopic fracture mode.

Effect of Temperature on Toughness

12.0 mm Thick Specimen: For 12.0 mm thick specimens, there is a significant increase in both the initiation and growth toughnesses at -185°C. J_i increased by about 45% and T_R by 85% when tests were conducted at cryogenic temperatures. Fracture in specimens at both temperatures was characterized by delaminations and TGS fracture, Table III. However, fracture of specimens tested at -185°C, which exhibited higher initiation and growth toughness, is associated with the occurrence of several very large delaminations on the order of 0.5 to 2.0 mm in depth, Figure 5. In addition to the observation of large delaminations, there was also an increase in the frequency of small delaminations on the order 0.05 to 0.50 mm in depth and between which shear fracture traversed only one or two grains (single grain slip) compared to the long range TGS observed at 25°C, Figure 5.

1.6 mm Thick Specimens: Similar to the results for the thicker specimens, for 1.6 mm thick specimens there is a significant increase in J_i, but only a slight increase in T_R when tests were conducted at -185°C. The increase in J_i was associated with a change in macroscopic fracture mode from ductile transgranular tearing at 25°C to small delaminations with TGS at -185°C, Figures 3B and 3D. The occurrence of delaminations along with TGS fracture at -185°C is related to increased cryogenic yield strength promoting elevated through-thickness stresses. At higher magnification, the fracture surface of the specimen tested at -185°C exhibited more planar shear facets, Figure 4. The observed differences in the microscopic and macroscopic fracture modes was not reflected in significant differences in the average tearing modulus values of 1.6 mm thick specimens tested at 25 and -185°C.

Fracture Morphology

Delamination Behavior

The δ' strengthening phase in 2090-T81 has an ordered structure and is sheared by dislocations during the deformation processes. Planar slip will preferentially occur on the weakened shear plane resulting in intense slip

bands which impinge on grain boundaries. Under conditions of sufficient triaxial constraint, delaminations will occur along these boundaries in specimens of the LT orientation prior to advance of the primary crack[12].

The higher initiation and growth toughnesses of 12.0 mm thick specimens tested at -185°C compared to specimens tested at 25°C is associated with the occurrence of large, deep delaminations on the order of 0.5 to 2.0 mm in depth, Figure 5. The occurrence of large delaminations may be related to the increase in through-thickness stresses at cryogenic temperatures. The increase in through-thickness stresses could be sufficiently high to offset the small observed increase in grain boundary failure strength and thus produce larger delaminations. The fracture mode transition from ductile transgranular fracture at 25°C to delamination with TGS fracture at -185°C can also be attributed to an increase in through-thickness stresses.

In addition to the observed occurrence of large delaminations in 12.0 mm thick specimens tested at -185°C, there was also the occurrence more numerous small delaminations, Figure 5. The number of small delaminations of the size 0.05 to 0.5 mm observed across a fractured cross section increased from approximately 10 at 25°C to 50 at -185°C. The increase in the number of small delaminations in the ligament between larger delaminations may be related to reduced cross slip and multiple slip at -185°C which reduces the probability of slip transmission to a neighboring grain. The shear failure which occurs within individual grains is possibly slip band cracking parallel to {111} planes[13,14]. Future work will investigate the mechanism of increased levels of small delaminations at cryogenic temperatures.

Transgranular Shear Fracture

TGS fracture was most apparent in 12.0 mm thick specimens tested at 25°C. Investigators have shown that prior to initiation of a TGS crack, delaminations or internal or external free surfaces must be present[15]. Fracture of the ligament between delaminations must occur for the primary crack to advance and therefore after delamination has occurred, fracture

toughness of the material is determined by the toughness of the ligament[16]. Initiation of TGS fracture in a ligament probably occurs when the stress concentration associated with the localized planar shear deformation initiates a microcrack within the band or at the band/matrix interface. At ambient temperature, the propagation of the TGS crack proceeds across numerous grains without crack deviation before arresting at a delamination, Figure 3A, and results in a lower T_R for the 12.0 mm specimens tested at 25°C compared to specimens tested at 185°C. Examination of electropolished specimen in the SEM BSe- mode showed that although this alloy is highly textured, the majority of grains within a TGS region were of differing orientation and suggests that the propagation of the crack in the TGS region does not occur solely by cooperative SBC parallel to {111} planes within individual grains. This observation lends credence to the hypothesis that failure in this region occurred primarily by long range, macroscopic TGS.

For 1.6 mm thick specimens tested at 25°C, regions of TGS fracture were limited to sheared regions at the specimen surfaces typical of fracture associated with planes of maximum shear stress, Figure 3B. Fracture in the center of the 1.6 mm thick specimen exhibited no long range TGS, consistent with the observed absences of internal delaminations and free surfaces. Fracture is again transgranular in nature, but appears to be more ductile than the TGS fracture observed for the thicker specimens. One goal of future work will be to understand the mechanisms associated with the ductile transgranular fracture process.

Intersubgranular Fracture

Consistent with the current investigation, Dorward observed a propensity for ISG fracture near the surface of 2090 sheet where the substructure was well developed and heavily decorated[7]. The more equiaxed decorated substructure of relatively higher angle subgrain boundaries are preferential sites for boundary precipitation. In this investigation, TEM analysis of the boundary particles revealed that they were primarily the T_1 (Al_2CuLi) phase. Precipitation of T_1 on subgrain boundaries could lead to strain localization at boundaries and result in the initiation of fracture by void

formation at the precipitate/subboundary interface. ISG separation is a relatively low energy event (low toughness) compared to TGS and ductile transgranular tearing; however, because the relative proportion of this type of fracture is small compared to the other fracture events it has little effect on the overall toughness of the specimen.

Recent Conclusions

1. The microstructure of 2090-T81 is inhomogeneous through the thickness of the plate and consists of pancake shaped grains elongated in the rolling direction with apparent subgrains exhibiting two different morphologies.
2. Grain boundary failure strength, as estimated by testing mildly notched ST tensile specimens, increases slightly at -185°C.
3. The standard J_{Ic} definition does not give a good estimate of the J level corresponding to the crack initiation toughness for all conditions examined in this investigation. An alternate definition of the J level at initiation, J_i, was employed by using a 0.1 mm offset from the blunting line.
4. Although the J_i initiation toughness of 12.0 and 1.6 mm thick specimens were similar at 25°C, fracture occurred by different modes. Fracture of 1.6 mm specimens appeared to be transgranular in nature, but more ductile than observed for 12.0 mm specimens.
5. At -185°C, specimens of both thicknesses exhibited an increase in crack initiation and growth toughnesses and fracture was characterized by delaminations and transgranular shear fracture. In addition there was an increased tendency for single grain slip and small delaminations at cryogenic temperatures.

Future Direction

Studies will investigate the specific influence of identified grain/subgrain structure on the evolution of fracture events. Work will continue on mechanisms which govern the nucleation and propagation of

transgranular fracture and single grain slip.

References

1. R.P. Gangloff, "NASA-UVA Light Aerospace Alloy and Structures Technology Program", University of Virginia, Proposal No. MSE-NASA/LaRC-5669-93, November, 1992.

2. R.P. Gangloff, "NASA-UVA Light Aerospace Alloy and Structures Technology Program", University of Virginia, Report No. UVA/528266/MSE93/112, March 1993.

3. J.A. Wagner and R.P. Gangloff: Scripta Metall., 1992, vol. 26, pp. 1779-1784.

4. D. Chu and J.W. Morris, Jr.,: in Light-Weight Alloys for Aerospace Application II, E.W. Lee and N.J. Kim eds., TMS-AIME, Warrendale, PA, 1991, pp. 99-105.

5. D. Chu and J.W. Morris, Jr.,: Metall. Trans. A, 1991, vol. 22A, pp. 1789-1799.

6. E.A. Starke, Jr. and F.S. Lin: Metall. Trans. A, 1982, vol. 13A, pp. 2259-2269.

7. R.C. Dorward: in Advances in Fracture Research, K. Salama, K. Ravi-Chandar, D.M.R. Tarplin and P.R. Rao eds.,Pergamon Press, Oxford, UK, 1989, pp. 2413-2422.

8. A.C. Mackenzie, J.W. Hancock and D.K. Brown: Eng. Frac. Mechanics, 1977, vol. 9, p. 167.

9. "Standard Test for J_{Ic}, A Measure of Fracture Toughness," Designation E813-89, Annual Book of ASTM Standards, ASTM, Philadelphia, PA, 1992, vol. 03.01, p. 732.

10. P.A. Paris, H. Tada, A. Zahoor and H. Ernst: in Elastic-Plastic Fracture, ASTM STP 668, Philadelphia, PA, 1979, pp. 5-36.

11. Unpublished NASA-LaRC Research.

12. K.T. Venkateswara Rao and R.O. Ritchie: Acta Metall., 1990, vol. 38, No. 11, pp. 2309-2326.

13. K.V. Jata and E.A. Starke: Metall. Trans. A, 1986, vol. 17A, pp. 1011-1026.

14. K.V. Jata and E.A. Starke, Jr.: Scripta Metall., 1988, vol. 22, pp. 1553-1556.

15. K.T. Venkateswara Rao and R.O. Ritchie: Mat. Sci and Tech., 1989, vol. 5, pp. 882-895.

16. K.S. Chan: Metall. Trans. A, 1989, vol. 20A., pp. 155-164.

Table I. Short Transverse and Longitudinal Failure Strengths of 2090-T81 at 25°C and -185°C from Subsize Specimens

Orientation	Failure strengths, MPa	
	25°C	-185°C
Short Transverse	611	637
Longitudinal	639	730

Table II. Fracture Toughness of 2090-T81

Temp °C	Thickness mm	J_{Ic} (kJ/m^2)	J_i** (kJ/m^2)	T_R	K_{JIc} (MPa$\sqrt{m}$)	K_{Ji} (MPa$\sqrt{m}$)
25°C	12.0*	10.0	9	1.9	29.6	28
		11.3	9	1.3	31.4	28
		9.9	9	1.2	29.4	28
		11.4	9	1.5	31.6	28
	1.6	12.1	9	2.4	32.5	28
		14.2	10	3.5	35.2	30
		17.0	13	2.7	38.6	34
-185°C	12.0*	18.1	14	3.0	42.2	37
		14.1	12	2.5	37.2	34
	1.6	17.7	32	3.3	41.7	56
		15.9	23	2.9	39.5	48

* Prepared with 1.2mm sidegrooves ** Estimates Only

Table III. Fracture Morphology of 12.0mm and 1.6mm Thick Specimens Tested at 25°C and -185°C

Thickness (mm)	Fracture Morphology	
	25°C	-185°C
12.0	Delaminations Transgranular Shear	Large Delaminations Transgranular Shear Single Grain Slip
1.6	Ductile Transgranular	Delaminations Transgranular Shear Single Grain Slip

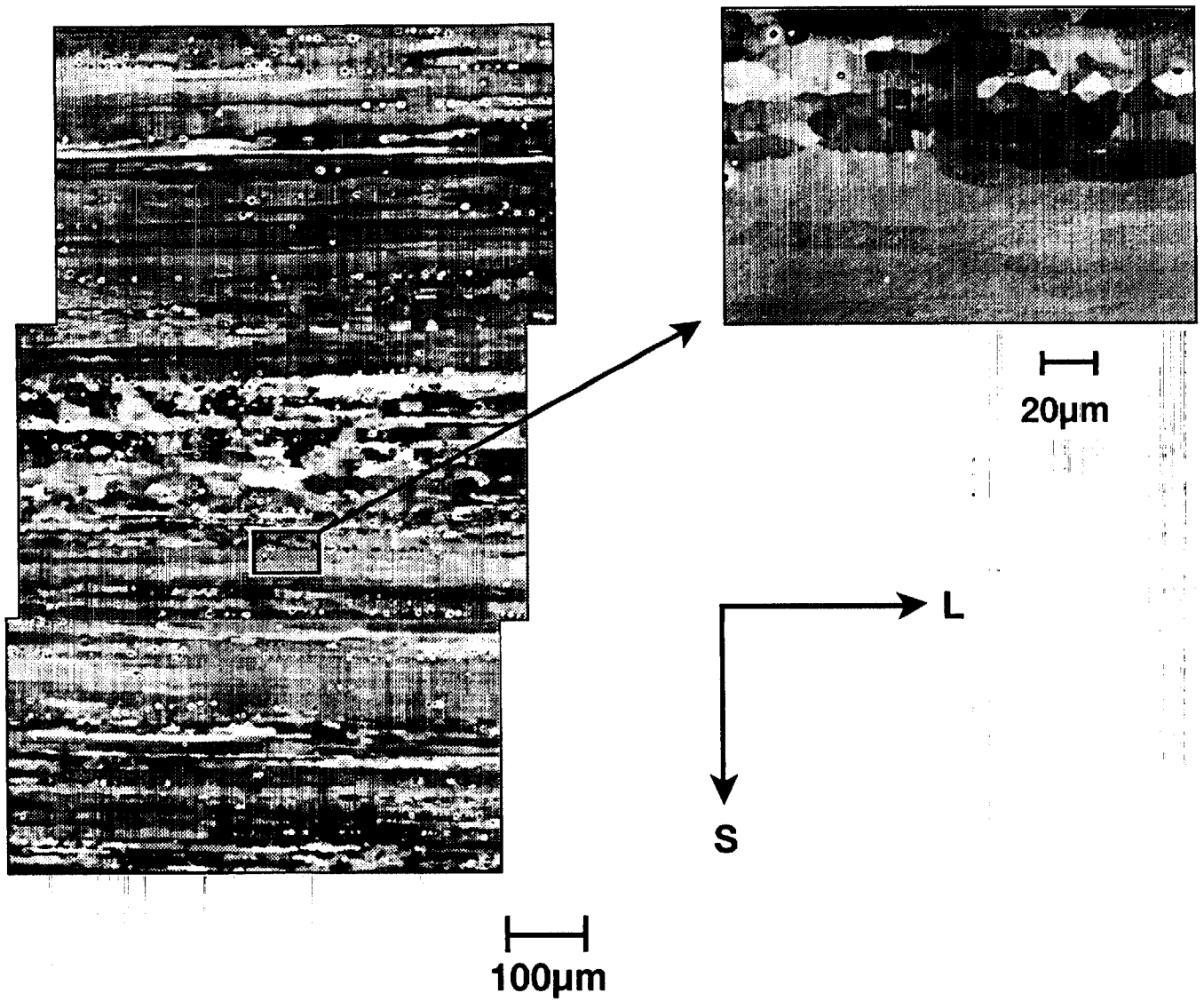

Figure 1. Through thickness grain structure of 2090-T81.

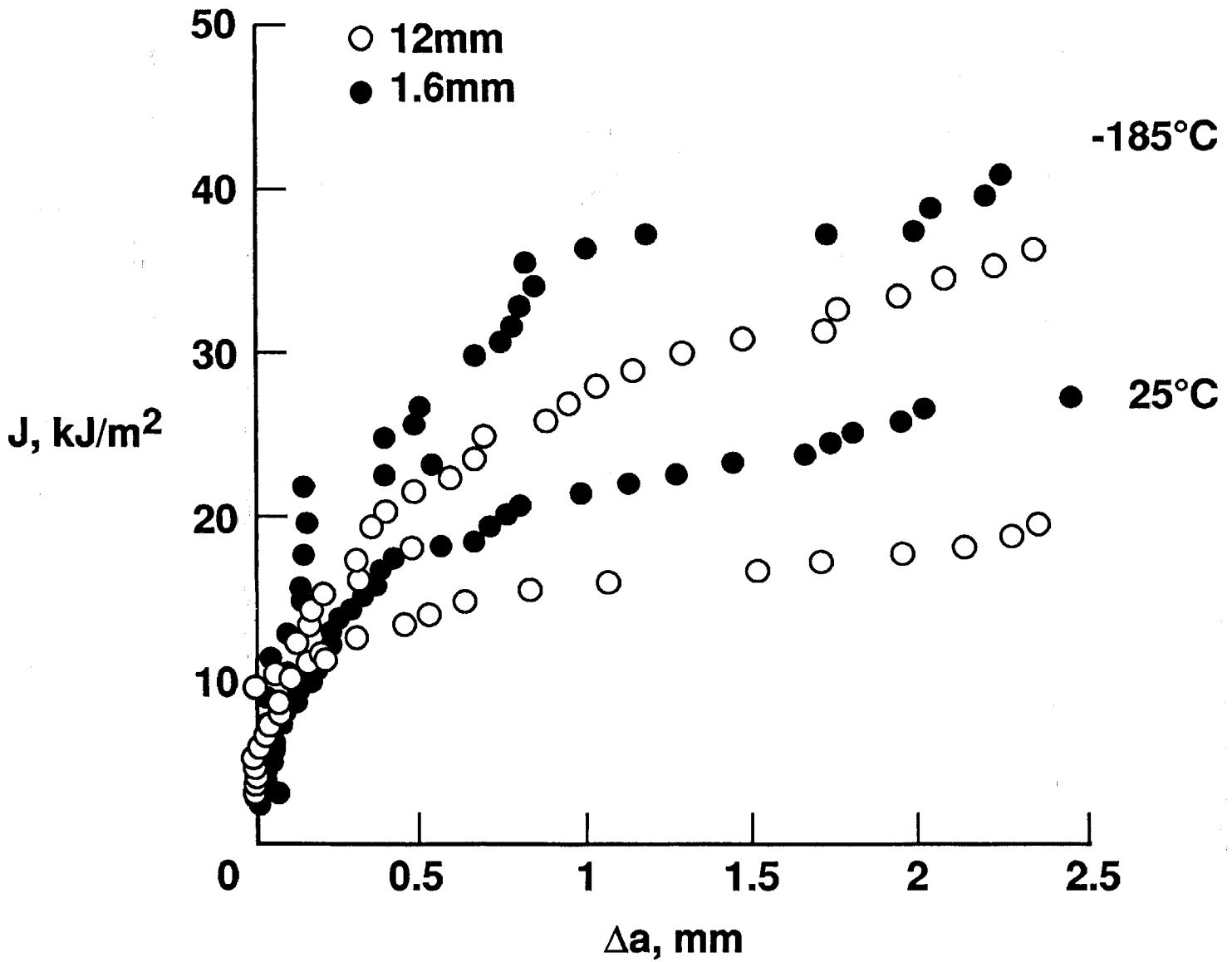

Figure 2. R-Curves for 2090-T81 specimens

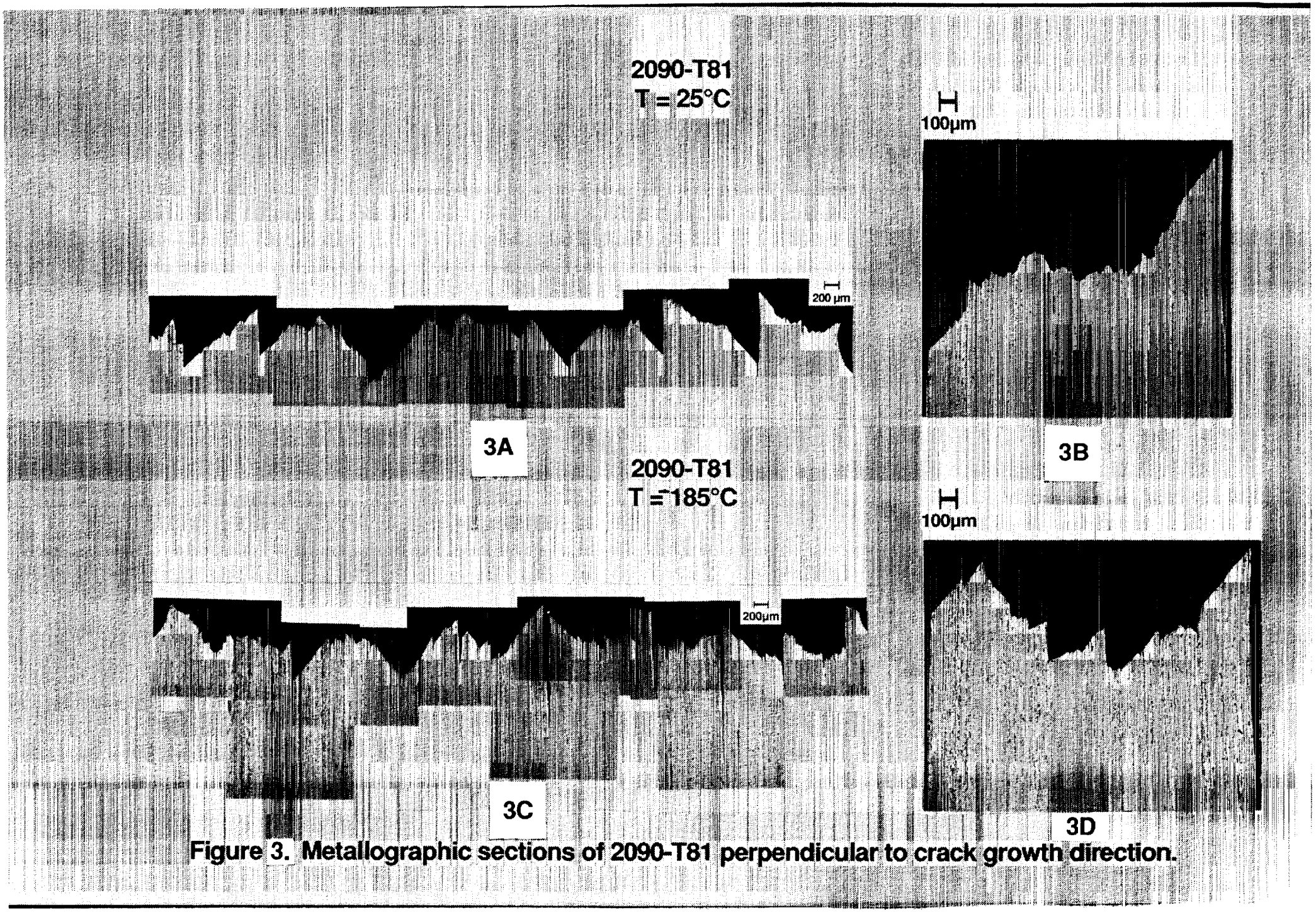

Figure 3. Metallographic sections of 2090-T81 perpendicular to crack growth direction.

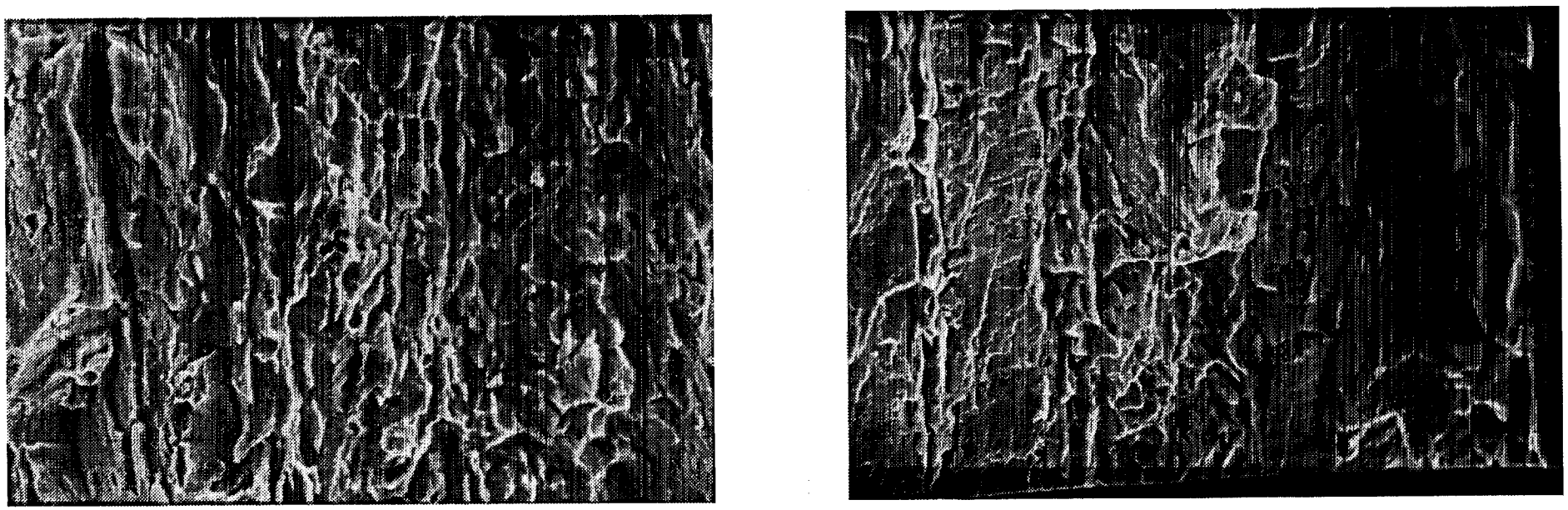

Figure 4. Fracture in central region of 1.6mm thick specimens.

cr frac

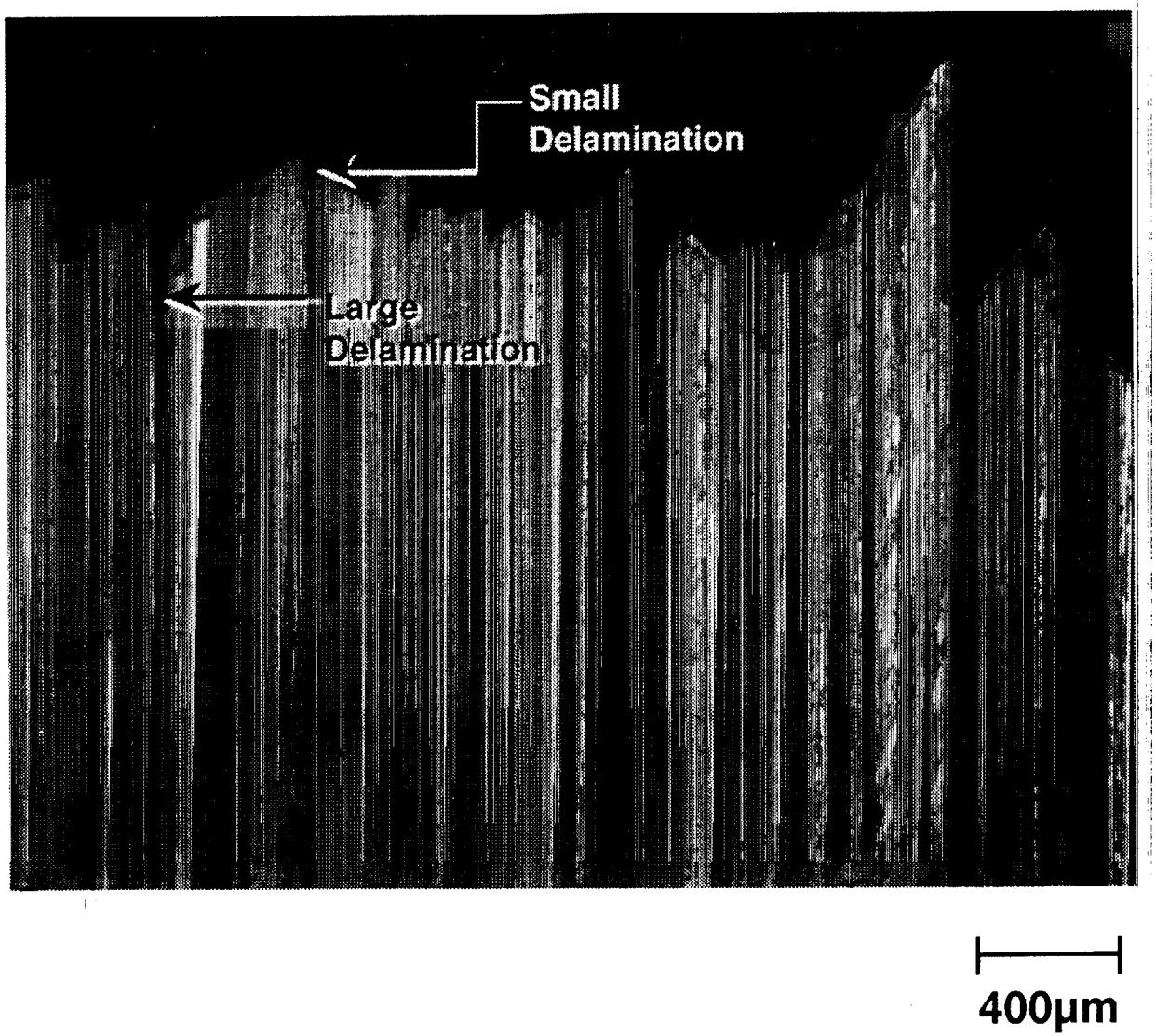

Figure 5. Fracture cross section of 2090-T81 tested at -185°C, cross polarized light image.

Project #3 The Effect of Cryogenic Temperature on the Fracture Toughness of Weldalite™ X2095

Cynthia L. Lach and Richard P. Gangloff

Objective

The objective of this research is to characterize the effect of cryogenic to mildly elevated temperature on the tensile deformation and fracture toughness of an emerging composition of Weldalite™-type alloys. We will determine quantitative stress versus strain data, and initiation and growth fracture toughnesses, as well as the associated microscopic fracture mechanisms, and conduct micromechanical modeling in order to understand temperature-dependent fracture.

Background

Aluminum-lithium-copper alloys are being developed to replace conventional 2XXX and 7XXX aluminum alloys for aerospace structural applications. Al-Li-Cu alloys such as 2090 offer increased stiffness and decreased density due to lithium, and exhibit increased strength and potentially increased fracture toughness with decreasing temperature from room to cryogenic levels[1-4]. Increasing toughness at cryogenic temperatures facilitates fracture mechanics damage tolerant designs because cold proof-testing is not required; a room temperature evaluation suffices. With the addition of elements such as Ag, Al-Li-Cu alloys exhibit exceptionally high yield strengths, that appear to further increase with decreasing temperature[5], without the necessity for post-solution treatment stretch deformation[6]. The fracture toughness of such alloy compositions must be understood as a function of temperature.

Technical Approach

The approach to this research was outlined in past renewal proposals[7,8].

Material

Thirteen-millimeter thick plates of two Weldalite™ compositions were selected for study to examine the limits of the Li and Cu levels for the alloy registered as AA2095[9]. Specifically, a high Li-Cu alloy (Al-4.64Cu-1.53Li-0.34Ag-0.37Mg-0.17Zr; wt%) at the upper extreme of the AA2095 composition specification[9], and a low copper alloy (Al-4.04Cu-1.00Li-0.37Ag-0.36Mg-0.15Zr; wt%) at the low end of the AA2095 composition specification and in the middle of the AA2195 specification[9] were chosen for evaluation.

The expectation is that the selected alloys will contain substantially different amounts of primary phase to enable examination of the effect of this feature on fracture toughness. Several artificial aging conditions, conducted at NASA-LaRC, were employed to vary yield strength, work hardening capacity, and the volume fraction and distribution of the θ' and T_1 strengthening precipitates. Metallurgical and temperature effects on toughness will be assessed for similar flow properties.

Deformation and Fracture

The approach of the proposed research will follow that developed by Wagner in Project #2. Measurements will produce uniaxial tensile stress-strain relationships, and J-Integral based crack initiation and growth fracture toughnesses. This latter method will enable determination of plane strain fracture toughness data from relatively thin specimens (eg. 3.9 mm thick), as well as an estimate of the plane stress crack growth resistance. Microstructural effects on the complete crack initiation and growth resistance relationship will be studied.

Progress During the Reporting Period

The emphasis of recent research has been on addressing the following three important issues[10,11].

(I) *The variability in replicate measurements of fracture toughness.* The question is whether such differences are intrinsic to the X2095 under study, or whether ASTM Standard E813 is inadequate for thin specimens of aluminum alloys. That is, what is causing the extreme variability in fracture

toughness?

(II) *The effect of temperature* on the tensile deformation and toughness of optimally processed X2095.

(III) *Identification of the mechanism* for temperature-(in)dependent fracture in optimally processed X2095.

The 4.6 wt% Cu-1.5 wt% Li and the 4.0 wt% Cu-1.0 wt% Li variants of Weldalite™ X2095 were characterized in terms of 25°C and -185°C tensile deformation behavior and fracture toughness. To investigate the effect of various strength levels on the fracture toughness of X2095, each alloy was aged at 143°C for 10, 20, 30 and 72 hours.

Issue I: Variability in replicate fracture toughness values.

Results obtained to date show that fracture toughness values, measured by replicate experiments, are unexpectedly and unacceptably variable. In each case fracture was by identical microvoid processes, and specimen microstructures and textures were similar, indicating no obvious metallurgical explanation for the toughness variability. (At the plate center, the high Cu-Li variant was fully recrystallized due to the action of the high volume fraction of primary phase particles, while the low Cu-Li variant was unrecrystallized over the thickness of the compact tension {C(T)} specimen located at the mid-plate thickness.) The 4.0Cu-1.0Li variant was received from two separate sources, but was reported to be from the same lot. Fracture toughness tests were conducted using {C(T)} specimens which were machined and heat treated in two separate batches. Experiments were conducted to determine if strength differences occurred due to heat treatment variations and caused toughness variability.

Hardness measurements (Rockwell A scale) were conducted at 25°C and -185°C on remnants of fractured round tensile and flat C(T) specimens. For the cryogenic hardness tests, both the specimen and the brale hardness indentor were submerged in liquid nitrogen and brought to equilibrium prior to indention. As shown in Table I, the C(T) specimen 4030FAF (4.0 wt% Cu-1.0 wt% Li alloy aged at 143°C for 30 hours) had significantly lower hardness than other similarly aged specimens, indicating an improper heat treatment. Thus,

the fracture toughness result for this specimen is discarded.

A survey of the furnace revealed a cold spot which was approximately 10°C cooler than the rest of the furnace. Specimen 4030FAF was perhaps in the cold spot of the furnace during the heat treatment. The 4.6 wt% Cu-1.5 wt% Li C(T) specimens that were heat treated for the second test set-up had slightly lower hardness values (i.e. lower yield strengths) which resulted in slightly higher fracture toughnesses. Temperature variations during the two heat treat runs could account for the slightly different hardness values. As a first step to understand the fracture toughness data in Table I, the measured hardnesses of the C(T) specimens were converted to tensile yield strength by the following calibration procedure.

The hardness of each fractured tensile specimen was measured on the surface of the 12.5 mm diameter round grip section, at the same temperature (25°C or -185°C) as the tensile test. Yield strength was correlated to hardness for each temperature and the two alloy variants. Figure 1 shows measured tensile yield strength plotted as a function of measured tensile bar hardness. For tests conducted at either 25°C (open symbols) or at -185°C (filled symbols), the correlation between hardness and yield strength is nearly linear and approximately equal for each alloy. At either temperature, the correlations are reasonably described by a single alloy composition-independent linear relationship, as replotted in Figure 2. The slopes of these relationships are likely to be statistically equal.

The relationship in Figure 2 between yield strength and hardness depends on temperature. It is well known that chilling to cryogenic temperatures increases both the yield strength and average work hardening capacity of Al-Li-Cu alloys. Since hardness is best related to the flow stress required to produce between 5 and 10% plastic strain, one would expect that hardnesses at -185°C would deviate to the right and below the yield strength-based trend line for 25°C, in contrast to the behavior that is reported in Figure 2. (This deviation is expected because higher work hardening at cryogenic temperatures should increase hardness to a larger degree than the offset yield strength. The trend line for 25°C is based on hardness changes

from aging which produces increased yield strength, but decreased work hardening.) Rather, the trend in Figure 2 indicates unexpectedly high yield strength and/or unexpectedly low hardness for the cryogenic case. This behavior could be explained by an anomalous tensile flow curve, for example exhibiting yield point-type behavior or initially low work hardening, at cryogenic temperatures. This possibility will be investigated as exact true stress versus true strain data are obtained during the next reporting period..

To better understand the variability in previously reported fracture toughness data (Table I), K_{IC} from J-R-curve experiments is plotted as a function of the calculated yield strength of each C(T) specimen in Figure 3. (The yield strengths of individual C(T) specimens were calculated by using the measured hardness values of the C(T) specimens in the linear strength-hardness relationships determined from the tensile bar tests.) The wide scatter that existed in the 30 hour aged specimens, fractured at 25°C in the first test set-up, is significantly reduced by comparing the hardness-based yield strengths to fracture toughnesses. Taken in total, the data in Figure 3 provide a sufficient basis for understanding and modeling the effects of alloy composition, microstructure and temperature on the fracture initiation toughness of X2095.

The data in Figure 3 must, however, be further tested and evaluated. For any constant temperature-composition-aging condition, the average hardness measured from the tensile specimen is lower than the corresponding value from the C(T) specimen. Three factors may contribute to this difference. C(T) hardnesses were obtained from flat surfaces, while the tensile specimens were round, a different Rockwell A indentor was employed for tensile specimen hardness experiments compared to the work with the C(T) specimens, and tensile hardnesses were taken near to the plate surface, while C(T) hardnesses (and tensile yield strengths) were obtained near the plate mid-plane. The importance of these factors is being investigated to finalize the important strength versus toughness trends in Figure 3.

Additionally, two discrepant C(T) samples from the second test set-up

(4072CF and 4020DF) must be further investigated, and the absolute values of the initiation toughnesses presented in Figure 3 must be utilized with caution. Both issues require understanding and critical analysis of the experimental procedure to determine the J versus crack extension (Δa) relationship, and the associated initiation toughness (K_{JIC}), as embodied in ASTM Standard E813. Determinations of the toughnesses in Figure 3 were hindered by irregular crack growth indications from unloading compliance. Either negative deviations from a calculated blunting line, or unexpectedly large crack growth increments were observed during the early stages of loading in several experiments. Second, the absolute toughness values in Figure 3 either equal or over-estimate the more conventionally determined plane strain fracture toughness, determined by the application of ASTM Standard E399 to acceptably thick specimens. The difference increases with decreasing alloy strength and for toughness levels above about 35 MPa$\sqrt{m}$.

The procedure for determining K_{JIC} in Figure 3 employs a 0.2 mm offset of the calculated blunting line. Since the C(T) specimens are thin, the R-curve is relatively steep because of some plane stress crack extension, following from the initial plane strain initiation event localized to the mid-thickness location at the fatigue crack perimeter. The definition of the point of crack growth initiation impacts the calculated toughness; values at the first detected crack growth can be significantly less than the values given by the offset blunting line intersection with the steeply rising R-curve. These former values may better approximate conventionally (ASTM E399) measured K_{IC}, while values from E813 may be high in spite of the fact that the thickness and remaining ligament sizes were larger than the sizes required by the standard for a valid plane strain initiation toughness. Since the standard has not been broadly applied to thin sheet aluminum alloys, we are not able to confidently conclude that the toughnesses in Figure 3 equal conventional E399 values.

While these details are important, the data in Figure 3 suggest that the significant variability in X2095 fracture toughness is traceable to strength differences. The fracture toughness of the low Cu-Li variant, unlike the high Cu/Li variant, strongly depends on yield strength; small changes in yield

strength result in large changes in fracture toughness. This yield strength dependency could explain the increased scatter in the fracture toughness data for the low Cu-Li alloy variant. The effect of chemistry on the fracture toughness behavior is apparent at any constant yield strength. For a given yield strength, the fracture toughness values were significantly higher for the low Cu-Li alloy variant at both test temperatures. This result is consistent with the large volume fraction of undissolved particles present because the composition of the high Cu-Li variant exceeds solid solubility at the solution treatment temperature that was employed, as discussed in previous progress reports.

Issue II: The effect of temperature on the toughness of optimally processed X2095.

For a given aging condition, both alloy variants maintained essentially constant fracture toughness as temperature decreased, while experiencing a significant increase in yield strength. Toughness did not increase with decreasing temperature, as expected based on limited literature data for several Weldalite™ compositions. Rather, close examination of the data in Table 1 and Figure 3 indicate occasional small decreases in K_{JIC} at the cryogenic temperature. Toughness did not decrease substantially, however, as might be expected based on the magnitude of the strength increase at cryogenic temperature. This latter result is significant, and requires micromechanical and mechanistic explanation. That is, we must determine if combinations of temperature dependent yield strength, work hardening exponent, elastic modulus and intrinsic fracture resistance (ductility); predicted by strain-based micromechanical modeling; accurately reproduce the measured trends in Figure 3.

An extended aging study of the X2095 alloy variants is underway to characterize the overaging behavior of the alloy.

Tensile and C(T) specimens were heat treated to peak age (4.0 wt% Cu-1.0 wt %Li alloy for 30 hours at 143°C and 4.6 wt% Cu-1.5 wt% Li alloy for 20 hours at 143°C), and were machined to proper test coupon specifications. Hardness tests of peak aged coupons for both X2095 alloys were conducted

from -185°C to room temperature. The hardness specimen and brale indentor were submerged in liquid nitrogen until equilibrium at -185°C was attained. After the liquid nitrogen vaporized, hardness tests were conducted with the corresponding temperatures recorded. The test results, shown on Figure 4, indicate the effect of temperature on the strength and work hardening properties of each peak aged alloy. Tensile tests of these peak-aged X2095 alloys are currently being conducted in order to determine modulus, yield strength work hardening and tensile reduction in area ductility data necessary to micromechanically model the fracture toughness trends in Figure 3. Detailed true stress versus true strain relationships will help in the analysis of the temperature-dependent yield strength versus hardness trend shown in Figure 2.

Conclusions

- oo For high and low Cu-Li variants of X2095 Weldalite™ and two test temperatures, tensile yield strength correlates linearly with hardness. While the correlations are independent of alloy chemistry, separate dependencies are observed for 25 and -185°C, suggesting a temperature effect on the shape of the stress versus strain relationship.
- oo Extreme variability in replicate fracture toughness values is in large part explained by modest differences in aged specimen hardness coupled with a strong yield strength dependence of K_{JIC}, particularly for the low Cu-Li alloy.
- oo For a given aging condition, the fracture toughness of both alloy variants is essentially constant with decreasing test temperature from 25 to -185°C, in spite of substantially higher yield strength at cryogenic temperatures.
- oo For constant yield strength, the 4.0Cu-1.0Li alloy has significantly higher fracture toughness at both test temperatures, consistent with the absence of significant undissolved particles.

Tasks for the Next Reporting Period

Fracture toughness experiments will measure the J-crack growth response, based on the automated unloading compliance method, for cryogenic to mildly elevated temperatures for the 4.0Cu-1.0Li variant of Weldalite™ X2095 aged at 143°C for 30 hours.

The uniaxial tensile deformation behavior of peak aged 4.0Cu-1.0Li will be measured at several temperatures (eg.: -185, -140, -125, -75, -25, 25, 107, and 135°C). Tensile yield strength, work hardening and fracture strain (reduction in area) will be characterized as a function of temperature.

The critical strain-based micromechanical model developed by Ritchie and coworkers will be employed to predict the temperature dependence of K_{JIC} based on measured tensile properties.

References

1. S. Suresh, A.K. Vasudevan, M. Tosten and P.R. Howell, "Microscopic and Macroscopic Aspects of Fracture in Lithium-containing Aluminum Alloys", Acta Metall., Vol.35, pp. 26-46 (1987).

2. J. Glazer, S.L. Verzasconi, R.R. Sawtell and J.W. Morris, Jr., "Mechanical Behavior of Aluminum-Lithium Alloys at Cryogenic Temperatures", Metall. Trans. A., Vol. 18A, pp. 1695-1701, (1987).

3. K.T. Venkateswara Rao, Y. Weikang and R.O. Ritchie, "Cryogenic Toughness of Commercial Aluminum-Lithium Alloys: Role of Delamination Toughening", Metall. Trans. A., Vol. 20A, pp.485-487 (1989).

4. K.V. Jata and E.A. Starke, Jr., "Fracture Toughness of Al-Li-X Alloys at Ambient and Cryogenic Temperatures", Scripta Metall., Vol. 22, pp. 1553-1556 (1988).

5. W.T. Tack and L.W. Loechel, "Weldalite TM 049: Applicability of a New High Strength, Weldable Al-Li-Cu Alloy", in the Proceedings of the Fifth International Aluminum-Lithium Conference, T.H. Sanders, Jr. and E.A. Starke, Jr., eds., Vol. III, MCEP Ltd., Birmingham, UK, pp. 1457-1467 (1989).

6. Alex Cho and W. A. Cassada, "Effect of Cu and Cu:Li Ratio on T6 and T8 Temper Properties of Al-Cu-Li-Mg-Ag Alloys", Presented at Aero Mat 91, Long Beach, CA, May (1991).

7. R.P. Gangloff, "NASA-UVa Light Aerospace Alloy and Structures Technology Program", Proposal No. MSE-NASA/LaRC-4841-91, University of Virginia, Charlottesville, VA (1992).

8. R.P. Gangloff, "NASA-UVa Light Aerospace Alloy and Structures Technology Program", Report No. MSE-NASA/LaRC-5691-93, University of Virginia, Charlottesville, VA (1993).

9. A. Cho, R.E. Greene, M.H. Skillingberg, W.A. Cassada, H.M. Edwards, and P.S. Fielding, "Status of High Strength Al-Li Alloy Development at Reynolds Metals Company", presented at Aeromat'93, Anaheim, Ca (1993).

10. R.P. Gangloff, "NASA-UVa Light Aerospace Alloy and Structures Technology Program", Proposal No. MSE-NASA/LaRC-5669-93, University of Virginia, Charlottesville, Va (1992).

11. R.P. Gangloff, "NASA-UVa Light Aerospace Alloy and Structures Technology Program", Proposal No. MSE-NASA/LaRC-6074-94, University of Virginia, Charlottesville, Va (1993).

Table I. Mechanical Properties of X2095 Alloy Variants

C(T) Specimen Number	143°C Age Time, hours	Test Temperature, °C	C(T) Hardness at Test Temperature, HRA	Calculated Yield Strength, MPa	K_{JIC}, MPa $m^{1/2}$
X2095 Alloy Variant (4.0wt%Cu1.0wt%Li)					
4010AF	10	25	52.40 ± 0.65	563.59	93.8
4020AF	20	25	55.12 ± 0.33	608.46	41.6
4020CF*	20	25	54.22 ± 0.74*	593.62	52.8*
4030AF	30	25	55.26 ± 0.26	610.77	48.6
4030CF	30	25	55.82 ± 0.54	620.01	35.7
4030EF	30	25	53.72 ± 0.59	585.37	53.0
4030FAF	30	25	**47.78 ± 2.48**	**487.36**	**64.6 Discard**
4030GF*	30	25	54.50 ± 0.77*	598.24	51.9*
4072AF	72	25	55.54 ± 0.36	615.39	34.4
4072CF*	72	25	55.78 ± 0.23*	619.35	***60.8* investigate***
4010BF	10	-185	54.92 ± 0.85	678.46	92.1
4020BF	20	-185	58.28 ± 0.41	727.19	40.8
4020DF*	20	-185	57.78 ± 0.81*	735.71	***79.3* investigate***
4030BF	30	-185	59.16 ± 0.48	750.71	41.6
4030DF	30	-185	59.42 ± 0.71	755.14	39.1
4072BF	72	-185	60.38 ± 0.81	771.50	33.3
X2095 Alloy Variant (4.6wt%Cu1.5wt%Li)					
4610AF	10	25	51.84 ± 0.53	569.72	28.9
4620AF	20	25	54.46 ± 0.34	611.08	23.6
4620CF*	20	25	52.84 ± 0.34*	585.51	31.6*
4672AF	72	25	56.12 ± 0.19	637.28	15.6
4672CF*	72	25	55.66 ± 0.38*	630.02	18.2*
4610BF	10	-185	56.62 ± 0.66	692.64	27.6
4620BF	20	-185	58.60 ± 0.48	716.91	19.9
4620DF*	20	-185	57.28 ± 0.33*	700.73	32.1*
4672BF	72	-185	59.90 ± 0.42	734.07	20.4
4672DF*	72	-185	60.24 ± 0.17*	737.01	23.1*

*Second heat treatment and test set-up

FILE:94HRAYScKjicTABLE

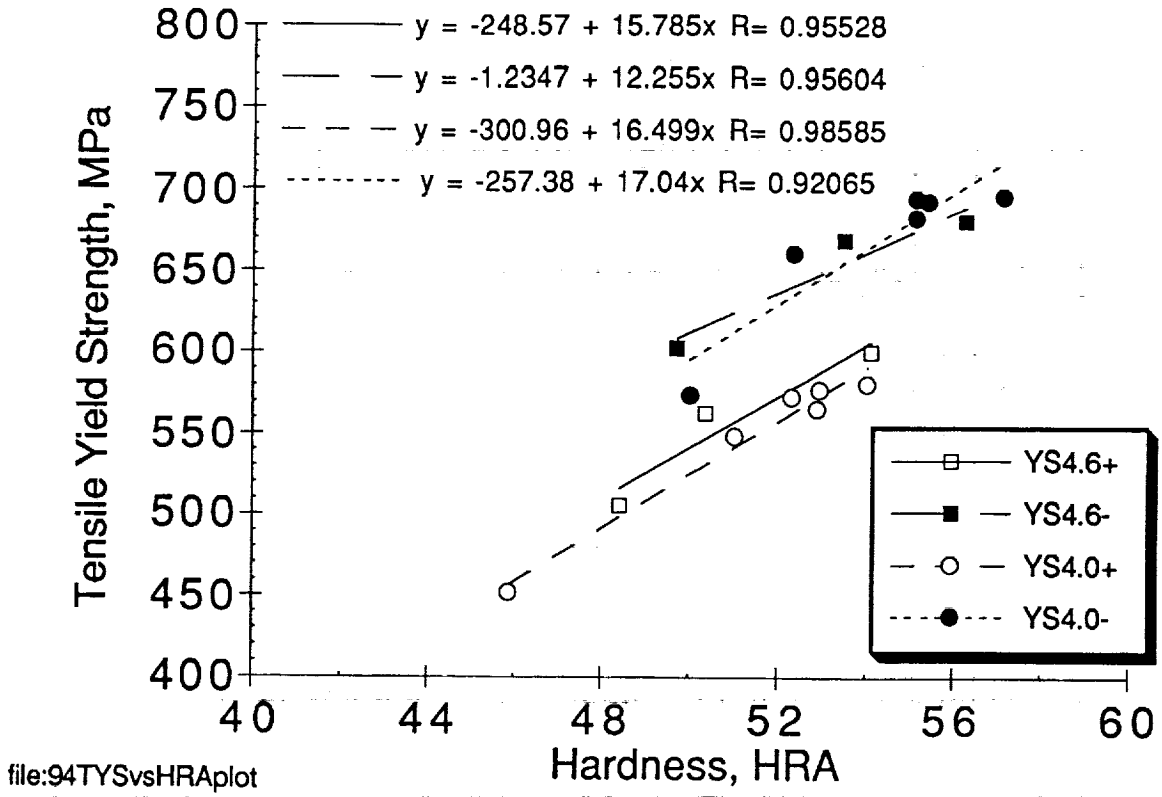

file:94TYSvsHRAplot

Figure 1. Effect of age, test temperature and hardness on yield strength of X2095 alloy variants.

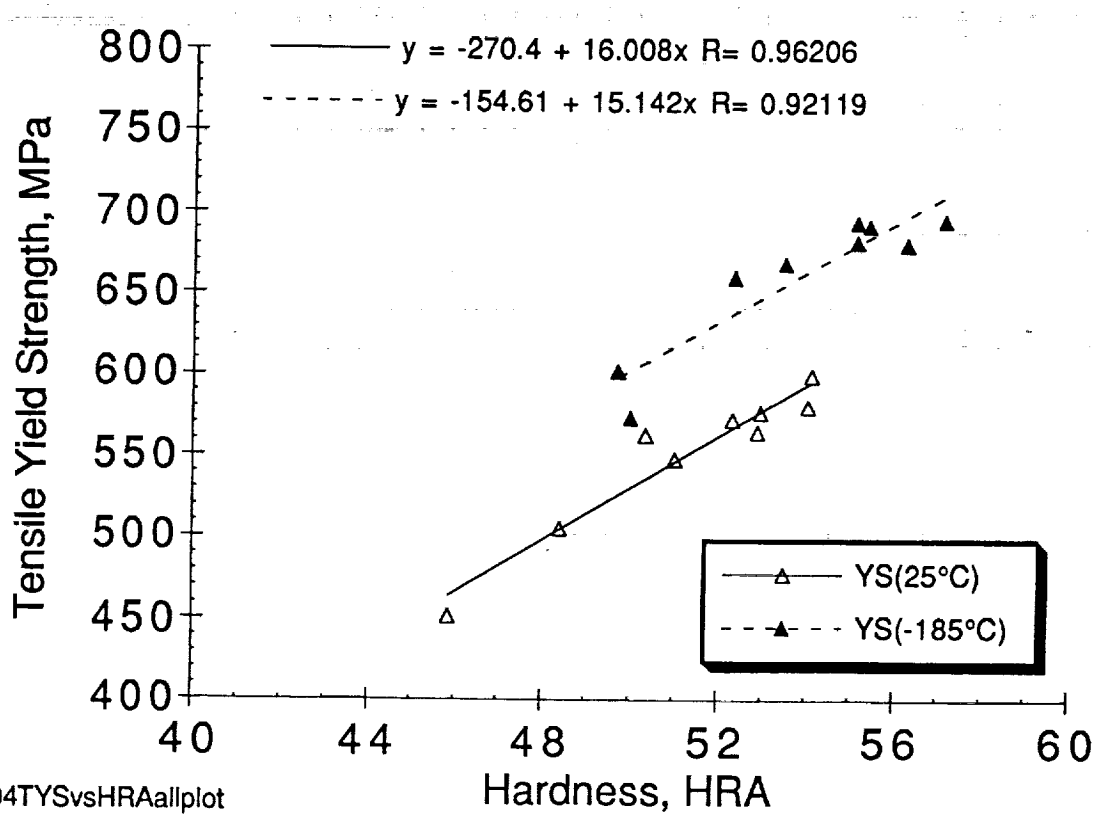

file:94TYSvsHRAallplot

Figure 2. Effect of temperature on the yield strength of X2095 alloy variants.

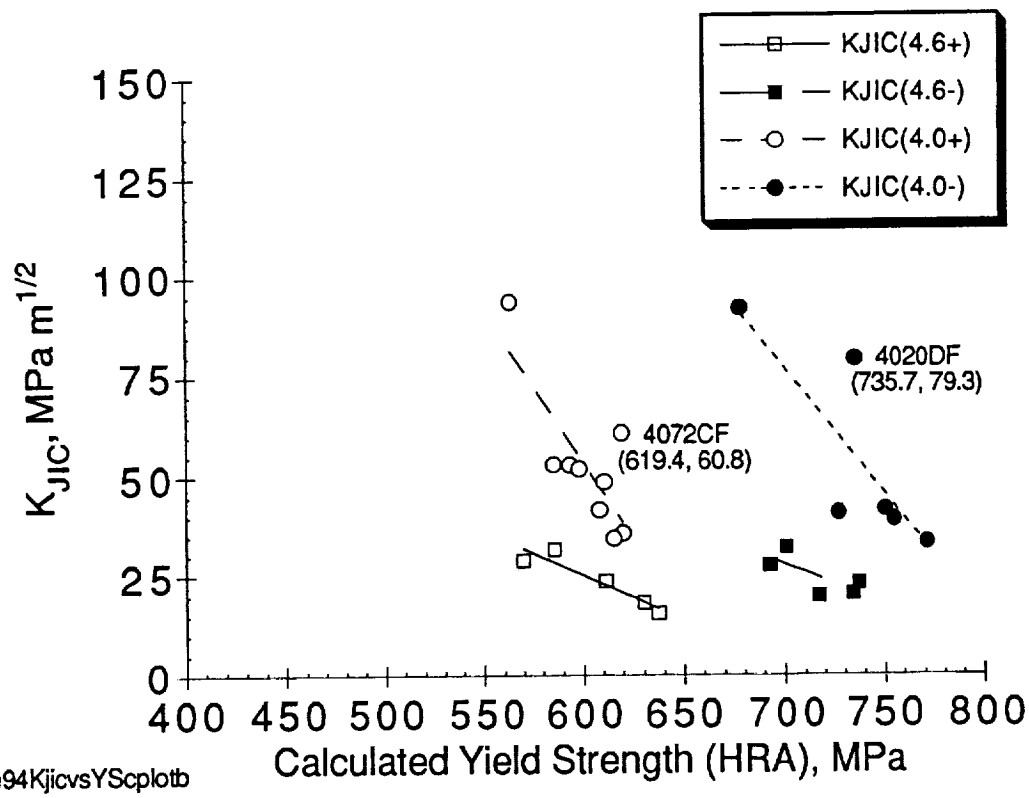

file94KjicvsYScplotb

Figure 3. Effect of yield strength on the fracture behavior of X2095 alloy variants.

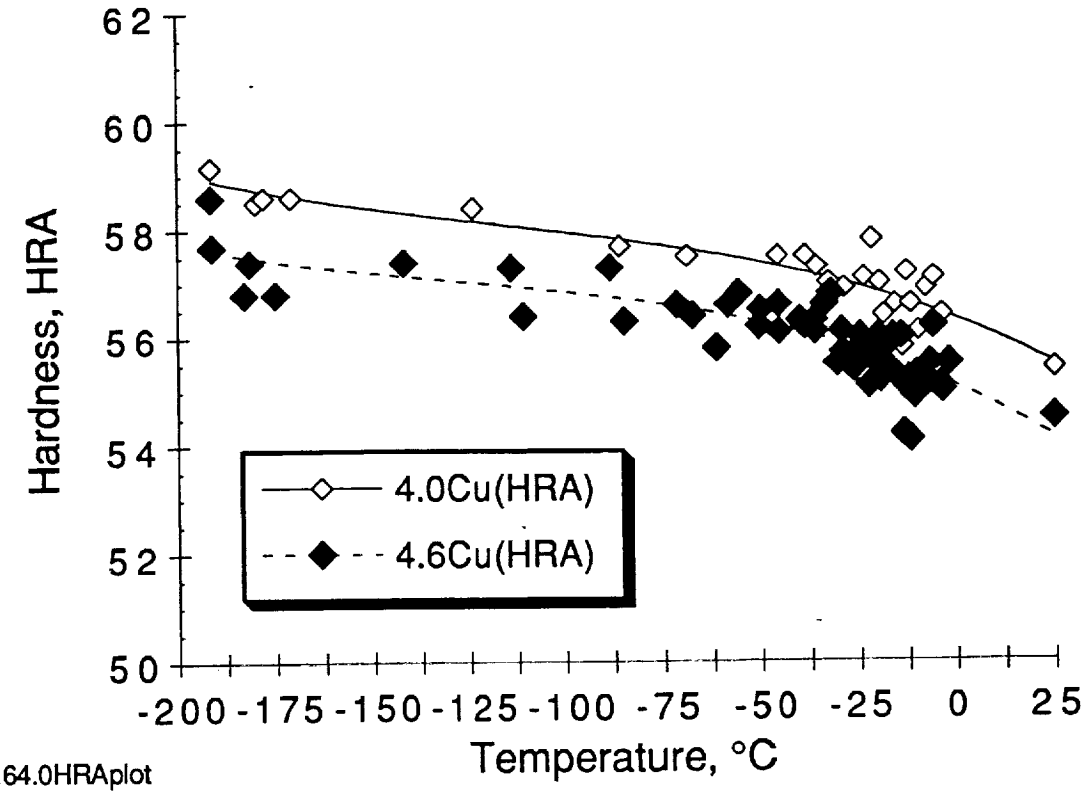

File:4.64.0HRAplot

Figure 4. Effect of temperature on the hardness of peak-aged X2095 alloy variants.

Project #4 Mechanisms of Localized Corrosion in Alloys 2090 and X2095

F. Douglas Wall and Glenn E. Stoner

Research Objectives

The overall objective of this project is to elucidate a mechanism for environmentally assisted fracture (EAC) in advanced Al-Li-Cu alloys based on the interactions of microstructural features and localized environments. Early objectives were focussed on determining likely pathways for anodic dissolution based crack propagation and proposing fundamental components of an occluded chemistry capable of causing EAC in Al-Li-Cu alloys. The most recent task has been to develop experimental techniques capable of quantitatively ranking material/stress-intensity/environment/applied electrochemical potential combinations in terms of the severity of resultant EAC. This report summarizes the results of the initial tasks and details the progress made in the latter endeavor.

Background

Proposed causes for the environmentally-assisted cracking (EAC) of Al-Li-Cu alloys include embrittlement by absorbed hydrogen[1-4] and dissolution directed along an active pathway[5-13]. The focus of this project has been on dissolution mechanisms and hydrogen effects will not be discussed. Hydrogen interactions with these alloys are being studied in by Smith and Scully in Project #5 of this grant.

Anodic dissolution (AD) based mechanisms for EAC in Al-Li-Cu alloys have been investigated by proposing a combination of aqueous environment and electrochemical potential for a propagating crack tip, identifying heterogeneities in the electrochemical behavior of microstructural features under these conditions and demonstrating the existence of a coherent crack path for selective dissolution of the identified features[7-13]. A key insight into the EAC process is the propensity of tensile samples not to fail under

constant immersion conditions in chloride solutions, but to rapidly fail after removal from constant immersion and exposed to laboratory air[5-7].

Experimentation performed by Holroyd[5], and later Craig[6], demonstrated that peak-aged 8090 (Al-Li-Cu-Mg) failed rapidly under conditions of pre-exposure embrittlement in which stressed samples are immersed in 3.5w/o NaCl solution for up to fifty days and removed into various non-aqueous environments. Failures demonstrated a strong dependance on the presence of CO_2 in the post-immersion environments; samples removed to environments void of CO_2 did not fail. Removal of the samples from the bulk NaCl solution has the effect of forming small localized cells at the pits or fissures where solution has been retained. Holroyd simulated the chemistry of the occluded cells by exposing shavings of material to aqueous chloride environments[5] and reported the development of an alkaline environment (pH of 8 to 10) containing lithium ions in the range $2x10^{-4}$ to $1x10^{-2}$.

Based on the high pH and the presence of Li^+ in the occluded environment coupled with the dependence on CO_2 for failures, Craig proposed the following[6]: (1) Under conditions of constant immersion, the aggressive NaCl environment depassivates the grain boundaries and does not allow for the initiation of a sharp crack, (2) Removing a sample from the bulk environment allows for generation of an alkaline environment due to the presence of CO_2, passivation of grain boundaries by precipitation of $LiAlO_2$ and propagation of an SCC crack due to the borderline active/passive condition.

Moran[7,8] duplicated the experimental approach established by Craig and Holroyd[5,6] to demonstrate that the phenomenon of pre-exposure embrittlement holds true for alloy 2090 (Al-Li-Cu). Contrary to Craig, Moran proposed that $LiAlO_2$ would precipitate independent of the presence of CO_2 and, therefore, CO_2 must play a more direct role in the formation of a passivating species - possibly Li_2CO_3.

Moran also suggested that the heterogeneous precipitation of the T_1 (Al_2CuLi) phase influenced the EAC behavior of these alloys[7] by providing an active pathway along sub-grain boundaries. Buchheit et al.[9-11] furthered the

argument for a T_1 based mechanism by studying the electrochemical behavior of a bulk ingot intended to simulate the T_1 phase. They determined that this phase is highly active compared to the matrix phase in a simulated crevice environment[10].

Continued work on 2090 by Buchheit and Wall[9,12,13] suggested that under specific conditions of environment, mechanical stress and applied potential there is a correlation between the electrochemical parameters of the T_1 and matrix (α-Al) phases and the EAC behavior of the bulk material. In a simulated occluded environment such as 0.6M NaCl + 0.1M Li_2CO_3 the breakdown potential (E_{br}) of α-Al is shifted to a more noble potential than that of the T_1 phase. The two E_{br} values define a potential window in which the T_1 phase is highly active while the matrix remains passive. Smooth bar tensile samples loaded to 60% of the alloy yield strength (YS) and polarized within this potential window showed rapid times-to-failure (less than 1 day), while samples polarized cathodic to the E_{br} value of the T_1 phase did not show any signs of localized attack after five days of testing[13]. These results show that a lithium carbonate crevice environment can result in rapid EAC failures of Al-Li-Cu alloys due to preferential dissolution along an active pathway.

The model described above does not provide a mechanism for crack propagation in the regions separating the active precipitates on the boundaries. The current research provides a re-evaluation of anodic dissolution based failures in Al-Li-Cu alloys and demonstrates the possible contributions of both the T_1 phase and a Cu-depleted region to crack propagation.

Technical Approach

Since the majority of the experimental techniques and results have been covered in detail in previous reports[14-17], this section will only provide a summary of this information. The new techniques developed during this reporting period will be covered in detail under heading five, "Progress this Period."

Potentiodynamic polarization experiments and scratching electrode experiments: These experiments were used to define conditions of environment and applied potential in which a microstructural pathway might become active while the bulk of the material remains passive. The two environments of interest are 0.6M NaCl + 0.1M Li_2CO_3 and 0.1M NaCl + 0.1M Na_2CrO_4. 99.99 wt% Al, Al-0.1 Cu, Al-1.0 Cu and Al-3.6 Cu were used to simulate various degrees of Cu-depletion and SHT 2095 was used to model the grain interiors. Information regarding electrochemical behavior was already available for the T_1 phase[10]. Breakdown potentials (E_{br}) from the potentiodynamic experiments indicate that potential windows exist where the matrix and Cu-depleted region are passive while the T_1 phase is highly active. Scratching electrode experiments performed on the 99.99 Al and SHT 2095 indicate that there are also potential windows where a Cu-depleted region would be active while the matrix remained passive. Additionally, the scratching electrode experiments show that the transition from repassivation to sustained corrosion occurs at a potential which is a function of Cu content in the Al-Cu binaries.

Straining electrode experiments: These experiments were intended to simulate the conditions of aqueous environment, applied potential and plastic strain in order to determine if significant differences in electrochemical behavior between α-Al and a Cu-depleted region could reasonably be expected under conditions likely to be encountered at a growing crack tip. The results indicate that in a simulated occluded environment (0.6M NaCl + 0.1M Li_2CO_3) at an applied potential consistent with the free corrosion of α-Al in this environment (approximately -0.700 V_{SCE}) the matrix phase spontaneously repassivates during plastic deformation while the Cu-depleted region anodically dissolves at an appreciable rate.

Time-to-failure experiments: These experiments were used to characterize the behavior of smooth bar tensile samples under conditions of constant load and applied electrochemical potential in the same environments investigated in the electrochemical characterization outlined above. Materials under investigation included short transverse samples of

alloys 2090 (Al-2 Li-2.5 Cu), 2095 (Al-1.0 Li-4.0 Cu) and 2124 (Al-4.0 Cu-1.5 Mg). In each environment there are two types of material response corresponding to materials polarized anodically and cathodically to a transition potential. Samples polarized cathodically to the transition potential showed no signs of localized corrosion for the length of the experiment (5 days) whereas samples polarized anodically to the transition potential demonstrated local sites of violent electrochemical activity resulting in sample failure within one day of exposure. In each environment the transition potential was found to lie in the vicinity of the E_{br} value for the T_1 phase as determined by potentiodynamic polarization studies. These results suggest a link between the electrochemical behavior of the T_1 phase and the behavior of the bulk alloy.

Constant load scratching electrode experiments: These experiments were a simple variation of the time-to-failure experiments. Samples were mechanically loaded, submerged in test solution, potentiostatically polarized, then scratched with a glass rod to initiate corrosion. From these experiments samples were ranked as either failures or no failures as a function of applied potential. The significant result from this experiment is that the transition from no-failure to failure occurs at a potential which is dependent on the temper of the alloy being tested. Increased aging tends to shift the transition potential to more cathodic potentials. This phenomenon could correspond to an increase in the extent of Cu-depletion along grain and sub-grain boundaries. It is not clear how such a temper dependence could be linked to the electrochemical behavior of an anodic phase such as T_1. Thus these experiments favor a Cu-depleted region as a controlling microstructure in rapid EAC failures for the prescribed conditions.

Experimentation performed on alloy 2124 revealed a transition potential for this material similar to those observed for alloys 2090 and 2095. Since 2124 does not contain lithium, the T_1 phase cannot precipitate in its microstructure; however, a Cu-depleted region is a feasible microstructural feature. This result adds support to the primary role of a Cu-depleted region controlling EAC behavior in these tests.

pH of simulated occluded chemistries: This task was the first step in an attempt to characterize the occluded chemistry that develops in isolated fissures in Al-Li-Cu alloys upon removal from a bulk solution. The primary goal was to establish a large ratio of material surface area to solution volume and monitor the changes that occur in solution chemistry. The initial solution was either 0.01M, 0.1M or 0.6M NaCl. Sample configurations included material shavings submersed in solution, small holes bored in a block of material and filled with solution, and a flat section of material with a puddle of solution deposited on the sample surface and enclosed in a high-humidity environment to prevent solution evaporation. In each case a microelectrode was used to monitor solution pH as a function of time. For experiments performed in the high-humidity cell the gaseous environment was controlled to determine the effect of the presence of oxygen. In all experiments an alkaline pH (8-10) was attained within three to five hours. The presence or absence of O_2 did not appear to affect the final pH attained although the initial response varied.

Capillary electrophoresis of simulated occluded chemistries: The solution chemistries generated in the pH experiments (Section 4.5) were analyzed using capillary electrophoresis (CE). This technique is able to separate ions due to differences in mobility through an electrolyte under a large potential field (20 kV). Ions are detected as a function of migration time by changes in UV absorbance and comparisons to absorbance peaks from standards can be used to quantify ion concentrations. From these tests it was determined that the high surface area to solution volume exposures resulted in solutions with Li^+ ion concentrations in the 1 to 3 mMol range. Thus, these results coupled with the pH measurements indicate that an alkaline lithium carbonate environment can develop in an occluded cell isolated from a bulk electrolyte (the carbonate ion being due to CO_2 dissolving from the atmosphere).

Progress this Period

Emphasis this reporting period has been placed on the development of

a controlled stress intensity experimental technique for determining crack propagation rate as a function of material, environment and applied electrochemical potential. Other efforts have included setting up an alternate immersion chamber for DCB specimens and developing a technique for testing EAC susceptibility of specimens in an environment of high surface area to solution volume ratio.

Crack growth rate studies: To the current stage in this research EAC susceptibility has been characterized by a simple failure/no failure criterion for smooth samples under constant load conditions. This technique has allowed for identification of critical electrochemical potentials for various types of behavior, but has not allowed for ranking of various microstructures in terms of EAC susceptibility. In order to provide quantitative information on the rates of crack growth in various microstructures a new test technique has been developed.

The goals for this experiment are to measure crack lengths as a function of time for specimens in an aqueous environment with imposed and thus controlled electrochemical and mechanical stresses. The specimens being used are wedge opening loading (WOL) samples which have a geometry similar to that of standard compact tension specimens.

In order to dictate electrochemical conditions, a cell has been machined which is capable of enclosing the sides and crack opening of the specimen while allowing for specimen extension. The cell has ports for solution intake and output as well as a chloridized silver reference electrode positioned to lay within the mouth of the machined crack opening. Within ports on the cell are two symmetrically located counter electrodes for providing electrochemical current to the growing crack.

Crack length measurements are performed by means of a direct current potential drop (DCPD) technique. A Sorenson model 10-25 power supply is connected to the top and bottom faces of the WOL specimen such that connections are centered along the loading axis of the sample. The potential field across the crack tip is measured by connections made to the front of the specimen diagonally opposed to one another on either side of the crack

opening. The voltage signal is amplified 10,000X by a Measurements Group model 2310 signal conditioning amplifier. As the crack grows, changes in the signal can be correlated to increases in crack length.

A screw driven table top Instron load frame has been used to provide the mechanical loading for the initial experiments. Extension rates as low as $5x10^{-6}$ inches/sec have been used to perform slow rising K experiments.

Software has been developed which is capable of monitoring the electrochemical and mechanical parameters of the experiment, controlling the load frame and running the crack length measurement equipment. The latter task involves computer switching of the DCPD current source at regular intervals and signal averaging in order to remove artifact potential signals due to metal-metal interfaces in the potential measuring loop.

Initial experiments have yielded promising results although there are still difficulties to be overcome in developing the technique. Figure 1 shows the type of data recorded for a rising K experiment. The primary difficulties thus far encountered concern the potential drop associated with current flowing down a restricted geometry. If the potential drop is of sufficient magnitude, then maintaining the required potential for rapid crack growth at the crack tip requires applying a significantly higher overpotential at the crack opening. However, too anodic of applied potential results in all features becoming active at the potential experienced by the sample surface. This results in preferred dissolution outside of the crack and no anodic current can reach the crack tip; consequently, the crack arrests.

Two methods are currently being investigated to counter the problem of potential drop in an occluded geometry. The first involves modification of the sample thickness. By reducing the thickness of the sample, the current path from the side of the sample to the crack front is decreased and the potential drop encountered will be reduced by the ratio of the new sample thickness to the previous sample thickness. For the geometries being considered the thickness is being reduced from 0.5" to 0.125" and the potential drop to the crack front should be reduced by a factor of four. The second method involves coating the sample sufficiently to prevent unwanted

surface corrosion thereby reducing current to portions of the sample other than the crack front.

Other than the problems from unwanted potential drop down the crack front, the experimental technique appears to hold promise for discriminating materials based on crack propagation rates. Refining this technique and applying it to the study of Al-Li-Cu alloys will be the primary focus for the next reporting period.

Alternate immersion of DCB specimens: These tests are intended to provide a more traditional comparison of EAC susceptibility for the research materials under investigation. DCB specimens will be subjected to alternating periods of exposure to 0.6M NaCl solution and ambient air. These experiments will be initiated shortly and results of this testing will be included in the next progress report.

EAC susceptibility under conditions of high surface area to solution volume ratio: The objective of these experiments is to evaluate the role of CO_2 and O_2 in the EAC behavior of Al-Li-Cu alloys. The technique involves loading flat dogbone type tensile specimens into G-49 type test rigs, placing the rig in a high humidity environment and wetting the sample surface with a small volume of chloride solution. The testing chamber is either aerated with laboratory air or purged with argon, oxygen or carbon dioxide. The data of primary interest is specimen time-to-failure as a function of environment although in the future solution chemistries may be studied by CE analysis at the completion of the experiment.

To date, dogbone specimens have been machined and stressed in the test rigs; however, no experiment has been maintained for more than about six hours due to evaporation of test solution. The problem of evaporation was not encountered using this apparatus on unstressed samples and was not anticipated for these experiments. During the next reporting period steps will be taken to remedy this problem and complete the test matrix.

Conclusions to Date

The conclusions reached are essentially the same as those reported in

the Fall progress report[17] but are restated here:

1. Scratching and straining electrode experiments performed on Al-Cu binaries and SHT 2095 indicate that the electrochemical behavior of the boundary features modeled by these materials (Cu depleted region and grain interior respectively) may dictate the requirements for rapid SCC failures in Al-Li-Cu alloys.
2. The temper dependance observed for the transition of no failures to rapid failures in constant load testing of alloys 2090 and 2095 supports the assertion that a Cu-depleted region plays a critical role in this failure mode for the conditions investigated.
3. The similarity in critical EAC potentials for alloys 2124, 2090 and 2095 can not be explained by T_1 precipitation on the sub-grain boundaries since this phase cannot exist in alloy 2124; however, a Cu-depleted region could account for the similarity in behavior.
4. Analysis of occluded environments in Al-Li-Cu alloys indicates the development of an alkaline environment containing dissolved lithium ions.
5. The development of a test technique to encompass simultaneous control of fracture mechanics and electrochemical parameters appears to be a promising endeavor. This technique should provide for the rapid quantification of EAC susceptibility of various Al-Li-Cu alloys as a function of stress intensity, aqueous environment and applied potential.

Future Work

The primary task for the next reporting period is to complete development of the WOL specimen testing technique. Once underway, this experimentation will be used to rank EAC susceptibility on the basis of prescribed mechanical and electrochemical stresses imposed on varying Al-Li-Cu microstructures. Other tasks will include completing alternate immersion testing of DCB specimens, performing the low solution volume/high humidity testing of flat dogbone specimens, and beginning a new phase of solution

chemistry analysis.

References

1. R. Balasubramaniam, D.J. Duquette, K. Rajan, Acta Metallurgica et Materialia, 39, 11(1991): pp. 2597-2605.

2. E.I. Meletis, Weiji Huang, Materials Science and Engineering, A148, (1991), pp. 197-209.

3. E.I. Meletis, W. Huang, "Environmentally Assisted Cracking in Al-Li Alloys," Al-Li Alloys V, E.A. Starke, Jr., T.H. Sanders, Jr., eds. (EMAS Wardley, UK, 1989), pp. 1309-1318.

4. E.I. Meletis, "Microstructural Effects on the Environment-Assisted Fracture Mechanisms of Al-Li Alloys," Parkins Symposium on Fundamental Aspects of Stress Corrosion Cracking, Eds. S.M. Bruemmer et al. (The Minerals, Metals & Materials Society, 1992).

5. N.J.H Holroyd, A. Gray, G.M. Scamans, R. Hermann, Aluminum Lithium Alloys III, C. Baker, P.J. Gregson, S.J. Harris, C.J. Peel, eds. (The Institute of Metals, London, 1986) p 310.

6. J.G. Craig, R.C. Newman, M.R. Jarret, N.J. Holroyd, J. de Physique, 48, C3 (1987): p.825.

7. J.P. Moran, Ph.D. Dissertation, University of Virginia, 1990.

8. J.P. Moran, G.E. Stoner, Aluminum Lithium Alloys V, T.H. Sanders, Jr., E.A. Starke, Jr., eds. (MCE Publications Ltd., Birmingham, UK, 1989), p.1187.

9. R.G. Buchheit, Ph.D. Dissertation, University of Virginia, 1991.

10. R.G. Buchheit, G.E. Stoner, Aluminum Lithium Alloys V, T.H. Sanders, Jr., E.A. Starke, Jr., eds. (MCE Publications Ltd., Birmingham, UK, 1989), p. 1347.

11. R.G. Buchheit, Jr., J.P. Moran, G.E. Stoner, Corrosion, 46, 8 (1990): p.610.

12. R.G. Buchheit, Jr., F.D. Wall, Jr., G.E. Stoner, "The Effect of Applied Potential in Static Load SCC Testing of 2090 in Cl^- and Cl^-/CrO_4^{2-} Environments," Proceedings of the Electrochemical Society - Environmentally Enhanced Fracture Symposium, Fall Meeting 1990 (Pennington, NJ, 1991).

13. R.G. Buchheit, Jr., F.D. Wall, Jr., G.E. Stoner,"Stress Corrosion Cracking of Al-Li-Cu-Zr Alloy 2090 in Aqueous Cl^- and Mixed Cl^-/CO_3^{2-} Environments," Corrosion/91, Paper no. 99, (Houston, TX: NACE, 1991).

14. F.D. Wall, G.E. Stoner, "Mechanisms of Localized Corrosion in Al-Cu-Li-Mg-Ag Alloy X2095 and Compositional Variations", in "NASA-UVa Light Aerospace Alloy and Structures Technology Program", Report No. UVA/528266/MSE92/109, University of Virginia (1992).

15. F.D. Wall, G.E. Stoner, "Mechanisms of Localized Corrosion in Alloys 2090 and X2095", in "NASA-UVa Light Aerospace Alloy and Structures Technology Program", Report No. UVA/528266/MSE92/111, University of Virginia (1992).

16. F.D. Wall, G.E. Stoner, "Mechanisms of Localized Corrosion in Alloys 2090 and X2095", in "NASA-UVa Light Aerospace Alloy and Structures Technology Program", Report No. UVA/528266/MSE93/112, University of Virginia (1993).

17. F.D. Wall, G.E. Stoner, "Mechanisms of Localized Corrosion in Alloys 2090 and 2095", in "NASA-UVa Light Aerospace Alloy and Structures Technology Program", Report No. UVA/528266/MSE113, University of Virginia (1993).

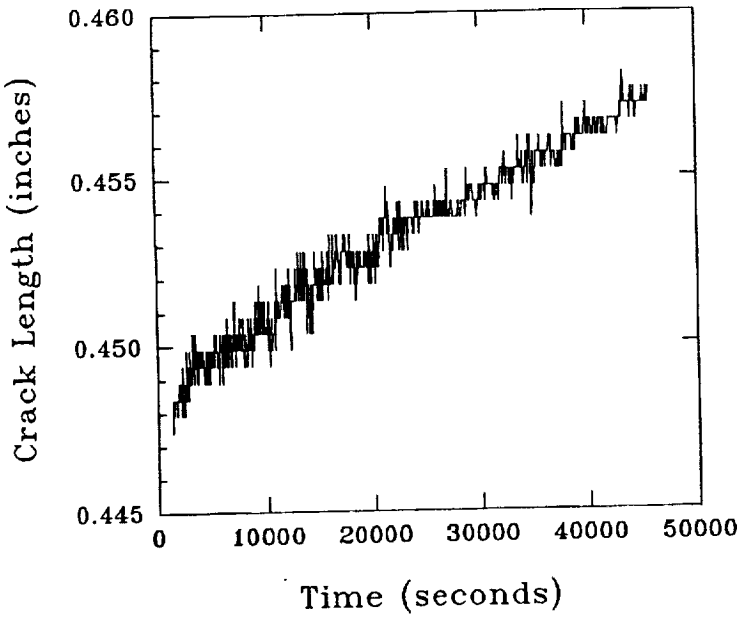

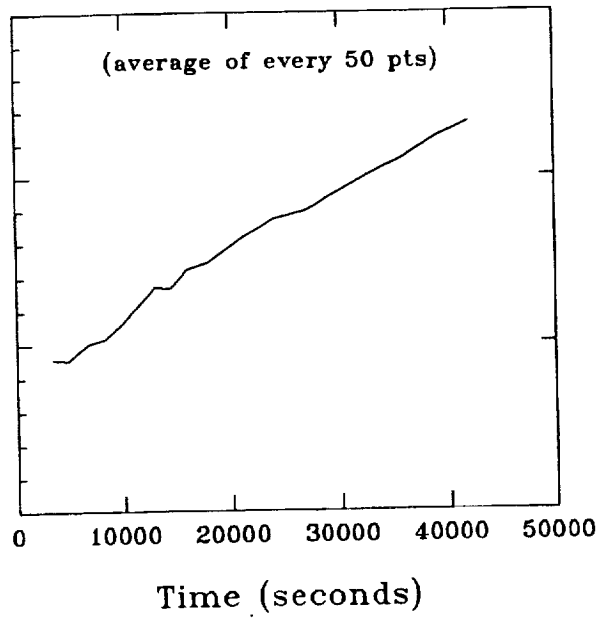

Sample 11059302
2095-A, S-L, WOL specimen

0.1M NaCl + 0.1M Na_2CrO_4 (aerated)

E_{appl}= < -510 V_{SCE}

Extension rate = $5x10^{-6}$ in/sec

Linear least squares fit of a vs t yielded da/dt=$1.95x10^{-7}$ in/sec

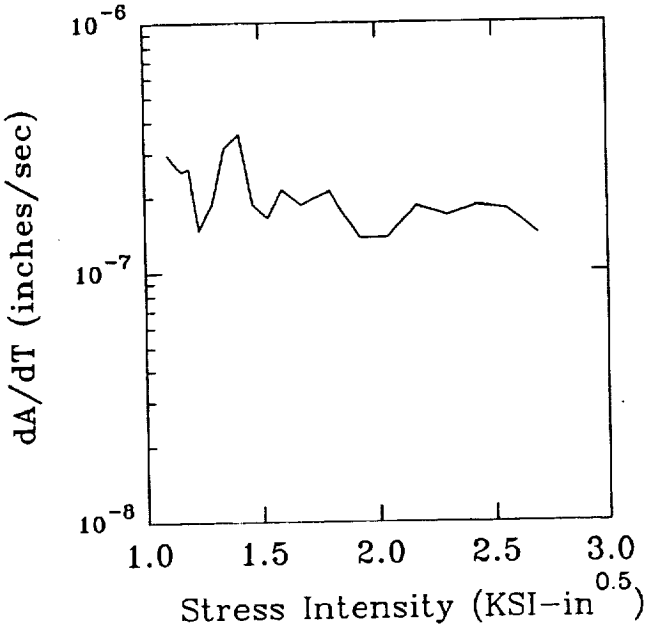

Figure 1. Results of Rising K Experiment

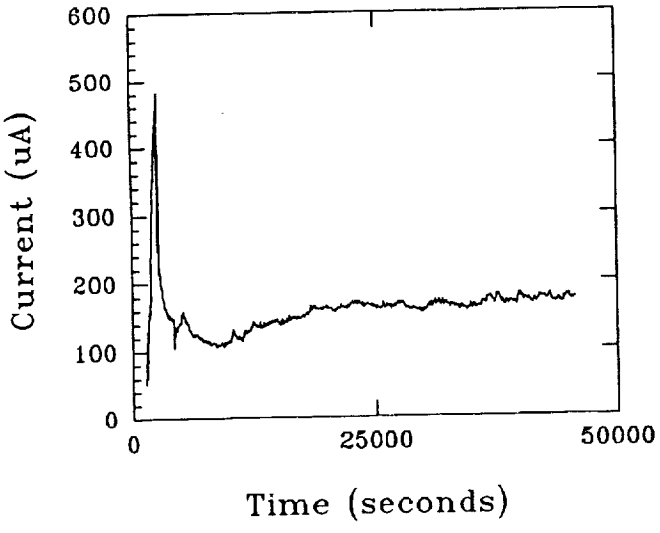

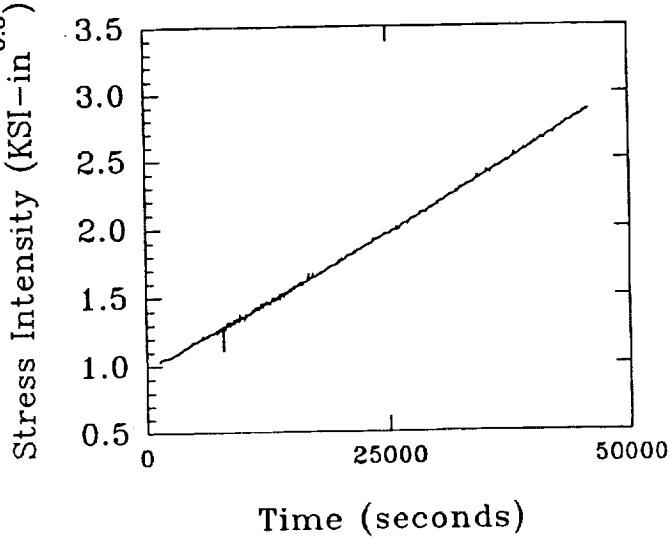

Project #5 Hydrogen Interactions in Aluminum-Lithium Alloy 2090 and Selected Model Alloys

S.W. Smith and J.R. Scully

Objective

The goal of this project is to develop a fundamental understanding of the effects of internal lattice and trapped hydrogen on the mechanical properties of selected Al-Li-Cu-X alloys. The present program focuses on unrecrystallized alloy 2090, recrystallized Al-Cu-Li-Zr alloys of varying grain size, and complimentary model alloys. We propose to (a) distinguish HEAC from aqueous dissolution controlled EAC, (b) correlate hydrogen induced EAC with mobile and trapped hydrogen concentrations, and (c) identify significant trap sites and hydride phases (if any) through utilization of model alloys and phases. The specific objectives for 1994 are discussed below.

Background and Problem Statement

The effect of absorbed hydrogen on the mechanical properties of Al-Li-Cu-X alloys is not fully understood. Deterministic models defining the relationship between fracture initiation toughness and internal hydrogen concentration are lacking. Recent work, however, has implicated an important role for hydrogen in these alloys. For Al-Li-Cu alloys intergranular, intersubgranular, and transgranular environmentally assisted cracking paths in aqueous solutions have been attributed to boundary T_1 dissolution,[1] T_1 dissolution with hydrogen uptake,[2] $AlLiH_4$ formation and cracking,[3,4] and hydrogen embrittlement.[5] An understanding of which of these metallurgical factors or others control hydrogen assisted cracking have not been clearly defined. Consequently, feedback on alloy design or thermomechanical processing which would enable greater resistance to hydrogen cracking is not available. The information developed here will provide diagnostic procedures for obtaining such information and a deterministic framework which will be useful for understanding the effects of internal hydrogen on ambient and

cryogenic temperature mechanical properties for emerging Al-Li-Cu-X alloys.

The methodologies developed will also be extendable to aluminum based materials under Advanced Metal Subsonic initiatives as well as High Speed Civil Transport Materials such as AA 2519, RX 818 or others. These alloys are of particular interest due to the possibility of detrimental boundary precipitation as a result of long-term thermal exposure. It is anticipated that a follow-up program proposed for 1995 will re-focus on one of these materials. The present study will continue to focus on conventional alloy 2090 sheet and complimentary model alloys. The development of a comprehensive understanding of the role hydrogen plays in these materials will aid several technological areas of interest to NASA. These include current applications for Al-Li-Cu alloys as well as the lifetime and reliability of aging aircraft. Even in the case of aqueous exposure, absorbed hydrogen may be a contributory if not dominant factor in the SCC of alloy 2090.[2]

Several problems are encountered when performing traditional hydrogen embrittlement tests on aluminum base alloys, thereby, making it impossible to unambiguously define the influence of hydrogen on mechanical properties such as ductility and fracture toughness. Three major problems, which have impeded progress have been identified in the literature.[6] These are: (i) intergranular and inter-subgranular fracture in Al-Li-Cu alloys when tested in the ST orientation in air or vacuum make it difficult to readily detect hydrogen induced fracture based on straight forward changes in fractography, (ii) the inherently low hydrogen diffusivity and solubility in Al alloys is further compounded by a native oxide which acts as a hydrogen permeation barrier; these factors complicate hydrogen, ingress, detection and quantification, and (iii) hydrogen effects are masked by dissolution assisted processes associated with T_1 precipitates on subgrain boundaries or concurrently with Cu depletion on such boundaries when mechanical testing is performed in aqueous solutions.

This project has been developed in a manner which will make it possible to circumvent these experimental barriers and develop a better understanding of the role hydrogen plays than that which is available in the

present literature. We also believe that information will emerge regarding hydrogen interactions in these alloys that will be relevant to HEAC in aqueous environments as well as for the cryogenic storage of hydrogen. Our goals will be accomplished by studying hydrogen uptake and the effect of hydrogen on mechanical behavior as non-competitive processes. The methods by which this will be performed, the results to date and the status of this project are reviewed below.

Technical Approach:

The research underway is separated into three major phases (a) hydrogen analysis of electrochemically pre-charged samples, (b) examination of mechanical properties (tensile properties and fracture toughness) under the influence of internal lattice and trapped hydrogen, and (c) correlation of hydrogen trapping with mechanical properties and fractography. The present report will document the results from thermal desorption spectroscopy experiments conducted over the last 2-3 quarters. Other aspects of the program are only briefly summarized and the reader is referred to previous reports.

Achieving internal hydrogen concentrations

Previous NASA reports document the procedures used to achieve internal hydrogen concentrations under conditions which are decoupled from aqueous dissolution.[7-10]

Internal hydrogen analysis

Thermal desorption spectroscopy will be emphasized as the primary method for performing hydrogen analyses in Al base alloys. Over the last reporting period research has been conducted on the analysis of absorbed hydrogen with the use of thermal desorption spectroscopy (TDS) and the effects of absorbed hydrogen on the mechanical properties of alloy 2090.[10] The TDS system that we have constructed is capable of reaching hydrogen partial pressure below 1×10^{-9} torr and uses a quadrupole mass spectrometer capable of distinguishing hydrogen from other desorbed gases.[9,10] Progress in the last 2-3 quarters has focused on hydrogen analysis of unrecrystallized

AA2090 sheet and several recrystallized Al-Li-Cu-Zr alloys.[10-11] In a previous report, the method has been used to examine hydrogen levels and hydrogen mobility at elevated temperature in AA 8009.[11]

Mechanical Testing and Fractography

Mechanical tests is being performed on hydrogen charged and uncharged materials in three different tempers (T3, UA - T3+5 hrs @ 160°C and PA - T3+25 hrs @ 160°C conditions), TL and LT orientations, as well as four unique microstructures.[10] The alloys studied consisted of one commercially available unrecrystallized sheet product (AA2090) and three model recrystallized sheet products of varying grain size. Continuous extension rate testing of smooth and notched specimens is performed on the unrecrystallized AA 2090 material after determining a high degree of susceptibility at 2.5×10^{-6} sec^{-1} engineering strain rate.[8] J-integral resistance curve testing has been performed on all four of the alloys in the three tempers described above using methods in accordance with ASTM standard E-813. These results are documented in previous NASA progress reports.[9-11] In general, hydrogen assisted cracking is observed in the UA condition when high angle boundaries are favorably oriented with respect to the applied tensile stress. Similar results are found in the PA condition except that fracture toughness in air is degraded and the preferred fracture path is already intergranular even before hydrogen is introduced.

Progress during reporting period

Thermal desorption spectroscopy tests have been conducted on pre-charged high purity aluminum, commercial unrecrystallized 2090 in the T3, UA and PA conditions as well as fine and coarse grain recrystallized Al-Li-Cu-Zr alloys in the UA and PA conditions. Preliminary results on pure aluminum have shown the presence of several trapping states excluding surface and mobile lattice hydrogen.[10] Throughout the last reporting period, research has concentrated on TDS of AA 2090.

Figure 1 illustrates a desorption spectra for AA 2090 in the T3 ageing condition, performed at a constant thermal ramp rate of 5°C/min. Five

separate desorption maxima have been identified on this plot. Although the trap states identified as 1 and 5 do not show as easily identifiable peaks since they are masked by peaks 2 and 4 respectively, one can notice a definite deflection in the curve at these points. This curve does not clearly identify peak 5, since it is very close to the maximum temperature obtained during the test, however it will become obvious in other data that there must be at least two separate trap sites contributing to the broad desorption curve formed by the overlap of sites 4 and 5.

In order to determine the binding energy of these trap sites, desorption analysis must be conducted at several different ramp rates. Figure 2 shows the results of desorption analysis performed at 5, 7.5 and 10°C/min, on AA 2090-T3 specimens that were pre-charged under identical conditions. As expected, the desorption maxima for each trap site is shifted to higher temperatures at faster thermal ramp rates. Moreover, the five trap sites can be identified in all three of these plots, with the exception of peak 5 in the 10°C/min test, since this experiment was not continued to a high enough temperature in order to clearly identify this trap state. However, the test performed at 7.5°C/min clearly shows the broadening of the curve produced by the total desorption of hydrogen from trap states 4 and 5. While approximate binding energies for these trap states can be calculated, the temperature at which the maximum desorption rate is produced for states 1, 2, 4 and 5 is not precisely known at this point. This is due to the fact that the results obtained are for the total desorption rate for all the states, for instance the actual maximum for state 4 may be at lower temperatures than identified, since there is some desorption of hydrogen from state 5 present at the maximum desorption rate for state 4. In order to get a precise evaluation of the binding energies of these trap sites, each site has to be identified and isolated or the overlapping desorption fields must be resolved better.

Thermal desorption analysis of AA 2090-UA, has also been performed to identify any changes in trapping characteristics with aging. Figure 3 shows a desorption spectra for a pre-charged specimen that was tested at a thermal

ramp rate of 5°C/min. There are 7 possible trapping states identified on this desorption curve. As in the case of the tests conducted on AA 2090-T3, several of the maxima overlap one another. Figure 4 shows desorption maxima for three AA precharged 2090-UA specimens tested at ramp rates of 2, 5, and 10°C/min. As with Figure 2, all the peaks are shifted to higher temperatures as the ramp rate is increased, however, the peaks can be identified in all of the plots. In addition to shifting the temperature for maximum desorption to higher temperatures for faster ramp rates, it becomes increasingly more difficult to resolve desorption maxima at fast ramp rates, as can be seen with peaks 3 and 4 as well as 5, 6 and 7 on the desorption curve for 10°C/min.

Results presented in previous reports[9,10] have shown that the susceptibility to hydrogen assisted cracking is strongly dependent upon aging condition. For this reason we have been trying to identify differences in hydrogen trapping characteristics as a function of aging time. Figure 5 shows desorption spectra for AA 2090 in the T3, UA and PA conditions. These samples were pre-charged under identical conditions (28 days cathodic polarization, sputter deposited Ni coating) and examined by TDS with the same temperature profile.

The spectra shows that AA 2090 in the T3 and UA conditions appear to have the same physical trapping states but that hydrogen partitioning is very different in the underaged condition. This difference in trapping behavior is most noticeable in the peaks marked 3 and 4. As previously shown the medium temperature peak is comprised of two trapping states (3, 4) for UA specimens while there appears to be only one trapping state for the T3 case. The trapping state labelled as 4 on the T3 and PA conditions is also present in the UA material, however, there is an additional state labelled as 3 which is overlapping this state to produce a desorption maxima that is the summed effect of these two trapping states. The downward slope for the UA material produced by the 3 and 4 trap sites curve is nearly identical to the downward slope on the curves for the T3 and PA material. This data shows the trap state identified as peak 3 in the UA material is not a significant trapping state

for AA 2090 in the T3 and PA conditions. One explanation for such a trapping state would be the presence of a coherent particle/matrix interface such as δ'. The δ' interface area is small in the T3 condition, maximized in the UA condition and decreases in the PA condition due to coarsening even though it remains coherent with ageing.[12] Hopefully, this explanation can be confirmed with the utilization of Al-Li binary alloys.

The next obvious difference in trapping behavior with these three aging conditions can be seen in the peaks identified as 1 and 2. The most noticeable feature of the curve created from trapping states 1 and 2 is that the area under the curve for the material in the T3 condition is much larger than for the other two materials, with the UA materials appearing to be slightly greater than the PA material. This trend is consistent with the notion that lithium in solid solution provides a weak trap site for hydrogen and that the number of sites of this nature decrease with aging. Hopefully, this explanation can also be confirmed with the utilization of Al-Li binary alloys. It is also observed that trapping state 2 possesses a higher binding energy for the T3 and PA material than in the UA condition. Although this may actually be the case, one possible explanation for this apparent shift in state 2 is due to overlap from state 1 in the UA case. In addition to a significant overlap between state 1 and 2, there is also a significant overlap between states 2 and 3 in the UA alloy, which further complicates the identification of the desorption maxima for state 2.

In order to distinguish the hydrogen trapping characteristics of high and low angle grain boundaries, TDS is also being performed on recrystallized Al-Li-Cu-Zr alloys. Figure 6 shows desorption spectra for commercial AA 2090, fine grain recrystallized and coarse grain recrystallized Al-Li-Cu-Zr all in the UA condition and tested with the same temperature profile. The hydrogen trapping behavior of these three alloys appears to be very similar, however, there has been insufficient testing on the recrystallized alloys to this point to draw any conclusions about possible differences in the hydrogen trapping behavior of the materials.

Conclusions

1) The hydrogen trapping state labelled as state 3 in Figure 3, 4 and 5 is minimized in the T3 and PA aging conditions, but is a significant trap site in the UA condition. This trapping state is affected by aging. Therefore we hypothesize that it may be representative of a coherent matrix/particle interface. Trapping state 3 could represent the coherent interface associated with the δ′ precipitate. The interfacial area of coherent δ′ is maximized in the UA condition and although there may still be some trapping of hydrogen at the δ′ interface in the T3 and PA conditions, the total interface area available would be greatly reduced and therefore the presence of this trap state may be masked by other features in the T3 and PA desorption spectra.

2) The area under the curve generated by trapping states 1 and 2 is maximized for the T3 condition and is much lower for the UA and PA conditions. It is possible that this behavior explains the increased hydrogen solubility correlated with lithium in solid solution in Li containing aluminum alloys.[13] In the T3 condition there is a significant amount of lithium within the aluminum matrix, thereby increasing the quantity of hydrogen that is soluble within the matrix relative to high purity Al. As AA 2090 is aged, matrix lithium is depleted, reducing the hydrogen concentration observed at low energy point defect sites.

Proposed research plan for the next reporting period

Research during the next reporting period will again focus on achieving parallel progress in three areas:

(1) Fracture mechanics testing of hydrogen pre-charged specimens using the J-integral R curve approach coupled with a limited number of slow strain specimens

(2) Fractographic analysis.

(3) Hydrogen analysis by thermal desorption spectroscopy with complementary hardness testing to examine possible aging during TDS

experiments.

J-integral hydrogen assisted fracture initiation data must be duplicated in the UA and PA tempers in the various orientations and performed for AA2090 in the T3 temper. In an attempt to obtain higher hydrogen concentrations in the compact tension specimens, potentiostatic charging will be performed at higher cathodic overpotentials. Longer charging time periods will also be explored to ensure uniform internal hydrogen concentration profiles. Under a limited number of conditions, the effect of load line displacement rate on fracture toughness will be investigated. Total hydrogen levels for these tests will be evaluated with the use of the TDS system. A major goal will be to try to identify the trapping states observed and correlate them with microstructural features present in these materials. Model binary Al-Cu and Al-Li alloys will aid in achieving this goal.

References

1. R.G.Buchheit, J.P.Moran and G.E.Stoner, Corrosion, Vol. 46, pp. 610-617, 1990.

2. E.I.Meletis, W.Huang, Mater.Sci. and Eng., Al48, P.197, 1991.

3. R.Balasubramaniam, D.J.Duquette, K.Rajan, Acta.Met., 39, pp. 2597-2605, 1991.

4. R.Balasubramaniam, D.J.Duquette, K.Rajan, Acta.Met., 39, pp. 2607-2613, 1991.

5. R.S.Piascik and R.P.Gangloff, Metall. Trans. A, in review.

6. T.D.Burleigh, Corrosion, Vol. 47, pp. 89-98, 1991.

7. S.W.Smith, J.R.Scully, "NASA-Uva Light Aerospace Alloy and Structures Technology Program," U.Va. Report No. UVA/528266/MS92/111, January 30, 1992.

8. S.W.Smith, J.R.Scully, "NASA-UVa Light Aerospace Alloy and Structures Technology Program," U.Va. Report No. UVA/528266/MS93/111, July 1992.

9. S.W.Smith, J.R.Scully, "NASA-UVa Light Aerospace Alloy and Structures Technology Program," U.Va. Report No. UVA/528266/MS93/112, March 1993.

10. S.W.Smith,J.R.Scully, "NASA-UVa Light Aerospace Alloy and Structures Technology Program," U.Va. Report No. UVA/528266/MS94/113, July 1993.

11. S.W.Smith, J.R.Scully, "NASA-UVa Light Aerospace Alloy and Structures Technology Program," SEAS Proposal No. MSE-NASA/LaRC-6074-94, November 1993.

12. J.R. Davis ed., *Aluminum and Aluminum Alloys,* ASM International, Materials Park, OH, 1993, pp. 122-123.

13. P.N. Anyalebechi, D.E.J. Talbot and D.A. Granger, *Light-Weight Alloys for Aerospace Applications,* E.W. Lee, E.H. Chia, and N.J. Kim eds. TMS, 1982, pp. 249-268.

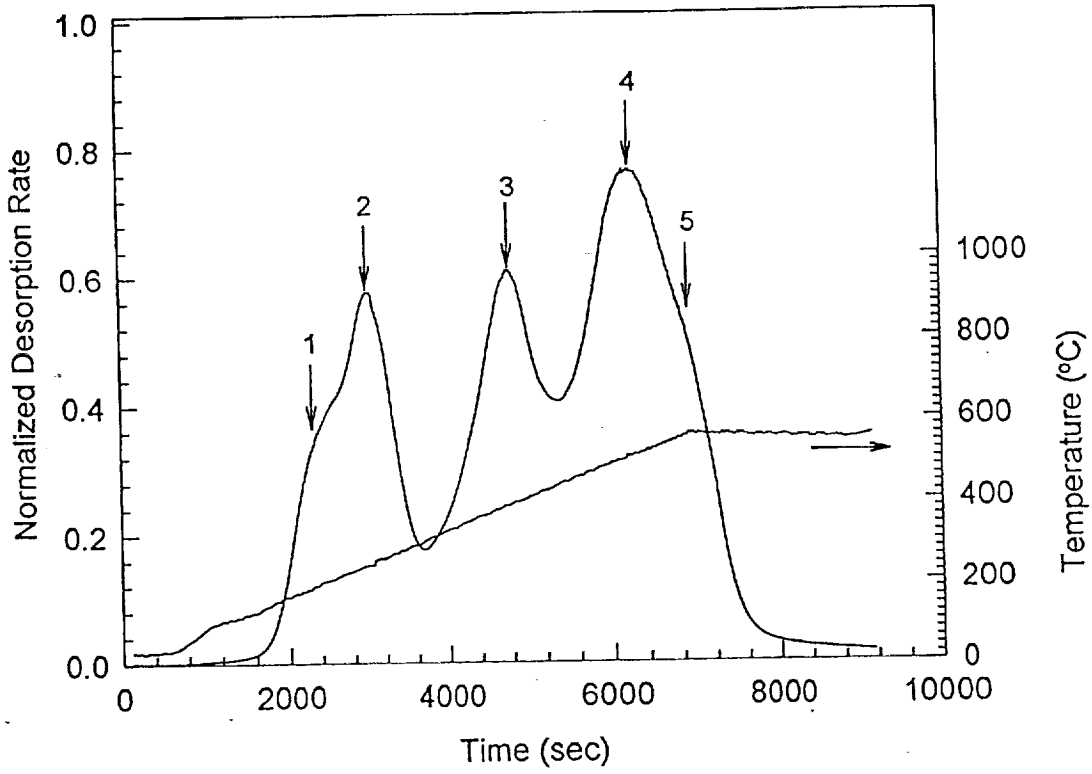

Figure 1. Desorption spectra for a pre-charged AA 2090 - T3 specimen, tested at 5°C/min.

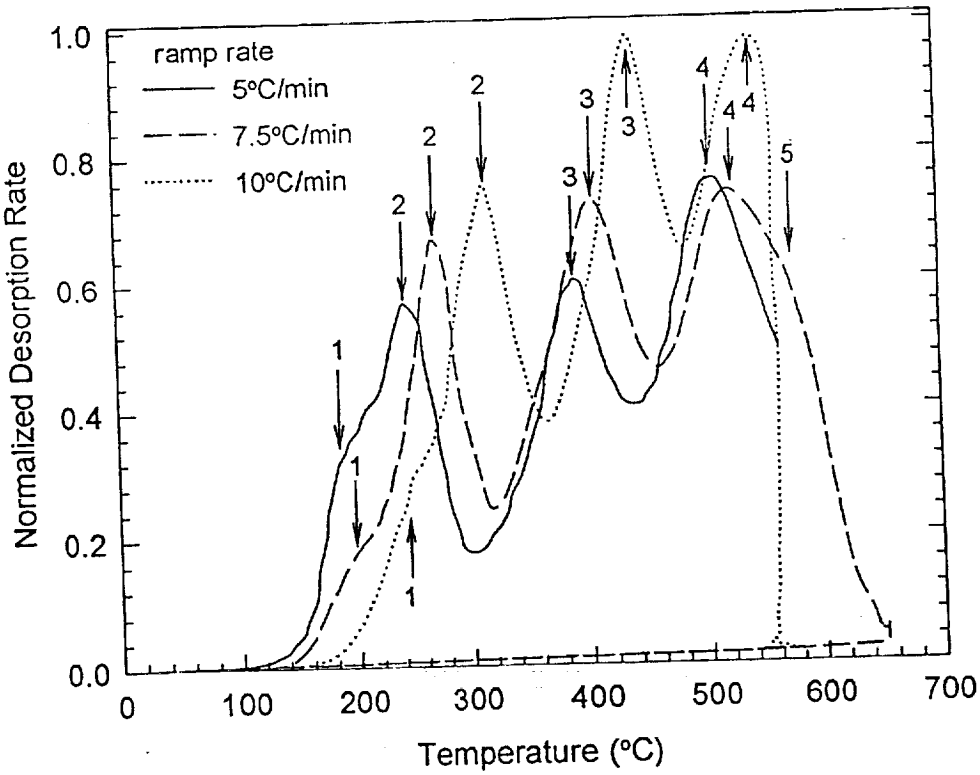

Figure 2. Desorption spectra for three pre-charged AA 2090 - T3 specimens, tested at 5, 7.5 and 10°C/min.

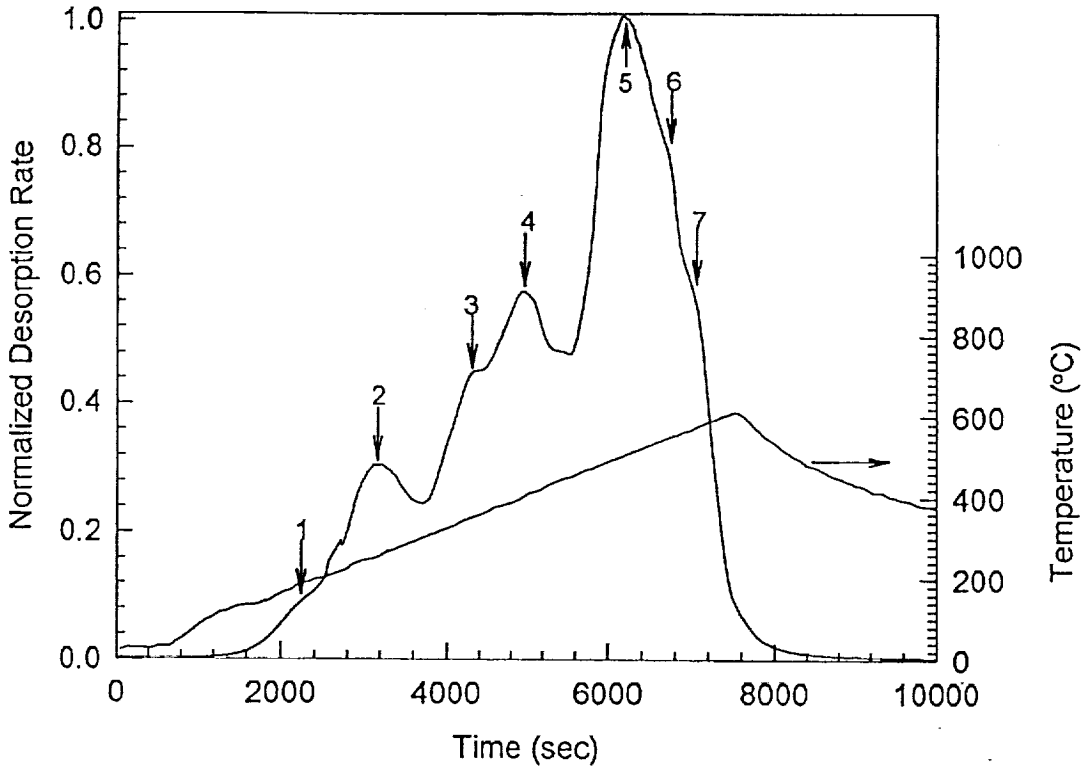

Figure 3. Desorption spectra for a pre-charged AA 2090 - UA specimen, tested at 5°C/min.

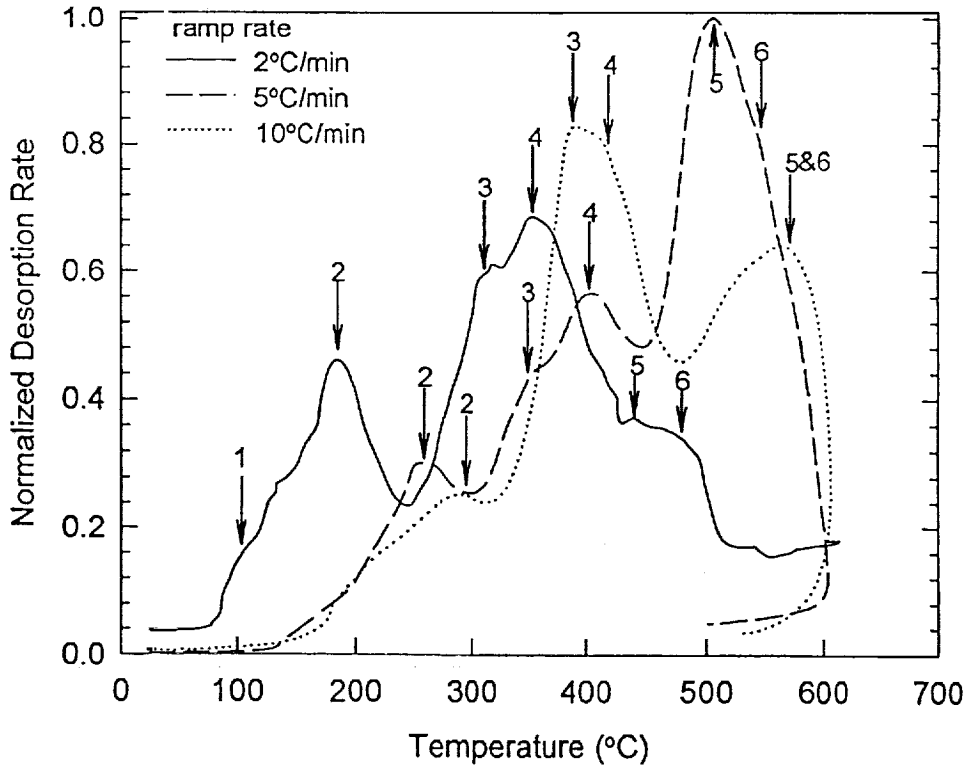

Figure 4. Desorption spectra for three pre-charged AA 2090 - UA specimens, tested at 2, 5 and 10°C/min.

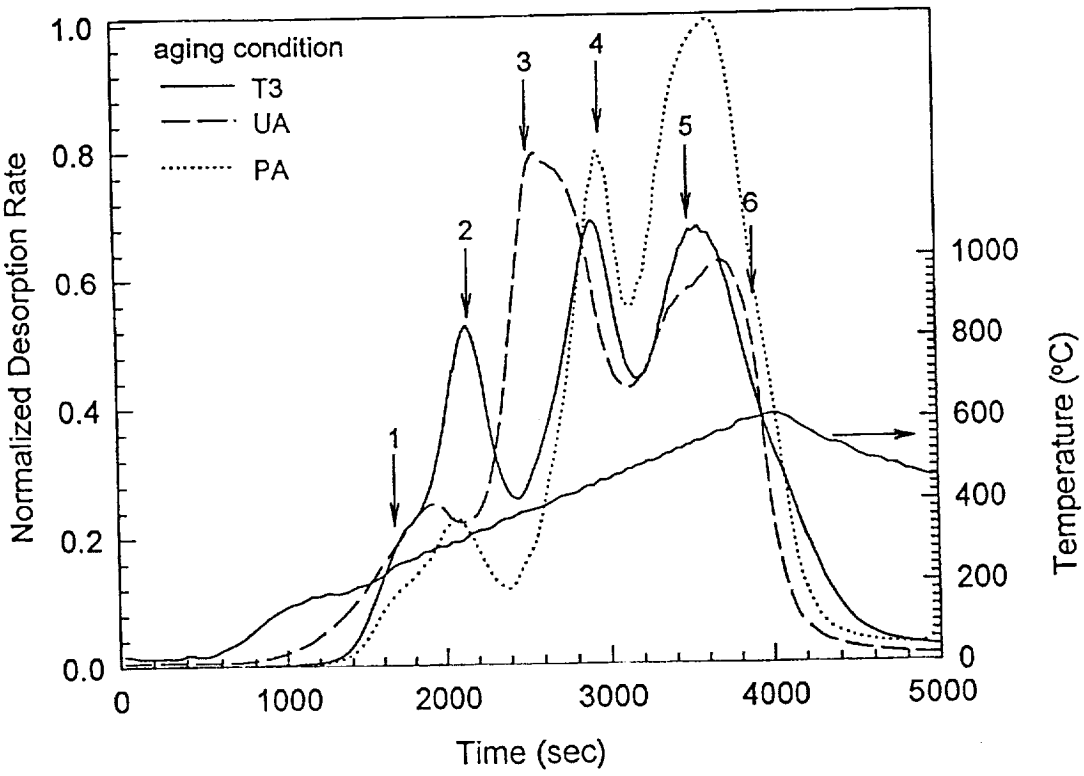

Figure 5. Desorption spectra for three pre-charged AA 2090 specimens aged to a T3, UA (T3 + 5 hrs. @ 160°C) and PA (T3 + 25 hrs. @ 160°C), tested at 10°C/min.

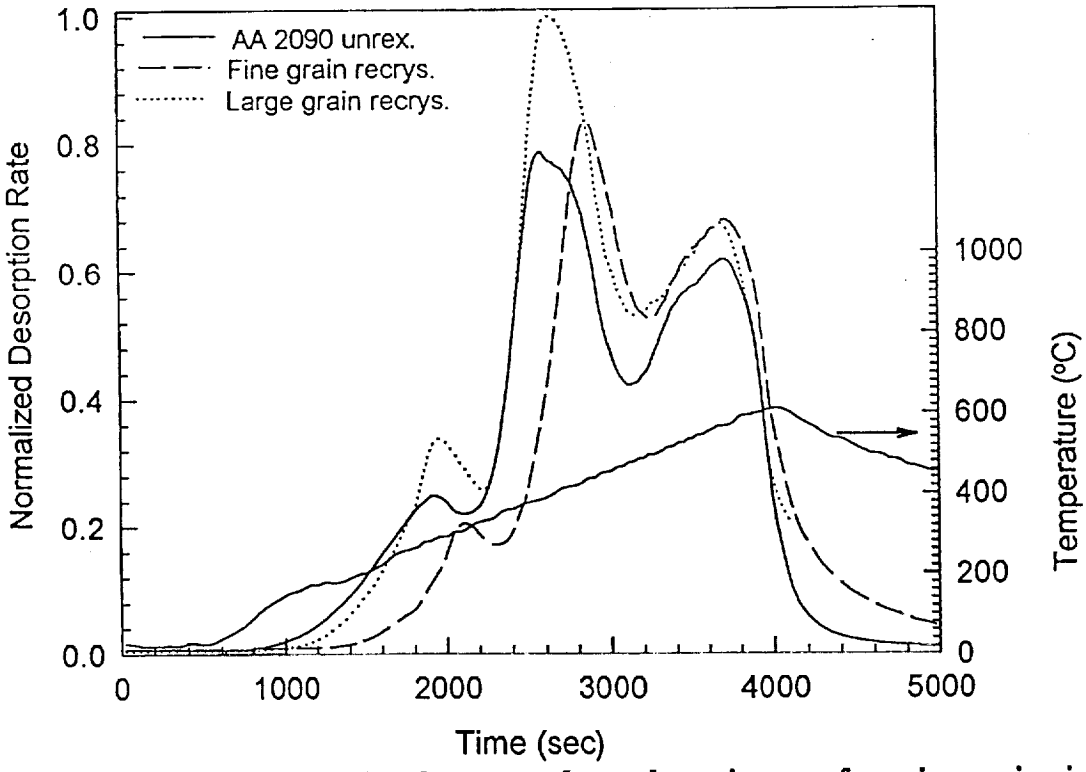

Figure 6. Desorption spectra for three pre-charged specimens of varying grain sizes in the UA condition, tested at 10°C/min.

Project #6 Metastable Pitting of Al Alloys in Halide Solutions

S.T. Pride and J.R. Scully

Background and Problem Statement

Pitting corrosion has a number of detrimental effects on structural aluminum base materials. These include creation of sites of stress concentration and localized occluded cell chemistry which, in turn, can lead to conditions favorable towards environmentally assisted cracking or fatigue[1,2,3]. One critical issue concerning aircraft aging is the pit size and shape required to initiate fatigue, intergranular corrosion, or stress corrosion cracking. This program addresses pitting phenomena in Al base alloys containing copper. In the case of aged Al-Cu binary alloys, pitting is induced by galvanic coupling between the q-Al_2Cu phase and the aluminum rich (copper depleted) matrix or grain boundary zone[3,4,5]. Similarly, pitting in AA2024 initiates at Cu depleted grain boundaries adjacent to S' (Al_2CuMg) precipitates. Thus, the underlying phenomena associated with model Al and Al-Cu materials should be extendable to more relevant structural alloys such as AA2024.

It is well established that metastable pits form at potentials below the pitting potential[4-8]. However, these pits are believed to repassivate when the oxide remnant covering the pit mouth ruptures either due to hydrogen evolution[9,10], structural instability as the pit mouth widens[6], or osmotic pressure[8]. Hence, metastable pits have a low probability of surviving for long time periods. Pits which initiate near or above the pitting potential associated with the stabilization of pit growth have a higher probability of growing for extended periods of time and of sustaining growth to large sizes even after the oxide cover ruptures[6].

Most laboratory studies cited in the literature focus on stable pit propagation and growth at high positive potentials[9-12]. Consequently, little is understood about pit nucleation and the electrochemical factors responsible for stabilizing pit growth as a result of the galvanic cell formed

by microstructural heterogeneities. For instance, electrochemical factors that control pit initiation and growth processes, especially those that govern the transition from metastable to stable pit growth, remain unclear. What are the criteria for pit stabilization? Additionally, little is known about the dynamics of the pit initiation and growth process. Is pit initiation stochastic in nature with each pitting event unrelated to those events occurring before and afterwards, or is initiation and stabilization of pits spatially or temporally dependent on the "progress" or "feedback" from other pit sites? To obtain possible answers to these questions various electrochemical techniques are used to examine pitting in pure Al, model bulk Al-Cu alloys, and Al-Cu alloy thin films. The issue of whether pitting events occur randomly or are somehow correlated will be subjected to thorough mathematical analysis. Analysis of pit transients is achieved through examination of (a) the applied current versus time record obtained at constant applied potential, or (b) both the galvanic potential and galvanic current versus time records acquired from two identical Al-Cu electrodes. More recently developed electrochemical methods based on the techniques of non-linear (chaos) dynamics will be employed in addition to more tradition approaches (electrochemical, spectral, statistical) to analyze these time records.

Objectives

The goal of the program is to improve the fundamental understanding of pitting nucleation and growth phenomena in Al alloy systems. Emphasis is placed on understanding electrochemical factors controlling the nucleation, propagation, and repassivation of pit sites in model Al alloys. To accomplish these goals conventional electrochemical analysis methods have been augmented with statistical, spectral, and chaos dynamics analyses methods suitable for characterizing the electrochemical voltage and current transients observed as a function of time that are associated with metastable pitting. To date, pitting on artificially aged Al-Cu alloys has been investigated and analyzed electrochemically. The goal for 1994 will be to concentrate more on the analyses of the metastable pitting transients with statistical, spectral,

auto-correlation and non-linear dynamic methods.

Technical Approach

Materials

Pure Al and Al-2%Cu have been emphasized as a model alloy to study metastable pitting. This binary alloy (made from 99.999% Al and 99.999% Cu) will provide a simpler system to study rather than commercial grade aluminum alloys. Bulk and thin film (0.8μm) Al-2%Cu alloys are used in this project. The thin film restricts pit dimensions in the direction perpendicular to the metal surface and provides a means to investigate the role of pit depth on factors possibly controlling pit growth and repassivation (such as ohmic and mass transport control). Preparation and properties of the thin films are described elsewhere[4,5]. In the case of thin films, non-isothermal heating and cooling of the thin film occurs during the sputter deposition process and aging conditions are not well defined. However, theta phase precipitates are observed in TEM studies[4,5]. The aging conditions for the bulk Al-2%Cu are i) held at 510° C for 2 hours to completely dissolve the Cu into the Al matrix, ii) quenched to room temperature, and iii) held at 246° C for 24 hours to form θ-Al_2Cu phase at the grain boundaries.

Results

Prior results concerning electrochemical analyses of metastable pitting of pure Al:

In prior work documented in the March and July Progress reports, constant potential experiments were conducted on high purity Al wire electrodes. Pure Al wire electrodes (99.999%, 0.25mm dia.) were used to simulate the Cu depleted grain boundary zone of the aged alloy containing equilibrium θ-Al_2Cu precipitates. Applied potentials were chosen which simulated galvanic coupling to theta phase precipitates. A large population of pit events were examined and compared to pits which achieved stabilization. As a diagnostic, chromate and nitrate inhibitors were added. From this work, the following conclusions were reached.

1. There is a distribution of pitting potentials due to the distribution of metastable pit current densities and pit current rise times for a population of metastable pits observed at any given potential within the range of pitting potentials observed.
2. The cumulative number of metastable pitting events increases with applied potential at fixed Cl^- concentration and increasing Cl^- at fixed applied potential.
3. At potentials below the pitting potential range, a gradual increase in initiation rate of metastable pitting per unit time is first observed suggesting an incubation process. This trend is followed by an exponential decay with exposure time once a maxima in the rate is achieved. This suggests that defects sites that are the most prone to pit initiation are gradually depleted.
4. Apparent metastable pit dissolution current densities at peak pit current ranged from 0.05 A/cm^2 to 10 A/cm^2.
5. Dissolution current densities for stable pits ranged from 1 A/cm^2 to 10 A/cm^2 with much larger apparent pit radii formed for time periods approximately equal to metastable pits life times.
6. Possible explanations for stabilization of a pit are a combination of anodic current densities considerably larger than 1 A/cm^2, high pit growth rates with time such that the product of pit current density and pit radius is greater than > 10^{-2} A/cm suggesting a fast rise in pit current with time, and a re-entrant pit geometry or initiation within a repassivated pit site.
7. Chromate and nitrate inhibitors operate in a number of ways to suppress pit stabilization. Among the beneficial influences of such aqueous inhibitors: Inhibitors decrease the metastable pit nucleation rate at a given potential and Cl^- concentration, which minimizes the chance for pit stabilization. This effect can be attributed to either incorporation of the inhibitor into the passive film or competitive adsorption with Cl^- for defect sites in the passive oxide. Inhibitors also minimize pit growth rates so that the criteria 10^{-2} A/cm is difficult to

attain. The exact role of the inhibitor during propagation is less certain. Competitive adsorption with Cl^- on bare Al, supporting electrolyte effects, or alteration of the potential of zero charge of the bare Al surface in the pit are possible ways in which the inhibitor ion may act.

8. CrO_4^{-2} was not found to improve the apparent rate of repassivation of metastable pits once formed.

Results during the reporting period

Emphasis during the past reporting period was placed on spectral, statistical and chaos dynamics analysis of galvanic current and potential time records obtained from galvanically coupled aged Al-2%Cu. The galvanic couple configuration was favored because the net galvanic current in the absence of metastable pitting transients was stationary over long time periods. This result is important when one seeks to utilize chaos analysis methods such as attractor reconstruction or next maxima analysis. Secondly, sampling frequency of 1000 Hz was found to be necessary in order to properly conduct next maxima analysis. Earlier results (July 93 Progress report) were repeated at this faster sampling frequency. Preliminary results at this greater sampling rate are discussed

Galvanic coupling experiments were conducted using two identical Al-2%Cu samples in deaerated NaCl solutions. The experiment setup consisted of a zero resistance ammeter (ZRA) to measure the current flow between the electrodes and a voltage follower to measure the open circuit potential (OCP) verses a saturated calomel electrode (SCE). Figure 1 shows the current (a) and the corresponding OCP (b) transients associated metastable pitting of bulk Al-2%Cu in 10^{-2}M NaCl. Expanded segments of these two time series illustrated the characteristic forms of the current and potential fluctuations (Figure 2). Note that a strong correlate exists between current transients and potential transients. Since both of the Al-2%Cu samples can undergo metastable pitting, the current fluctuations can occur in both the positive and negative directions with fast absolute increases in the currents and slower returns to the baseline current. However, the corresponding OCP fluctuations have the

typical form of rapid decrease in potential and a slow return to the baseline potential which occurs when either of the samples experiences metastable pitting.

These Al-2%Cu alloys can also undergo intergranular corrosion (igc). This only occurs at higher Cl^- concentrations and after the alloys have experienced metastable pitting for a period of time. Figure 3 show the current and OCP transient behaviors for galvanic coupled bulk Al-2%Cu which experience metastable pitting for the first 150 seconds (labeled metastable pitting on this figure) and then around 350 seconds it is believed that one of the samples begins to corrode intergranularly (labeled igc on this figure). The igc lasted about 200 seconds before the sample repassivated. Each time the latter continual transient behaviors were observed igc was found after the experiments by optical microscopy. In the cases where igc was not observed by microscopy the second type of current and OCP transient behavior was also not observed.

Galvanic coupling experiments were performed using thin films (~1 μm thickness) in order to study the effect of limited growth depth on metastable pitting and also to increase the uniformity of test samples. The thins films have mirror like finishes as received and therefore do not require polishing as the bulk materials do. Thus the thins films are likely to be more uniform from sample to sample than the bulk alloys which have been abrasively polished. The thin films do appear to more resistance to metastable pitting than bulk alloys. The reason for the thin films being more resistance to metastable pitting is not understood at this time. The thin films seem to undergo significant amounts of metastable pitting only at high Cl^- concentrations (1M to 1.5M) as can be seen in the cumulative number of metastable pitting event per unit area plot (Figure 4).

Some of the samples were imaged by SEM after the current transients were collected to verify that the each current transient corresponded to an individual metastable pitting event. Good agreement was found between number of current transients and the number of metastable pits found on the surfaces at a magnification of 1000X. Also the range pit sizes calculated from

the current transient were in good agreement with the range of sizes determined from the images. The sizes obtained from the images were slightly larger than the current transient sizes as expected due to addition current supplied by the formation of H_2 (see earlier report).

Proposed Research Plan for 1994

In 1994 a greater emphasis will be placed on conducting galvanic couple experiments. Both bulk Al-2%Cu and Al-2%Cu thin films will be examined. There will also be a greater focus on applying statistical, spectral, and chaos dynamics techniques to analyze the pitting transients obtained from this experiment. It is expected that Sheldon Pride will complete laboratory experiments and spend a large portion of time applying these analysis methods as well as writing a Ph.D. dissertation.

References

1. K. Urushino and K. Sugimoto, Corrosion Science, 225, 19 (1979).

2. K. Sugimoto, K. Hoshino, M. Kageyama, S. Kageyama, and Y. Sawada, Corrosion Science, 709,15 (1975).

3. J.R. Galvele and S.M. DE Micheli, Corrosion Science, 795,10 (1970).

4. J.R. Scully, R.P. Frankenthal, K.J. Hanson, D.J. Siconolfi, and J.D. Sinclair, J. Electrochem. Soc., 137, 1365 (1990).

5. J.R. Scully, "Proceedings of the Symposium on Critical Factors in Localized Corrosion", G.S. Frankel and R.C. Newman, Editors,144, Vol.92-9, 1992.

6. D.E. Williams, J. Stewart, and P.H. Balkwill, "Proceedings of the Symposium on Critical Factors in Localized Corrosion", G.S. Frankel and R.C. Newman, Editors, 36, Vol.92-9, 1992.

7. R. Holliger and H. Bohni,"Proceedings of the Symposium on Computer Aided Acquisition and Analysis of Corrosion Data", M.W. Kendig, U. Bertocci, and J. Strutt, Editors, ECS PV 85-3, 200- 209 (1985).

8. P.C. Pistorius and G.T. Burstein, "Concerning the Nature of Pitting as Studied by The Examination of Current Transients," In Proceedings of the 5th International Conference of the South African Corrosion Institute, Johannesburg, South Africa, August 1990.

9. T. Hagyard and J.R. Santhiapillai, J. Appl. Chem., 323, 9 (1959).

10. G.S. Frankel, Corrosion Science, 30(12), 1203- 1218, (1990).

11. H. Kaesche, "Localized Corrosion", R.W. Staehle, B.F. Brown, J. Kruger, (1974).

12. F. Hunkeler and H. Bohni, Corrosion, 37(11), 645-650, (1981).

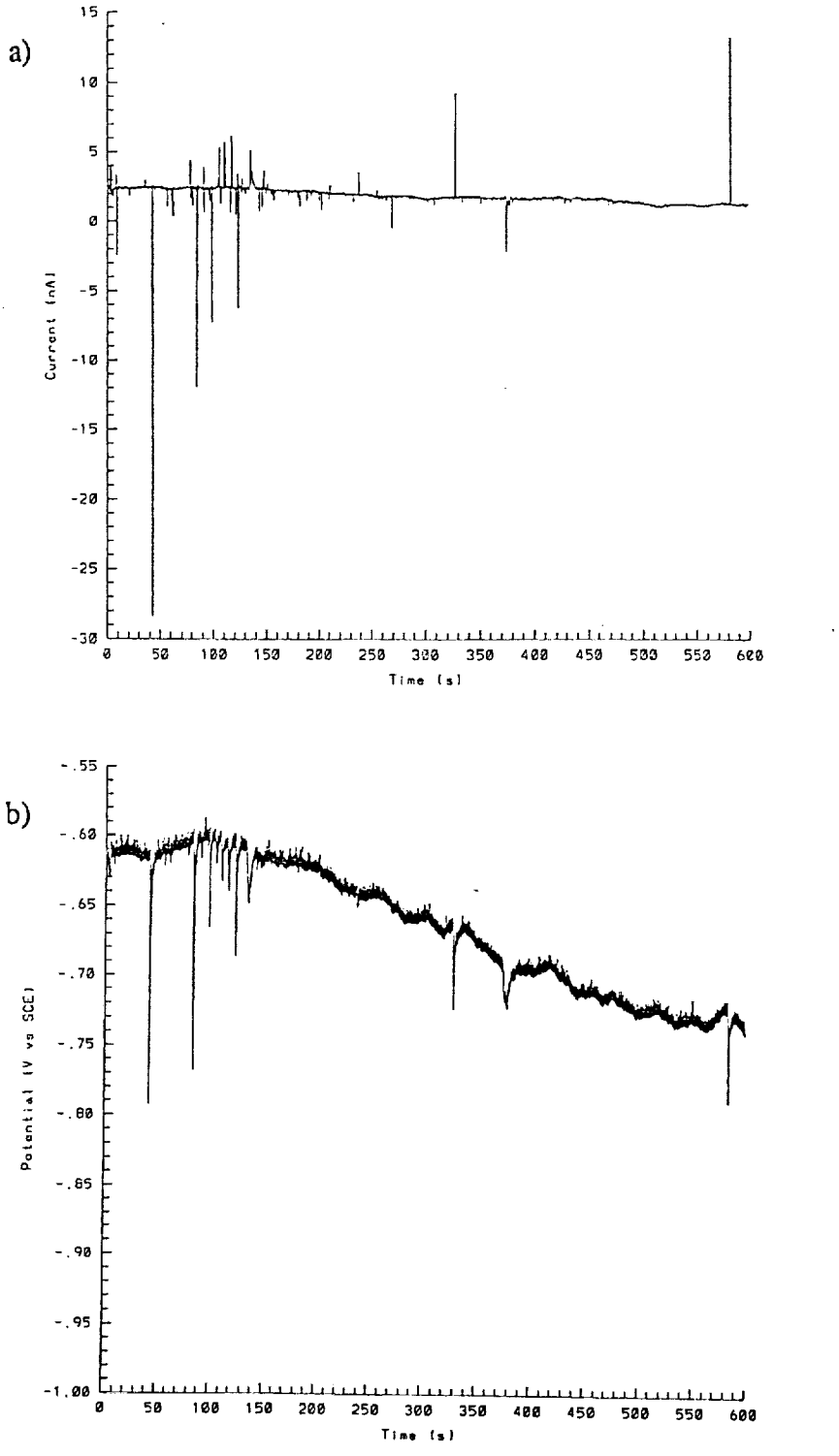

Figure 1: Time series showing current transient (a) and the corresponding OCP transient (b) behaviors associated with metastable pitting of two identical galvanic coupled bulk Al-2%Cu samples in deaerated 10^{-2}M NaCl solution. Exposed areas = 0.002cm^2.

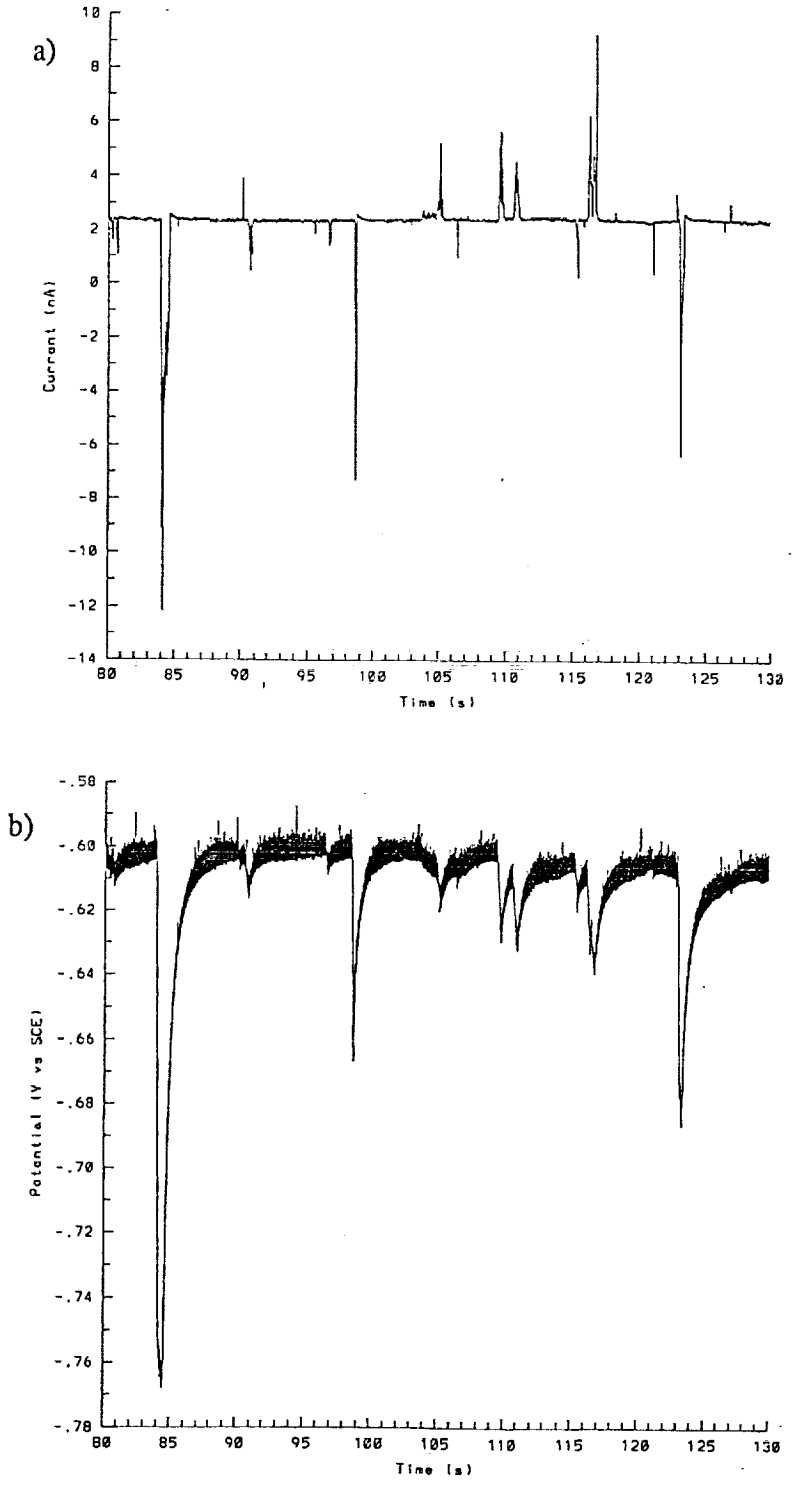

Figure 2: Sections of the time series shown Figure 1a and b showing the correlation between the current transients and the OCP transients. (a) - current, (b) - OCP.

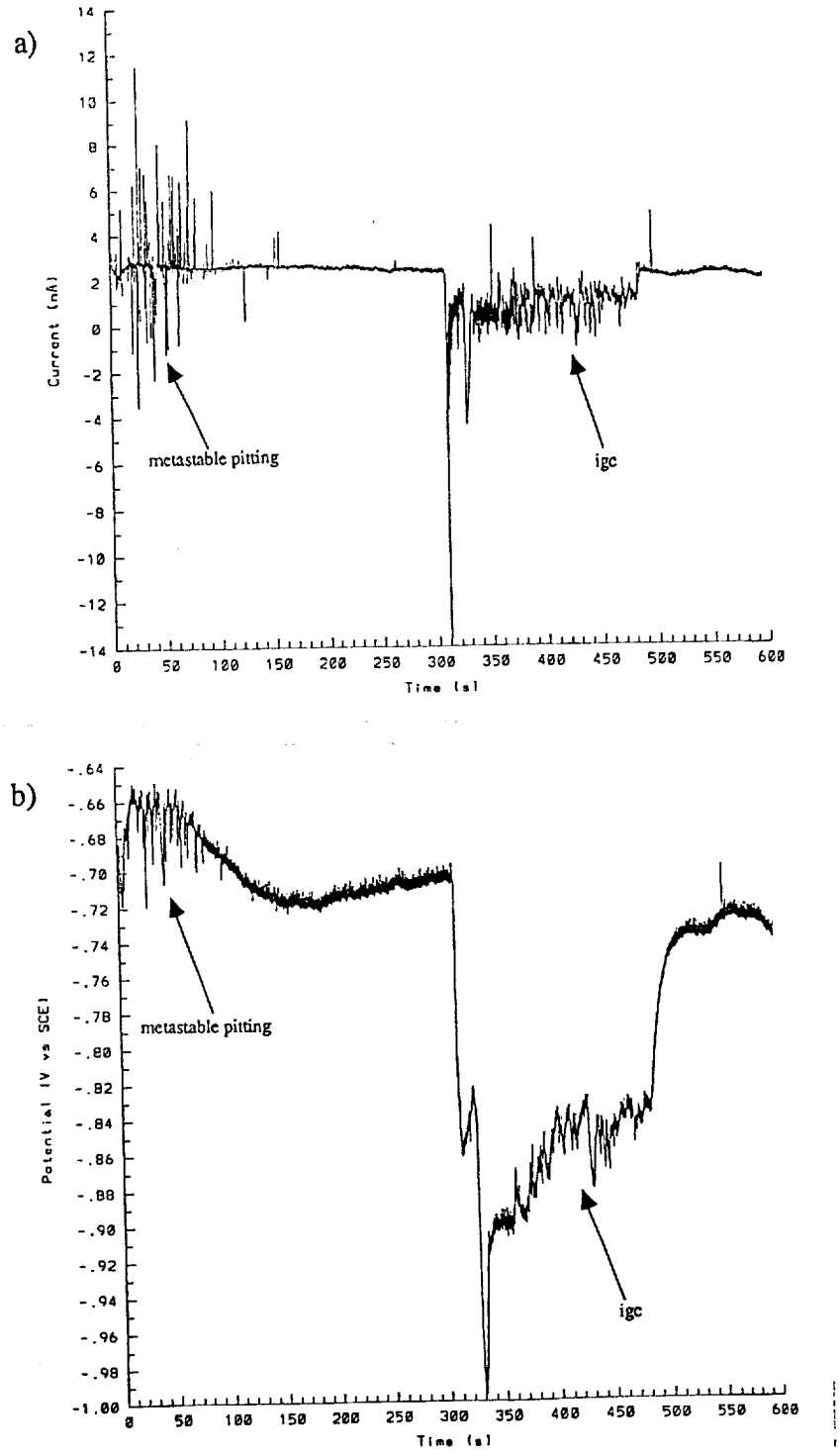

Figure 3: Time series showing current transient (a) and the corresponding OCP transient (b) behaviors associated with metastable pitting and igc of two identical galvanic coupled bulk Al-2%Cu samples in deaerated 0.1M NaCl solution. Exposed areas = 0.002cm^2.

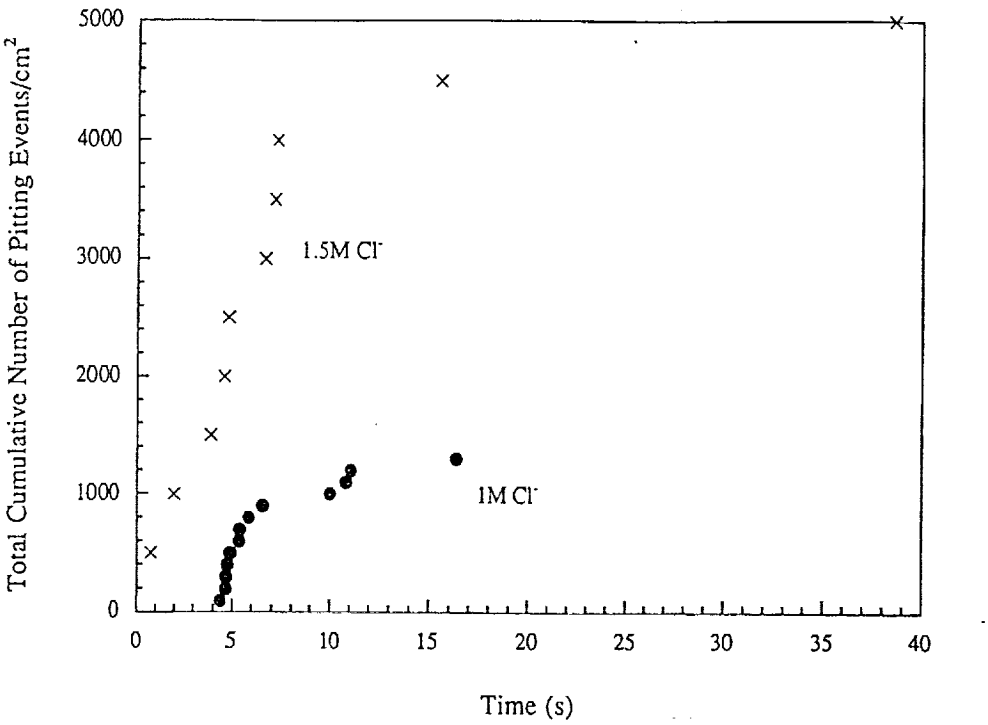

Figure 4: Total cumulative number of metastable pitting events of two identical galvanic coupled Al-2%Cu thin films in deaerated NaCl solutions of different concentrations. Exposed areas = 0.01cm^2.

Project #7 Investigation of the Effect of Thermal Treatment on the Mechanical Properties of Ti-1100/SCS-6 Composites

Douglas B. Gundel and F.E. Wawner

Research Objective

The overall objective of this research is to characterize the effect of thermal exposure, both isothermal and cyclic, on the mechanical properties of Ti-1100/SCS-6 composites. Important current objectives include a comparison of the degradation produced by thermal cycling versus the equivalent isothermal exposure in air, and modelling of the strength degradation.

Background and Approach

The Ti-1100/SCS-6 composites evaluated in this study were fabricated at NASA Langley Research Center. These materials were subjected to thermal exposure at UVA and evaluated for microstructural changes, tensile properties in longitudinal and transverse directions, and fracture characteristics. Scanning electron microscopy was utilized to delineate microstructure and any associated changes with environmental exposure. It is anticipated that an upper practical temperature limit will be defined for utilization of this composite system. Fracture analysis was conducted by SEM to relate interface and microstructure contribution to the failure process.

Modelling of the longitudinal strength was accomplished by the use of concepts and equations developed by other researchers. The partial embrittlement and cracking of the matrix during the exposure and the possible degradation of the fiber and interface properties may necessitate the modification of established models.

The overall approach has been outlined previously [1].

Research Progress

Composite samples for the completion of the mechanical property evaluation portion of the present study have only recently been obtained.

The work completed in the last reporting period has therefore been mainly theoretical in nature. The recently-obtained samples contain a high degree of fiber-fiber contact, possibly due to the relatively thick matrix foils employed during their manufacture. As reported previously, fiber contact is extremely detrimental to samples exposed in the transverse orientation due to the rapid diffusion of oxygen along the line of contact. For this reason, and the limited availability of fabricated panels, the recently received panels will be utilized to study the response of longitudinally-oriented samples to thermal exposure.

Limited experimental work on the depth of penetration of the oxygen along the fiber matrix interface has been completed. The specimens used were single-ply Ti-1100/SCS-6 composites fabricated at NASA-LaRC, which contained very few instances of fiber-fiber contact. The panels were sectioned into smaller pieces that were then exposed in air at temperatures of 700, 750 and 800°C, for times up to 100 hours. Optical micrographs of the composite cross-sections following exposure at 700 and 800°C for 50 hours are given in Figure 1. The lighter-shaded area near the interface is titanium that has absorbed a significant amount of oxygen. It can be observed that the depth of attack into the titanium (perpendicular to the interface) is much greater for the case of the higher temperature, but the depth of attack into the sample along the interface is nearly the same for both. The application of thermal cycling in addition to the high temperature exposure did not increase the depth of attack. These observations suggest that the depth of penetration along the interface is dependent upon some temperature-independent factor. Another indicator of this is the constant depth of diffusion of oxygen into the titanium in the direction perpendicular to the interface. This suggests that the oxygen penetrated to a certain distance almost immediately upon exposure. A possible reason for this rapid ingress along the interface is a common amount of damage to the fiber-matrix interface that is incurred upon sectioning the composite. This may stem from the relaxation of axial residual stresses in the matrix that then causes fiber-matrix debonding to a certain depth in the sample. The oxygen can then

penetrate along this debonded interface very quickly upon exposure.

Some limited exposures have been completed on longitudinal samples. Two panels were sectioned into samples. Both were fabricated with two matrix foils on each outer surface, and one matrix ply (~ 9 mils) between each fiber layer (4 fiber layers total). Only the embrittled layer resulting from fabrication was removed by chemical etching from the first panel (thick panel), while the outer matrix ply was also removed from the second (thin panel). The thicker panels had a fiber volume fraction of 0.14, and the thinner panels had a volume fraction of 0.17. Unfortunately, etching of the latter panel resulted in more matrix removed from one side than the other. A greater matrix thickness on one side resulted in significant sample bending upon cooling from high temperatures, and therefore gave unequal axial stress distributions in the matrix on the opposite surfaces. The axial stress is important in producing cracking of the embrittled matrix layer, so with this panel it was not possible to investigate the effect of outer-ply matrix thickness on cracking in this material. Additionally, the uneven matrix thicknesses resulted in an asymmetrical attack of the outer fiber layers by the oxygen, thereby resulting in a more difficult situation to model. These experiments will be performed on the panels that have just recently been

Table I

Composite and Fiber Strength

	Average Fiber Strength (ksi)		Composite Strength (ksi)
	Outer Plies	Inner Plies	
Thin Panel			
As-Fabricated	383±80	347±100	178
800°C, 100h (air)	379±40	367±63	127
Thermal Cycling in air (150-800°C, 100 h)	375±60	361±90	130
Thick Panel			
As-Fabricated	383±80	347±100	158

received.

Samples from these panels were, however, isothermally exposed at 800°C for 100 hours, and thermally cycled from 150 to 800°C for 100 hours. The cycled samples were held at high temperature for approximately 10 minutes, thereby resulting in 12 minute cycles. The cycled samples were therefore exposed to a less severe thermal exposure in terms of diffusion of oxygen through the titanium. Fibers were extracted from the isothermally exposed samples and as-fabricated (AF) samples in order to determine any changes in their strength. The etching was accomplished using a 20% bromine in methanol solution. The fibers were separated into two groups: those from the two plies closer to the surface, and those from the two inner plies. The composite strength was also measured and the results are given in Table I. It can be seen that the fiber strength was not significantly degraded by the exposure, but that of the composite was.

Figure 2 is the fracture surface of a sample from the thin panel that was exposed in air at 800°C for 100 hours. The presence of the cleavage-like matrix fracture surface around the edge of the sample is a result of oxygen embrittlement of the titanium. The embrittled titanium has been shown to fail at low strains in a tensile test, and therefore this matrix does not contribute to the overall composite strength. The composite strength degradation is therefore most probably the result of environmental attack of the matrix. It is clear in this micrograph that oxygen from the air has embrittled some of the titanium surrounding the fibers. The embrittled layer, however, did not penetrate further than the first row of fibers. The embrittlement of the matrix surrounding the outer layer of fibers did not seem to increase the amount of fiber pullout, thereby suggesting that the interface was not degraded by the exposure. In the future, embrittlement of the titanium near the center of the composite will be attempted.

A plot of the fiber strength values (one-inch gauge length) from the as-received panel revealed that the distribution was bimodal, with the high strength group centered about 400-450 ksi, and the low-strength group near 200-250 ksi. Approximately 25% of the fibers failed in the low-strength

regime. The fiber strengths were then separated into two populations, and the data sets were individually fit to Weibull distributions. A Weibull distribution has the form:

$$P_s(\sigma) = e^{-\frac{L}{L_o}\left(\frac{\sigma}{\sigma_o}\right)^m} \quad (1)$$

$P_s(\sigma)$ is the survival probability of the fiber, L is the gauge length of the sample being tested, L_o is the gauge length of the original population, σ_o is the characteristic strength of the original population, and m is the Weibull modulus. The Weibull modulus of the low-strength population was found to be approximately 9.0, while that of the high-strength group was found to be 8.3. The characteristic strength values were 225 and 426 ksi for the low and high strength populations, respectively. Fibers etched from the exposed panels also exhibited a bimodal distribution.

Composite Strength Modelling

Modelling of the composite strength following thermal exposure is a major goal of this project. This requires a thorough understanding of the mechanisms that lead to composite failure in the as-fabricated and exposed condition. Degradation of the fiber, matrix and the interface will lead to changes in the composite strength, but the overall composite strength is dependent on the mechanism of the failure. For example, if the matrix is embrittled, it may not contribute to the composite strength (due to severe cracking at a low applied stress), unless the fiber strength is degraded to zero; the strength of the composite will then be determined by the cracking stress of the matrix. Determination of the properties of the individual components following exposure is therefore critical in determining the failure mechanism of the composite, and modelling the composite strength.

One of the questions that needs to be addressed is the effect of a lower strength fiber population on the composite strength. The low strength fibers are presumed to be the result of the development of surface flaws on the

fibers, and are only present in the gauge length of approximately 25% of the fibers in the as-received state. It is possible that the flaws developed while handling the fiber or during composite fabrication. Other work has suggested that surface flaws tend to develop upon thermal exposure of the composite or uncomposited fiber in air. After thermally cycling SCS-6/Ti-24Al-11Nb, Revelos and Smith [2] noted the development of a low strength population and attributed it to the degradation of the SCS layer. Earlier work in the present study [3], in which SCS-6 fibers were individually exposed at 800°C for 700 h in air, indicates that long-term exposures in air can cause the growth of surface flaws on the fiber that initiate low-strength failure. These findings may suggest that the percentage of fibers in the low strength group in the present study may increase with a sufficiently severe thermal exposure. A model for the effect of these low strength flaw sites on the overall composite strength is therefore necessary.

Composite strength models assume either global or local load sharing. Global load sharing (GLS) describes the case in which the load carried by a failed fiber is evenly distributed to the other fibers (such as in a fiber bundle). Local load sharing (LLS) is the case in which the fiber break creates a high strength concentration on the neighboring fibers, thereby increasing their likelihood of failure. According to He *et al.* [4], LLS conditions are promoted by high interfacial sliding resistance (τ), high volume fraction fibers, and low matrix-to-fiber stiffness. In a composite, GLS leads to cumulative fiber breaking, whereas LLS leads to non-cumulative damage.

Local Load Sharing

Under LLS, failure of one fiber may cause complete failure of the composite. The stress at which the first fiber failure will occur, in terms of the Weibull parameters, was derived by Zweben[5]:

$$\sigma_f = \sigma_o \left[\frac{L_o(m-1)}{NLm} \right]^{\frac{1}{m}} \qquad (2)$$

The term σ_f is the stress on the fiber at failure of the first flaw, and N is the number of fibers present. Application of this equation is straightforward for a single-moded fiber strength population, but is more difficult when two or more modes are encountered. An estimate of the stress of the first fiber break in a bimodal distribution may be obtainable by using the Weibull parameters of the low strength population and choosing N to be the number of fibers that fail with a low strength at L. For the present case, σ_o=225, m=9.0, N~30, and L/L_o=1, therefore the first break is expected at 152 ksi. From this value, a conservative estimate of what the composite strength (σ_c) might be under the most severe local load sharing conditions can be calculated using the ROM (rule-of-mixtures) equation:

$$\sigma_c = \sigma_f V_f + \sigma_m V_m \qquad (3)$$

σ_m is the matrix stress at the failure stress of the composite, and V_f and V_m are the fiber and matrix volume fraction, respectively. Using σ_m =130 ksi, and V_f =0.17, the composite strength can be calculated to be 134 ksi, which is much lower than the measured value (Table I).

Global Load Sharing

Mixed Fiber Bundle Strength: The effect of a bimodal fiber strength distribution on the composite strength under GLS conditions can be approached by first considering the bundle strength degradation when a fraction of (F_2) low strength fibers is mixed with a high strength group. For a fiber strength distribution with a single mode of failure, the ultimate bundle strength (σ_b) can be derived as:

$$\sigma_{b,\mu} = \sigma_o \left(\frac{L}{L_o} me\right)^{-\frac{1}{m}} \qquad (4)$$

Using a similar method to derive the strength of a mixed bundle, the initial equation is :

$$\sigma_b = \sigma_f \left(1 - \frac{n}{N}\right) \tag{5}$$

σ_b is the stress on the bundle, σ_f is the stress on the unbroken fibers, n is the number of failed fibers, N is the total number of fibers, and the term (1-n/N) is the survival probability of the fibers in the bundle. The bundle stress is defined as the load on the bundle divided by the original cross sectional area of the fibers in the bundle. For a mixed fiber bundle with N_2 fibers in the low strength distribution, and N_1 fibers in the high strength distribution, where $N_1/N = F_1$ and $N_2/N = F_2$, the total survival probability can be expressed as:

$$P_{sT} = F_1 P_{s1} + F_2 P_{s2} \tag{6}$$

P_{sT} is the total survival probability of the mixed bundle, and P_{s1} and P_{s2} are the survival probabilities of Groups 1 and 2, respectively. When this P_{sT} is substituted into the expression for the bundle strength, and the survival probabilities are expressed in terms of the Weibull parameters (where $L=L_o$), the following equation results:

$$\sigma_b = \sigma_f F_1 \, e^{-\frac{L}{L_{o1}}\left(\frac{\sigma_f}{\sigma_{o1}}\right)^{m1}} + \sigma_f F_2 \, e^{-\frac{L}{L_{o2}}\left(\frac{\sigma_f}{\sigma_{o2}}\right)^{m2}} \tag{7}$$

The next step is to maximize the bundle strength by setting the derivative with respect to σ_f equal to zero, which yields:

$$0 = F_1 e^{-\frac{L}{L_{o1}}\left(\frac{\sigma_f}{\sigma_{o1}}\right)^{m1}} \left[1 - m1 \frac{L}{L_{o1}}\left(\frac{\sigma_f}{\sigma_{o1}}\right)^{m1}\right] + F_2 e^{-\frac{L}{L_{o2}}\left(\frac{\sigma_f}{\sigma_{o2}}\right)^{m2}} \left[1 - m2 \frac{L}{L_{o2}}\left(\frac{\sigma_f}{\sigma_{o2}}\right)^{m2}\right] \tag{8}$$

When the parameters are substituted in this equation, the value of σ_f at the ultimate strength of the bundle can be determined. Two maxima in the curve given by Equation 8 may result and these can be interpreted as the bundle

strength which is dominated by fibers in Groups 1 or 2. The larger of these values is the correct one to choose as the actual bundle strength. Simple modification of this analysis can be made to determine the effect of three or more fiber strength distributions.

Equations 7 through 8 will now be investigated to determine the effect of substituting high strength fibers with low strength fibers. The higher strength distribution used in this example will have an m of 10, and a σ_o of 100 arbitrary units. The lower strength distributions will have an m of 10, and characteristic strengths of 25, 50, and 75 units. Figure 3 is a plot of the strength of the resulting bundle versus the percent of fibers from the lower strength fibers. When the bundle strength of the low strength fibers is much lower than that of the higher strength fibers, the bundle strength of the mixture of the two is predicted to decrease according to the volume fraction of high strength fibers multiplied by their bundle strength. Eventually, when there is a high enough percentage of the low strength fibers, they begin to dominate the overall bundle strength. Failure of the low strength bundle will then result in failure of the entire bundle.

The higher the bundle strength of the low strength fibers, the lower the volume fraction where the transition occurs. At volume fractions lower than the transition, the bundle strength can be calculated by multiplying the bundle strength of the high strength fibers by their volume fraction. At volume fractions higher than the transition, the overall bundle strength is composed of a contribution from both groups of fibers. The contribution from the lower strength fibers is equal to their bundle strength multiplied by their volume fraction, while the contribution from the high strength fibers is due to the fibers in the high strength group that have a strength near the resulting mixed bundle strength. The magnitude of their contribution does not seem to be simply related to the fiber bundle strengths and volume fractions; it can, however, be determined from the plot of Figure 3.

The effect of the gauge length of the mixed bundle was investigated in the plot of Figure 4. A decrease in the gauge length will cause an increase in the bundle strength of the high and low strength fibers. The group with

the smaller Weibull modulus undergoes a higher percentage increase in its bundle strength, as can be seen in Figure 4. This produces a shift in the transition volume fraction to lower values.

The important trends determined here are that the bundle strength of the mixed fibers depends on the bundle strength of the individual groups. When the bundle strengths of the groups are nearly the same, the strength of the mixed fiber bundle is lower than predicted by the rule-of-mixtures. When the strength of the second group is much lower than that of the first, the overall strength of the bundle drops according to the bundle strength of the high strength group multiplied by its volume fraction. Eventually, a transition point is reached and the mixed fiber bundle strength no longer decreases at such a high rate.

Mixed Flaw Bundle Strength: The bundle strength of fibers that contain more than one flaw, thereby resulting in more than one strength distribution, is not the same as the case of a mixture of two different fiber populations. There are two significant differences when the flaw sites are on the same fiber: 1) The percentage of fibers that will fail in the low-strength distribution is dependent on the gauge length, and 2) A single fiber may fail at a particular stress due to flaws from one or the other distribution.

Any random gauge length is assumed to contain a high strength flaw site, but some contain an additional low strength flaw site. The higher strength flaw has been suggested to be the result of imperfections at the carbon-core/deposit (SiC) interface [6]. The spacing of the low-strength flaws is not known but it is assumed that it is much less than the gauge lengths investigated in this analysis; therefore there will be at least one of the high strength flaws in the gauge, and the strength of the fiber will be limited by these flaws. The low strength flaws are most probably sites on the fiber surface that were formed during processing of the composite or handling of the fiber. The size of the flaws at the core/deposit interface is smaller than those at the surface, but their mean spacing is much less. The tested gauge lengths of fibers do not all contain the low strength flaws, and therefore only a percentage of the fibers fail at this stress. If one of three fibers fail at a low

stress, and the gauge length is one inch (25.4 mm), then there is only one of the surface flaws per three inches, on average. This means that at smaller gauge lengths, fewer flaws would be encountered. For example, if the new gauge length is 0.5 inches, only one in six fibers would fail in the low strength regime. In this way, the fiber distribution, and therefore the overall survival probability, is dependent on the gauge length tested. This effect is in addition to the dependence of the probability on the gauge length that is contained in the Weibull formulation (Equation 1). This relationship can be written as:

$$F_2 = \frac{L}{L_o} F_{2o} \tag{9}$$

F_{2o} is the fraction of fibers that fail in the low strength group at the initial gauge length, L_o, and F_2 is the fraction that fail at any other gauge length. The value of F_2 cannot be larger than one, meaning that at F_2=1, low strength-producing flaws will cause failure of the fiber, and the bundle strength can be predicted by Equation 4. Equation 9 predicts that the mixed flaw bundle strength will become less dependent on the low strength flaws as the gauge length is reduced. This is an important point for Ti/SCS-6 (under GLS), in that the matrix reduces the effective gauge length of the fiber, thereby allowing cumulative fiber breaking. Figure 5 is a plot of the mixed flaw bundle strength when only the gauge length dependence given by Equation 9 is employed, and the slight overlap of the distributions is ignored. It is clear that the Group 2 flaws have a lesser influence on the bundle strength when the bundle gauge length is small.

The other significant difference between the bundle containing two groups of fibers with separate strength distributions and fibers containing both sets of flaws is that the failure probability is no longer the simple addition of the individual failure probabilities multiplied by their respective volume fractions ($1-P_{st}$). An additional analysis to account for the fibers which contain flaws from both distributions (i.e. the overlap region) is necessary. The fibers with both flaws can only fail once, and therefore the failure

probabilities are not simply additive. This effect may be important, but is difficult to include in the analysis and is not expected to significantly alter the numerical results of the analysis detailed above; however, an attempt to include this overlap effect is currently underway. The important factor for composites when two flaw sites are active on one fiber is the decrease of fibers in the low-strength population that arises due to the gauge length decrease (Eqn. 9).

Composite Strength: The reason for the development of a model for the strength of a mixed bundle is that GLS composite strength models use the bundle strength at a characteristic gauge length as the fiber contribution to be inserted into Equation 3. A recently-developed model that has been reported to be relatively successful at predicting the strength of Ti/SCS-6 composites is that of Curtin [7]. In his formulation, the interfacial sliding resistance, τ, is an important factor. Using the technique of fiber push-out and pull-out, researchers have estimated τ to be on the order of 30-150 MPa in titanium/SCS-6 systems [8,9,10]. Curtin's analysis leads to the following equation:

$$\sigma_f = \sigma_{avg}\left[\left(\frac{1}{m+2}\right)^{\frac{1}{(m+1)}}\left(\frac{m+1}{m+2}\right)\right]\left[\frac{4\tau L_o}{d_f \sigma_{avg} ln2}\right]^{\frac{1}{(m+1)}} \qquad (10)$$

The term σ_{avg} is the average strength of the fiber at gauge length L_o. The first factor of Equation 10 yields the typical rule-of-mixture (ROM) result when used in Equation 3. The second factor includes the bundle strength of the fiber at gauge length L_o, and is nearly equal to the value of $(me)^{-1/m}$ given in Equation 4 above. The third factor effectively reduces the tested fiber length from the L_o value to that of the characteristic length, and therefore includes the support of the fibers by the matrix. As reported by Curtin [7], the use of Equation 10 combined with Equation 4 provides a reasonable estimate of the strength of Ti/SCS-6 composites.

The method used by Curtin can also be employed to determine the fiber contribution when the fibers in the composite contain high and low strength flaws. In Curtin's analysis, the probability of a single-moded fiber

failure can be replaced with Equation 6, and the effect of the gauge length (Equation 9) can also be included in the probability. The reason that Equation 6 can be utilized in the present case, is that overlap of the distributions does not occur if the measured values are employed. This change in the derivation, however, does not permit a simple analytical solution, but numerical results are obtainable. Other values used to calculate the composite strength were 7.25 ksi (50 MPa) for the interfacial sliding resistance, and 130 ksi for the matrix contribution. After the fiber contribution was calculated by the modified Curtin analysis, Equation 3 was used to calculate the composite strength. A composite strength of 174 ksi is found for the as-received strength using a value of F_{2o}= 0.25, and a V_f of 0.17. This is not significantly different from the value that can be calculated from Equation 10 above using the Weibull parameters of only the high strength failures. For the thicker composites (V_f=.14), the strength predicted by this model is 166 ksi. The Curtin GLS model, modified for the present mixed flaw distribution on the fibers, therefore predicts that with sufficient interfacial strength (the matrix supports the fibers), the introduction of a second population of low-strength flaws with a low frequency (spacing > 1 inch) will produce only a very small decrease in the composite strength. When the spacing of the second flaw distribution becomes closer to the characteristic fiber length in the composite, the fiber contribution will approach that given by Curtin's original model using the low-strength Weibull parameters.

The prediction of the GLS model is closer to the actual as-received strength than that of the LLS model. It must be remembered, however, that the LLS prediction is a conservative estimate of the strength under LLS conditions. Experimental evidence supporting the existence of GLS in the present case is the detection of numerous audible "pings" prior to composite failure. This indicates that many fibers failed before the sample failed, thereby suggesting cumulative damage, or GLS. Sectioning of the sample, which has not yet been performed, may verify that the same fiber fails in several different places before the composite fails.

Conclusions

1. The distance that oxygen diffuses along the fiber-matrix interface (of a well-spaced fiber) and embrittles the adjacent titanium is approximately 1-2 mm for isothermal exposures in air at 700 and 800 hours for times up to 100 hours. The application of thermal cycling does not increase this distance. The penetration distance along the interface appears to be dominated by some temperature-independent factor. The amount of titanium that is embrittled is much greater for the higher temperature/longer term exposures due to higher diffusion rates through the titanium.
2. Preliminary composite exposures in air have been completed. Etched-out fiber tensile tests indicate that fiber strength is not severely degraded by the exposure, even in cases where the oxygen has embrittled the titanium surrounding the fibers. The composite strength degradation has therefore been attributed to matrix embrittlement. Additionally, the lack of fiber pullout where the matrix was embrittled suggests that the fiber-matrix interface was not weakened by the exposure.
3. Composite strength models are being developed for the case of a bimodal fiber strength distribution. A bimodal distribution is present in the as-fabricated (AF) condition, and it may become more severe upon thermal exposure. Under LLS conditions, the low-strength flaws may cause a severe loss of composite strength; however, under GLS, the observed second distribution of flaws is not expected to affect the strength. The measured AF strength is near that predicted by Curtin's GLS model.

Future Goals

1. Use newly-received panels to continue the investigation of the effect of isothermal exposure in air on the composite and component properties.

2. Compare the results of the isothermally exposed samples to those of the thermally cycled samples.
3. Investigate the effect of a thick surface matrix layer on the protection of the composite strength from environmental degradation.
4. Model the cracking of the outer matrix layer using simple residual stress analyses.
5. Continue to develop and modify models to predict the strength of the as-received and thermally exposed composites.

References

1. F.E. Wawner, D.B. Gundel, Renewal Proposal submitted to NASA, Grant No. NAG-1-745, November 1993.

2. Revelos, W.C., Smith, P.R. (1992). Effect of Environment on the Thermal Fatigue Response of an SCS-6/Ti24Al-11Nb Composite. *Met. Trans.* **23A** 2, 587-595 (1992).

3. M.L. Gambone, D.B. Gundel, F.E. Wawner, "The Effect of Isothermal Exposure on SiC Fibers," Presented at the 17th Annual Conference on Composites, Materials, and Structures, January 10-15, 1993, Cocoa Beach, Florida.

4. M.Y. He, A.G. Evans, W.A. Curtin, The Ultimate Tensile Strength of Metal and Ceramic Matrix Composites, *Acta metall. mater.* **41** 3, 871-878, (1993).

5. C. Zweben, Tensile Failure of Fiber Composites *AIAA J.* **6** 12 2325-2331 (1968).

6. Wawner, F.E., in Fiber Reinforcements for Composite Materials, Ch. 8, A.R. Bunsell, Ed., pp. 371-425, Elsevier, New York (1988).

7. W.A. Curtin, Ultimate Strengths of Fibre-Reinforced Ceramics and Metals. *Composites* **24** 2, 98-102 (1993).

8. J.I. Eldridge, Fiber Push-out Testing of Intermetallic Matrix Composites at Elevated Temperatures, in Intermetallic Composites II, D.B. Miracle, D.L. Anton, J.A. Graves. Eds., MRS Symposium Proceedings, San Francisco, CA, (Materials Research Society, V. 273, Pittsburgh. PA) 1992.

9. P.D. Warren, T.J. Mackin A.G. Evans, Design, Analysis and Application of an Improved Push-Through Test for the Measurement of Interface Properties in Composites. *Acta. metall. mater.* 40 6, 1243-1249 (1992).

10. D.B. Marshall, M.C. Shaw, W.L. Morris, Measurement of Interfacial Properties in Intermetallic Composites, presented at the Titanium Aluminide Composites Workshop, Orlando, FL, May, 1990 (WL-TR-91-4020, Wright-Patterson AFB, Ohio, 1991).

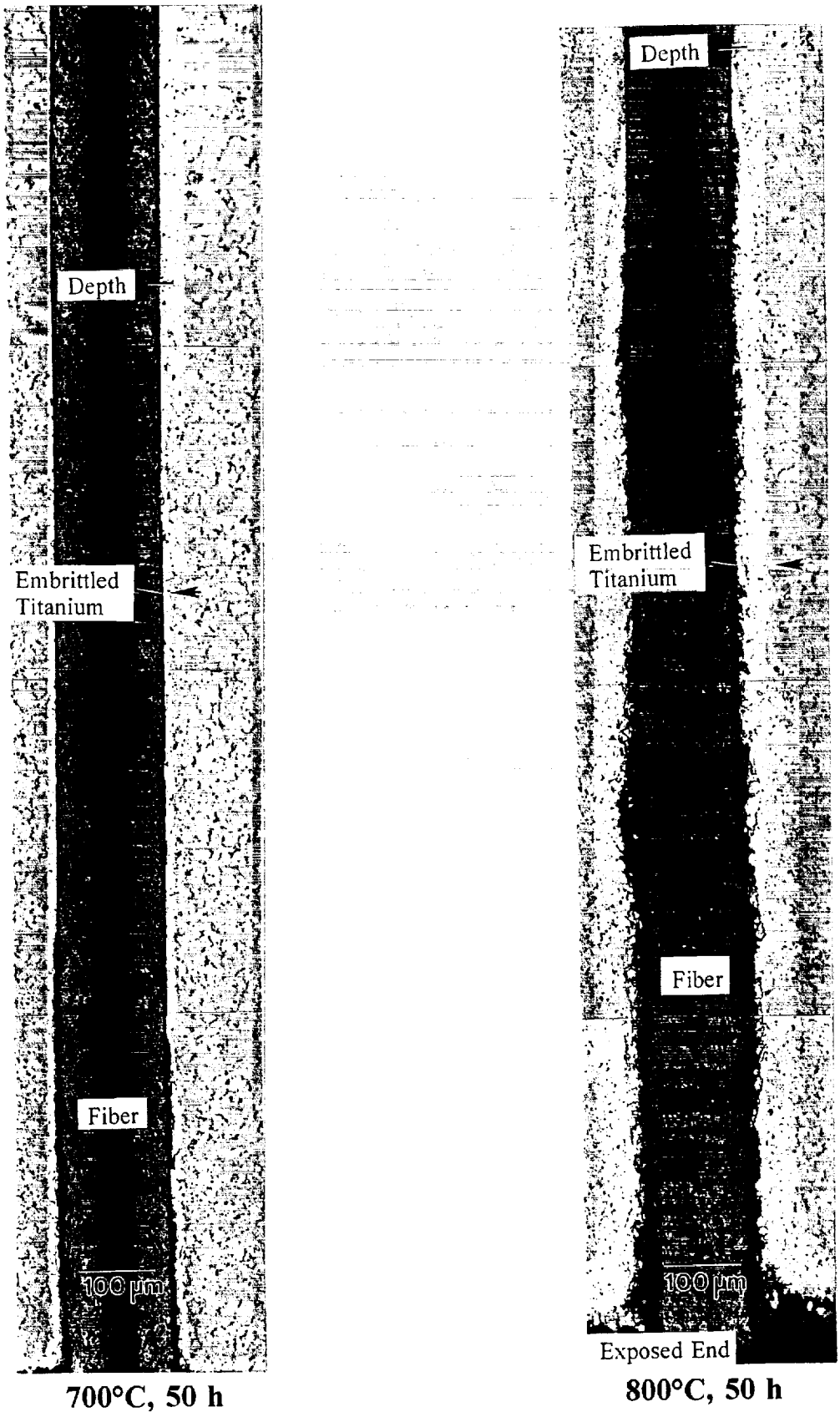

Figure 1. Longitudinal cross-sections of samples exposed in air at 700 (a) and 800°C (b) for 50 hours. The exposed fiber end is at the bottom. The diffusion distance along both interfaces is nearly the same, while the oxygen penetration into the titanium (perpendicular to the interface) is greater for the higher temperature exposure.

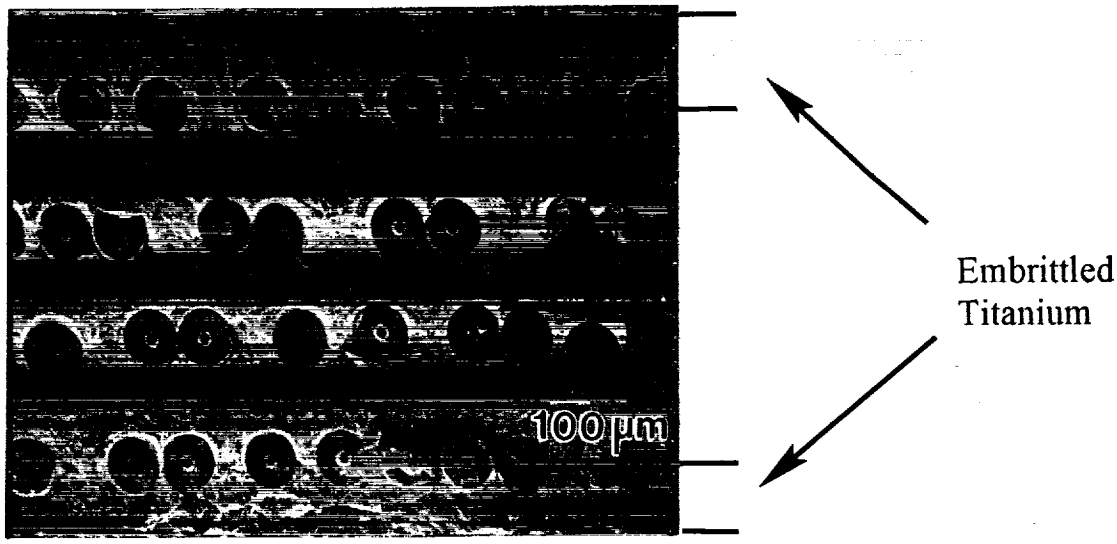

Figure 2. Fracture surface of thin sample (17 v/o) exposed at 800°C for 100 hours. Oxygen-embrittled titanium is present near the sample edges.

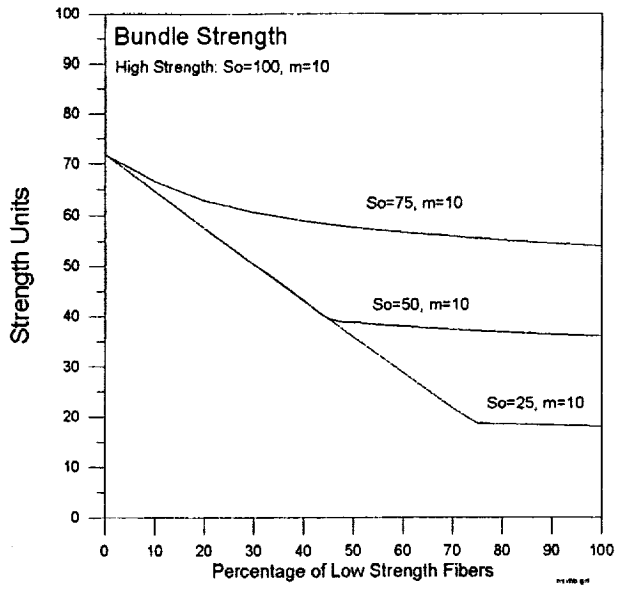

Figure 3. Strength of a bundle at $L=L_o$ versus the percentage (F_2) of low strength fibers from Group 2 mixed with high strength fibers from Group 1 ($S_o = \sigma_o$)

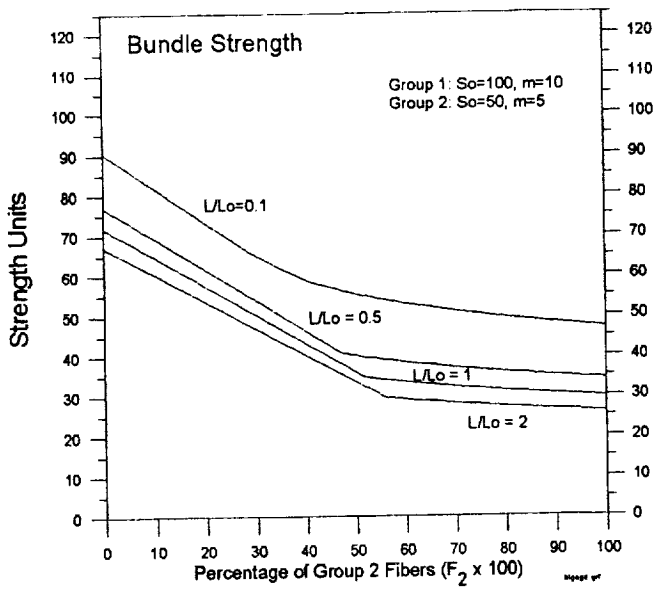

Figure 4. Strength of a mixed fiber bundle at various gauge length ratios.

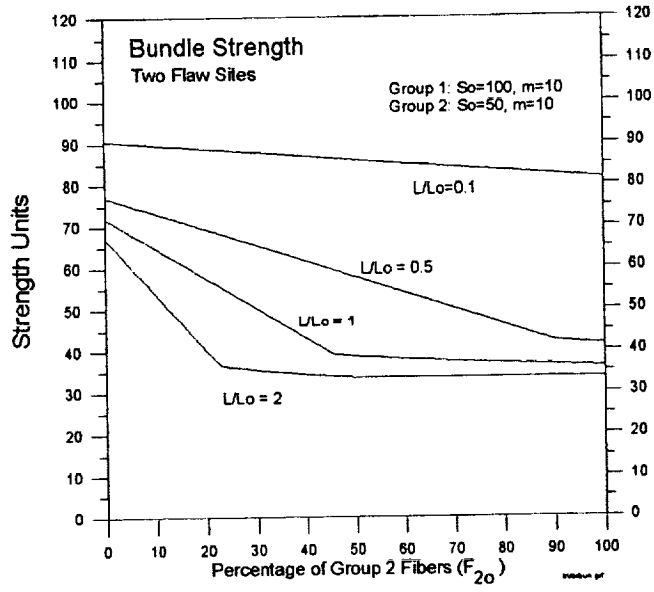

Figure 5. The effect of changing the tested gauge length on the strength of a bundle of fibers with mixed flaws (see text).

Project #8 Processing and Superplastic Properties of Weldalite™ Sheet

Mark Lyttle and John A. Wert

Objectives

The objectives of this research project are to establish the cause of anisotropic and variable superplastic properties of Weldalite sheet, and to identify the thermomechanical processing steps that introduce the anisotropy and variability.

Progress During the Reporting Period

During 1993, two major tasks have been completed within the scope of the present project. First, analyses have been conducted for the two Weldalite alloys, designated 049 and X2095, to characterize evolution of the microstructure and microtexture during the initial stages of superplastic forming. These tests have shown that microstructure/microtexture changes during uniaxial extension of specimens oriented parallel to the longitudinal and transverse directions are similar to changes previously observed in Al-Zr-Si and Al-Cu-Zr-Si alloys, but did contain distinctive aspects. Differences between the microstructural evolution during initial straining in the various alloys and orientations were quantitatively interpreted using models which simulate the mechanisms thought to foster microstructure/microtexture evolution.

Second, simulative models of microstructure/microtexture evolution during concurrent straining and annealing have been formulated. The three models involve subgrain rotation associated with boundary sliding, subgrain rotation associated with slip, and grain neighbor switching. A fourth model addressing the effect of (sub)grain growth was also developed to examine the possibility of significant microstructural evolution in the absence of grain boundary sliding. In addition, to aid in the evaluation of microstructures, a new method for characterizing the misorientation of grain boundaries was developed to complement the previously developed method for

characterizing the distribution of boundary misorientation angles.

Experimental Observations

The techniques used for concurrent straining and annealing experiments have been described previously [1,2], including specific temperatures, holding times, and initial strain rates for the Al-Zr-Si and Al-Cu-Zr- Si alloys. For the Al-Cu-Li-Ag-Mg-Zr alloy, tensile specimens with the tensile axis parallel to the rolling direction (L) and the long transverse direction (T) were heated to the test temperature of 773 K in approximately 0.5 h, and were held at that temperature to stabilize for 0.16 h prior to straining at an initial strain rate of 6.6×10^{-4} s^{-1}. Tests were interrupted at true strains (ϵ) of 0.11, 0.21 and 0.47; and the tensile specimens were rapidly quenched in water. TEM foils in the tensile axis/short transverse direction plane were prepared, and measurements of grain orientation and boundary misorientation were performed as described previously [1,2].

Grain orientation and boundary misorientation data for Al-0.24Zr-0.1Si and Al-4.1Cu-0.28Zr-0.1Si alloys (compositions are given in weight percent) have been previously reported [1,2] and are included for comparison with model results. Similar experimental observations have been made within the scope of the current project for Weldalite™ alloys designated 049 (Al-4.76Cu-1.27Li-0.37Ag-0.33Mg-0.13Zr) and x2095 strained in the longitudinal direction and in the transverse direction. Detailed observations of grain orientation changes during straining in the transverse direction have not been reported previously for a superplastic alloy.

The microstructural evolution in the transverse and longitudinal tensile specimens is compared in Table I. The experimental results show that the rate of grain rotation in the Weldalite tensile specimens of both orientations decreases as strain increases. In the strain interval 0 to 0.21, the microstructure evolves rapidly, transforming the initial microstructure containing predominantly low-angle boundaries into a microstructure containing predominantly high-angle boundaries. Only limited additional evolution of the boundary misorientation distribution occurs in the strain

interval 0.21 to 0.47. The stress-strain curves exhibit flow stress peaks in the strain interval 0.2 to 0.3, near the end of the rapid boundary misorientation evolution phase. These findings are consistent with the view that the initial microstructure is not conducive to superplastic flow, but that the boundary conversion process that occurs in the strain interval 0 to 0.21 transforms enough boundaries from the low-angle to the high-angle range to permit deformation by a grain boundary sliding process. The opportunity for grain boundary sliding to contribute significantly to the total strain causes the flow stress to decrease from the peak value.

The relative rates of boundary misorientation evolution for the two specimen orientations indicate that evolution toward high-angle boundaries occurs more rapidly in the transverse orientation than in the longitudinal orientation. In the transverse specimen orientation, the evolution to a predominantly high-angle boundary microstructure occurred almost entirely before a strain of 0.11 although the flow stress continued to increase up to a strain of 0.21. In the longitudinally oriented specimens, microstructural evolution continued to a strain of 0.21 and the flow stress increased to a peak at a strain of 0.27. The lower flow stress and less rapid microstructural evolution in the longitudinal specimens indicates the presence of an initial microstructure that is more suited to superplastic flow. In contrast, transverse specimens exhibit a higher flow stress peak at a lower strain, and more rapid microstructural evolution. Thus, the mechanisms responsible for plastic flow in the strain interval before the peak flow stress appear to induce more rapid continuous recrystallization when the initial microstructure is less suited to superplastic flow.

Recent observations by other researchers [3] suggest that, for some aluminum alloys, grain boundary sliding may not explain the microstructural evolution that occurs during continuous recrystallization. This conclusion is based on the assumption that grain translation is the principal manifestation of grain boundary sliding. For approximately equiaxed grains and strains less than 0.40, experimental observations and geometrical predictions indicate that little grain neighbor translation occurs.

Concluding that grain boundary sliding does not occur during the initial stages of deformation of some aluminum alloys, Blackwell and Bate [3] postulate that the primary mechanism for the generation of high-angle grain boundaries during continuous recrystallization is grain growth. To evaluate that hypothesis, we conducted some calculations based on simple 2-D geometrical models of ideal deformation bands. By varying the spacing of the high-angle boundary planes and assuming ideal deformation bands (all internal boundaries are low-angle boundaries), the change in fraction of low-angle boundaries as a function of grain size and deformation band width can be observed. From these observations, a relationship was derived relating low-angle boundary fraction to grain size and deformation band width. A plot based on this relationship is shown in Figure 1.

The results reveal that, while grain growth does reduce the low-angle boundary fraction, for the alloys studied the reduction is insufficient to explain the evolution of boundary misorientations that occurs up to a strain of 0.21. Thus, (sub)grain rotation must occur in addition to the secondary processes of grain neighbor switching and grain growth to produce the observed changes in boundary misorientation.

Using the models to characterize the evolution observed in Weldalite and in the two other aluminum alloys, the relative contribution of each mechanism has been roughly determined. Table II displays the predicted contribution of each mechanism during continuous recrystallization for a traditional superplastic aluminum alloy. Since the mechanisms that contribute the most to microstructural evolution, grain rotation and grain neighbor switching, are directly dependent on grain boundary sliding, development of an initial microstructure to facilitate grain boundary sliding could enhance a material's superplastic properties.

Figure 2 shows boundary misorientation axis distributions from the Weldalite grip sections in which the boundaries have been classified into three categories. Figure 3 displays the same information from the Weldalite alloys at a strain of 0.47. The difference in the number of points in each stereographic triangle is due to the relative numbers of each type of

boundary in the microstructures.

Examination of boundary misorientation axes of grip section specimens plotted on a unit stereographic triangle reveals no preferential rotation axis orientation for low-angle boundaries. Misorientation rotation axes for boundaries with low-angle misorientations are distributed evenly throughout the entire stereographic triangle. Adjacent subgrains in a deformation band share similar crystal orientations, but appear to have random rotation axis orientations. In the Weldalite specimens deformed to a strain of 0.47 the relative concentration of low-angle boundaries has decreased, but the distribution of their misorientation axes is still fairly random over the entire stereographic triangle.

In the grip sections, no high-angle boundaries have misorientation axes orientations near [001]. For very high-angle boundaries (>50°), rotation axes can only fall in a restricted sector of the stereographic triangle, approximately within 5° of the arc from [011] to [111]. However, the other high-angle boundaries ($10° < \theta < 50°$) would be expected to be more uniformly distributed throughout the triangle if there was no preferential rotation axis orientation, but these boundaries also appear to cluster away from the [001] pole. At a strain of 0.47, misorientation axis orientations of high-angle boundaries have spread out into slightly more of the stereographic triangle. This may reflect (sub)grain rotation away from the lattice orientations found in the initial deformation microstructure and transformation of low-angle boundaries in the initial microstructure to boundaries of greater that 10° misorientation over the entire triangle.

Conclusions

Mechanisms dependent on grain boundary sliding are primarily responsible for the microstructural evolution that occurs during continuous recrystallization. Therefore, it would be desirable to have a microstructure that facilitates grain boundary sliding in a rolled sheet prior to superplastic forming. Some desirable initial microstructural elements include a lower

fraction of low-angle boundaries, high-angle boundary planes oriented out of the rolling plane, and narrower deformation bands.

References

1. H. Gudmundsson, D. D. Brooks and J. A. Wert, Acta Met., 39 (1991), 19.

2. D. D. Brooks, H. Gudmundsson and J. A. Wert, in Hot Deformation of Aluminum Alloys, edited by T.G. Langdon, H.D. Merchant, J.G. Morris and M.A. Zaidi (Warrendale: TMS, 1991), 55.

3. P. L. Blackwell and P. S. Bate, Met. Trans., 24A (1993) 1085.

Table I - Low-angle Boundary Percent for Experimental Observations and Model Calculations

	049		x2095	
	L	T	L	T
Experimental Results				
Grip (ε=0)	55	47	38	56
ε = 0.11	52	20	70	26
ε = 0.21	35	10	37	20
ε = 0.47	32	29	22	31
Model Results				
5° Rotation	53	37	29	43
10° Rotation	26	20	14	23
Slip (ε~0.5)	59	53	34	48
Switching (ε~0.5)	34	30	31	49
5° Rotation & Switch	23	24	24	39

Table II - Relative contribution of each proposed mechanism toward continuous recrystallization during the initial stages of superplastic forming.

	Low-angle Boundary Fraction Reduction	Average Contribution to Continuous Recrystallization
Grain rotation	10-20	50%
Grain neighbor switching	5-15	33%
Grain growth	0-5	16%
Slip	negligible	0%
Total	15-40	100%

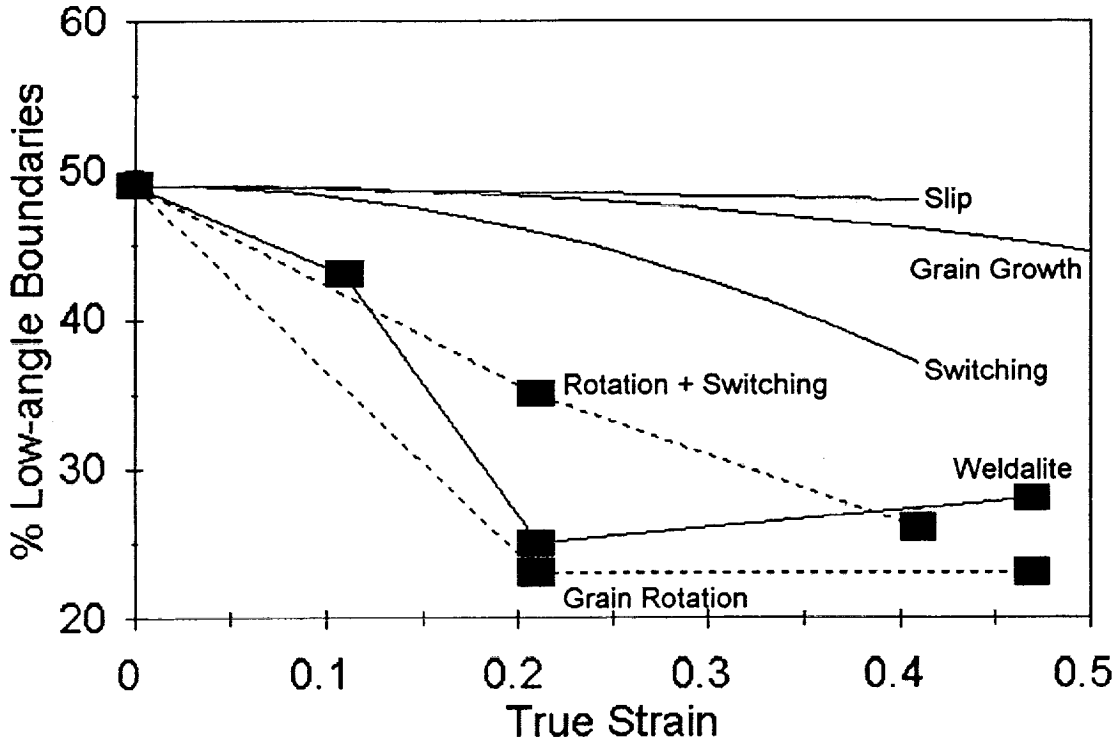

Figure 1 - Modeled predictions of each mechanisms effect on the low-angle boundary fraction of Weldalite during initial straining.

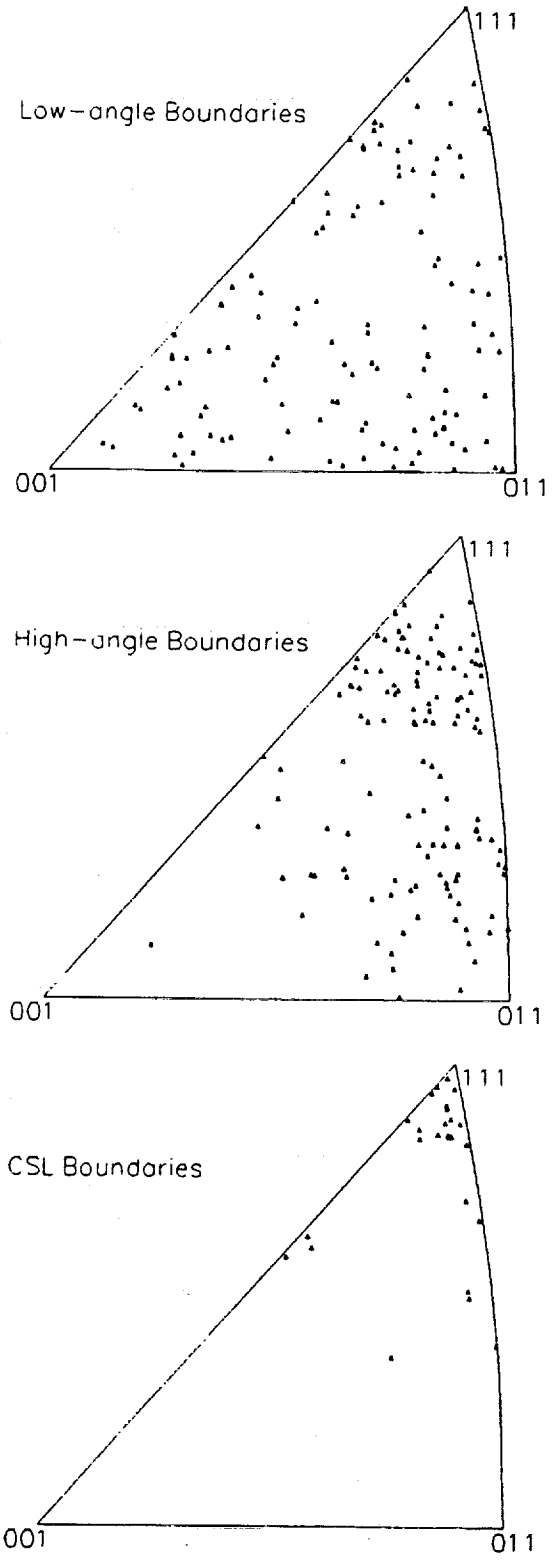

Figure 2 - Misorientation distributions on a unit stereographic triangle for boundaries from the grip sections of all Weldalite specimens (strain = 0).

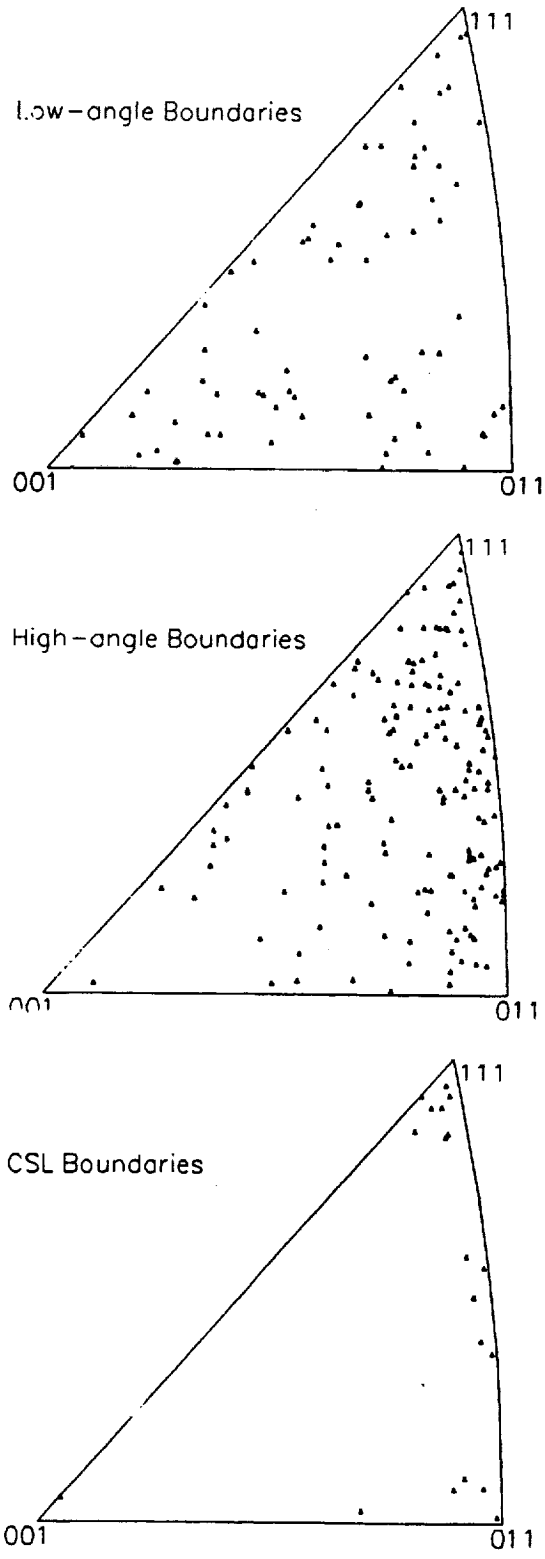

Figure 3 - Misorientation distributions on a unit stereographic triangle for boundaries from the gauge sections strained to 0.47 of all Weldalite specimens.

Project #8 Evaluation of Wide-Panel Aluminum Alloy Extrusions

Mark Lyttle and John A. Wert

Objectives

The objective of this project is to model the effects of microstructure and texture on the yield strength in wide panel aluminum alloy extrusions. Modeling results will be used to predict the locations and tensile axis orientations corresponding to minimum yield strength where localized yielding could readily occur in service.

Progress During the Reporting Period

Since work on this task formally started in October 1993, only limited technical progress can be reported. The following paragraphs describe progress on two aspects of the project.

Preparation of Integrally-Stiffened Extruded Panels

The technique for manufacturing integrally stiffened panels from tubular extrusions has been developed in Russia, The process involves extrusion of a large diameter tube with longitudinal integral stiffeners. The tube is then slit and flattened using specialized rolling equipment. Since the equipment for preparing these panels is already available in Russia, extrusions for use by NASA will be processed there. Reynolds Metals Co. has shipped 12 extrusion billets to Russia, six each of alloys 2195 and X2096. The original schedule called for extrusion and subsequent processing to be completed by October 1993. However, as a result of the large and variable number of participants and the somewhat chaotic situation in Russia, delays have occurred.

Dr. A. Cho from Reynolds Metals Co. will travel to Russia in February of 1994 for the purpose of observing and documenting extrusion and processing of the integrally stiffened panels to be delivered to NASA. His observations are expected to provide significant new insight into the

processing steps involved in fabrication of the integrally stiffened panels. The panels should be available to NASA shortly after this period.

Modeling of the Anisotropy of Yield Strength

The popLA orientation distribution function (ODF) program package [1] available for Los Alamos National Laboratory has been implemented at the University of Virginia. While the integrally stiffened extrusions which this project is directed toward are not yet available, we have used the popLA program to analyze texture data for a rolled aluminum alloy. Three pole figures were obtained using the Siemens texture goniometer at UVa. The intensity data files collected using the older equipment at UVa require modification prior to their use with the popLA program package. After modifying the texture data files using a filtering program, the texture data are input into the popLA program. Various analysis capabilities are available in the popLA package; we have used three of these capabilities for analysis of texture data.

First, the ODF was analyzed and plotted using the WIMV method [1]. Figure 1 shows the ODF of the rolled aluminum alloy plotted using Kocks angles (ϕ, ψ, Θ) [2]. Second, the harmonic coefficients (W_{lmn}) were obtained. These coefficients are needed for the precipitate strengthening analysis described by Bate, Roberts, and Wilson [3,4]. Lastly, the weighted-grain method was used to perform in-plane yield strength anisotropy calculations, giving the results shown in Figures 2 and 3. Here, the Taylor factor is represented as a function of tensile axis orientation relative to the longitudinal direction. Two results are indicated: one for equiaxed grains (fully constrained) and one for pancake-shaped grains typical of rolled aluminum alloys (relaxed constraints). The Taylor factor has a minimum value close to 45; consistent with the lower value of yield strength commonly observed for this tensile axis orientation in rolled aluminum alloys.

Tasks for the Next Reporting Period

Uniaxial tensile tests of as-solutionized specimens will be conducted in several orientations (along the extrusion axis, transverse axis, and in several intermediate orientations) to verify the calculated Taylor factors. Using the texture data, predictions of the Taylor/Bishop-Hill yield anisotropy will be directly compared with yield strengths obtained during uniaxial tensile testing. Because of microscopic variations in texture in the extruded panel, tensile specimens must be small enough to ensure that there is a consistent microstructure throughout a single tensile specimen.

Upon verification of the calculated Taylor factors, work can begin on the technologically relevant problem; prediction of the influence of precipitates on the yield anisotropy. Texture and microstructural analyses will be performed on specimens aged to form certain precipitates. From Taylor/Bishop-Hill yield anisotropy predictions, a baseline yield strength with no precipitate strengthening can be determined. After observing the yield strength increase due to precipitate formation, possible correlations between yield surface changes and precipitate size, morphology, and orientation will be examined.

References

1. J. S. Kallend, U. F. Kocks, A. D. Rollett, and H. R. Wenk, Materials Science and Engineering, A132 (1991) 1.

2. U. F. Kocks, in Eighth International Conference of Textures of Materials, edited by J. S. Kallend and G. Gottstein (Warrendale: TMS, 1988), 31.

3. P. Bate, W. T. Roberts and D. V. Wilson, Acta Metallurgica, 29 (1981) 1797.

4. P. Bate, W. T. Roberts and D. V. Wilson, Acta Metallurgica, 30 (1982) 725.

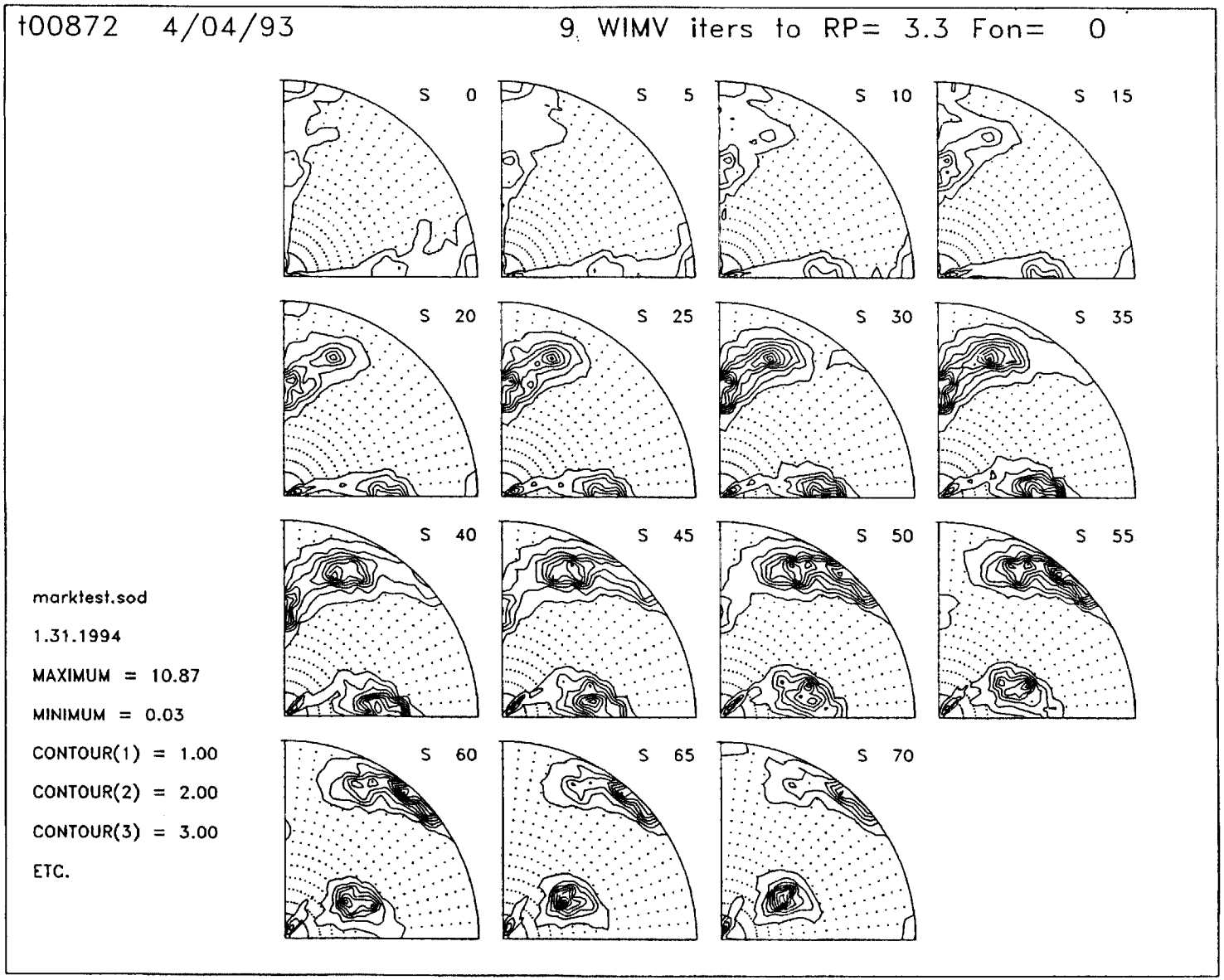

Figure 1 - Orientation distribution function of a rolled aluminum alloy plotted using Kocks angles (ϕ;ψ,Θ).

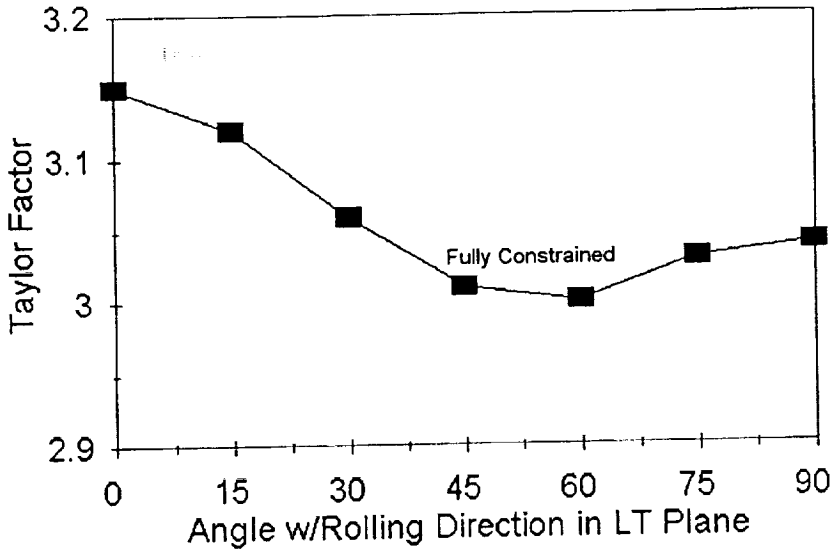

Figure 2 - Dependence of Taylor factor on tensile orientation calculated from pole figure data.

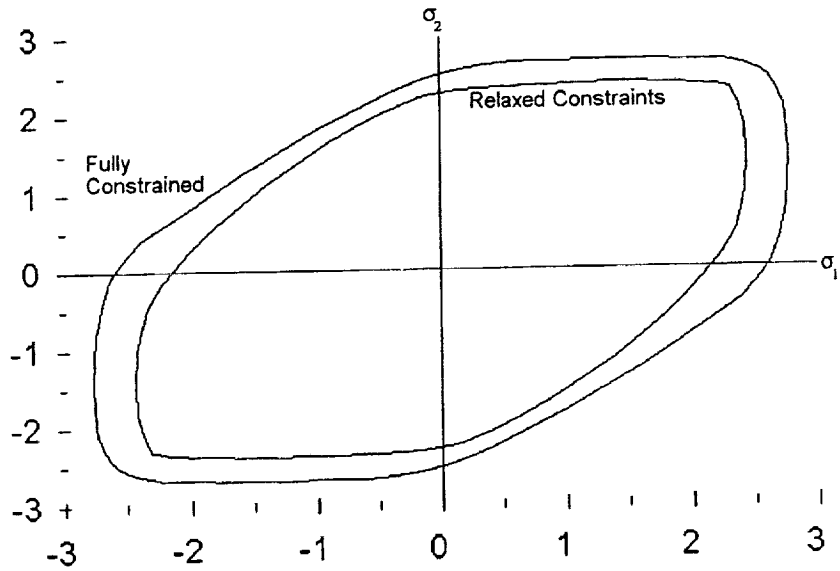

Figure 3 - Calculation of the yield surface with principal stresses coincident with the L and T directions of the rolled plane of an aluminum alloy for a fully constrained system of grains and for a system of pancake-shaped grains (relaxed constraint). Yield strength is normalized by the critical resolved shear stress.

Project #9 PRECIPITATION HARDENING AND MICROSTRUCTURAL STABILITY IN Al-Si-Ge AND Al-Si-Ge-Cu ALLOYS

H.J. Koenigsmann and E.A. Starke, Jr.

Background and Problem Statement

A recently developed age-hardenable Al-Si-Ge alloy utilizes a fine and uniform distribution of SiGe particles which have an estimated critical size for the transition from shearing to looping by dislocations at the yield stress of about 2 nm. These features result in a high degree of hardening for a small volume fraction of particles. [1,2]

The SiGe particles can be expected to be more thermally stable than the precipitates of other age-hardenable aluminum alloys due to the low solubility of both Si and Ge in Al and the incoherent precipitate interface. The low strength of the ternary Al-Si-Ge alloys can be increased by the addition of Cu since the quaternary Al-Si-Ge-Cu alloys have a higher number of precursory clusters during quenching which act as nucleation centers for the diamond structure SiGe precipitates during aging. [3,4]

Objective

The objectives of this project are to investigate the microstructural evolution and thermal stability as well as the fracture behavior in recently developed Al-Si-Ge and Al-Si-Ge-Cu alloys.

Summary of Previous Results

As compared to binary Al-Si and Al-Ge alloys, diamond structure precipitates in ternary Al-Si-Ge alloys are found to nucleate at a much finer scale and with a lower tendency to overaging under comparable conditions. The aging characteristics of the ternary alloys are not affected by prior low temperature aging or preaging cold work. [3,4]

The addition of less than 2.5 wt.% Cu does not affect the distribution

PAGE 154 INTENTIONALLY BLANK

of the SiGe particles and leads to an increase of the hardness level by about 60%. However, the addition of more than 2.5 wt.% Cu results in the nucleation of θ' (Al_2Cu) precipitates in addition to the diamond structure SiGe precipitates; the rapid coarsening of the θ' precipitates leads to a rapid overaging of the θ' containing alloys. Additional strengthening of the matrix by Mg, Zn, Ag or by traces of Mn, In, Sn, Zr is not observed. [3]

Approach

Ternary Al-1.02Si-0.95Ge (wt.%) and quaternary Al-1.00Si-0.99Ge-2.57Cu (wt.%) alloys were provided by ALCOA. These alloys have a nearly identical composition except for Cu so that the influence of Cu independent of other factors could be studied. In addition, a 25 gm ingot of a ternary Al-0.51Si-1.99Ge (wt.%) alloy was prepared in our department using an induction furnace. Since Si has a smaller and Ge has a larger atomic diameter than Al, the composition of the last alloy was chosen in such a way that the atomic size misfit is compensated after the formation of pairs of Si and Ge.

Optimum homogenization temperatures of 500°C for the ternary alloys and of 490°C for the quaternary alloy were selected based on the thermal analysis using a Perkin Elmer Differential Scanning Calorimeter (DSC). The alloys were successfully homogenized within 30 hrs, solution heat treated at 490°C (ternary alloys) or 480°C (quaternary alloy), and water quenched. Different quench rates (using horizontal and vertical air furnaces for the solution heat treatment) and quench media (room temperature water and ice water) were applied in order to study the influence of these quench effects on the mean diameter of SiGe precipitates in peak-aged alloys. Both the ternary and the quaternary alloys were aged in air furnaces at 160°C for up to 16 days and at 120°C for up to 60 days.

Vickers microhardness measurements were performed at room temperature using a Kentron Microhardness Tester AK. Samples for Transmission Electron Microscopy (TEM) were prepared using standard techniques; all TEM examinations were conducted using a Philips EM 400T. The average radii of the diamond structure precipitates were determined by

quantitative stereological methods [5] and corrected for truncation and overlap [6]; foil thicknesses were determined under two-beam conditions from oscillations in intensity of Convergent Beam Diffraction Patterns (CBED) [7].

Peak-aged samples of the ternary and quaternary alloys provided by ALCOA were kept in oil bathes at 200°F (93°C), 250°F (121°C), and 300°F (149°C), and Vickers microhardness measurements were performed over a period of 10 days at the temperature of the corresponding oil bath using a Nikon High-Temperature Microhardness Tester QM.

Results and Discussion

Figures 1a and 2a show the average diameters of the diamond structure SiGe precipitates in the ternary Al-1.02Si-0.95Ge (wt.%) and quaternary Al-1.00Si-0.99Ge-2.57Cu (wt.%) alloys after different aging times for aging temperatures of 160°C and 120°C, respectively (note the different time scales used for the two temperatures). The magnitude of the values is in correspondence with the estimated particle size for the transition from shearing to bypassing [2] which is related to the size at which such particles form from a cluster.

The linear relationship between the cube of the average radii and the aging time predicted by the coarsening theory by Lifshitz [8] and Wagner [9] is depicted for the SiGe precipitates in the ternary and quaternary alloys for the two aging temperatures in Figs. 1b and 2b, respectively. The relationship is roughly linear, but all four curves show a similar deviation. A better fit is observed if one considers a linear relationship between the fifth power of the average radii and the aging time (Figs. 1c and 2c). This corresponds to the observation made by Merle and Fouquet [10] who investigated the coarsening of θ' in Al-Cu alloys. Merle and Merlin [11] were able to explain this behavior based on the hypothesis of heterogeneous nucleation of ledges due to the impingement of precipitates. This hypothesis leads to an exponent of 5.5 which agrees rather well with the experimental results.

The coarsening rate for both the ternary and the quaternary alloys is

significantly greater at 160°C than at 120°C as can be expected from the exponential temperature dependence of the diffusion coefficient. The average radii for the diamond structure SiGe precipitates are at both aging temperatures slightly greater in the quaternary alloy than in the ternary alloy although the chemical composition of both alloys is nearly identical. However, the difference between the average diameters of the SiGe precipitates in the two alloys at a given aging time and temperature is well within the error bars of the measurements (Figs. 1a and 2a).

The coarsening theory by Lifshitz and Wagner predicts that the variation of the mean radius, r, with time, t, is given by the following equation [12]:

$$r^3 - r_o^3 = 8\gamma D c_o V_m^2 (t - t_o)/9RT \qquad (1)$$

where r_o is the mean particle radius when coarsening commences at the time t_o, γ is the specific precipitate-matrix interfacial free energy, D and c_o are the diffusivity and the equilibrium molar concentration at the given temperature, T, respectively, V_m is the molar volume of the precipitate, and R has its usual meaning. The interfacial energy can be estimated from the slope of the graphs in Figs. 1b and 2b using equation (1). Diffusivity data of Si in Al and Ge in Al were taken from [13]. The ratio between Si and Ge was taken into account for each alloy, but the influence of Cu was neglected. The equilibrium concentration was estimated from [14] and a value of 0.2 wt.% was used. The molar volume was calculated based on the values given in [2] for Si and Ge diamond cubic structures. The interfacial energy values shown in Figs. 1b and 2b are in the expected range; differences are probably due to significant errors in low temperature diffusivity data [12].

A higher quench rate using a vertical instead of a horizontal furnace for the solution heat treatment had only a small effect on the average diameter of the SiGe precipitates after peak-aging at 160°C: the average precipitate diameter decreased from 8.0 nm to 7.7 nm for the ternary Al-1.02Si-0.95Ge (wt.%) alloy and from 8.7 nm to 8.3 nm for the quaternary Al-1.00Si-0.99Ge-

2.57Cu (wt.%) alloy. Quenching into ice water instead of room temperature water had no measurable effect on the average SiGe precipitate diameter.

The average diameter of the SiGe precipitates can be decreased significantly if the composition of the ternary alloy is chosen in such a way that the atomic size misfit is compensated. After peak-aging at 160°C the average precipitate diameter decreased from 8.0 nm for the Al-1.02Si-0.95Ge (wt.%) alloy to 5.0 nm for the Al-0.51Si-1.99Ge (wt.%) alloy. Using the modified Orowan equation [1]:

$$\Delta\sigma_p \approx Gb\sqrt{f}/d \qquad (2)$$

where $\Delta\sigma_p$ is the contribution of the SiGe particles to the yield strength, G is the shear modulus of the matrix (26 GPa [1]), b is the Burgers vector (0.284 nm [1]), f is the volume fraction and d is the diameter of the particles, an increase of $\Delta\sigma_p$ by a factor of 1.5 can be expected even if the volume fraction of the SiGe particles is slightly decreased in the new alloy due to cost considerations.

Fig. 3 shows the Vickers microhardness measurements for the peak-aged ternary Al-1.02Si-0.95Ge (wt.%) and quaternary Al-1.00Si-0.99Ge-2.57Cu (wt.%) alloys carried out at the temperature of the corresponding oil bath. The slope of the curves decreases with increasing time and decreasing temperature for both alloys. In contrast to previous results obtained for a quaternary alloy with a Cu content of 2.7 wt.% which was compared to a ternary alloy, the slope of the curves for the quaternary alloy is now similar to that of the ternary alloy. This is possibly due to the lower Cu content which might result in a lower coarsening rate of θ'.

Conclusions

The relationship between the cube of the average radii of the SiGe diamond structure precipitates in the ternary Al-1.02Si-0.95Ge (wt.%) and quaternary Al-1.00Si-0.99Ge-2.57Cu (wt.%) alloys and the aging time at 160°C and 120°C is roughly linear as predicted by the coarsening theory by Lifshitz

[8] and Wagner [9]. However, a better fit is observed if one considers a linear relationship between the fifth power of the average radii and the aging time as explained by Merle and Merlin [11]. The difference between the average diameters of the SiGe precipitates in the ternary and quaternary alloys at a given aging time and temperature is well within the error bars of the measurements. The estimated precipitate-matrix interfacial energy of 500 to 800 mJ/m^2 is in the expected range.

An increase of the yield strength of the ternary alloy by a factor of about 1.5 can be expected if the composition of the alloy is chosen in such a way that the atomic size misfit cancels.

Future Work

The combined effects of different quench rates and quench media on the mean diameter of the SiGe precipitates in ternary Al-1.02Si-0.95Ge (wt.%) and quaternary Al-1.00Si-0.99Ge-2.57Cu (wt.%) alloys after peak-aging at 120°C (instead of 160°C) will be studied. The coarsening behavior of the SiGe precipitates in the ternary Al-0.55Si-2.02Ge (wt.%) alloy at 160°C will be investigated using TEM, and the specific precipitate-matrix interfacial energy will be calculated.

Tensile tests will be conducted with a ternary Al-0.55Si-2.02Ge (wt.%) alloy using the 810 Material Test System in order to confirm the prediction that the yield strength can be increased significantly for an alloy in which the atomic size misfit is compensated. Furthermore, the volume fraction of voids in this alloy will be determined as a function of strain and aging time using a pycnometer [15]. The fracture behavior of the alloy will be related to the SiGe precipitates based on the dislocation model for void nucleation developed by Goods and Brown [16].

References

[1] E. Hornbogen and E.A. Starke, Jr., Acta Met. 41, 1993, pp. 1-16.

[2] E. Hornbogen, A.K. Mukhopadhyay, and E.A. Starke, Jr., Z. Metallkde 83, 1992, pp. 577-584.

[3] E. Hornbogen, A.K. Mukhopadhyay, and E.A. Starke, Jr., Proc. 3rd Int. Conf. "Aluminum Alloys - Their Physical and Mechanical Properties", Trondheim, Norway, June, 1992, pp. 199-207.

[4] E. Hornbogen, A.K. Mukhopadhyay, and E.A. Starke, Jr., Scripta Met. 27, 1992, pp. 733-738.

[5] E.E. Underwood and E.A. Starke, Jr., Proc. ASTM-NBS-NSF Symp. "Fatigue Mechanisms", Kansas City, Mo., 1978, ASM, 1979, pp. 633-682.

[6] E.E. Underwood, Quantitative Stereology, Addison-Wesley, 1970, pp. 187-188.

[7] W.A. Cassada III, M.S. Thesis, UVa, 1985, pp. 72-75.

[8] I.M. Lifshitz and V.V. Slyozov, J. Phys. Chem. Solids 19, 1961, pp. 35-80.

[9] C. Wagner, Z. Elektrochemie 65, 1961, pp. 581-591.

[10] P. Merle and F.Fouquet, Acta Met. 29, 1981, pp. 1919-1927.

[11] P. Merle and J. Merlin, Acta Met. 29, 1981, pp. 1929-1938.

[12] J.D. Boyd and R.B. Nicholson, Acta Met. 19, 1971, pp. 1379-1391.

[13] M. Bishop and K.E. Fletcher, Int. Met. Rev. 17, 1972, pp. 203-225.

[14] I.J. Polmear, Light Alloys, Hodder & Stoughton, 1989, p. 18.

[15] J.A. Walsh, M.S. Thesis, UVA, 1988, pp. 39-40.

[16] S.H. Goods and L.M. Brown, Acta Met. 27, 1979, pp. 1-15.

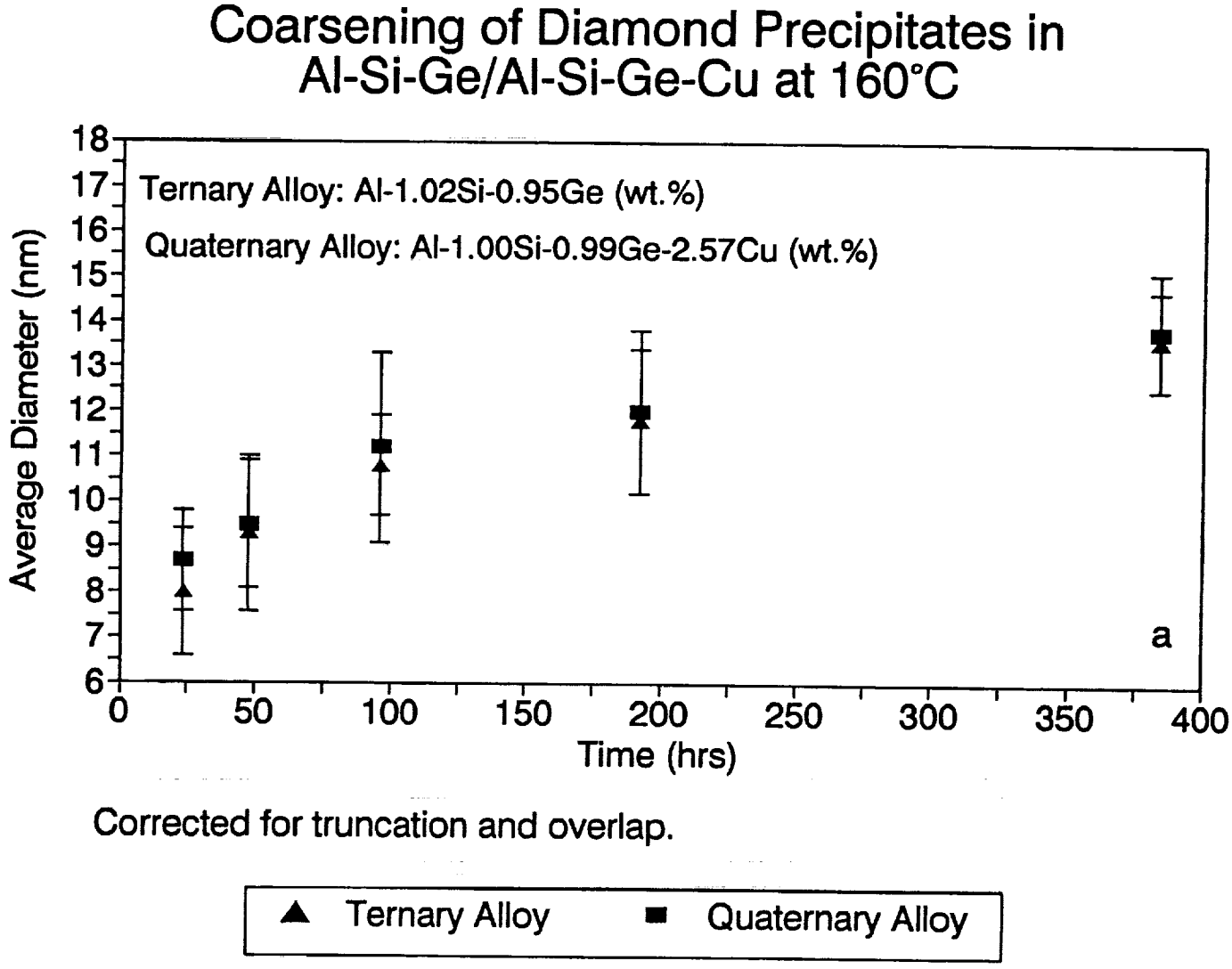

Fig. 1. Coarsening behavior of SiGe diamond structure precipitates in the ternary and quaternary alloys aged at 160°C. (a) Average diameters. (b) Relationship between cube of average radii and aging time. (c) Relationship between fifth power of average radii and aging time.

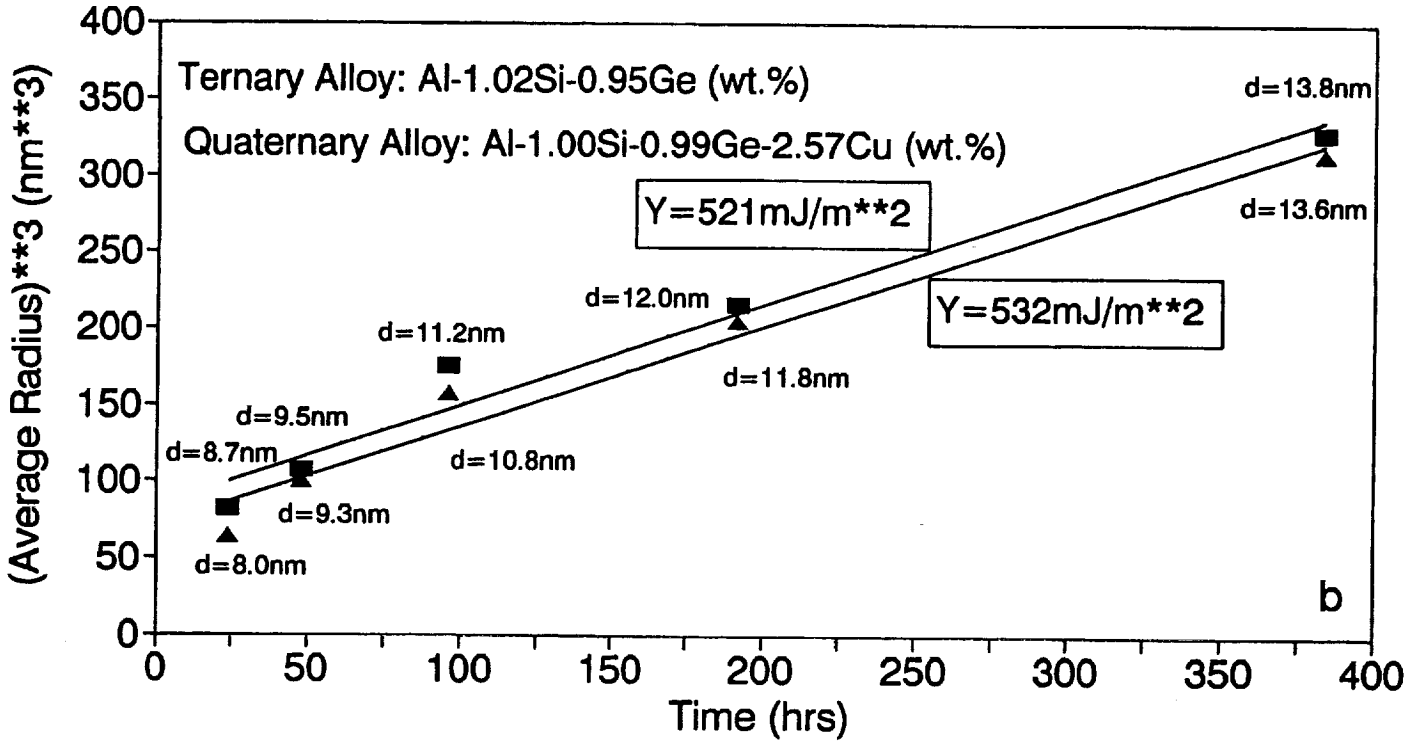

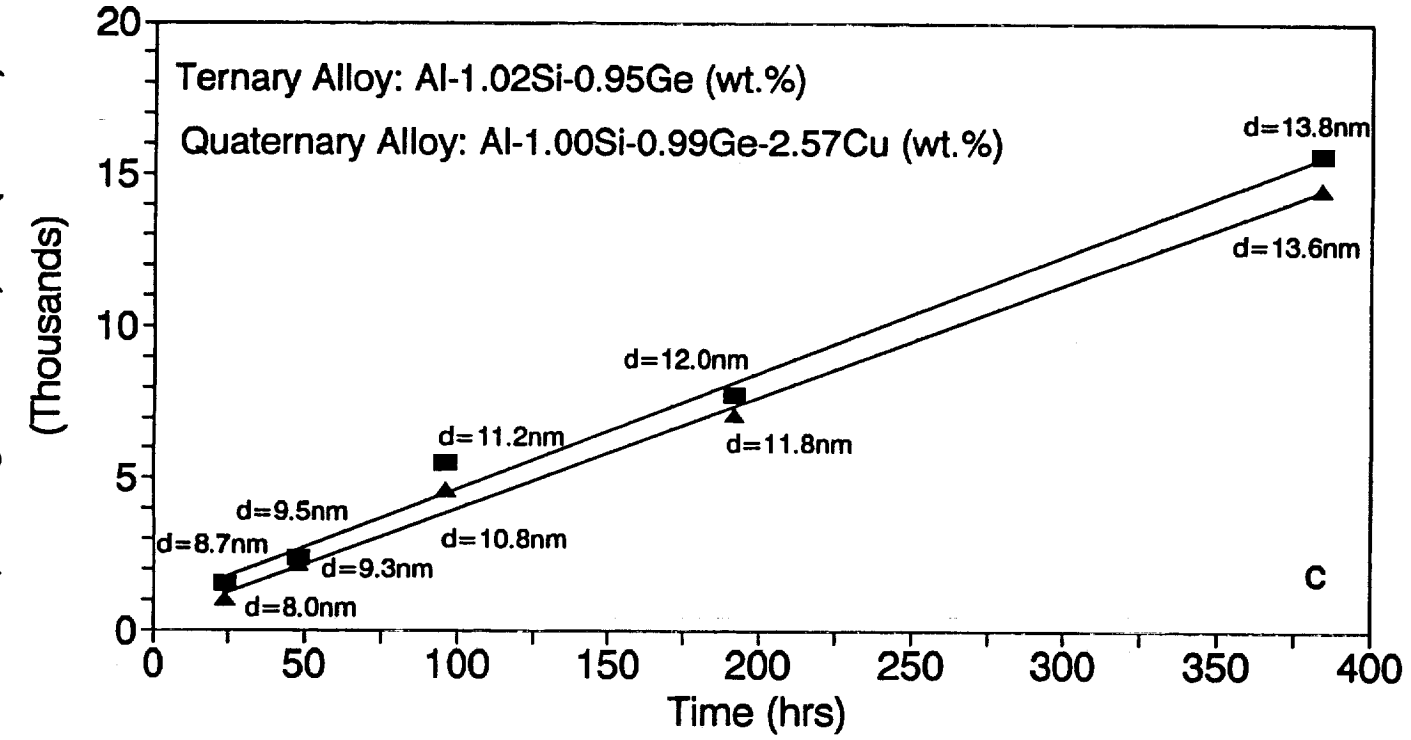

Fig. 1 (continued).

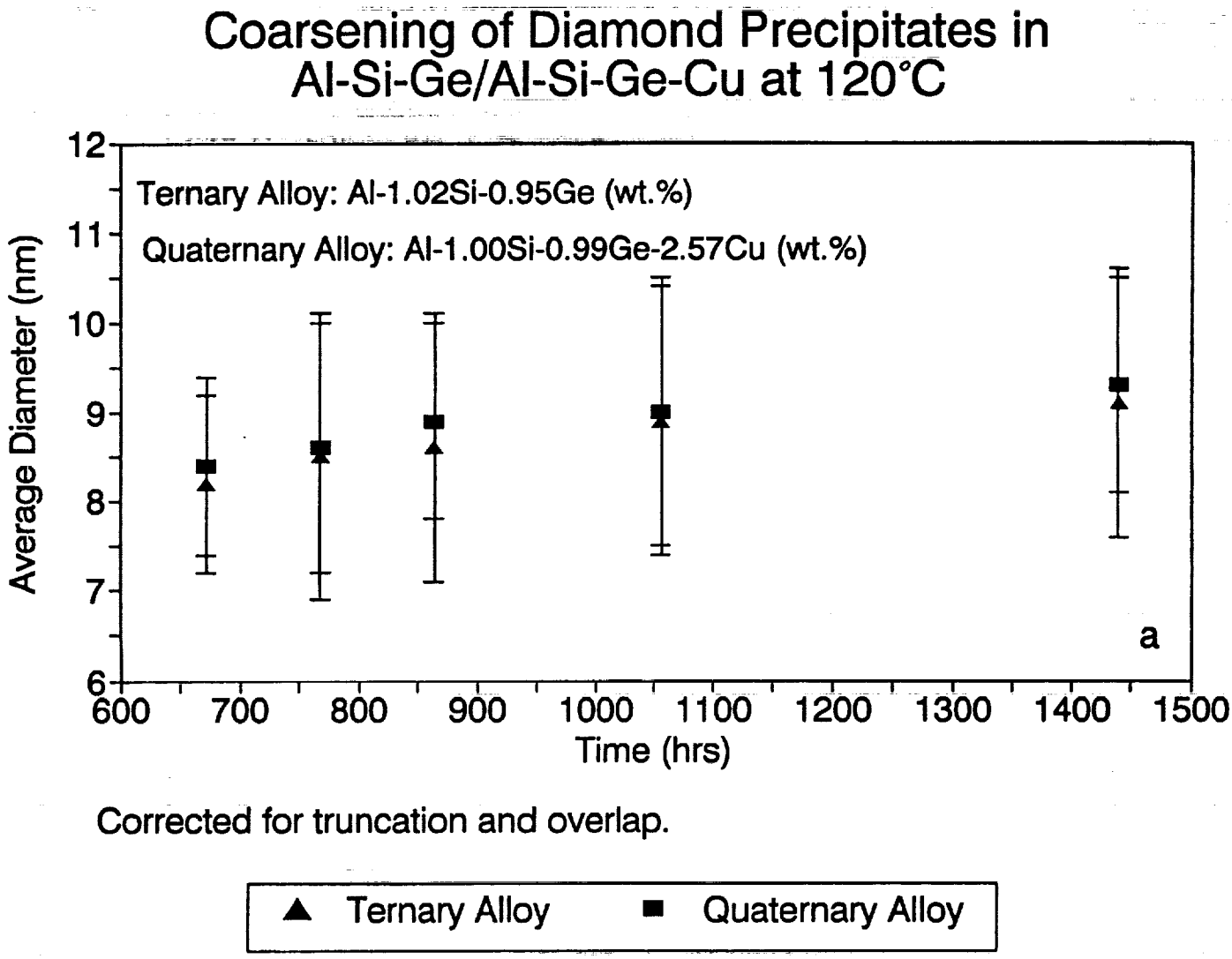

Fig. 2. Coarsening behavior of SiGe diamond structure precipitates in the ternary and quaternary alloys aged at 120°C. (a) Average diameters. (b) Relationship between cube of average radii and aging time. (c) Relationship between fifth power of average radii and aging time.

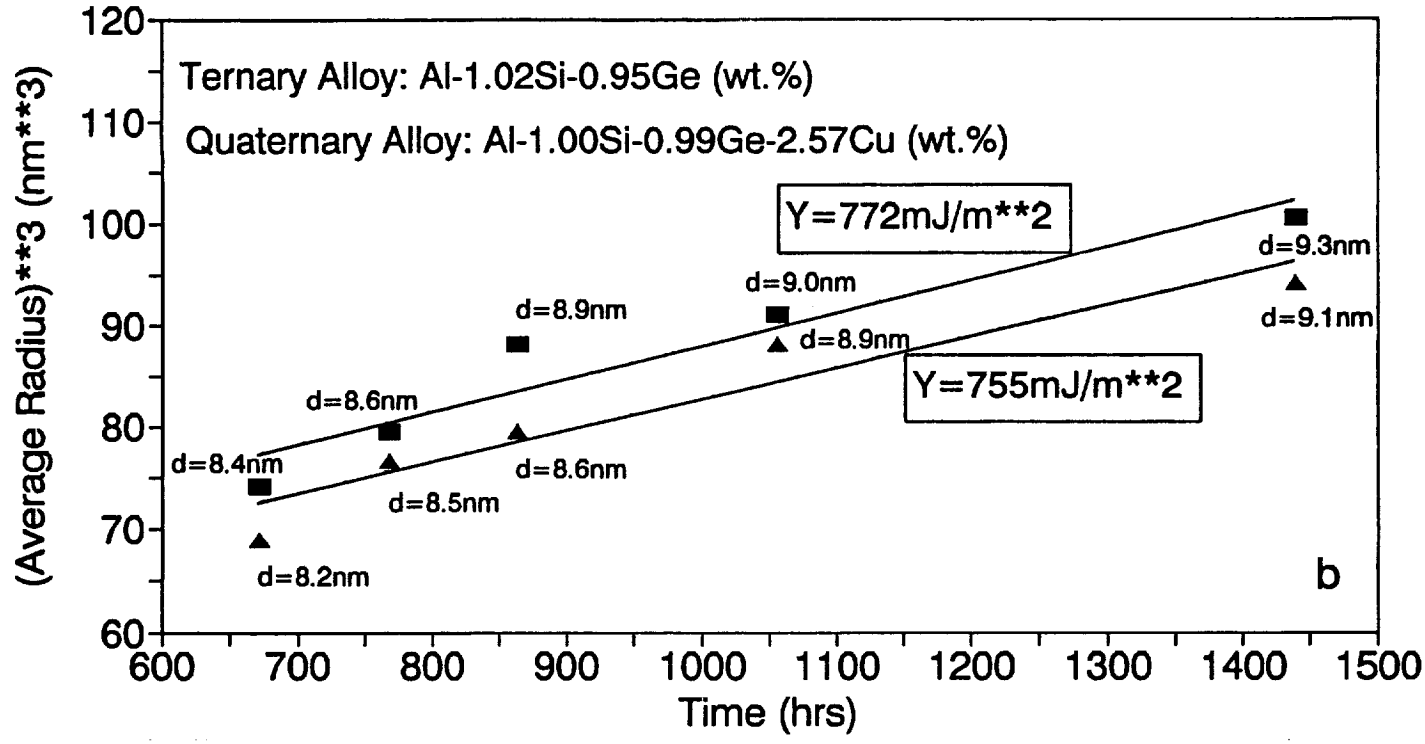

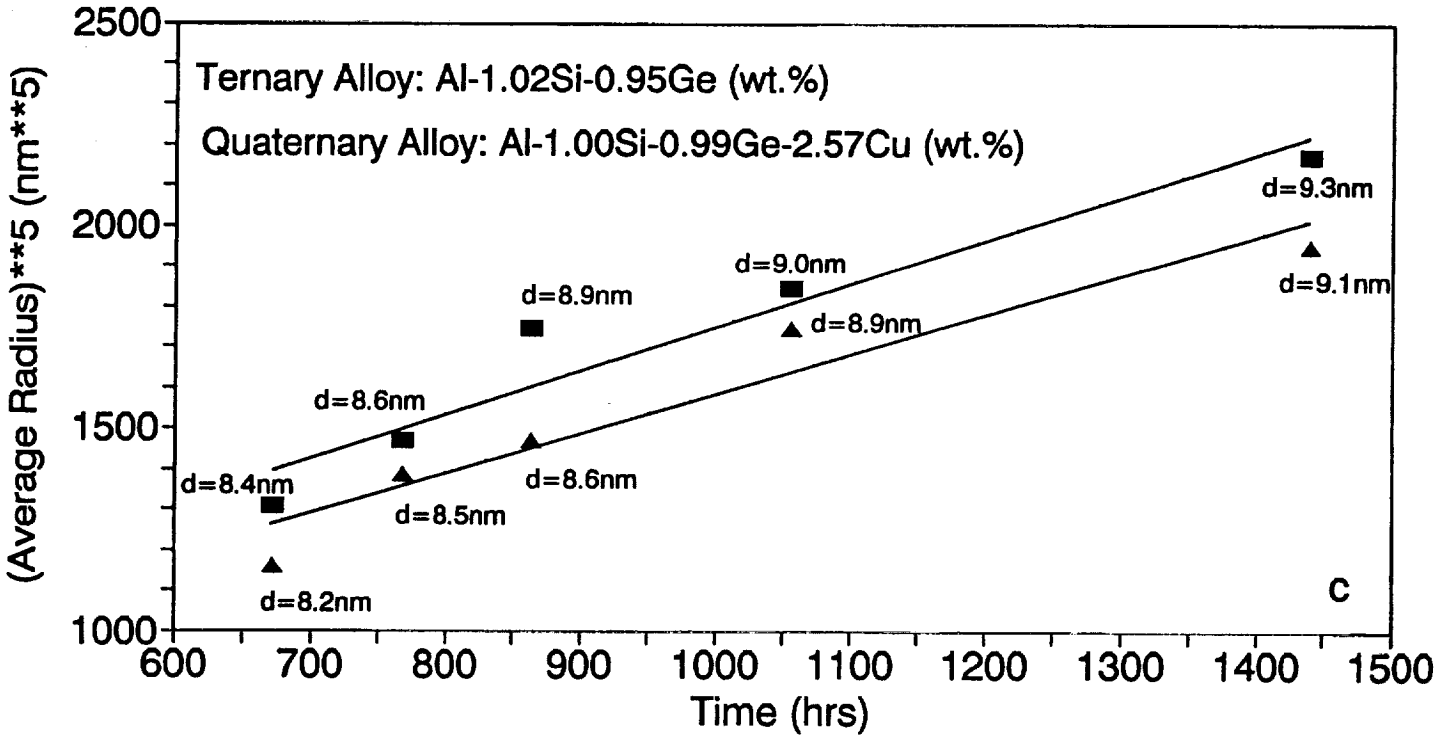

Fig. 2 (continued).

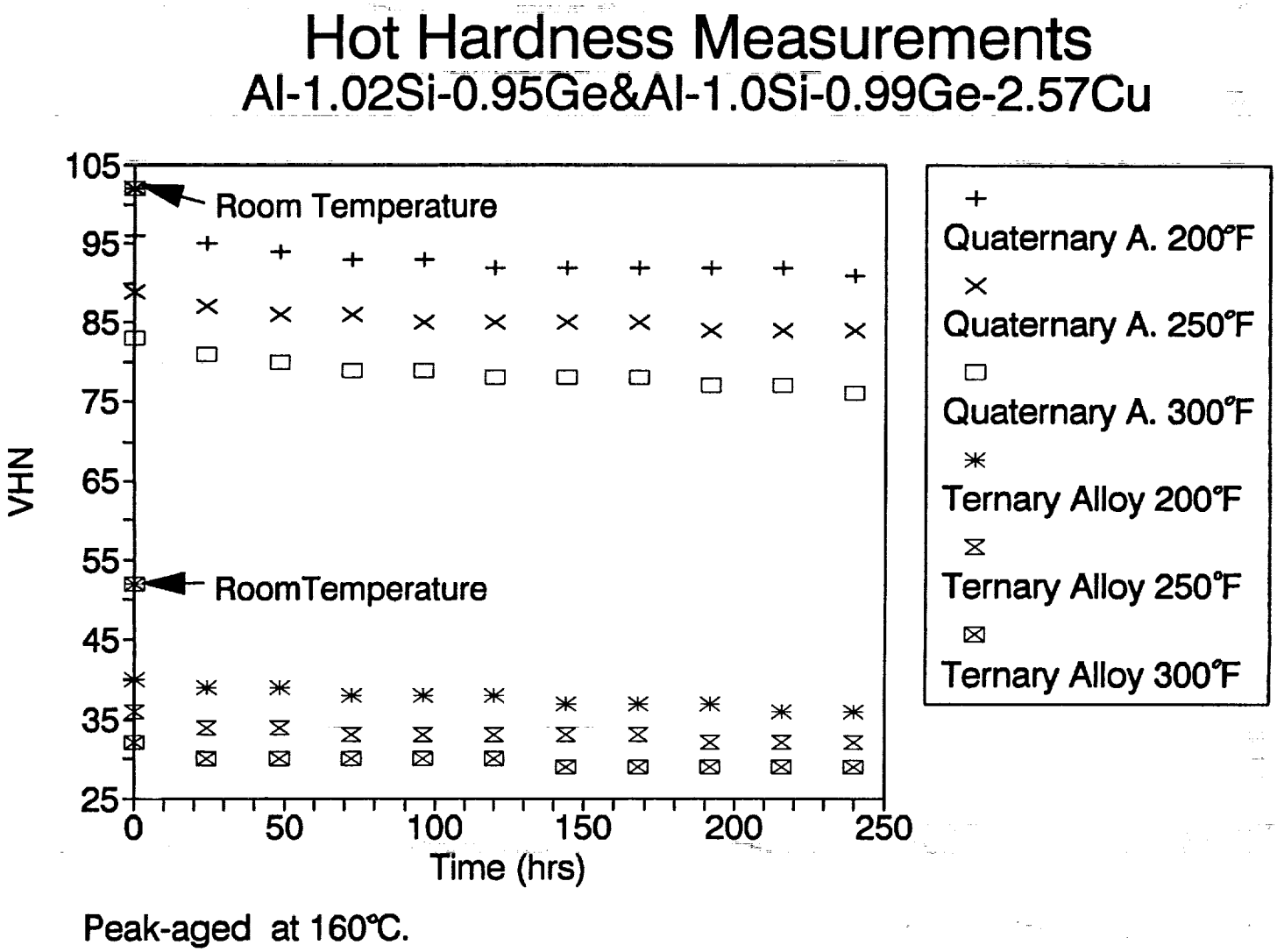

Fig. 3. Vickers microhardness measurements at elevated temperatures for the ternary and quaternary alloys.

Project #10 Environmental Effects in Fatigue Life Prediction: Modeling Crack Propagation in Light Aerospace Alloys

Mark Mason, Sang-Shik Kim and Richard P. Gangloff

Objectives

The long term objective of this project is to establish data and models for predicting environment enhanced fatigue crack propagation (FCP) kinetics for light aerospace structural alloys, particularly titanium and high strength aluminum alloys. This work is necessary to augment computer-based fatigue life prediction codes such as NASA-FLAGRO.

As outlined in the 1993 renewal proposal, there are three approaches to this goal. One task is focusing on improved linear superposition predictions of FCP in the AA7075/aqueous NaCl system. A second study is emphasizing environmental-crack closure interaction effects which govern the complex shape of FCP rate versus stress intensity range laws in Ti-6Al-4V. A third program is focused on environmental fatigue crack propagation in advanced 7000 series alloys and on mechanistic modeling of crack tip damage. The first task will continue through 1994, as Messrs Mason and Richey achieve the MS degrees in the late Fall to Winter of this year. The second project terminated at the end of this reporting period, as Dr. Kim completed his two-year Post-doctoral research appointment and begins employment in Korea. The third program was initiated in January of 1994, upon the arrival of a new graduate student, Mr. Zuhair Gasem.

Project #10A Dynamic Strain Rate Effects on Aqueous Environmental Cracking in AA7075-T651

Mark Mason and Richard P. Gangloff

Objective

The objective of this research is to enhance the predictive capability of damage tolerant fatigue life prediction codes, particularly NASA-FLAGRO. This effort concentrates on determining relevant inputs to a superposition model

in order to more accurately model environmental fatigue crack growth. The focus is on determining the role of crack tip strain rate in intergranular environmental cracking of high strength precipitation hardened aluminum alloys.

Background

The alloy chosen for study was well-characterized AA7075-T651. Wedge-opening-load specimens were machined in the S-L orientation, with the fatigue precrack parallel to the rolling plane of this 5 cm thick plate product. The environment was aqueous 2.5% NaCl with HCl to achieve a pH of 3 and with a sodium-chromate inhibitor to protect the fracture surfaces for microscopic observations. Various mechanical loading modes are being employed.

Although constant load-line displacement experiments revealed a low threshold stress intensity for quasi-static load environmental cracking (K_{ISCC} ≈ 5 MPa√m), the Stage II plateau crack growth rate for this material-environment system is slow ($da/dt_{II} \approx 2 \times 10^{-9}$ m/sec). Corrosion fatigue (CF) crack growth rates (da/dN) are chloride enhanced by five-fold compared to cracking in moist air, as measured at several constant stress intensity ranges (ΔK) and sine-wave loading frequencies (f). Consistent with the findings of Speidel and Holroyd, linear superposition of inert environment fatigue crack growth rate and per cycle integration of da/dt_{II} substantially underpredicts the magnitude of this corrosion fatigue effect.[1-3] In spite of the low value of K_{ISCC}, linear superposition predicts a vanishingly small enhancement of da/dN for normal loading frequencies between 0.005 and 50 Hz. Conventional superposition is ineffective because of the very low da/dt_{II}, compared to the frequencies examined, and as determined by a quasi-static load experiment with the associated slow crack tip strain rates.

Recent Progress

Experimental Results

CF crack propagation rates were measured for 7075-T651 in 2.5%

sodium chloride plus 0.5% sodium chromate at two constant stress intensity range (ΔK) levels of 8.7 and 17 MPa√m with a load ratio (R) of 0.1. Growth rate was measured as a function of the frequency (f) of the sine waveform, varying from 0.01 Hz to 20 Hz. Da/dN versus inverse frequency of sinusoidal loading at each ΔK are shown in Fig. 1. Growth rates at constant ΔK were calculated from least squares fitting of crack length (a) versus cycle number (N) for crack growth increments of at least 2.5 mm, as measured by a direct current potential drop (DCPD) technique. Each WOL specimen had 20 mm of available crack growth to maintain validity of the stress intensity and DCPD solutions for this geometry. The testing procedure involved progressing from highest to lowest frequency in increments of 0.05 a/W (W is specimen width), with at least two higher frequency segments conducted once the stress intensity validity limit of a/W = 0.7 was exceeded to compare with the earlier high frequency data. Final visual crack length measurements were within 3% of those calculated from DCPD measurements, causing only a small deviation of less than 1.0 MPa√m in applied stress intensities compared to the constant target values. The filled circle was measured in a separate experiment with 7075-T651, subjected to continuously decreasing ΔK at 5 Hz. The two horizontal arrows note fatigue crack growth rates for S-L 7075-T651 in moist air at 5 Hz. The data in Fig. 1 show that CF propagation rates in this alloy-environment system are independent of, or perhaps weakly depend on frequency at each ΔK level.

The linear superposition model approximates the environmental enhancement of da/dN as the product of a constant time-based crack growth rate (da/dt) and (1/f). Since the growth rate data for 7075-T651 are independent of frequency for the two applied stress intensities, either da/dt and frequency are functionally related with crack tip strain rate as an important variable, or a mechanism exists unique to corrosion fatigue, precluding the use of stress corrosion cracking inputs to a corrosion fatigue model. The crack surface film rupture model suggests that crack tip strain rate is a key factor in governing da/dt and relating da/dt to da/dN. Since the average crack tip strain rate during fatigue is substantially faster than that

during crack growth under constant displacement, strain rate differences may compromise superposition.

Rising load R-curve-type experiments indicated that increasing the crack tip strain rate from the creep levels typical of the static displacement case does not enhance environmental cracking.[3] Rising load testing does not appear to provide a means of defining da/dt versus K to improve superposition modeling.

7075-T651 is not susceptible to enhanced chloride cracking under high frequency, very low ΔK "ripple" loading. Bayles and coworkers reported a ripple load effect for 7075 in NaCl and at stress intensities below K_{ISCC}, however, the ΔK of the ripple load was above the threshold stress intensity for corrosion fatigue.[4] These literature results likely involved a substantial amount of crack tip process zone volume damage by cyclic deformation and are not useful to test the hypothesis that highly localized near-crack tip surface plastic strains can enhance electrochemical reactions and increase da/dt above the quasi-static load value. In an effort to separate enhanced stress corrosion cracking from near-threshold corrosion fatigue behavior, a very low ripple load was chosen ($\Delta K \approx 0.65$ MPa$\sqrt{m}$). The data plotted in Fig 2 show negligible differences between the constant stress intensity case and the addition of this low ΔK ripple load. These experiments are designed to rupture protective crack surface films, and to promote local dissolution and hydrogen uptake without process zone fatigue damage. Both loading cases show stress corrosion crack velocities that are equivalent to da/dt_{II} generated by earlier constant displacement experiments. Ripple load testing does not appear to provide a means of defining more accurate da/dt versus K relationships for superposition modeling.

Results from corrosion fatigue experiments at a mid-range constant stress intensity ($\Delta K = 10$ MPa$\sqrt{m}$ and $R = 0.1$), and using a trapezoidal waveform, indicate no waveform or time dependence for the loading and unloading rates and hold times tested. Comparison of the two measured corrosion fatigue crack growth rates, calculated by a least squares fit of crack length versus cycle number data presented in Fig 3, shows that CF da/dN is

essentially constant for relatively rapid rise/fall trapezoidal waveforms with K_{max} hold times of 0.1 and 5 seconds. That is, these crack growth rates for environmental cracking under trapezoidal loading show no frequency dependence, as plotted in Fig 1. These results are consistent with the data for the wider frequency range studied with sine loading. (The arrows in Fig. 1 show the resulting fatigue crack growth rates after scaling midrange ΔK da/dN values to a ΔK of 8.7 MPa$\sqrt{m}$ using a Paris relation.) From comparison of adjusted crack growth rates for the trapezoidal loading case, no discernable difference in da/dN exists between loading waveforms.

Verification of these data by future experiments, and exploration of both environmental fatigue cracking mechanisms and crack tip strain rate effects, are necessary in order to model corrosion fatigue crack propagation. Results to date show that simple or modified superposition concepts are not useful approaches for the majority of high strength aluminum alloys.

Comparison with Literature Results

Saff and coworkers successfully employed trapezoidal loading with varying hold times to define da/dt versus K data that were useful in predicting time-dependent da/dN during environmental fatigue crack growth in high strength steels and nickel-based superalloys.[5] The average time-based crack growth rate, $da/dt_{AVERAGE}$, was calculated from the difference in measured da/dN at two hold times that differed by about 100-fold. That is, from linear superposition:

$$\log (da/dt)_{AVERAGE} = \log (\tau_H) - \log (da/dN_{TH} - da/dN_{SHORT\ HOLD\ TIME})$$

where τ_H is the long hold time at any maximum K level where da/dt is determined. The trapezoidal waveform/hold-time results in Figs. 1 and 3, showing da/dN independent of hold time, indicate that this approach will not provide useful da/dt versus K data for superposition modeling of da/dN in the aluminum alloy/chloride system.

The frequency independence of CF da/dN for the 7075-T651 (S-L)/acidified NaCl system shown in Fig. 1 is important and must be explored.

Qualitatively, from the hydrogen environment embrittlement perspective, this result suggests that ionic transport within the occluded crack solution is sufficiently fast so as to supply crack tip surface electrochemical dissolution and atomic hydrogen production reactions without being growth rate limiting for the times investigated[6]. Secondly, these results suggest that such surface reactions progress rapidly to a saturation level and are not rate limiting[6]. Finally, frequency-independent CF suggests that hydrogen diffusion into the crack tip fatigue process zone is rapid and not rate limiting. The first two speculations are consistent with extensive growth rate data and modeling by Wei and coworkers, albeit largely based on studies of aluminum alloys in water vapor and steels in electrolytes[6]. While the transient electrochemical reaction kinetics have not been reported, it is reasonable to expect fast solution mass transport and surface reaction for straining surfaces of aluminum alloys in concentrated chloride solution.

The speculation that hydrogen diffusion is not rate limiting, and the specific data in Fig. 1 are, however, inconsistent with results by Holroyd and Hardie who report a power-law dependence of CF crack growth rate and microscopic cracking mode on reciprocal frequency for S-L oriented 7017-T651 in neutral seawater.[2] (Loading frequencies were varied from 0.1 to 70 Hz and frequency affected da/dN for ΔK levels between about 10 and 25 MPa$\sqrt{m}$. Da/dt_{II} equaled 4×10^{-8} m/sec.) Similar results were presented by Knott and Green for S-L oriented 7475-T6 in acidified sodium-chromate inhibited aqueous chloride[7]. (Loading frequencies were varied from 0.5 to 10 Hz and frequency affected da/dN for ΔK levels that were not clearly reported. Da/dt_{II} was not reported.) These workers rationalize the observation that da/dN increases with decreasing frequency based on increasing time promoting hydrogen diffusion in the crack tip plastic zone. This notion was accepted by Kim and Manning as the basis for modeling the magnitude of frequency-dependent da/dN during CF[8].

It is not understood why the behavior of 7075 (Fig. 1) is different from that of peak aged S-L 7017 and 7475. Hydrogen diffusion could, however, be rate nonlimiting because of very short distances for transport from the crack

tip surface to sites of CF damage in the process zone, or because of dislocation transport of atomic hydrogen. Hardie and Knott did not specify the distance over which hydrogen transports, however, it is probably on the order of 20% of the cyclic plastic zone diameter, or 1 to 2 μm beneath the crack tip surface[9]. If this distance is sufficiently large to limit hydrogen diffusion, because of the slow hydrogen diffusivity in aluminum (perhaps 10^{-10} cm^2/sec or roughly 25 seconds for extensive hydrogen transport over 1 μm), then either dislocation transport or discontinuous fatigue crack advance could eliminate the rate limitation, resulting in the observed frequency independence[9].

Selines and Pelloux reported frequency-independent CF at low ΔK for L-T 7075-T6 in neutral NaCl; da/dN equaled 5.1 x 10^{-4} mm/cycle at ΔK of 8.7 MPa√m for slow-rising sawtooth loading at frequencies of 0.1, 1 and 10 Hz[10]. These results are in excellent agreement with the low ΔK data in Fig. 1. In contrast at high ΔK, CF growth rates increased by about 50% with this two order of magnitude decrease in frequency. (At ΔK of 17 MPa√m, for example, da/dN increased from 2 x 10^{-3} mm cycle to 3.4 x 10^{-4} mm cycle.) This result contradicts the high ΔK data in Fig. 1, and is consistent with the general observation that CF in many material-environment systems is frequency-independent at lower stress intensities and frequency-dependent (either purely time-dependent or time-cycle-dependent) at higher ΔK levels[11]. Additionally, low ΔK CF in 7075-T6 was independent of the rising load rate for fixed cycle frequency, however, faster rising load rates resulted in reduced da/dN at higher ΔK[10].

In early work, Speidel recognized that both "true corrosion fatigue", which is environment enhanced but frequency-independent and cycle dependent da/dN; and "stress corrosion under cyclic loading", which is environment enhanced frequency-dependent (or cycle-time dependent) da/dN, can occur depending on a variety of mechanical, metallurgical and chemical variables[12]. His limited data showed "true corrosion fatigue" for S-L 7075-T73 in 3.5% NaCl at 80°C (ΔK levels of 12 and 15 MPa√a and frequencies from 0.001 to 2 Hz). While these results and qualitative characterizations are

consistent with the data in Fig. 1, Speidel did not comment on the mass transport and surface reaction origins for these different behaviors. Speidel did not speculate on the reason why some aluminum alloys show both phenomena, while others only show frequency independent behavior in electrolytes. These notions will be explored as we analyze the data from this study.

The film rupture/transient dissolution model predicts that da/dN is proportional to the product of reciprocal loading frequency, the electrochemical dissolution charge passed between film rupture events, and the average crack tip strain rate per load cycle[13,14]. Estimation of these terms for typical repassivating metals in various electrolytes leads to the predictions that the time based crack growth rate (da/dt) increases with the square root of the crack tip strain rate (or approximately with the square root of f), while CF da/dN is proportional to $f^{(\beta-1)}$ where β is on the order of 1/2[11]. These predictions are inconsistent with the results presented in Figs. 1 and 2, and with the previously reported independence of da/dt on the applied rising load rate.

Conclusions

1. Time-based environmental crack growth rates, input to the linear superposition model, are an order of magnitude too small to predict the measured significant effect of environment on fatigue crack growth for the susceptible 7075/aqueous NaCl system and typical loading frequencies.
2. 7075-T651 is not susceptible to enhanced chloride cracking under high frequency, very low ΔK "ripple" loading. Applied strain rate does not appear to additionally affect the time-based rate of environmental cracking.
3. Corrosion fatigue crack propagation rates for corrosion fatigue of S-L oriented 7075-T651 in acidified and chromate inhibited aqueous NaCl are independent of, or only weakly depend on loading frequency.

4. There is no discernable difference in the effect of sine and trapezoidal cyclic loading waveforms on fatigue crack propagation in this alloy-environment system. Corrosion fatigue crack growth rates at two constant stress intensity levels are independent of hold time at maximum stress intensity and of total cycle time. Hold time-based corrosion fatigue experiments do not appear to provide improved time-based crack growth rate data for use in superposition modeling.

Future Direction

The loading frequency independence of corrosion fatigue crack propagation kinetics in S-L 7075-T651/NaCl will be confirmed for high ΔK levels.

Corrosion fatigue crack growth rates will be measured as a function of wide-ranging hold times to confirm the inability of the hold-time CF approach to provide improved da/dt data for linear superposition modeling.

Experiments involving trapezoidal load waveforms will be utilized, along with crack tip strain rate model estimations, to probe the effect of crack tip strain rate on da/dt, and to relate such data to CF. Future testing strategies will involve adjusting the loading portion of the trapezoidal waveform, while maintaining a constant cycle period.

Scanning electron microscopy will compare the environmental fracture morphologies produced by constant displacement, constant displacement rate, corrosion fatigue, ripple loading, and trapezoidal loading experiments. We will seek to define the similarities and differences in the microscopic modes of quasi-static and fatigue cracking, as a tool to determine the proper way to model corrosion fatigue.

Mr. Mason will commence employment with Allied Signal at the Hopewell Plant as a Reliability Engineer upon the completion of his Master of Science degree. His anticipated completion date is September of 1994.

References

1. M.O. Speidel: Metall. Trans. A, (1975), 6A, pp. 631-651.

2. N.J.H. Holroyd and D. Hardie: Corrosion Science, (1983), 23, pp. 527-546.

3. M.E. Mason, Sang-Shih Kim, and R.P. Gangloff: NASA-UVa Light Aerospace Alloy and Structures Technology Program. University of Virginia, Proposal No. MSE-NASA/LaRC-5691-93, July 1993.

4. B.A. Bayles, P.S. Pao, S.J. Gill, and G.R. Yoder (1993): in Proceedings of the 47th Meeting of the Mechanical Failures Prevention Group, Virginia Beach, VA, April 13-15, 1993.

5. H.D. Dill and C.R. Saff, "Environment-Load Interaction Effects on Crack Growth", Advanced Metallic Structures, McDonnell Aircraft Company, St. Louis, MO, Report No. AFFDL-TR-78-137, August, 1978.

6. R.P. Wei and R.P. Gangloff, in Fracture Mechanics: Perspectives and Directions, ASTM STP 1020, R.P. Wei and R.P. Gangloff, eds., ASTM, Philadelphia, Pa, pp. 233-264 (1989).

7. A.M. Green and J.F. Knott, in Advances in Fracture Research, ICF 7, K. Salama, K. Ravi-Chandar, D.M.R. Taplin and P. Rama-Rao, eds., Pergammon Press, Oxford, pp. 1747-1756, 1989.

8. Y.H. Kim and S.D. Manning, in Fracture Mechanics, Fourteenth Symposium, Volume 1, ASTM STP 791, J.C. Lewis and G. Sines, eds., ASTM, Philadelphia, PA, pp. 446-462, 1983.

9. R.S. Piascik and R.P. Gangloff, "Environmental Fatigue of an Al-Li-Cu Alloy: Part III - Modeling of Crack Tip Hydrogen Damage", Metall. Trans. A, in review (1994).

10. R.J. Selines and R.M. Pelloux, Met. Trans., Vol. 3, pp. 2525-2531, 1972.

11. R.P. Gangloff, in Environment Induced Cracking of Metals, R.P. Gangloff and M.B. Ives, eds., NACE, Houston, TX, pp. 55-109 (1990).

12. M.O. Speidel, in Stress Corrosion Research, Hans Arup and R.N. Parkins, eds., Sijthoff & Noordhoff, Alphen aan den Rijn, Netherlands, pp. 117-176, 1979.

13. F.P. Ford and P.L. Andresen, in Advances in Fracture Research, K. Salama, K. Ravi-Chandar, D.M.R. Taplin and P. Rama-Rao, eds., Pergammon Press, Oxford, pp. 1571-1584, 1989.

14. P.L. Andresen and F.P. Ford, J. Pressure Vessel Technology, Vol. 115, pp. 353-358, 1993.

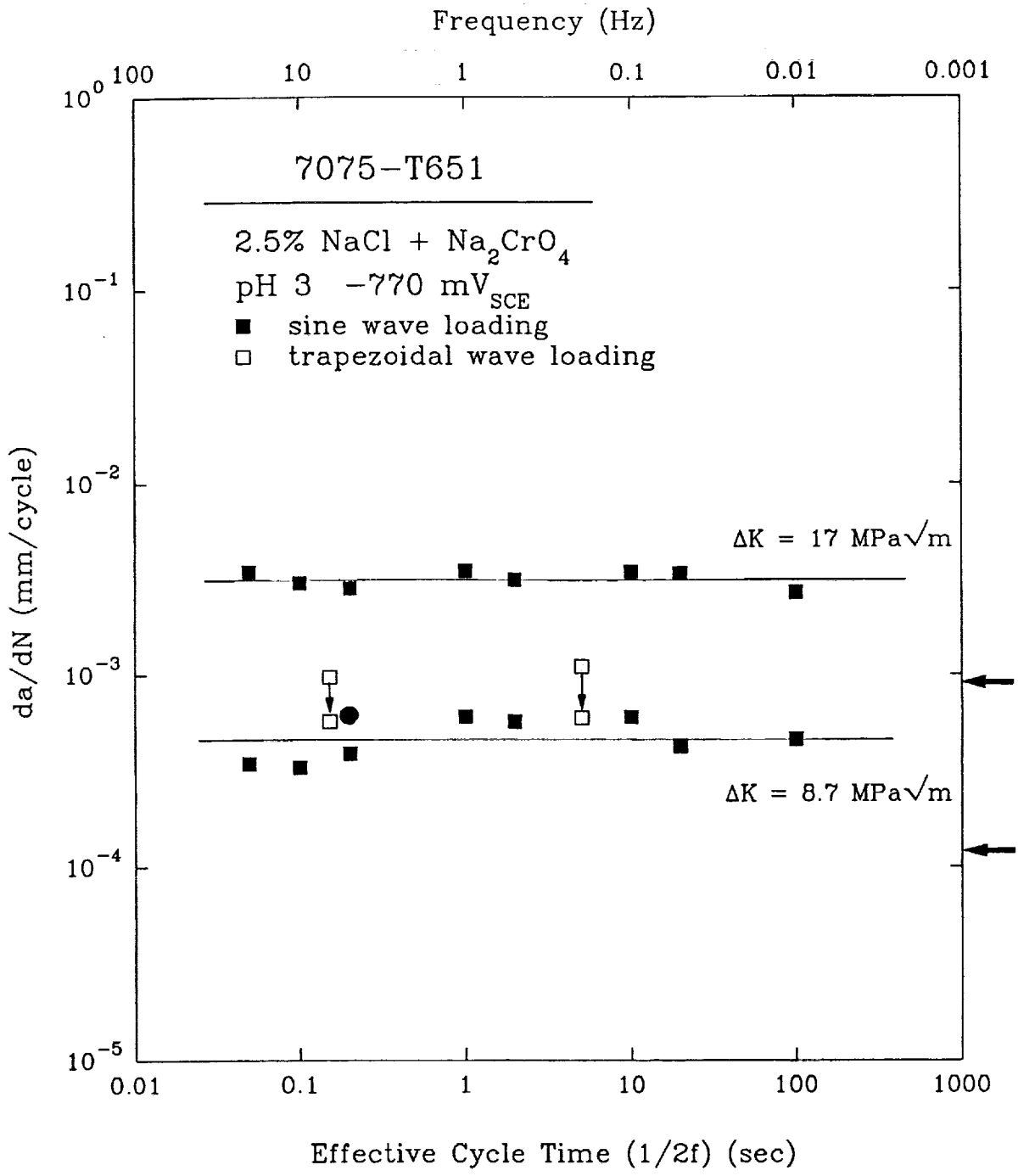

Fig 1 Frequency Dependence at fixed ΔK

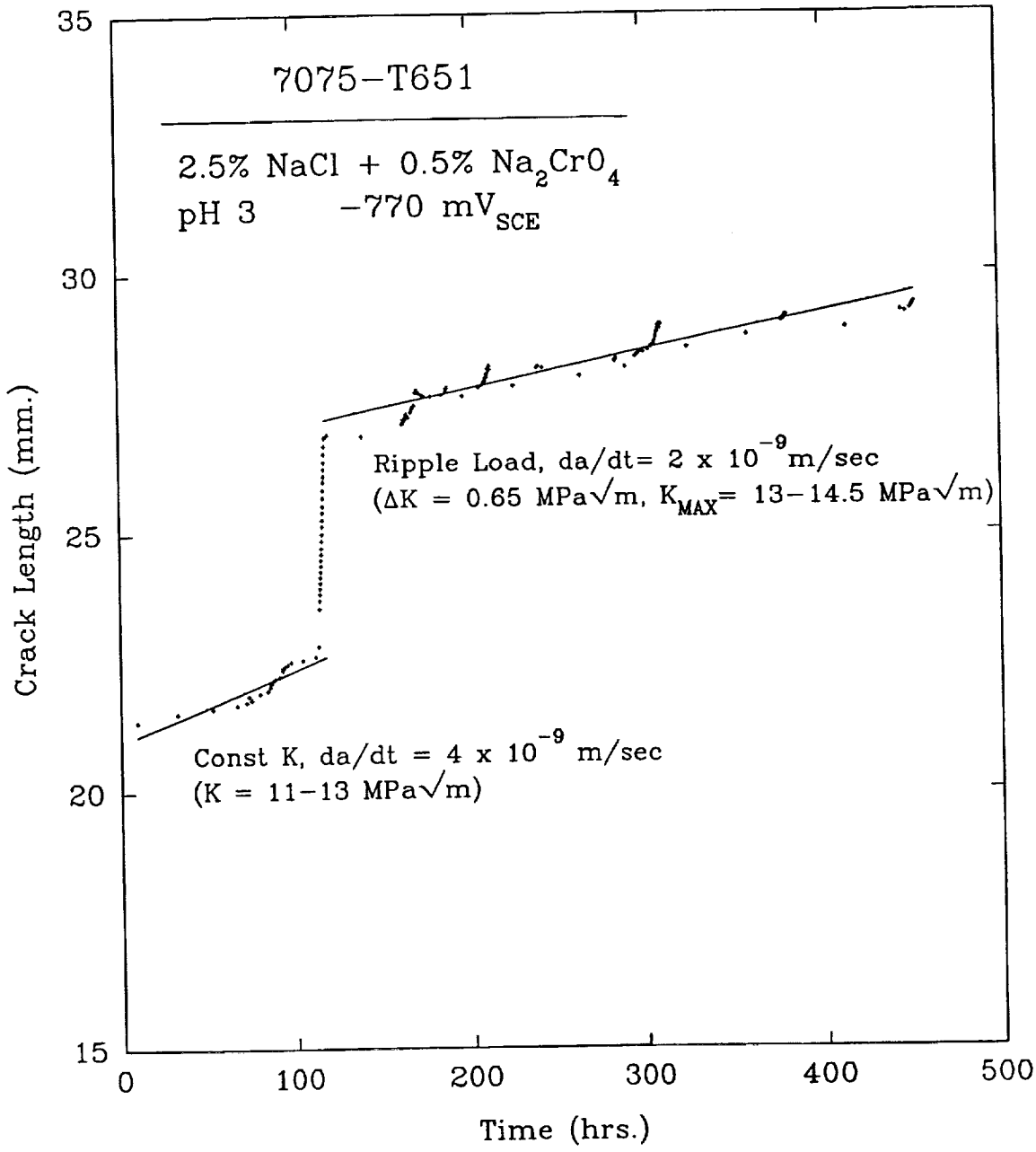

Fig. 2 – Low ΔK Ripple Loading

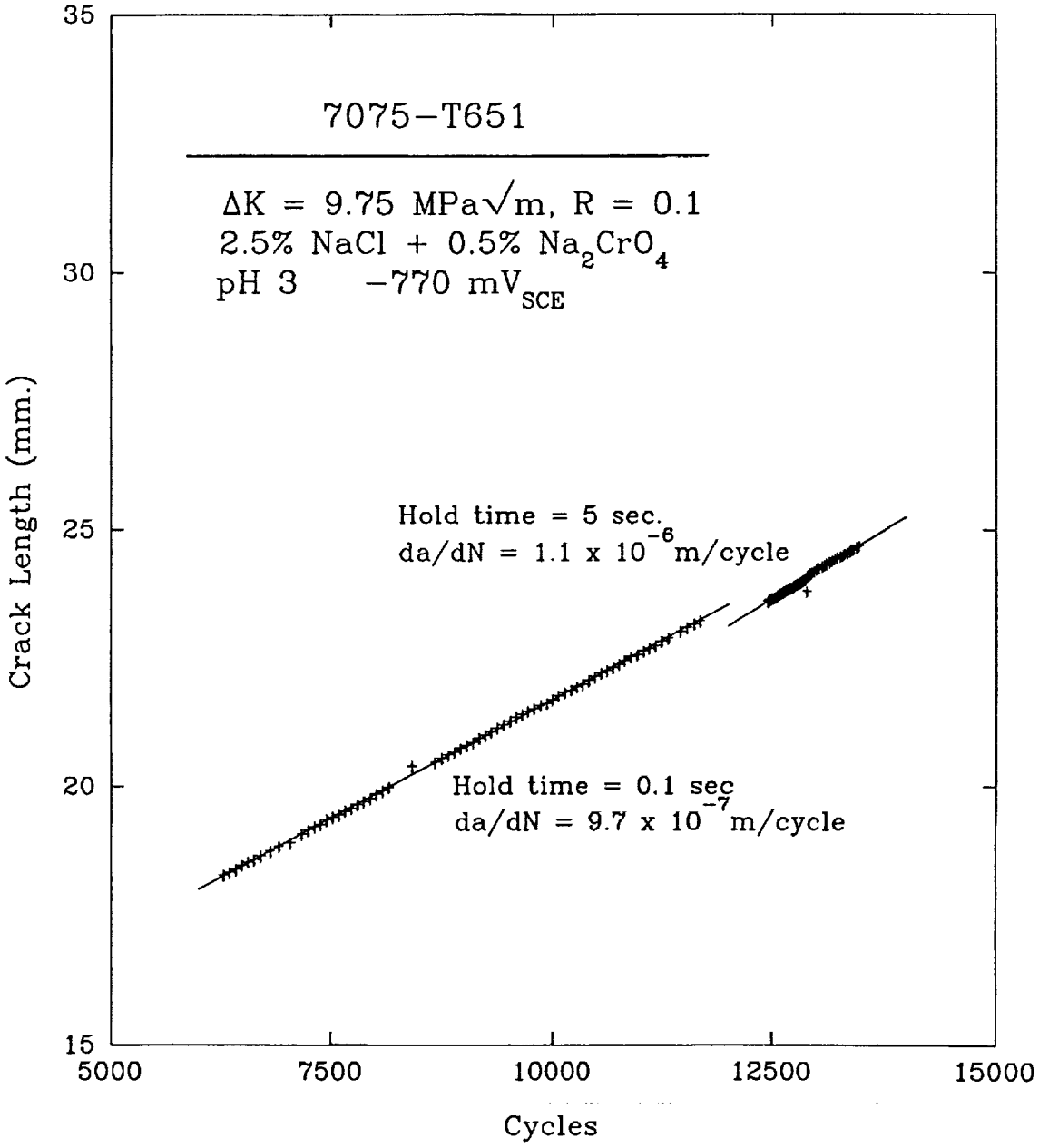

Fig 3 – Trapezoidal Loading at a constant ΔK

Project #10B **Environmental Effects on Fatigue Crack Propagation and Closure in Titanium Alloys**

Sang-Shik Kim and Richard P. Gangloff

Objective

The objective of this research is to enhance the predictive capability of existing damage tolerance fatigue life prediction codes, particularly NASA FLAGRO, by incorporating environmental effects on FCP behavior. Specific goals are to:

- oo Characterize intrinsic and extrinsic environmental da/dN-ΔK kinetics for a titanium alloy in aggressive environments, as a function of R ratio.
- oo Understand environment-sensitive crack closure phenomena and mechanisms, including the effects of ΔK and R ratio.
- oo Understand the contributions to so-called transition behavior in FCP rate versus stress intensity laws.

Current Status

This project terminated at the end of this reporting period. Results to date contribute to our understanding of the factors that influence the extrinsic and intrinsic stress intensity range dependence of FCP rate. This work is presented in the following paper which is being prepared for journal publication.

ENVIRONMENT AND R-RATIO EFFECTS ON FATIGUE CRACK PROPAGATION TRANSITIONS IN Ti-6Al-4V (ELI)

Introduction

Aluminum-[1-5], titanium-[6-12], and nickel-based alloys[13] as well as steels[14,15] exhibit a complex relationship between fatigue crack propagation (FCP) rate (da/dN) and stress intensity range ($\Delta K = K_{max} - K_{min}$). This behavior is reasonably described by multiple power law segments, compared to the single power law proposed by Paris and latter modified to include near-threshold cracking[16]. Crack growth laws must be well characterized and

understood in order to predict da/dN-ΔK relationships for use in damage tolerant FCP life prediction codes such as NASA-FLAGRO[17].

Several mechanisms have been proposed for changes in the power-law exponent with varying ΔK, as summarized in the Discussion, however, the dominant causes are not well understood[1-9,14,15,18]. These mechanisms involve intrinsic crack tip plasticity-based and environmental damage mechanisms; the relationship between da/dN and ΔK can also be affected by extrinsic fatigue crack closure. In spite of the significance of crack closure in determining FCP rates[19,20], this factor has not been typically considered in tests of the proposed causes of transitions in FCP kinetics.

For FCP in steels and aluminum alloys in ultra-high vacuum, Petit demonstrated that Stage II FCP is well described by single power-law relationships, over a wide ΔK range nearing the threshold[18,21]. Single power law behavior was confirmed by experiments with precipitation hardened aluminum alloys in vacuum, with no evidence for a Stage II to I transition at low ΔK[1,2,22,23]. Similar behavior was observed for an α/β titanium alloy in ultra-high vacuum or highly purified argon, with the important addition of a single transition (at a relatively high effective ΔK level) to a crystallographic mode of FCP (Stage I-like) which persisted with decreasing ΔK to the near-threshold regime[18,21,24]. Single slope transitions were also reported for α/β titanium alloys in less inert environments, where the environmental effect could not be ruled out. Critically, multiple slope transitions were reported for the same alloys in moist air, distilled water or aqueous chloride environments[8,10,12]. It is premature to conclude that an environmental element is a requisite for multi-slope transition behavior, however, this is a possibility.

The objective of this study is to establish the closure-free (intrinsic) transition FCP behavior for Ti-6-4 in moist air and aqueous 1% NaCl, with emphasis on higher ΔK (Stage II) conditions. This alloy is selected because FCP is strongly environment-sensitive, with multiple transitions reported for moist air and aqueous chloride environments[6-8,10-12,25,26], but with a single Stage II power-law dependence of da/dN on ΔK for ultra-high vacuum[21]. The

effect of crack closure is approximated by unloading compliance measurements for each environment, coupled with determination of the effect of stress ratio ($R = K_{min}/K_{max}$) on crack closure and environmental FCP.

Experimental Procedure

Mill annealed (MA: four hours at 750°C, furnace cooled) Ti-6-4 (Ti-6.17Al-4.33V-0.025V-0.011N-0.19Fe-0.12O-0.0055H in wt.%) in the ELI (extra low interstitial) condition was used for the present study. The microstructure of 12.7 mm thick plate of this alloy consists of equiaxed α, with an average grain size of 8 to 10 μm and a small quantity of retained β, as shown in Figure 1. Values of yield strength, K_{ISCC} for 3.5% NaCl, and K_{IC} are 940 MPa (vendor measured), 23 to 35 MPa$\sqrt{m}$, and 65 to 75 MPa$\sqrt{m}$, respectively, for MA Ti-6-4[10,27]. LT-orientation compact tension (CT) specimens with width (W) of 63.5 mm and thickness (B) of 6.4 mm were prepared from the central portion of the plate. Specimens were fatigue precracked at a constant K_{max} of 20 MPa$\sqrt{m}$ to a/W of 0.25.

FCP experiments were conducted in a servo-hydraulic machine in moist air and 1% NaCl at a fixed electrode potential of -500 mV_{SCE}. Constant R ratios of 0.1, 0.4 and 0.7 were employed. A sinusoidal loading frequency of 5 Hz was selected to produce a substantial environmental effect in a reasonable time of 5 to 7 days[10]. Da/dN-ΔK behavior was established for continuously decreasing ΔK by computer-automated load-shedding with C equalling -0.06 mm^{-1} in accordance with ASTM E647-91. Limited FCP experiments were performed with a constant K_{max} of 27.5 MPa$\sqrt{m}$; R increased from 0.1 to 0.85 with decreasing ΔK. Crack length and crack closure were measured by the global unloading compliance technique with a cantelever-clip gauge mounted across the notch mouth for both environments. Crack length (a) was calculated from unloading compliance and stored in the computerized data acquisition system at Δa/W increments of 0.002. Da/dN was established by using an incremental polynomial method to somewhat average local data variations compared to the secant method. Load-displacement data pairs were analyzed to identify the crack closure load (P_{cl}) corresponding to the first

deviation in slope, operationally defined at an offset of 2% from the linear compliance response. Load-displacement data were simultaneously recorded with an X-Y recorder. P_{cl} values, manually determined from the first nonlinearity in the unloading portion of these data, agreed with the automated calculations of closure load which are reported here.

The aqueous environmental system is shown in Figure 2. The plexiglass chamber is mechanically sealed with a rubber gasket to the top and bottom portions of the CT specimen. These sections are connected with a flexible Latex rubber sheet to contain the solution while not interfering with compliance measurements of fatigue crack closure. The solution, 1 wt% NaCl dissolved in distilled water, was continuously circulated through the chamber at a rate of approximately 50 ml/min. The CT specimen is maintained at a fixed electrode potential of -500 $\pm$ % mV_{SCE} with a potentiostat, platinum mesh counter electrode, and two Ag/AgCl reference electrodes positioned on both sides of the specimen along the crack path. The counter electrode is isolated from the chamber and positioned in separate beaker.

Experimental Results

Figure 3 presents da/dN versus applied ΔK for Ti-6-4 in: (a) moist air and (b) 1% NaCl at -500 mV_{SCE} at R ratios of 0.1, 0.4 and 0.7 at 5 Hz. Figure 3b includes FCP rates at a constant K_{max} of 27.5 MPa$\sqrt{m}$ with varying R ratios from 0.9 to 0.1. Regardless of environment, da/dN for Ti-6-4 increases with increasing R at any ΔK. The R-ratio effect is largest in the low ΔK regime for each environment. Figure 4a demonstrates the deleterious effect of the moist air and aqueous NaCl environments relative to FCP in inert highly purified argon[24]. Similar degradations are observed at higher R ratios. The environmental effect is dominant in the low and high ΔK regimes, while it is lessened at intermediate ΔK levels, regardless of R ratio. Figure 4a shows the results of the current experiments are in good agreement with literature data for MA Ti-6-4 in aqueous NaCl at identical R and loading frequency[10,24].

The da/dN versus applied ΔK relationships for Ti-6-4 in each

environment and R-ratio are complex, with multiple power law regions. The NaCl environment promotes a more complex relationship compared to FCP in moist air. To analyze this behavior, crack growth rate data were fit with power law segments which vary with ΔK. Two parameters, m (the slope of the power law on a logarithmic plot) and ΔK_T (the applied stress intensity range at the intersection of adjacent power laws) characterize FCP transition behavior. This approach is illustrated in Figure 4a for FCP in the Ti-6-4/moist air and NaCl systems at R of 0.1. Extensive da/dN-ΔK data were analyzed by least squares of each power law segment to define m and ΔK_T, with alternate values plotted for clarity in Figure 4a. This analysis approach is approximate because FCP behavior is not necessarily defined by power laws, and the stress intensity interval for each power law was subjectively defined.

Table I summarizes the effects of R-ratio and environment on m_i and ΔK_{Ti} defined in Figure 4a. Several trends are notable. For FCP in moist air, da/dN exhibits similar three-transition behavior at each stress ratio. Aqueous NaCl further complicates the shape of da/dN versus ΔK for Ti-6-4 at R ratios of 0.1 and 0.4, where an additional transition (transition IIA) is evidenced between ΔK_{T1} and ΔK_{T2}. (Transition IIA is not observed at R of 0.7, or at a constant K_{max} of 27.5 MPa$\sqrt{m}$.) Otherwise, the transition behavior is qualitatively similar for the two environments. These results are similar to the limited inert environment data in Figure 4a, where m_3 and m_2 for argon are equivalent to the moist air (3.4 and 8.3) and chloride (3.9 and 6.0) values for R of 0.1; ΔK_{T2} is only somewhat higher. For moist air, Increasing R tends to lower each of the transition points; ΔK_{T0}, ΔK_{T1} and ΔK_{T2}; with a more complex dependence indicated for FCP in NaCl. Since the shape of da/dN versus ΔK may be influenced by closure, the complex effects of R in Table I are not detailed, pending consideration of da/dN versus the effective stress intensity range.

Table I
Effects of R-ratio and environment on m_i and ΔK_{Ti} for mill annealed Ti-6-4.

Env.	R	m_3	ΔK_{T2} (MPa√m)	m_{2A}	ΔK_{T2A} (MPa√m)	m_2	ΔK_{T1} (MPa√m)	m_1	ΔK_{T0} (MPa√m)
Air	0.1	3.4	14.9			8.3	10	4.0	7.2
	0.4	3.3	12			5.6	7.4	4.9	6
	0.7	3.7	11			4.8	6.1	3.2	
NaCl	0.1	3.9	14.4	10.8	12.7	6.0	9.4	3.8	7
	0.4	5.3	9.5	12.6	9	3.8	7.0	4.8	4.4
	0.7	7.0	10.5			5.3	6.9	3.1	3.9
	V*	2.9	12.3			5.4	7.0	3.2	

V*: Constant K_{max} of 27.5 MPa√m with varying R- ratio.

In this study, the role of closure is simply approximated by the effective stress intensity range (ΔK_{eff}), calculated based on the difference between the applied K_{max} and K_{cl} calculated from the globally measured P_{cl}. Da/dN, correlated with ΔK_{eff}, may be reasonably closure-free and hence representative of intrinsic FCP kinetics. Determination of the precise crack tip stress intensity range, which drives FCP in concert with crack closure, is complicated by the mechanics of the closure process; it is unlikely that closure begins below a single stress intensity, but rather is distributed over a portion of the load-cycle. Crack closure effects are particularly ill-defined at lower applied ΔK levels. The following results must be improved by local measures of closure contact during environmental FCP, coupled with micromechanical modeling of such closure.

The effect of crack closure on da/dN depends on applied ΔK, R and environment. The normalized crack closure stress intensity factor, K_{cl}/K_{max}, is plotted versus applied ΔK for Ti-6-4 in moist air and 1% NaCl at applied R-ratios of 0.1, 0.4 and 0.7. At R of 0.7, crack closure is not detected for either environment, K_{cl} is therefore less than K_{min} and applied ΔK is not closure-affected. At R of 0.4, no crack closure is detected for the moist air case, while

K_{cl} exceeds K_{min} for FCP 1% NaCl. At R of 0.1, a similar closure level is evidenced for each environment, suggesting an important influence of K_{cl} on the applied ΔK for each case. No closure was detected at any applied ΔK level in the constant K_{max} test in 1% NaCl. The data in Figure 5 are consistent with literature results; Shih and Wei reported that K_{min} exceeded K_{cl} above R of 0.3 for MA Ti-6-4 in moist air[24]. When present, the closure is particularly dominant in the low ΔK region and gradually decreases with increasing ΔK for each environment.

The data in Figure 5 were employed to examine the effects of R and environment on the intrinsic stress intensity dependence of FCP rate for Ti-6-4. Figure 6 presents da/dN versus the effective stress intensity range ($\Delta K_{eff} = K_{max} - K_{cl}$) for Ti-6-4 in moist air and 1% NaCl, at three R-ratios, mirroring the data in Figure 3. In so far as this procedure eliminates the crack closure effect on ΔK, the data in Figure 6 demonstrate that increasing stress ratio has no effect on environmental FCP in Ti-6-4. Crack growth in the chloride is enhanced relative to FCP in moist air at any ΔK_{eff}. The complex dependence of da/dN on ΔK_{eff} remains, regardless of R ratio and analogous to the da/dN versus applied ΔK in Figure 3. Figure 4b is analogous to Figure 4a and includes closure-corrected data for MA Ti-6-4 in ultra-high vacuum[21]. This figure shows similar multiple-sloped power laws for intrinsic FCP in the aggressive environments, but a simple two-slope relationship for the vacuum case. The additional transition (IIA) for FCP in NaCl is observed based on the closure corrected data in Figure 4b.

Intrinsic transition stress intensity levels and power law slopes ($\Delta K_{Ti,eff}$ and $m_{i,eff}$) from least squares analyses of closure-corrected crack growth rates are presented in Table II. Closure-corrected $m_{i,eff}$ and $\Delta K_{Ti,eff}$ values are less sensitive to applied R-ratio and environment than m_i and ΔK_{Ti} in Table I. For FCP in moist air, ΔK_{Ti} values are essentially R-independent, varying about the averages bounding each segment by less than $\pm$10% with increasing applied R from 0.1 to 0.7. The m values for each of the three power-law regions vary by between $\pm$6% and $\pm$25% of the average slope with increasing R. Considering FCP in NaCl, the transition ΔK levels vary by up to $\pm$17% about

the mean for each segment and with increasing applied R. Other than the addition of the IIA transition for NaCl, moist air and chloride transitions appear to occur at constant and R-independent effective stress intensity levels (mean values are: $\Delta K_{T2,eff}$ = 9.9 MPa√m ±16%, $\Delta K_{T1,eff}$ = 6.7 MPa√m ±10%, $\Delta K_{T0,eff}$ = 4.7 MPa√m ±28%), at least for the former two transitions. Agreement is particularly good for the R of 0.1 comparison.

Table II

Effects of R-ratio and environment on $m_{i,eff}$ and $\Delta K_{Ti,eff}$ for MA Ti-6-4

Env.	R	$m_{3,eff}$	$\Delta K_{T2,eff}$ (MPa√m)	$m_{2A,eff}$	$\Delta K_{T2A,eff}$ (MPa√m)	$m_{2,eff}$	$\Delta K_{T1,eff}$ (MPa√m)	$m_{1,eff}$	$\Delta K_{T0,eff}$ (MPa√m)
Air	0.1	3.4	11.5			6.9	7.1	3.5	5.1
	0.4	3.3	12			5.6	7.4	4.9	6
	0.7	3.7	11			4.8	6.1	3.2	
NaCl	0.1	3.5	11.8	7.8	9.9	5.1	6.8	3.1	3.8
	0.4	5.3	8.3	12.6	7.9	3.4	6.0	3.7	3.4
	0.7	7.0	10.5			5.3	6.9	3.1	3.9
	V*	2.9	12.3			5.4	7.0	3.2	

V*: Constant K_{max} of 27.5 MPa√m with varying R ratio.

Considering slopes, $m_{1,eff}$ and $m_{2,eff}$ appear to be both R and environment-independent, with some variability affecting the latter values. $m_{2A,eff}$ and $m_{3,eff}$ may increase with increasing applied R-ratio. At this time, the transition results in Table II can only be qualitatively interpreted. Power-law segments are plotted in Figure 7, without data points.

Discussion

The experimental results of this study show that moist air and aqueous chloride substantially enhance rates of fatigue crack propagation in α/β Ti-6-4. Data are in good agreement with previous characterizations of this alloy/environment system[10,24]. This deleterious environmental effect is often traced to hydrogen environment embrittlement involving titanium-hydriding,

lattice or boundary decohesion, or enhanced localized plasticity; however; crack tip film rupture and dissolution may contribute to or dominate cracking[10,12,28]. The current study does not address this controversy.

The experimental results in Figures 4 and 7 show that the stress intensity range dependence of da/dN is complicated by the action of each environment compared to FCP in the Ti-6-4/argon or vacuum systems. There are several explanations for this behavior, including extrinsic crack closure and intrinsic damage mechanism transitions.

Crack Closure in Ti-6-4

The issues are: (1) does environment alter the magnitude and contribution of fatigue crack closure, (2) do closure variations explain the complex da/dN versus applied ΔK relationship, and (3) what is the effect of stress ratio on FCP for Ti-6-4 in aggressive environments. FCP rates in Ti-6-4 are sensitive to R-ratio in the low ΔK regime for both moist air and NaCl (Figure 3), as typically reported for metals including titanium alloys[19]. The R-ratio effect at low ΔK is generally attributed to an enhanced crack closure contribution. As shown in Figure 5, crack closure is important in the near-threshold ΔK regime at R of 0.1, and gradually decreases with increasing ΔK. Several hypotheses are possible for enhanced closure at low ΔK, including[19]: (a) small CTOD relative to asperity heights or phase transformation expansion (roughness-induced), (b) small plastic zone size promoting a single shear damage mechanism (roughness-induced), and (c) increased sliding and fretting between mating crack faces (oxide-induced). The plasticity-induced closure contribution, on the other hand, may decrease with decreasing ΔK.

The data in Figure 5 are insufficient to determine if environment, applied ΔK, or R affect the magnitude of crack closure in MA Ti-6-4 and the important governing mechanisms. Closure levels were not measured during unloading or loading below K_{min}, and FCP experiments were not conducted in vacuum. While aqueous NaCl appears to promote crack closure in Ti-6-4 at R of 0.4, similar closure levels are observed for the lower stress ratio experiments where an extensive range of K levels was considered. There is no apparent physical reason for environment-enhanced closure, only at the

intermediate stress ratio.

The measured closure levels in Figure 5 are consistent with plasticity-induced closure. A model by Newman[29] predicts that such closure is important, but only below an R-ratio of 0.4. (For example, the predicted K_{cl}/K_{max} for R of 0.1 is 0.30 and 0.45 for R equalling 0.4 considering the strength level of Ti-6-4 under study.) These predictions generally agree with the experimental results in Figure 5 for closure in moist air and NaCl. Plasticity-induced closure does not, however, explain the possible effect of the chloride environment on enhancing K_{cl} at R of 0.4, or at very low ΔK and R of 0.1. Reaction products from aqueous corrosion within the occluded crack, and fretting damage, do not dramatically enhance crack closure at R of 0.1 and relative to moist air for the majority of the stress intensities examined. There is no electrochemical reason to expect that such is the case. Fatigue crack surface roughness was not measured, however, SEM analysis did not indicate any obvious differences with varying environment, R or ΔK. There is no evidence for strong roughness-induced closure for the conditions represented in Figure 5. Our results are insufficient to establish the more subtle roles of corrosion product, roughness, hydride, or environment-enhanced plasticity mechanisms for closure. None-the-less, crack closure measurements yield several insights pertinent to corrosion fatigue in the titanium alloy/chloride system.

Comparison between Figures 3 and 6 shows that the approximate crack closure correction eliminates the effect of R-ratio on FCP rates for each environment. The observed effect of R is therefore due to a reduced crack closure contribution to the applied stress intensity range with increasing R. This result is interesting, particularly for FCP in chloride solutions, because of the paucity of data and modeling pertinent to the effect of stress ratio on intrinsic corrosion fatigue crack propagation rates[28]. The present results show that, at any effective ΔK level, increasing R does not affect the magnitude of the environmental enhancement of da/dN. This result is reasonable because K_{max} never exceeded the likely threshold for monotonic load environmental cracking. (A strong effect of R is expected when this

threshold is exceeded and when static load crack speeds are substantial compared to the loading frequencies and inert environment FCP rates[11].) For corrosion fatigue at lower stress intensities, increasing R may have little effect on da/dN because damage is controlled by cyclic plastic strains within the crack tip process zone, and hence by ΔK_{eff}. Maximum crack tip stresses do not increase with increasing R. The distance over which these tensile stresses act increases with R at fixed ΔK, however, this is of no consequence because this distance is large compared to the cyclic process zone, even at low R.

A second point is that crack closure does not explain the complex dependence of da/dN on ΔK for MA Ti-6-4 in either environment. Generally identical multiple-power law segments were observed, independent of whether growth rates were correlated with applied or effective stress intensity range. A portion of the variability in transition points and power law exponents, with changing R and environment (Table I), is eliminated by the ΔK_{eff} analysis. This result confirms that transition behavior is due to changes in one or more intrinsic damage mechanisms, and not crack closure. The closure-free FCP data in Figures 4b, 6 and 7 are useful in testing the various hypotheses for such mechanisms.

FCP Transitions in Ti-6-4

Several mechanisms have been proposed for changes in the FCP power-law exponent with increasing ΔK, including transitions: (1) from plane strain to plane stress[3], (2) from a damage accumulation-discontinuous crack advance process to per cycle FCP[15], (3) from microstructure sensitive to microstructure insensitive FCP associated with the plastic zone diameter exceeding the spacing of one or more dominant barriers to slip[4-8], (4) in plastic deformation mode which in turn affects a microscopic damage mechanism change[9], (5) in the microscopic paths and proportions of environmental damage mechanisms[1,2], (6) involving superposition of time-cycle-dependent[10] or time-dependent[14] environmental cracking modes, (7) involving the mass transport rate limiting process[18], and (8) from Stage I to

Stage II FCP[21].[4]

T2 Transition The first point to consider is the extent to which environment is a necessary element of transition FCP behavior in Ti-6-4. Results for Ti-6-4 by Petit[21], as well as by Shih and Wei[24], show that FCP in a highly purified inert environment is characterized by a single growth rate transition at ΔK_{Teff} of 11 MPa√m.[5] Irving and Beevers reported this transition at an applied ΔK of 9 MPa√m (R = 0.35; closure is assumed to be unimportant) for MA Ti-6-4 in an impure vacuum[8]. Above 11MPa√m, FCP in Ti-6-4/vacuum is Stage II, while faceted and potentially crystallographic cracking is observed at stress intensities below the transition[21]. Meyn reported a similar transition from Stage II to crystallographic-slip plane-based cracking in MA Ti-8Al-1Mo-1V/vacuum, but at a high ΔK level (21 MPa√m at R = 0 with no consideration of crack closure) that was above the levels considered during this study[12].

The low R data in Figure 4 show that a transition in da/dN occurs at this ΔK level of 11 MPa√m for both Ti-6-4 in both moist air and NaCl. This behavior was observed for each of the three R-ratios and each environment, as shown by the values of $\Delta K_{T2,eff}$ in Table II. Based on this result, the T2 transition appears to be mechanically-based; environment is not a requisite for the slope change at this ΔK level. Mean stress intensity does not affect

---

[4] Stage II is defined as cracking that is macroscopically normal to the applied Mode I stress, and involves multiple slip-based damage processes and a noncrystallographic crack path. Stage I FCP is based on crystallographic cracking and damage involving a single slip system, involves Modes I and II, and is typically observed for microcracks or long crack at near-threshold ΔK levels.

[5] Shih and Wei report a single transition at an applied ΔK of 15 MPa√m at R of 0.05. From Figure 5, this corresponds to ΔK_{Teff} of 11 MPa√m since K_{cl} should equal 4 MPa√m if closure in vacuum and moist air is assumed to be similar. The Shih-Wei microstructure was mill annealed, similar to that in Figure 1, however, the Petit microstructure was more complex because of water quenching from the two phase field, followed by aging to precipitate α in β and to decompose martensitic α.

$\Delta K_{T2,eff}$, suggesting that the cyclic character of process zone strains dominate fatigue damage and da/dN transition behavior. These results support the notion that the T2 transition is related to crack tip plasticity-microstructure interactions, or perhaps the transition from per-cycle to discontinuous FCP. These speculations must be supported by fractographic analyses.

ΔK- and environment-based changes in the microscopic fracture mechanism are being examined by scanning electron microscopy. Figure 8 shows SEM fractographs of mill annealed Ti-6-4 fatigued at an R-ratio of 0.1 and ΔK_{eff} values of: (a) 6 MPa√m, (b) 10 MPa√m, (c) 15 MPa√m, for FCP in moist air, and (d) 10 MPa√m for 1% NaCl. This figure demonstrates a change in fracture mode at different ΔK values. Large facets with river patterns are observed at a ΔK of 15 MPa√m, while small ill-defined facets with an average size of approximately 10 μm appear for moist air FCP at ΔK of 7 MPa√m.

Conclusions

The effects of environment (moist air and 1% NaCl at -500 mV_{SCE}) and R-ratio (0.1, 0.4, 0.7 and constant K_{max}) on FCP rates and crack closure were experimentally examined for mill annealed Ti-6-4 (ELI), an α/β titanium alloy. Emphasis was placed on transitions in the power law relationship between da/dN and applied as well as effective ΔK. Several conclusions are drawn.

1) FCP in mill annealed Ti-6-4 is enhanced by NaCl relative to moist air, and by moist air relative to data reported for purified argon or vacuum, over a wide range of applied ΔK and R. Environmental FCP occurs at stress intensities below the monotonic load threshold, K_{ISCC}.
2) Based on global compliance measurements, crack closure levels are similar for FCP in moist air and NaCl at low R, with a potential environmental effect on closure observed for intermediate R. Data are insufficient to define the effect of environment and R on absolute crack closure levels. Limited results are, however, generally consistent with a strong contribution from plasticity-induced closure.
3) For each environment, da/dN increases with increasing R at constant applied ΔK, but is constant with increasing effective ΔK, suggesting

that mean stress intensity does not influence intrinsic rates of environmentally enhanced FCP below K_{ISCC}.

4) Ti-6-4 exhibits multi-sloped power law relationships between da/dN and ΔK, for FCP in both moist air and NaCl, in contrast to a single transition reported for FCP in inert environments. Aqueous NaCl increases the complexity of the da/dN-ΔK relationship by causing an additional transition, consistent with reports of cyclic stress corrosion cracking below the monotonic threshold.
5) The multi-sloped relationship between da/dN and ΔK remains after crack closure correction, suggesting that closure is not a central factor for determining the transition behavior in Ti-6-4. When da/dN is correlated based on effective ΔK from global compliance, individual power law slopes, and the stress intensity ranges at transition points, are similar for each environment. The single transition response for FCP in vacuum also adheres to this behavior.
6) The mechanisms for transition behavior in Ti-6-4/moist air or NaCl likely involve interaction between crack tip plasticity and microstructure, however, specific micromechanical and environmental contributions are not delineated.

Future Work

Work is in progress to better correlate microscopic fracture paths with the transition behavior for Ti-6-4 in the aggressive environments. At present we do not understand the underlying fatigue fracture mechanisms, and how the change in fracture mechanism links to transition behavior. The micromechanical explanation for the T2 transition must be determined. While FCP occurred for nominally plane strain at all ΔK levels examined, eliminating a stress state explanation for FCP transitions in this system, the other cited hypotheses must be tested. The role of environment in the T2 transition must be considered. Similar work is required to understand the growth rate changes occurring at the lower ΔK levels. While the T2A transition appears to be related to the superposition of cylcic stress corrosion cracking for NaCl

but not moist air, the origins of the T1 and T0 transitions are unclear. Such analyses will be completed before this paper is submitted for publication.

References

1. R.S. Piascik and R.P. Gangloff, Metall. Trans. A., Vol. 22A, pp. 2415-2428 (1990).
2. R.S. Piascik and R.P. Gangloff, Metall. Trans. A., Vol. 24A, pp. 2751-2762 (1993).
3. J.A. Feeney, J.C. McMillan and R.P. Wei, Metall. Trans. A., Vol. 1, pp. 1741-1756 (1970).
4. G.R. Yoder, L.A. Cooley and T.W. Crooker, Scripta Metall., Vol. 16, pp. 1021-1025 (1982).
5. R.J.H. Wanhill and L. Schra, "Corrosion Fatigue Crack Arrest in Aluminum Alloys", Report NLR-TR-87128-U, National Aerospace Laboratory, Netherlands (1987).
6. G.R. Yoder, L.A. Cooley and T.W. Crooker, Metall. Trans. A., Vol. 8A, pp. 1737-1743 (1977).
7. G.R. Yoder, F.H. Froes and D. Eylon, Metall. Trans. A., Vol. 15A, pp. 183-197 (1984).
8. P.E. Irving and C.J. Beevers, Metall. Trans., Vol. 5, pp. 391-398 (1974).
9. S.B. Chakrabortty and E.A. Starke, Jr., Metall Trans. A., Vol. 10A, pp. 1901-1911 (1979).
10. D.B. Dawson and R.M. Pelloux, Metall. Trans. A., Vol. 5A, pp. 723-731 (1974).
11. R.J. Bucci, PhD Dissertation, Lehigh University, Bethlehem, PA (1970).
12. D.A. Meyn, Metall. Trans., Vol. 2, pp. 853-865 (1971).
13. R.J. Walter, J.D. Frandsen and R.P. Jewett, in Hydrogen Effects in Metals, I.M. Berstein and A.W. Thompson, eds., TMS-AIME, Warrendale, PA, pp. 819-827 (1981).
14. M.O. Speidel, in Stress Corrosion Cracking and Hydrogen Embrittlement of Iron Based Alloys, J. Hochmann, J. Slater, R.D. McCright and R.W. Staehle, eds., NACE, Houston, TX, pp. 1071-1094 (1977).
15. K.S. Chan, Metall. Trans. A., Vol. 24A, pp. 2473-2486 (1993).
16. P.C. Paris, M.P. Gomez and W.E. Anderson, The Trend in Engineering, Washington State Univ., Vol. 13, No. 1, pp. 9-14 (1961).
17. R.G. Forman, V. Shivakumar, J.C. Newman, Jr., S.M. Piotrowski and L.C. Williams, in Fracture Mechanics: Eighteenth Symposium, ASTM STP 945, ASTM, Philadelphia, PA, pp. 781-803 (1988).
18. H.J. Gudladt and J. Petit, Scripta Metall., Vol. 25, pp. 2507-2512 (1991).
19. R.O. Ritchie, Intl. Metall. Rev., Vol. 20, pp. 205-230 (1979).
20. Mechanics of Fatigue Crack Closure, ASTM STP 982, J.C. Newman and W. Elber, eds., ASTM, Philadelphia, PA (1988).
21. J. Petit, "Modeling of Intrinsic Fatigue Crack Propagation", in Theoretical Concepts and Numerical Analysis of Fatigue, in press (1993).

22. D.C. Slavik, C.P. Blankenship, Jr., E.A. Starke, Jr. and R.P. Gangloff, "Intrinsic Fatigue Crack Growth Rates for Al-Li-Cu-Mg Alloys in Vacuum", Metall. Trans. A, Vol. 24A, pp. 1807-1817 (1993).
23. D.C. Slavik, PhD Dissertation, University of Virginia, Charlottesville, VA (1993).
24. T.T. Shih and R.P. Wei, Engr. Frac. Mech., Vol. 6, pp. 19-32 (1974).
25. M.O. Speidel, M.J. Blackburn, T.R. Beck and J.A. Feeney, in Corrosion Fatigue, Chemistry, Mechanics and Microstructure, O. Devereux, A.J. McEvily and R.W. Staehle, eds., NACE, Houston, TX, pp. 324-345 (1972).
26. M.D. Halliday and C.J. Beevers, Intl. J. Fracture, Vol. 15, pp. R27-R30 (1979).
27. A.J. McEvily, Atlas of Stress-Corrosion and Corrosion Fatigue Curves, ASM International, Metals Park, OH (1990).
28. R.P. Gangloff, in Environment Induced Cracking of Metals, R.P. Gangloff and M.B. Ives, eds., NACE, Houston, TX, pp. 55-109 (1990).
29. J.C. Newman, Jr., Intl. J. Fracture, Vol. 24, No. 3, pp. R131-135 (1984).

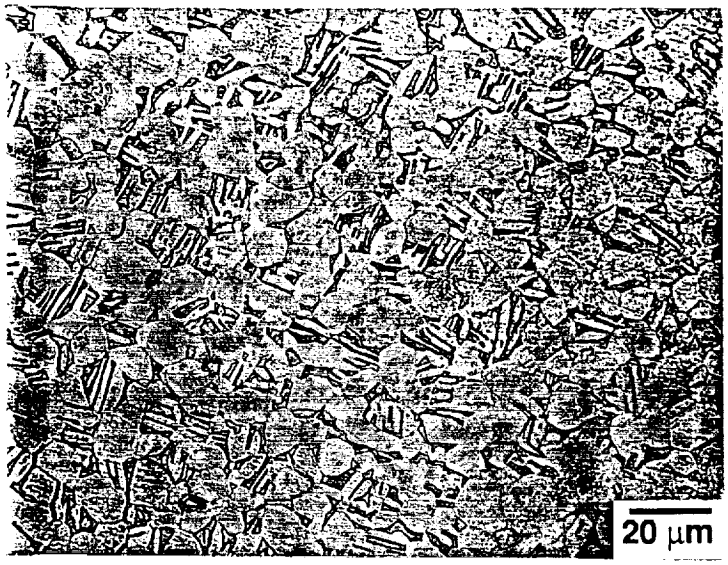

Figure 1. Microstructure of mill-annealed Ti-6-4 ELI.

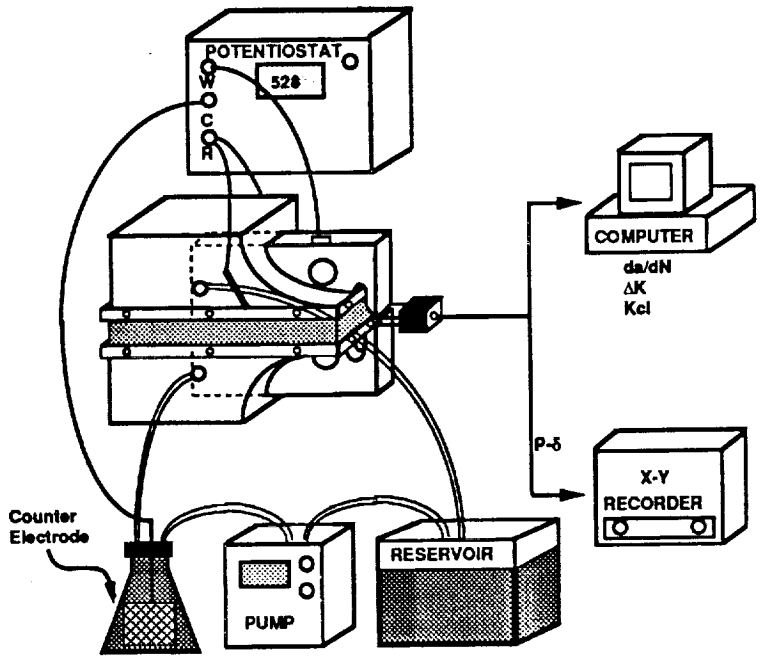

Figure 2. Illustration of the environmental fatigue experiment.

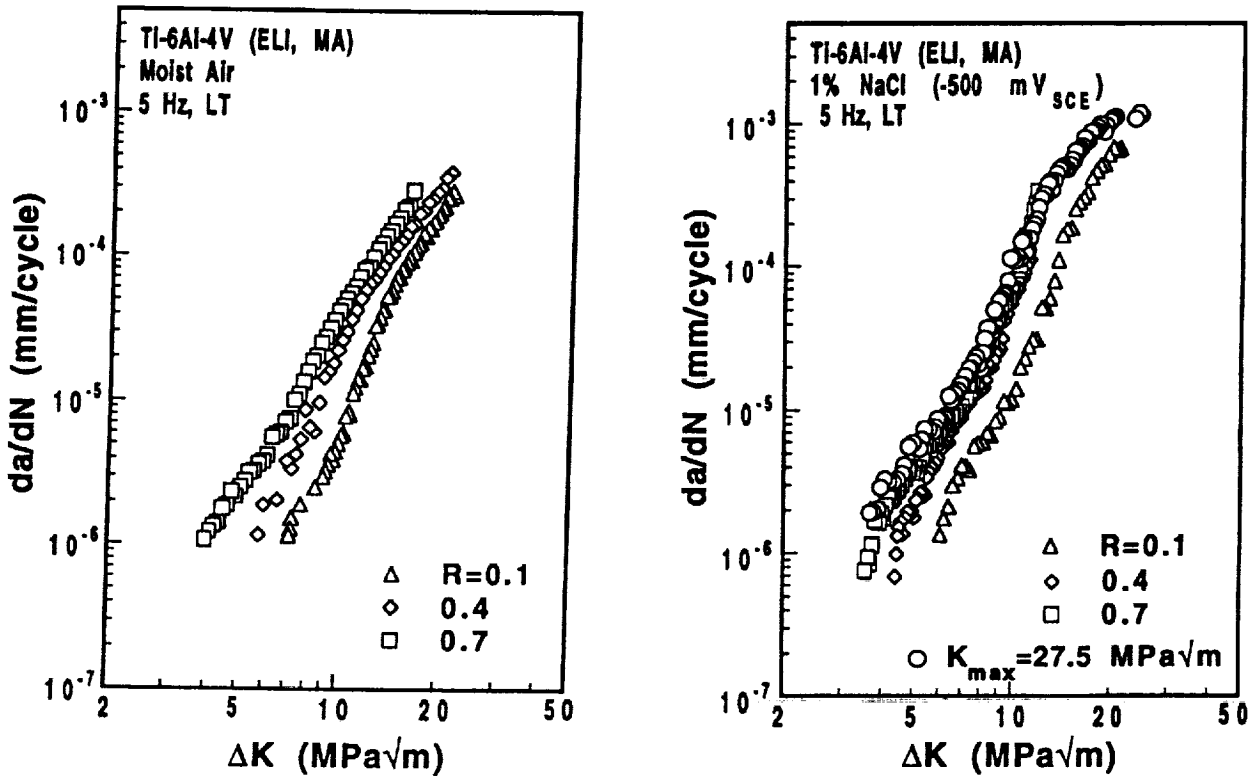

(a) (b)

Figure 3. Da/dN vs applied ΔK for Ti-6-4 in: (a) moist air and (b) 1% NaCl, at R ratios of 0.1, 0.4 and 0.7, and at constant K_{max} of 27.5 MPa√m.

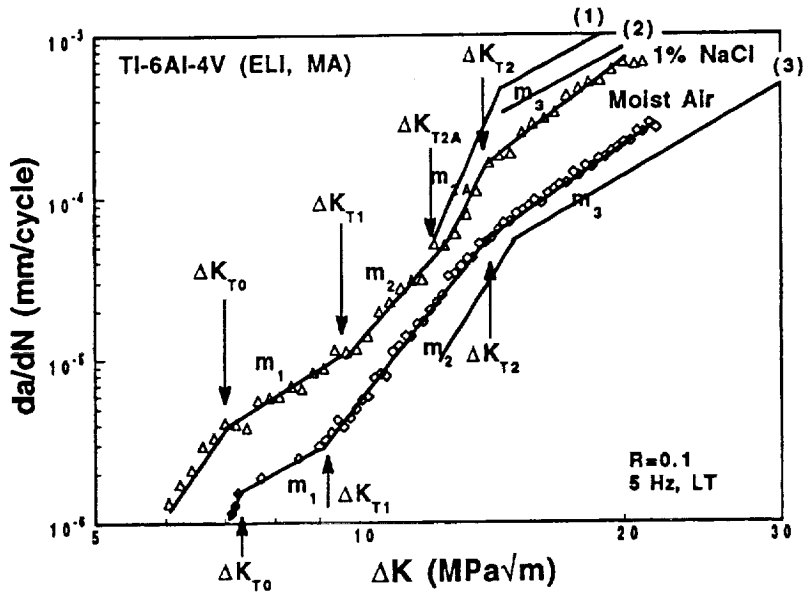

(a)

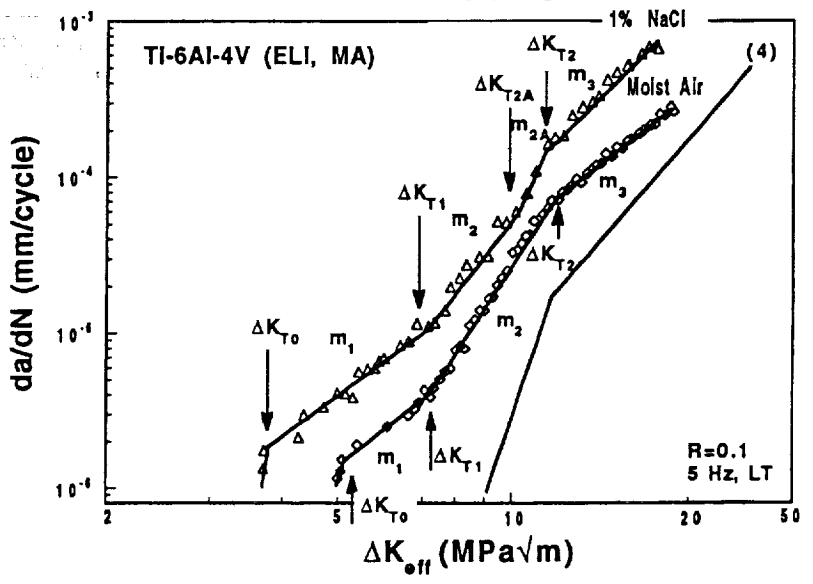

(b)

Figure 4. Definition of the m and ΔK_T values in: (a) da/dN-ΔK and (b) da/dN-ΔK_{eff} for Ti-6-4 in moist air and 1% NaCl at an applied R of 0.1. Literature data: (1) Dawson and Pelloux (NaCl, 5 Hz, R=0.1), (2) Shih and Wei (NaCl, 5 Hz, R=0.05), (3) Shih and Wei (Argon, 5 Hz, R=0.05) and (4) Petit (Vacuum, R=0.1)

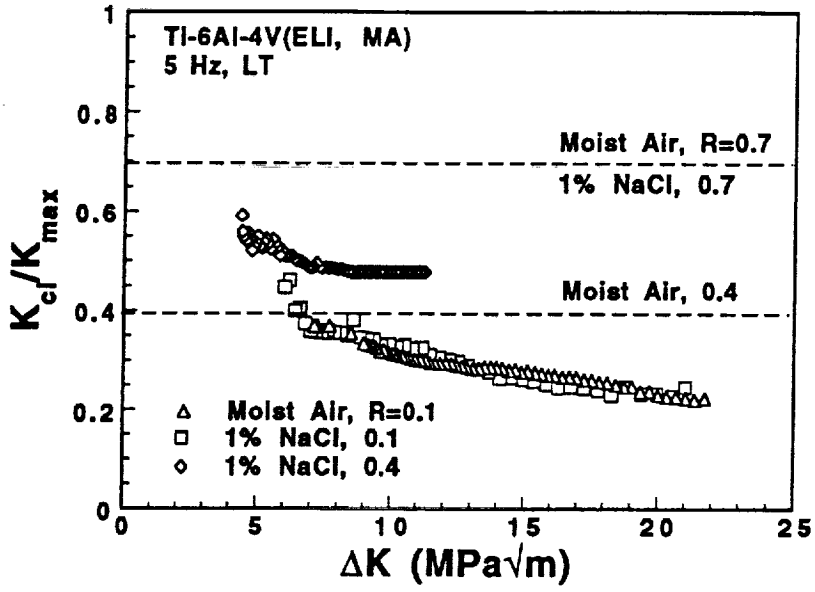

Figure 5. K_{cl}/K_{max} vs ΔK for Ti-6-4 in moist air and 1% NaCl at various R ratios.

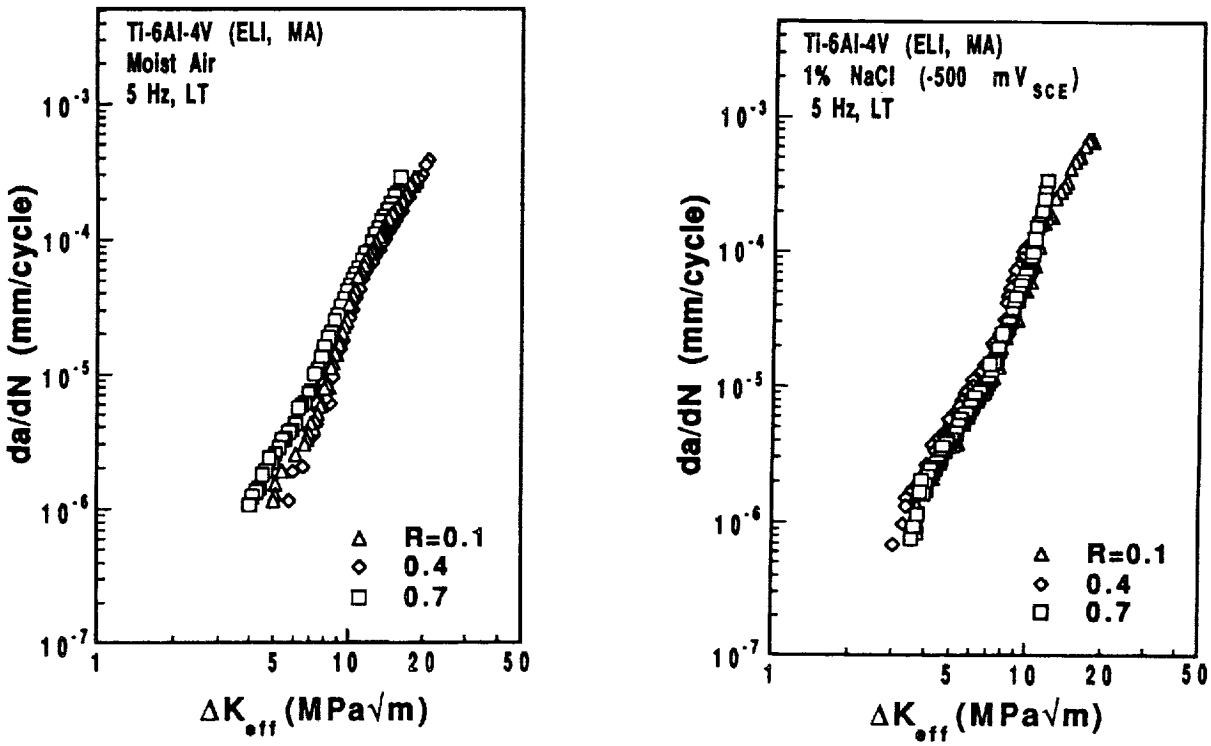

(a) (b)

Figure 6. Da/dN-ΔK_{eff} for Ti-6-4 in: (a) moist air and (b) 1% NaCl at R ratios of 0.1, 0.4 and 0.7.

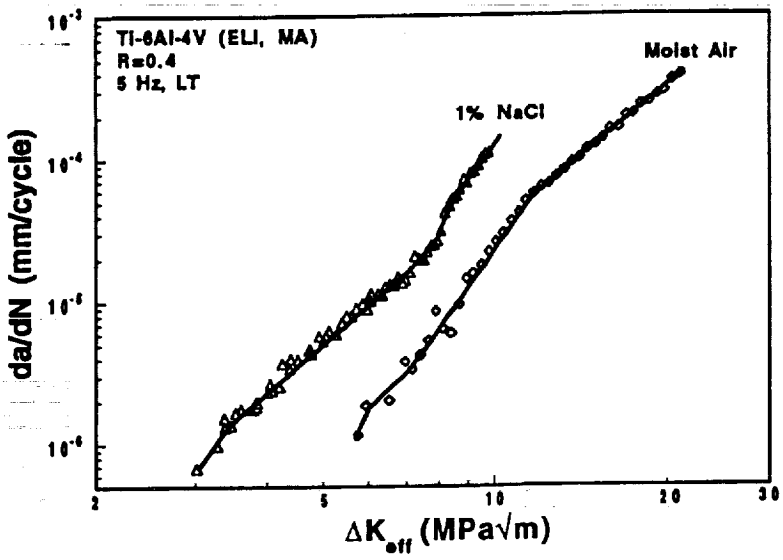

(a)

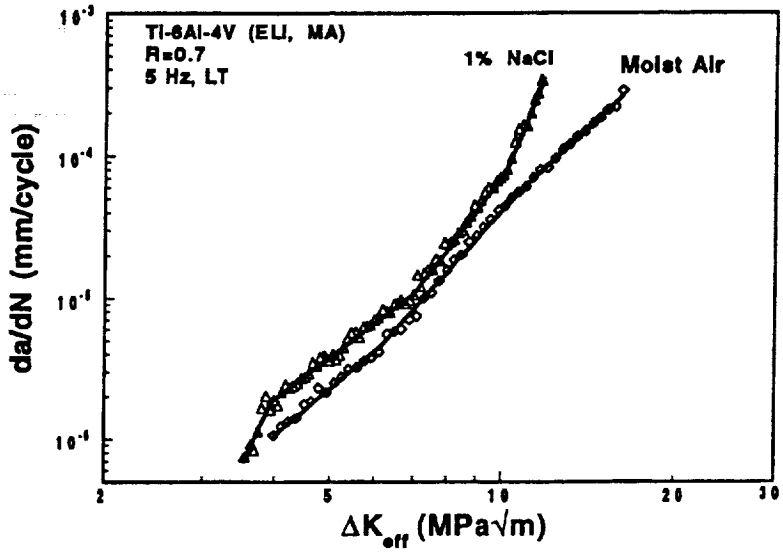

(b)

Figure 7. Comparison of the closure-free transition behavior of Ti-6-4 in moist air and 1% NaCl at R ratios of (a) 0.4 and (b) 0.7.

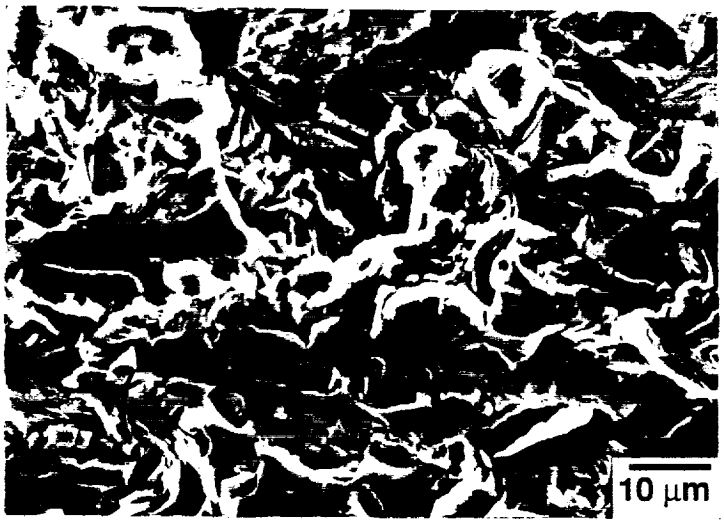

(a)

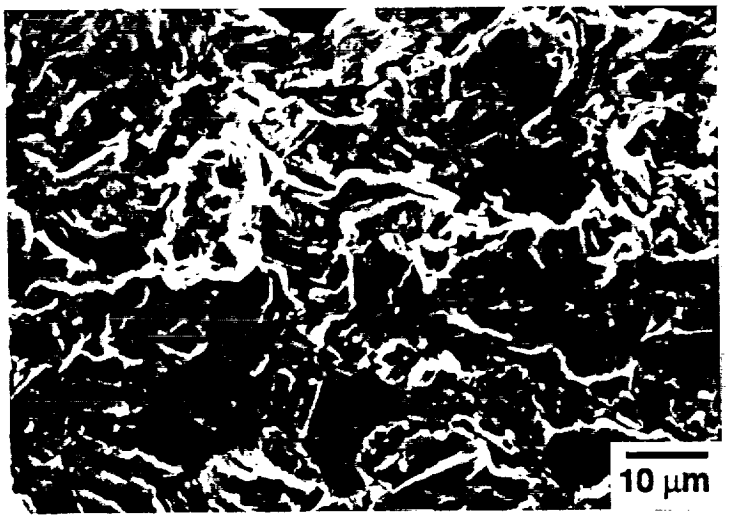

(b)

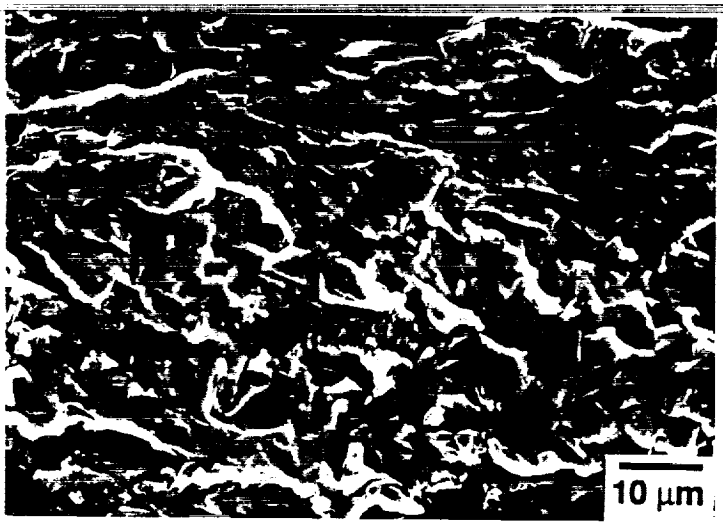

(c)

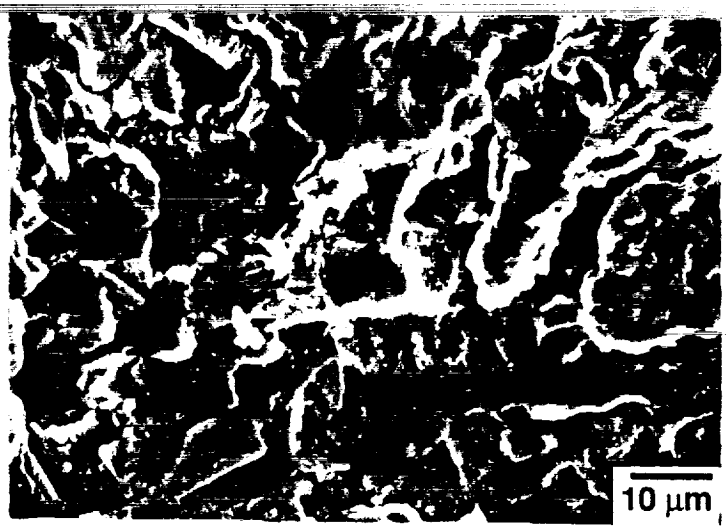

(d)

Figure 8. SEM fractographs of mill annealed Ti-6-4 fatigued at R of 0.1 and ΔK_{eff} of: (a) 6 MPa√m, (b) 10 MPa√m, (c) 15 MPa√m, in moist air, and (d) 10 MPa√m in 1% NaCl.

Project #11 Experimental Study of the Nonlinear Viscoplastic Response of High Temperature Structures

Marshall F. Coyle and E.A. Thornton

Objectives

The main objective of this research program is to investigate experimentally the viscoplastic response of thermal structures for high speed flight. An additional objective is to provide high quality data for validation of finite element analysis using unified viscoplastic constitutive models.

Approach

Simplified structures of representative high temperature superalloys and/or advanced aluminum alloys will be designed and tested. These alloys will display typical biaxial stress states with appropriate temperatures and stress gradients. The simplified structures will provide well-defined thermal and structural boundary conditions.

Research Progress

The testing of 15 in. x 10 in. x 1/8 in. thick rectangular Hastelloy-X plates has been completed. Three series of experiments were performed. The first two deal with the thermal buckling of Hastelloy-X plates. In the third series, an isothermal Hastelloy-X plate is loaded with a point load.

In the first two experimental series, Hastelloy-X plates were heated transiently with a quartz heat lamp focused on the plate centerline. Parallel edges of the plate are maintained at constant temperature by chill water flow through coolant tubes. The plate was supported at only four points to provide well-defined thermal and structural boundary conditions. These two series demonstrated global bending caused by in-plane spatial temperature gradients and initial plate warpage. Small initial warpage with compressive membrane thermal forces was sufficient to initiate substantial transverse bending. Test series one was presented in the January to June 1992 progress

report. The Hastelloy-X plate was instrumented with 29 thermocouples and 15 LVDTs. It was oriented in the test frame so it would displace downward (away from the lamp) when heated. Test series two was presented in the July to December 1992 and January to June 1993 progress reports. The Hastelloy-X plate was instrumented with 14 strain gages, 20 thermocouples, and 16 LVDTs. It was oriented in the test frame so it would displace upward (towards the lamp) when heated.

In the third experimental series, a Hastelloy-X plate was loaded with a concentrated load normal to the plate. The plate was supported at the same four points as in the previous thermal tests. Test series three examined possible sources for experimental errors in the thermal buckling tests along with providing data to aid in validation of finite element codes. This test series was reported in the January to June 1993 progress report. In this test series, a 15 in. x 10 in. x 1/8 in. Hastelloy-X plate was supported at four points and loaded at the center with a concentrated load normal to the test plate. The results did not reveal any serious problems with the setup or procedures used for the thermal buckling test series. Nevertheless, it did point out areas where care should be taken. Such an area is the point support torques. It was shown that over-tightening of point supports can adversely affect results.

A contractor's report has been completed on the Hastelloy-X plate experiments. It reports on heat lamp characterization, buckling experiments, and the isothermal plate tests. The report is intended to be a comprehensive document that describes the test program and presents the complete set of data. The report describes in detail the test setups and procedures used for both the lamp characterization, thermal buckling, and isothermal tests. The report also describes and gives the associated accuracies for the instrumentation used. It also contains tabulated data from the thermal buckling tests and an empirical equation that describes the heat flux that was applied to the thermal buckling plate tests.

Planning for thermal buckling tests of stiffened panels has been initiated. Figure 1 shows a proposed test panel. Effort was directed at

designing a panel which could be machined out of a thick metallic plate rather than attempting to attach stiffeners to a thin plate. The materials considered include those that are being considered for the High Speed Civil Transport. Figure 2 shows a plot of specific tensile yield strength for various materials verses temperature. The 2024 aluminum alloys were also plotted since they are readily available. The Ti-6Al-4V titanium alloy has been chosen for the stiffened panel material. This is due to its strength and used in aerospace applications. It is also readily available in thick plates that can be machined into stiffened panels.

Several stiffened panel concepts were modeled with finite elements. The stiffened panels consisted of a 15 in. x 10 in. x 1/8 in. plate with 3/8 in. high x 1/8 in. wide stiffeners (see Figure 1). The number of stiffeners were varied from 0 to 10 and were evenly spaced. For example, Figure 1 shows a panel with 4 stiffeners. The panel was supported with four point supports which were located at each corner of the panel. Two different loadings were applied. The first loading consisted of a 100 lb point load normal to the panel applied at the center. A thermal load was used for the second loading. A tent-like temperature distribution was applied to the panel (see Figure 3). The results for these finite element analysis are given in Figure 4. Figure 4 shows that the greatest change in deflection verses change in stiffeners occurs between 0 and 3 stiffeners and then tapers off. A panel with three stiffeners would have a stiffener along the centerline. It was felt that would make instrumentation more difficult. A panel with four stiffeners has been selected (see Figure 1). The finite element results along with certain instrumentation considerations made this a good choice.

A new test fixture has been designed to facilitate testing of stiffened panels. The fixture is shown in Figure 5. It will allow panels up to 2 in. thick to be tested and will also allow a 10 in. x 15 in. panel to be rotated about the Z-Axis. Therefore, a panel can be heated parallel to the stiffeners, perpendicular to the stiffeners or any angle in between. This fixture also contains some refinements of its predecessor. The heat lamp mount allows the lamp be interchanged between the test fixture and the lamp

characterization stand easily. It also incorporates alignment devices to aid in aligning point supports, the LVDT mounting plate, and the test panel.

Plans for the Future Research

In the next six months, three Titanium panels with stiffeners will fabricated. Two of these panels will then be instrumented with strain gages, thermocouples, and LVDTs. Also, the new test frame will be fabricated. A series of thermal buckling experiments similar to that of the Hastelloy-X plates will be preformed. The third panel will be instrumented with LVDTs and have an isothermal point load test performed.

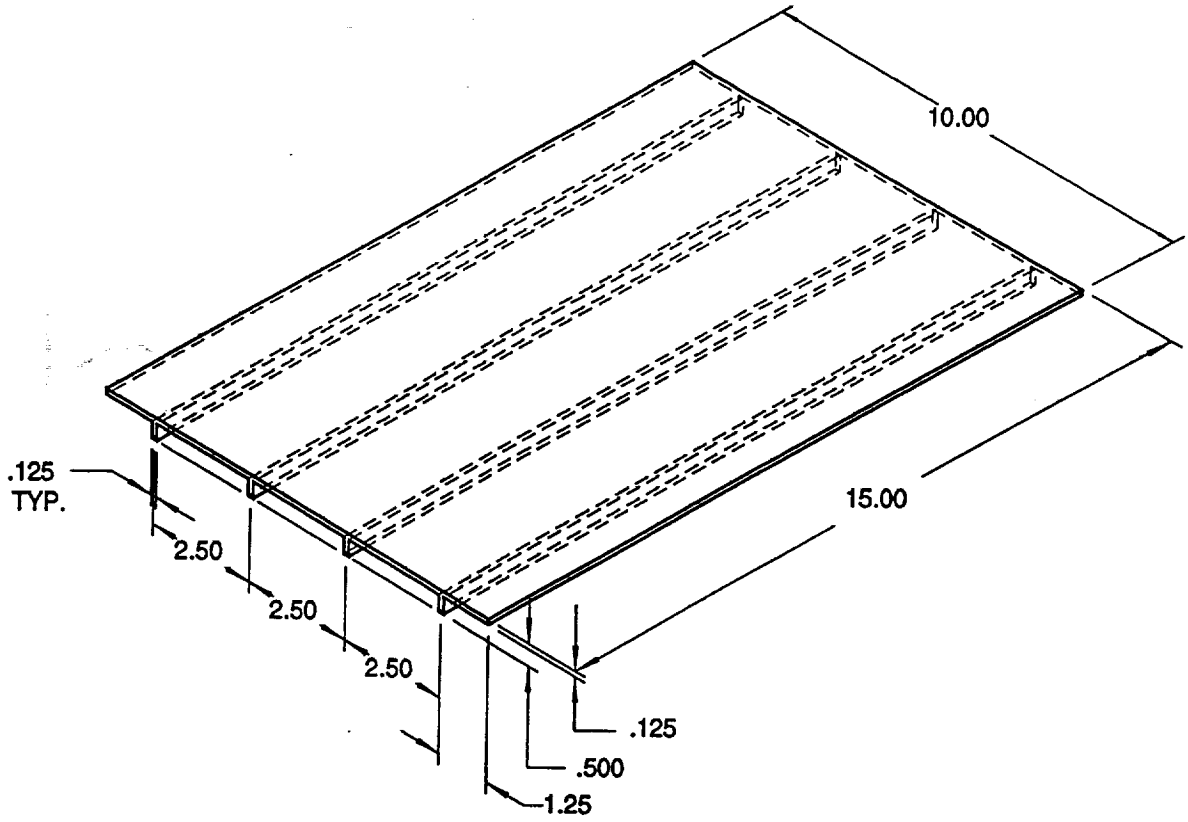

Figure 1: Titanium Test Panel

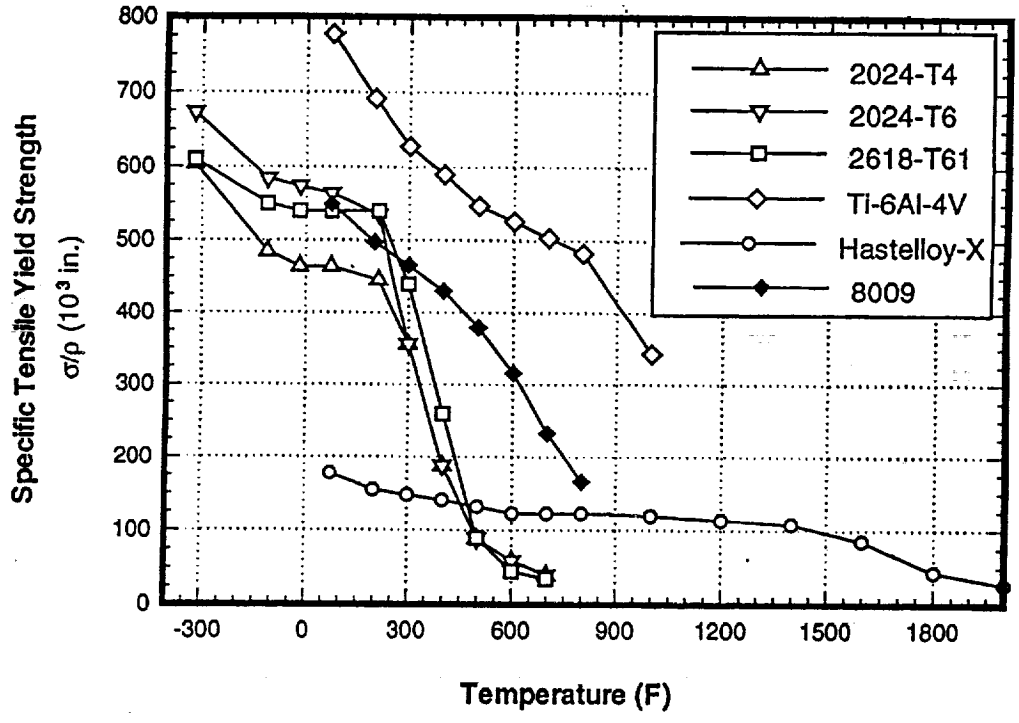

Figure 2: Material Properties at Different Temperatures

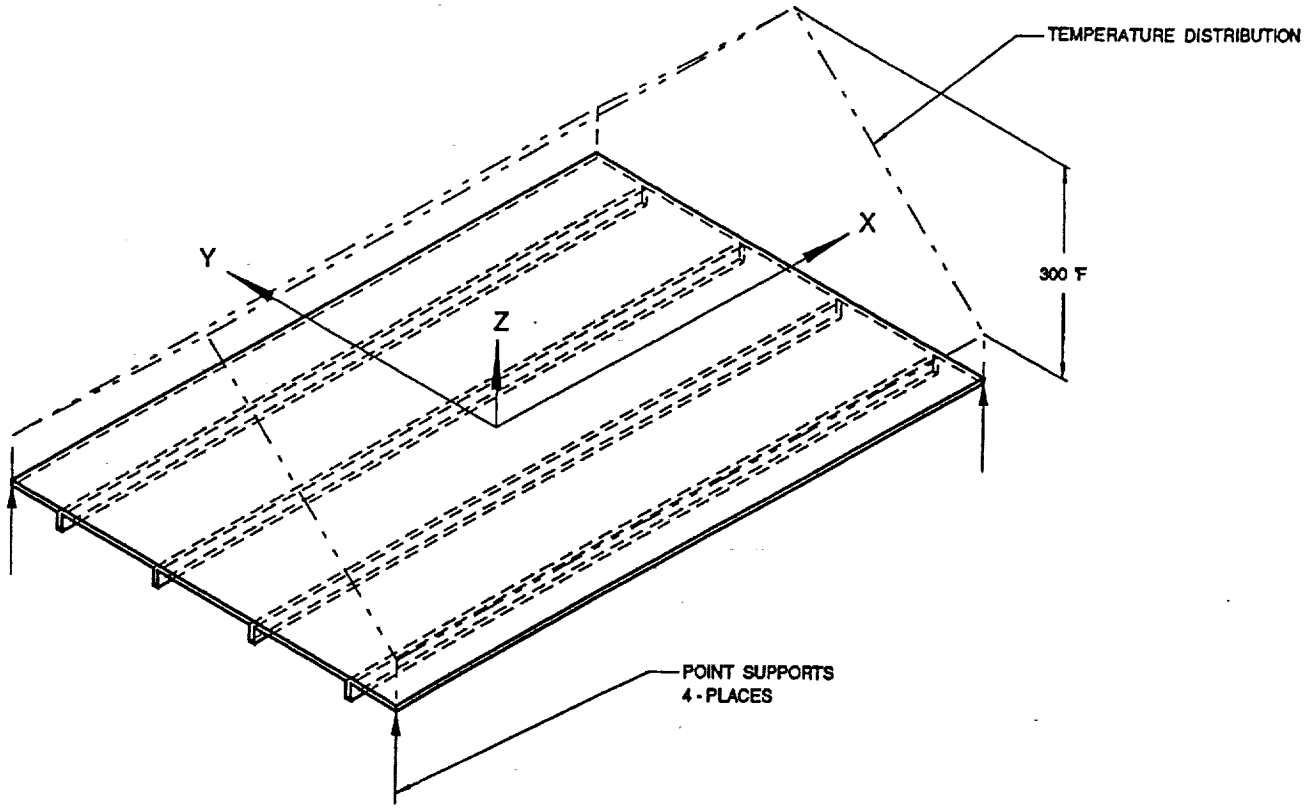

Figure 3: Tentlike Temperature Distribution used in Finite Element Model

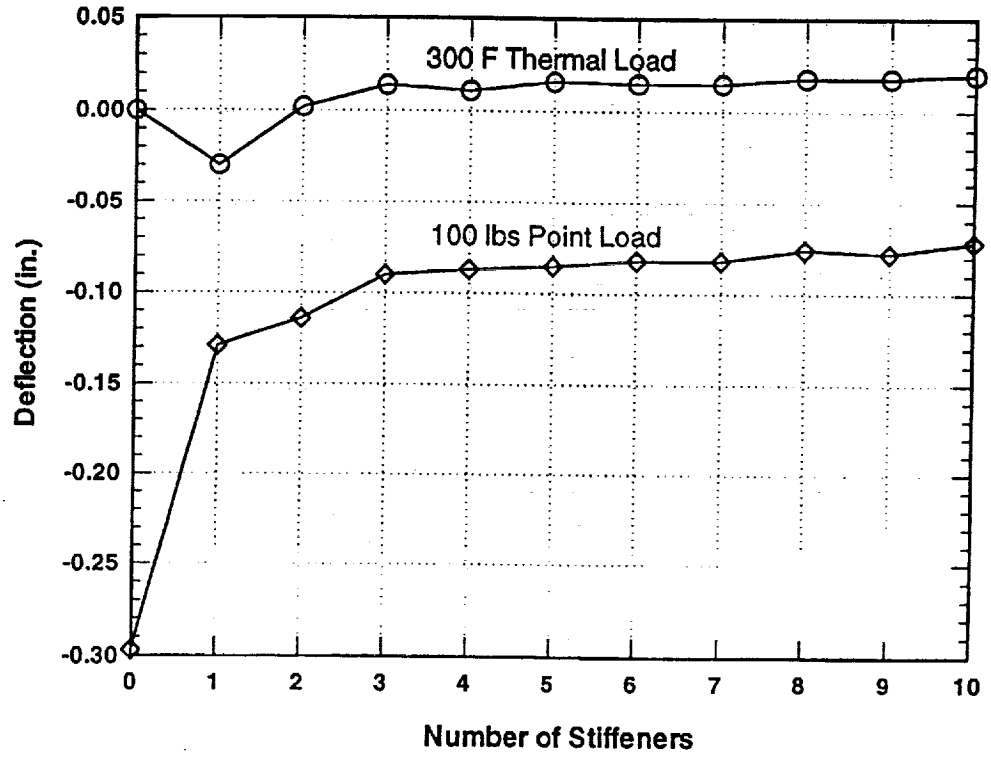

Figure 4: Finite Element Results for Titanium Stiffened Panel

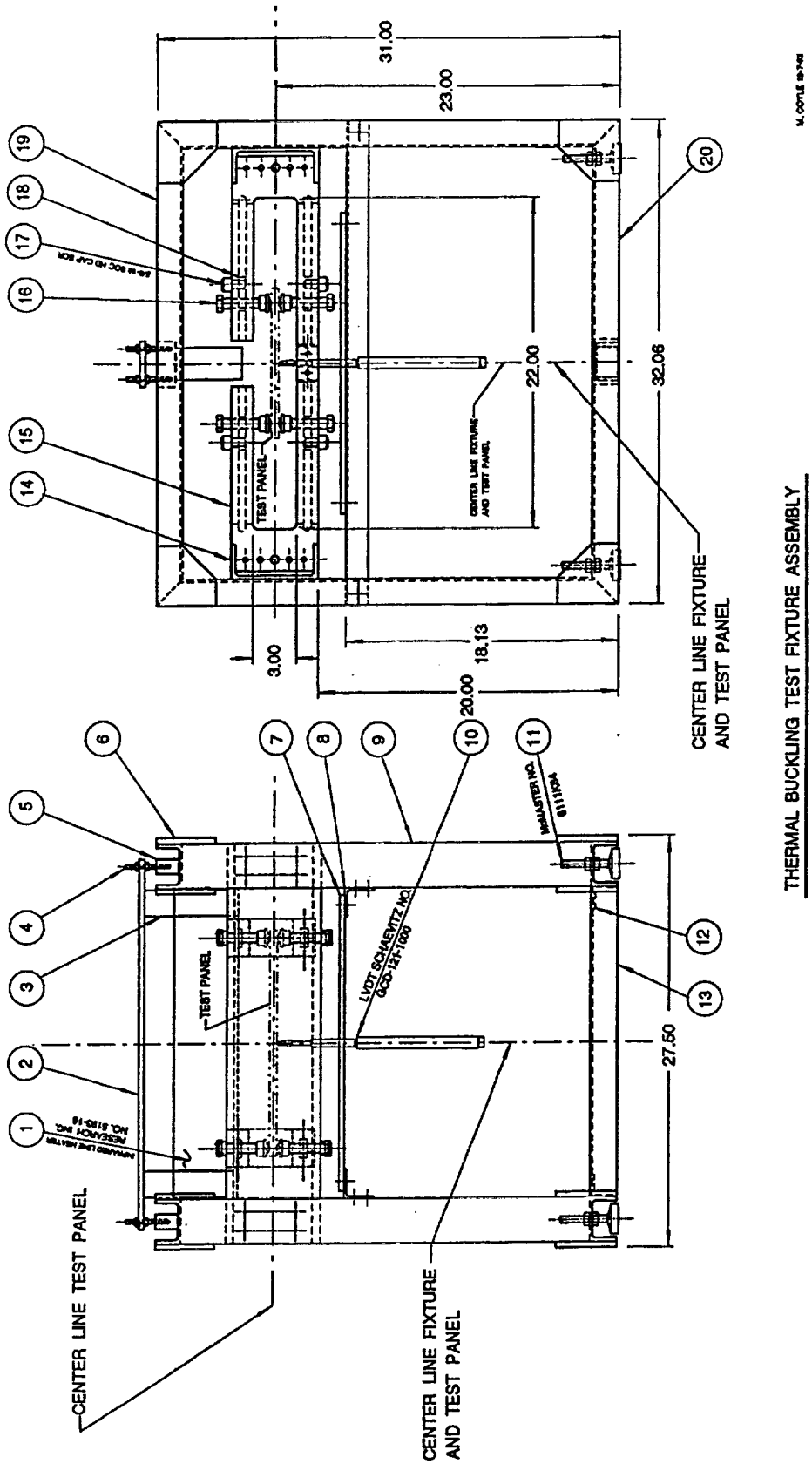

Figure 5: New Thermal Buckling Test Frame

APPENDIX I: GRANT PUBLICATIONS (July 1 to December 31, 1993)

1. M.T. Lyttle and J.A. Wert, "Modeling of Continuous Recrystallization in Aluminum Alloys," Journal of Materials Science, accepted for publication, 1994.

2. M.T. Lyttle and J.A. Wert, "Simulative Modeling of Continuous Recrystallization of Aluminum Alloys," Conference Proceedings from 1993 TMS-ASM Materials Week, in press.

3. M.T. Lyttle, "Simulative Modeling of Continuous Recrystallization of Aluminum Alloys", MS Thesis, University of Virginia, Charlottesville, VA, January, 1994.

4. E.A. Thornton, "Thermal Buckling of Plates and Shells", Applied Mechanics Reviews, Vol. 46, No. 10, October, 1993, pp 485-506.

APPENDIX II: GRANT PRESENTATIONS (July 1 to December 31, 1993)

1. R.P. Gangloff and R.G. Kelly, "Occluded Site Chemistry and Modeling Environmental Fatigue in Aluminum Alloys", FAA/NASA-LaRC Working Group on Fatigue, Lehigh University, Bethlehem, PA, November, 1993.

2. R.P. Gangloff, "Environment-Enhanced Fatigue Crack Propagation in Advanced Al-Li-Cu-X Alloys", Detroit Section of TMS-AIME, Detroit, MI, November, 1993.

3. R.P. Gangloff, "Elevated Temperature Fracture of RS/PM Aluminum Alloys", Department of Materials Science, University of Michigan, Ann Arbor, MI, November, 1993.

4. M.T. Lyttle and J.A. Wert, "Simulative Modeling of Continuous Recrystallization of Aluminum Alloys," 1993 TMS-ASM Materials Week, Pittsburgh, PA, October, 1993.

APPENDIX III: GRANT PROGRESS REPORTS (January, 1988 to July, 1993)

1. R.P. Gangloff, G.E. Stoner and R.E. Swanson, "Environment Assisted Degradation Mechanisms in Al-Li Alloys", University of Virginia, Report No. UVA/528266/MS88/101, January, 1988.

2. R.P. Gangloff, G.E. Stoner and R.E. Swanson, "Environment Assisted Degradation Mechanisms in Advanced Light Metals", University of Virginia, Report No. UVA/528266/MS88/102, June, 1988.

3. R.P. Gangloff, G.E. Stoner and R.E. Swanson, "Environment Assisted Degradation Mechanisms in Advanced Light Metals", University of Virginia, Report No. UVA/528266/MS89/103, January, 1989.

4. R.P. Gangloff, "NASA-UVa Light Aerospace Alloy and Structures Technology Program", UVa Report No. UVA/528266/MS90/104, August, 1989.

5. R.P. Gangloff, "NASA-UVa Light Aerospace Alloy and Structures Technology Program", UVa Report No. UVA/528266/MS90/105, December, 1989.

6. R.P. Gangloff, "NASA-UVa Light Aerospace Alloy and Structures Technology Program", UVa Report No. UVA/528266/MS90/106, June, 1990.

7. R.P. Gangloff, "NASA-UVa Light Aerospace Alloy and Structures Technology Program", UVa Report No. UVA/528266/MS91/107, January, 1991.

8. R.P. Gangloff, "NASA-UVa Light Aerospace Alloy and Structures Technology Program", UVa Report No. UVA/528266/MS91/108, July, 1991.

9. R.P. Gangloff, "NASA-UVa Light Aerospace Alloy and Structures Technology Program", UVa Report No. UVA/528266/MS92/109, January, 1992.

10. R.P. Gangloff, "NASA-UVa Light Aerospace Alloy and Structures Technology Program", UVa Report No. UVA/528266/MS93/111, July, 1992.

11. R.P. Gangloff, "NASA-UVa Light Aerospace Alloy and Structures Technology Program", UVa Report No. UVA/528266/MSE93/112, March, 1993.

12. R.P. Gangloff, "NASA-UVa Light Aerospace Alloy and Structures Technology Program", UVa Report No. UVA/528266/MSE93/113, July, 1993.

DISTRIBUTION LIST

1-2	Mr. D. L. Dicus Contract Monitor Metallic Materials Branch, MS 188A NASA Langley Research Center Hampton, VA 23681
3-4*	NASA Scientific and Technical Information Facility P. O. Box 8757 Baltimore/Washington International Airport Baltimore, MD 21240
5	Mr. Richard J. Siebels Grants Officer, M/S 126 NASA Langley Research Center Hampton, VA 23681-0001
6	Dr. Darrel R. Tenney Materials Division NASA Langley Research Center Hampton, VA 23681
7	Dr. Charles E. Harris Mechanics of Materials Branch NASA Langley Research Center Hampton, VA 23681
8	Mr. W. Barry Lisagor Metallic Materials Branch NASA Langley Research Center Hampton, VA 23681
9	Mr. T.W. Crooker Code RM NASA Headquarters Washington, DC 20546
10	Dr. Robert S. Piascik Mechanics of Materials Branch NASA Langley Research Center Hampton, VA 23681
11	Mr. W. Brewer Metallic Materials Branch, MS 188A NASA Langley Research Center Hampton, VA 23681

12 Mr. Thomas T. Bales
Metallic Materials Branch, MS 188A
NASA Langley Research Center
Hampton, VA 23681

13 Dr. M.J. Shuart
Aircraft Structures Branch
NASA Langley Research Center
Hampton, VA 23681

14 Dr. James H. Starnes, Jr.
Aircraft Structures Branch
NASA Langley Research Center
Hampton, VA 23681

15 Dr. William F. Bates
Lockheed Aeronautical Systems Co.
86 South Cobb Drive
Marietta, GA 30063-0648

16 Dr. Alex Cho
Reynolds Metals Co.
4th and Canal Street
Richmond, VA 23261

17 Mr. E.A. Colvin
Alcoa Technical Center
Route 780, 7th Street Road
Alcoa Center, PA 15069

18 Dr. L.M. Angers
Alcoa Technical Center
Route 780, 7th Street Road
Alcoa Center, PA 15069

19 Dr. Ravi Kahandal
McDonnell Douglas Aerospace
Mail Stop 36-90
3855 Lakewood Blvd.
Long Beach, CA 90846

20 Mr. Fred Casey
Space Transportation Systems Division
Rockwell International
Dept. 289 MC/AC56
12214 Lakewood Blvd.
Downey, CA 90241

21	E.A. Starke, Jr.; UVA
22-24	R.P. Gangloff; MS&E
25	G.E. Stoner; MS&E
26	J.A. Wert; MS&E
27	F.E. Wawner; MS&E
28	J.R. Scully; MS&E
29	E.A. Thornton; MAE
30	C.T. Herakovich; CE and AM
31-32	H. Earnhardt, Clark Hall
33	SEAS Preaward Administration Files
34	Mr. Gwyn Faile Code ED 24 Marshall Space Flight Center Huntsville, AL 35812
35	Mr. Brian McPherson Code ED 24 Marshall Space Flight Center Huntsville, AL 35812
36	Mr. William E. Quist Boeing Aerospace and Electronics Aerospace Group Mail Stop GH-CJ P.O. Box 3707 Seattle, WA 98124
37	Dr. Howard G. Nelson NASA-Ames Research Center EEM: 213-3 Moffett Field, CA 94035
38	Dr. R.G. Forman Mail Code ES-5 NASA-L.B. Johnson Space Flight Center Houston, TX 77058

39 Professor A.K. Noor
Center for Computational Structures Technology
NASA Langley Research Center
Hampton, VA 23681

40 Prof. A.K. Ghosh
Department of Materials Science and Engineering
University of Michigan
2102 Dow Building
Ann Arbor, MI 48109-2136

41 Dr. D. Ferton
Pechiney Centre de Recherches
De Voreppe
B.P. 27 -- 38340 Voreppe
FRANCE

42 Dr. John Papazian
Grumman Aerospace & Electronics
Mail Stop A02-026
Bethpage, NY 11714-3582

43 Dr. Richard Lederich
McDonnell Douglas Aircraft Company
Mail Stop 111-1041
P.O. Box 516
St. Louis, MO 36166

*One reproducible copy Updated March, 1994